north west cancer research

UNIVERSITY OF LIVERPOOL

A three-dimensional study of mitotic spindle ultrastructure

Faye Margaret Nixon

June 2016

Supervisors:
Dr. Stephen Royle
Prof. Ian Prior

This thesis was submitted in accordance with the requirements of the University of Liverpool for the degree of Doctor of Philosophy

Abstract

The mitotic spindle is the complex machinery that enables a cell to segregate its genetic material faithfully. Without fidelity in this process, genetic abnormalities may occur which, in turn, can lead to cancer. Microtubules of the mitotic spindle are bundled together to form kinetochore fibres which contribute to the movement of replicated chromosomes during cell division, helping to ensure the DNA is equally divided.

Electron microscopy has long been used to observe inter-microtubule bridges within kinetochore fibres and, although they are thought to confer stability to the fibres thus ensuring faithful mitosis, their identity and function is yet to be fully established. These inter-microtubule cross-linkers were thought to be simple structures, providing a bridge directly between two microtubules. Here, three dimensional electron microscopy was used to examine these cross-linkers in unprecedented detail – revealing a complex network of microtubule connectors which we have termed 'the mesh'.

To establish the functional role of the mesh, levels of a known microtubule crosslinker, the TACC3-chTOG-clathrin complex, were manipulated. In cells with too much mesh, kinetochore microtubules were found to be disorganised – forming tighter clusters within fibres and deviating from their parallel trajectories. Kinetochore fibres were also found to contain more microtubules than in control cells, and took longer to complete mitosis. These observations provide evidence that the mesh plays a functional role in the organisation within kinetochore fibres, directly impacting the ability of the cell to divide successfully.

In addition to fine kinetochore fibre structure, scanning electron microscopy was optimised to examine changes to the whole spindle structure after manipulation of the mesh. This revealed changes to spindle architecture when microtubule-associated proteins were altered, and offers insight into how cancer can be initiated when these proteins are dysregulated.

Pre-chapter contents

List of Figures and Tables

1. Introduction

2. Materials and Methods

3. Kinetochore fibres contain a network of microtubule connectors – the mesh

4. Manipulating the mesh influences kinetochore fibre organisation

5. Serial Block Face-SEM can be used in conjunction with TEM to provide a more complete picture of spindle architecture

List of abbreviations

2D	Two-dimensional
3D	Three-dimensional
AFM	Atomic force microscopy
ALK	Anaplastic lymphoma kinase
aMT	Astral microtubule
APC/C	Anaphase promoting complex/cyclosome
ATP	Adenoside tri-phosphate
BSA	Bovine serum albumin
CCAN	Constitutive centromere associated network
CCP	Clathrin coated pit
CCV	Clathrin coated vesicle
Cdc20	Cell division cycle 20
Cdk	Cyclin-dependent kinase
CENP	Centromere protein
CHC	Clathrin heavy chain
chTOG	Colonic, hepatic tumour overexpressed gene
CID	Clathrin interaction domain
CIN	Chromosomal instability
CLEM	Correlative light-electron microscopy
CME	Clathrin-mediated endocytosis
CMV	Cytomegalovirus
DAPI	4',6-diamidino-2-phenylindole
ddH_2O	Double-distilled water
DMEM	Dulbecco's Modified Eagle Medium
DNA	Deoxyribonucleic Acid
EDTA	Ethylenediaminetetraacetic acid
EGF	Epidermal growth factor
EGFR	Epidermal growth factor receptor
EGTA	Ethylene glycol tetraacetic acid
EM	Electron microscopy
ER	Endoplasmic reticulum
ESCRT	Endosomal sorting complexes required for transport

FS	Freeze substitution
FBS	Foetal Bovine Serum
G1	Gap-1 phase
G2	Gap-2 phase
GA	Glutaraldehyde
GBM	Glioblastoma
GDP	Guanosine di-phosphate
GFP	Green fluorescent protein
GTP	Guanosine tri-phosphase
HPF	High Pressure Freezing
HURP	Hepatoma up-regulated protein
IF	Immunofluorescence
ipMT	Inter-polar microtubule
KDP	Knock-down proof
K-fibre	Kinetochore fibre
KMN	KNL-1/Mis12/Ndc80 complex
kMT	Kinetochore fibre microtubule
KS	Knock-sideways
LCI	Live cell imaging
LM	Light microscopy
LGN	Leucine-glycine-asparagine repeat-enriched protein
MAP	Microtubule-associated protein
MIA	Multiple Image Alignment
MCC	Mitotic checkpoint complex
MT	Microtubule
MTOC	Microtubule organising centre
Ndc80	Nuclear division cycle 80 complex
NEBD	Nuclear envelope breakdown
NTD	N-terminal domain
NuMA	Nuclear and mitotic apparatus protein
NuSAP	Nuclear and spindle associated protein
OE	Over-expressing
OsO_4	Osmium Tetroxide
PCM	Peri-centriolar matrix
PIPES	1,4-Piperazinediethanesulfonic acid

PBS	Phosphate-buffered saline
PFA	Paraformaldehyde
PRC1	Protein regulator of cytokinesis 1
SAC	Spindle assembly checkpoint
SBF-SEM	Serial block face scanning electron microscopy
SEM	Scanning Electron Microscopy
TACC3	Transforming Acidic Coiled Coil protein 3
TCH	Thiocarbohydrazide
TEM	Transmission Electron Microscopy
TFE3	Transcription factor binding to IGHM enhancer 3
TPX2	Targeting protein for Xklp2
TRE	Tetracycline Response Element
Rb	Retinoblastoma
RPE1	Retinal pigment epithelial cells
RT	Room temperature
rtTA	Reverse tetracycline-controlled transactivator
UA	Uranyl Acetate
γTuRC	Gamma tubulin ring complex

Acknowledgements

I would like to thank several people who have helped me through the last three years, and made the completion of this thesis possible.

First I would like to thank my supervisors, Stephen Royle and Ian Prior. Steve has been enthusiastic and supportive throughout my time in his lab, which has helped me to realise my potential. Ian has been a great second supervisor, always on hand to offer his advice and another perspective on this project.

I am also grateful to members of the Royle lab (past and present) who have helped me over the years, and members of the MCBB for making my move to Warwick so easy and my experience there so enjoyable.

A special thanks goes to Alison Beckett, who has spent many hours teaching me about electron microscopy over the past three years. We shared many (packets of) biscuits, and she helped me through my first year in Liverpool, for which I am truly grateful.

Most importantly, I would like to thank my family. Their love, support and encouragement means the world to me - and if I have achieved anything in my life so far, it is down to them.

Finally, Neil - the most unexpected finding of my Ph.D. Thank you for everything.

This work was generously funded by North West Cancer Research.

1. Introduction

1.1 The Cell Cycle

The mammalian cell cycle is a series of tightly regulated events, the purpose of which is to duplicate genetic material and ultimately segregate this material into two new daughter cells. The tight coordination and regulation of this process is vital, as any errors during cell division may result in new daughter cells with incorrect genetic material, such as too many or too few chromosomes – a state known as aneuploidy.

Aneuploidy has been recognised as a hallmark of cancer for many years (Hansemann, 1890; Boveri, 1914) although the relationship between aneuploidy and cancer is yet to be fully understood – is it a cause or a consequence of tumourigenesis? Not only cancer, aneuploidy is also associated with birth defects such as Down's Syndrome, or Trisomy 21, where a child inherits three copies of chromosome 21 as a result of incorrect cell division during gametogenesis in its parents (DeGrouchy, 1970).

The cell cycle can be divided into stages: Interphase, comprising of three phases – G1 (Gap-1), S (synthesis)-phase and G2 (Gap-2); mitosis; and cytokinesis. The phases contained within interphase allow the cell to grow, synthesise new DNA, and prepare for mitosis. During mitosis, the newly synthesised DNA is segregated into two halves of the cell, and in cytokinesis cleavage of the mother cell produces two new daughter cells.

The process of cell division is tightly controlled in order to prevent errors. The main molecules involved in this regulation are the cyclin-dependent kinases (Cdks) and their functional partners, the cyclins. Cdks were first identified in *S. pombe* and *S. cerevisiae* as molecules essential for cell division (Russell and Nurse, 1986). The cyclins were discovered independently in sea urchin eggs as an array of proteins that were expressed and destroyed in waves throughout the cell cycle (Evans et al., 1983; Malumbres and Barbacid, 2005). The synergy between the cyclins and Cdks

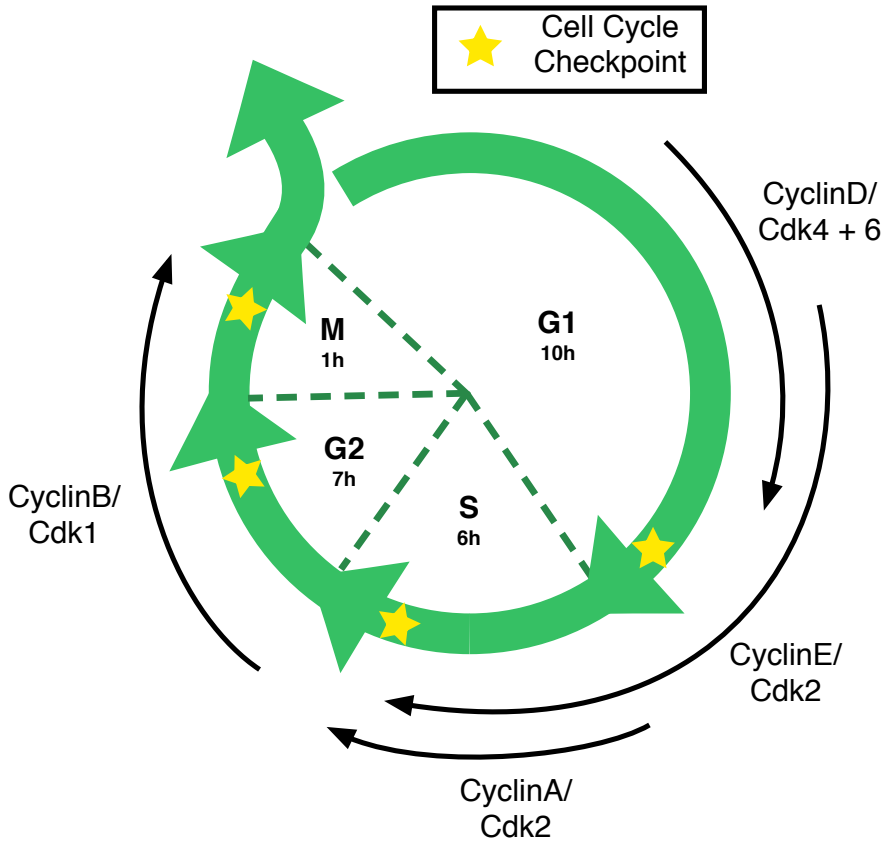

Figure 1.1: The cell cycle. This figure shows a schematic diagram of the phases of the cell cycle, including the approximate duration of each stage in HeLa cells in culture and the contribution of cyclins and Cdks to progression through these stages. Regulation of progression through the cell cycle is achieved by phosphorylation and dephosphorylation, synthesis and degradation of these proteins – coupled with checkpoints throughout which prevent uncontrolled progression and cell division. Without cell cycle control cells can propagate unhindered, potentially resulting in aneuploidy and cancer.

was established in 1989 when interaction was reported between key cell cycle players – Cdk1 and the A- and B-type cyclins (Nurse, 1990). Throughout G1, many genes that are required during the cell cycle begin to be transcribed. Upon arrival of mitogenic signals, cyclin D proteins are transcribed, enabling the Cdk4/6-cyclin D complex to phosphorylate the Retinoblastoma (Rb) family of proteins (Sherr and Roberts, 1999; Ciemerych and Sicinski, 2005). This phosphorylation results in the de-repression of the replication machinery, allowing DNA synthesis to begin. Rb proteins are also responsible for the transcription of cyclin E which forms a complex with Cdk2 (Odajima et al., 2011). Cdk2-cyclin E inactivate Rb proteins thereby releasing the cells from activation by mitogenic signals (Chen et al., 2009; Marais et al., 2010). Cdk2-cyclin E is required for the completion of G1 and is essential for DNA replication, and therefore must be inactivated to prevent the re-replication of DNA during S-phase (Hwang and Clurman, 2005).

Cyclins A and B are transcribed throughout S-phase (Chen et al., 2009; Marais et al., 2010). Cdk2, no longer in complex with cyclin E is free to bind cyclin A and induce the phosphorylation of proteins that are needed for the completion of S-phase. Throughout G2, cyclin A is degraded, but cyclin B continues to be synthesised allowing cyclin B-Cdk1 complexes to form. This is a particularly important association as cyclin B-Cdk1 phosphorylates a large number of proteins that are required for the induction of mitosis, including golgi disassembly, chromosome condensation and centrosome separation (Nigg, 2001). The Anaphase Promoting Complex/Cyclosome (APC/C) induces the degradation of cyclin B-Cdk1 via ubiquitination, signalling exit from mitosis (Harper et al., 2002). Cells may then continue rounds of cell division, or enter G0 (“quiescence”) where no proliferation takes place. See Figure 1.1 for schematic of the stages of the cell cycle.

The study described in this thesis focusses on human cells and so the following introductory information describes mammalian cell division, where centrosomes (described in more detail in section 1.3) act as the primary organising centre for the developing mitotic spindle.

1.2 Stages of mitosis

1.2.1 Prophase

Prophase is the first stage of mitosis and is marked by several alterations and rearrangements within the cell. DNA becomes supercoiled upon initiation of chromatin condensation (Kimura and Hirano, 1997). This forms chromosomes consisting of two identical sister chromatids – each destined for segregation into a new cell. Centrosomes, the microtubule (MT) organising centres (MTOCs) of the cell, relocate to either side of the nucleus having been duplicated in interphase, and MT asters radiate out from them, marking a significant increase in MT nucleation (Kuriyama and Borisy, 1981) and dynamics (Saxton et al., 1984). MTs and centrosomes are discussed in greater detail in section 1.3. These duplicated centrosomes, consisting of two centrioles, will form the poles of the dividing cell thus influencing the site of cleavage into two daughter cells. The membraneous organelles of the cell including the golgi apparatus and endoplasmic reticulum (ER) undergo fragmentation and vesiculation to aid in the equal partitioning of these organelles between the new cells (Birky, 1983). The onset of mitosis also marks the cessation of clathrin-mediated endocytosis (CME) as the increase in membrane tension demands assistance from the actin cytoskeleton for CME to occur, while the actin is otherwise engaged in forming the rigid cortex of the mitotic cell (Kaur et al., 2014). The cell passes the "point of no return' in late prophase with rapid activation of cyclin B-Cdk1, at which time the cell is committed to division (Pines and Rieder, 2001). The end of prophase sees nuclear envelope breakdown (NEBD), releasing the chromosomes into the cytoplasm.

1.2.2 Prometaphase

The goal of prometaphase is to congress the newly-liberated chromosomes at the cell equator in a bioriented manner – with each sister chromatid stably attached to opposite poles in preparation for segregation into either hemisphere of the cell. To do this the cell utilises the mitotic spindle apparatus, which matures during this stage of mitosis. The basic functional unit of the mitotic spindle is the microtubule, a protein polymer that forms part of the cell cytoskeleton. In one mechanism of spindle

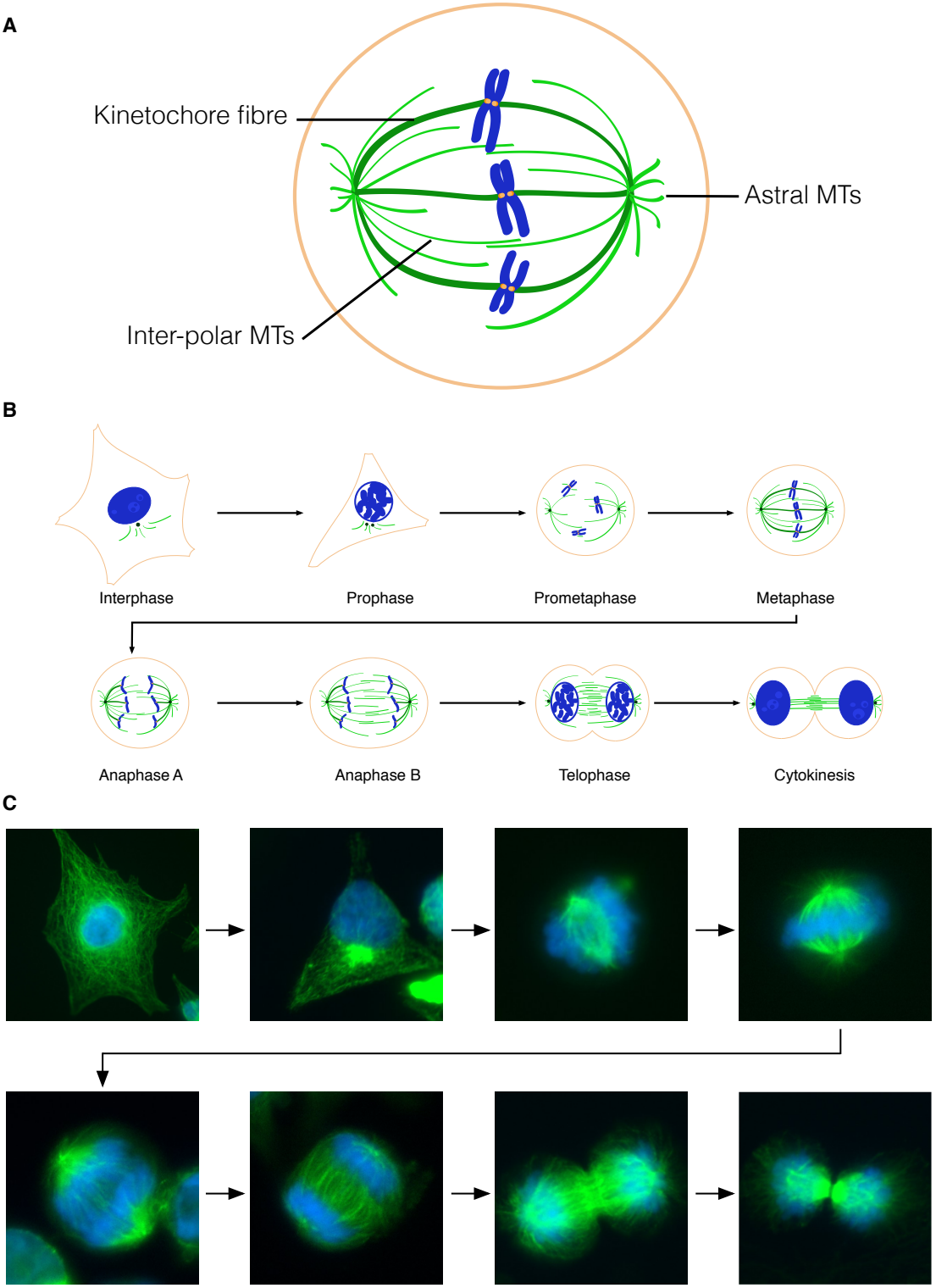

Figure 1.2: The stages of mitosis. A: cartoon representation of a metaphase cell, illustrating the positions of the astral MTs, the inter-polar MTs, and the K-fibre bundles as they extend out to contact the kinetochores of each sister chromatid, aligned on the metaphase plate at the cell equator. **B**: cartoon representation of a cell's progression through mitosis – from aligning the chromosomes in prometaphase, to separating them during anaphase, and dividing the cell itself in cytokinesis. This is coupled with equivalent fluorescent images in **C**. In all cases, DNA is shown in blue and MTs/tubulin shown in green.

assembly, MTs are nucleated at the centrosomes at either pole of the cell and radiate out from this point into the cytosol in order to capture free chromosomes. A bipolar spindle apparatus is essential for successful mitosis and the two growing MT asters promote its formation. As MTs grow radially from the centrosomes, the likelihood of encountering a chromosome is increased (McIntosh et al., 2002). The dynamic instability exhibited by these MTs results in their rapid polymerisation and depolymerisation (Desai and Mitchison, 1997). In this way, they can quickly explore the cell space around the centrosomes for chromosomes (Holy and Leibler, 1994). In fact, cells are capable of assembling a bipolar spindle through several methods which can act cooperatively, and in conjunction with MT dynamics and the action of motor proteins, to result in a functional spindle apparatus. Spindle assembly pathways are discussed in greater detail in section 1.3.1.4. The kinetochore is a complex protein assembly at the centromere of each sister chromatid and is the site of attachment between chromosomes and the mitotic spindle (discussed in greater detail in section 1.3.1.6). Once amphitelic attachment of each sister chromatid occurs – sister kinetochores are stably attached to opposite poles – the action of MT dynamics and motor proteins within the spindle reposition the chromosomes to the cell equator, termed the metaphase plate, in a process known as congression. MTs stably attached to both the pole and the kinetochore are termed kinetochore MTs (kMTs) and are protected from depolymerisation.

In addition to capture of kinetochores by kMTs, populations of MTs termed astral MTs (aMTs) and interpolar MTs (ipMTs) also develop in prometaphase. aMTs radiate from the centrosome to the cell cortex and play an important role in the anchoring of centrosomes. ipMTs extend from the centrosome to the chromosomes, interacting with ipMTs from the opposite pole via motor and MT-associated proteins (MAPs) and help to keep spindle poles separated in space (McIntosh and Pfarr, 1991). The mitotic spindle, and the classes of MT found within it, are described further in section 1.3.

When all chromosomes are bioriented on the metaphase plate, prometaphase is complete.

1.2.3 Metaphase

Upon reaching metaphase, the chromosomes have congressed to the metaphase plate, with each sister chromatid stably-attached to opposite poles via their respective sister kinetochores. Bundles of kMTs, (termed Kinetochore fibres, or K-fibres) continue to accumulate MTs into the rest of the bundle. K-fibres contain 20-40 kMTs in mammalian cells, and it is these fibres that are responsible for the generation of force required to segregate the sister chromatids in anaphase. K-fibres create tension and cause stretching of kinetochores and centromeric DNA through net lengthening and shortening of the fibres causing Poleward (P) or Antipoleward (AP) movements of the kinetochores. These P and AP movements manifest themselves as kinetochore oscillations on the metaphase plate and allow for the stabilisation of kMT-kinetochore attachments and the generation of tension within the kinetochore. These conditions are needed for the satisfaction of the Spindle Assembly Checkpoint (SAC) and thus progression to anaphase (Nezi and Musacchio, 2009). The SAC prevents anaphase from occurring until all chromosomes are bioriented and stably-attached to K-fibres, thus maintaining the integrity of the genetic material and preventing aneuploidy (Musacchio and Salmon, 2007).

When the SAC is active, a mitotic checkpoint complex (MCC) inhibits the Anaphase Promoting Complex/Cyclosome (APC/C) (Musacchio and Salmon, 2007) preventing degradation of cyclin B-Cdk1 and separation of sister chromatids. Checkpoint proteins at the kinetochore play an integral role in this process. A Mad1-Mad2 complex at the kinetochore produces a form of Mad2 which inhibits activation of the APC/C by Cdc20 (Musacchio, 2011). However, when kinetochores accumulate kMTs and tension is generated, Mad1-Mad2 becomes depleted from kinetochores (Musacchio and Salmon, 2007; Maldonado and Kapoor, 2011), Cdc20 activates the APC/C, resulting in the initiation of anaphase. Cohesin keeps sister chromatids attached to each other until the metaphase to anaphase transition (Nasmyth et al., 2000), at which point separase acts to cleave cohesin and release sister chromatids. The activation of the APC/C initiates this by degrading securin, the protein keeping separase inactive until the cell is cleared for anaphase (Uhlmann et al., 1999; Uhlmann et al., 2000).

1.2.4 Anaphase

After proteolysis of cohesin causes the loss of connection between sister chromatids, each sister can be segregated to opposing poles, in a process called anaphase. Two mechanisms of action are utilised to do this. In anaphase A, the normal MT flux which maintains a constant spindle length (Ganem and Compton, 2006) by assembly of tubulin subunits at MT plus-ends at the chromosomes coupled with disassembly at the poles, undergoes a switch whereby tubulin is no longer incorporated into the plus-ends of kMTs and they begin to depolymerise. kMTs remain attached to kinetochores, thus resulting in poleward chromatid movements (Gorbsky et al., 1987; Gorbsky et al., 1988; Mitchison and Salmon, 1992; Compton, 2002). In anaphase B, spindle elongation occurs as antiparallel ipMTs at the spindle midzone are crosslinked by the motor kinesin-5 which slides them apart (Sharp et al., 1999; Sharp et al., 2000; Sharp et al., 2000b; McIntosh and McDonald, 1989; McIntosh et al., 1979; Saxton and McIntosh, 1987). These two complementary processes result in the separation of the sister chromatids, although the contribution of each varies in different organisms (Brust-Mascher and Scholey, 2011).

1.2.5 Telophase

Telophase marks the stage at which the separated sister chromatids are further partitioned by the formation of a new nuclear membrane, derived almost entirely from the ER membrane that was fragmented at the onset of mitosis (Larijani and Poccia, 2009), and the ingression of the cell membrane along the cleavage plane at the cell equator. As the nuclear envelope reforms, the genetic material decondenses. Accumulation of actin and myosin II at the cleavage furrow is required for assembly of the acto-myosin contractile ring, the responsibility of which is to mediate the ingression of the membrane (Cao and Wang, 1990). As the contractile ring causes constriction of the membrane, the ipMTs become more densely packed, at which point the action of MT-crosslinking proteins becomes especially important. For example, the functions of the MAP65 family members (PRC1 in humans) are important for forming the central spindle structure (Jiang et al., 1998), and for the recruitment of signalling and motor proteins to this structure (Subramanian et al., 2010; Neef et

al., 2005). These processes mark the end of mitosis and the beginning of the final event of cytokinesis: abscission of the two daughter cells.

1.2.6 Cytokinesis

Cytokinesis is the last step in the process of cell division – the point at which the two new daughter cells are physically separated from one another. The point of ingression of the cell membrane, the cleavage furrow, occurs at the equator of the cell where there is an abundance of interdigitating antiparallel MTs between the chromatids as they are segregated – the midzone (Bringmann and Hyman 2005; Dechant and Glotzer, 2003). At the furrow, actin and myosin are organised into the actomyosin contractile ring, regulated by the local activation of the GTPase RhoA at this site (Jantsch-Plunger et al., 2000). As this ring constricts, the midzone MTs are bundled tightly to form the midbody. Abscission is the final cytokinetic event, where the two cells are divided, and this process is mediated by the ESCRT machinery which provides the necessary constrictive force (Elia et al., 2011; Guizetti et al., 2011; Carlton et al., 2008). It is vital that this event is controlled, to ensure that the DNA has been faithfully segregated and prevent damage to any lagging chromosomes. Cdk1 is in part responsible for this temporal control, being inactivated at the metaphase to anaphase transition (Barr and Gruneberg, 2007; Wurzenberger and Gerlich, 2011). Aurora B kinase also controls this process, providing a “NoCut” checkpoint preventing premature abscission (Mendoza et al., 2009; Steigemann et al., 2009; Norden et al., 2006). ESCRT proteins form the scission machinery, generating the constrictive force required to complete cytokinesis (Carlton et al., 2008; Guizetti et al., 2011; Elia et al., 2011). Figure 1.2 shows a diagrammatic representation of the stages of mitosis.

1.3 Microtubules and the mitotic spindle

MTs have many important functions in cells both in interphase and mitosis – including cell migration (Bershadsky et al., 1991; Liao et al., 1995), transport of cargo in vesicles via motors proteins (Schnapp and Reese, 1989; Schroer et al., 1989), and the growth of axons in the developing nervous system (Yamada et al., 1971.,

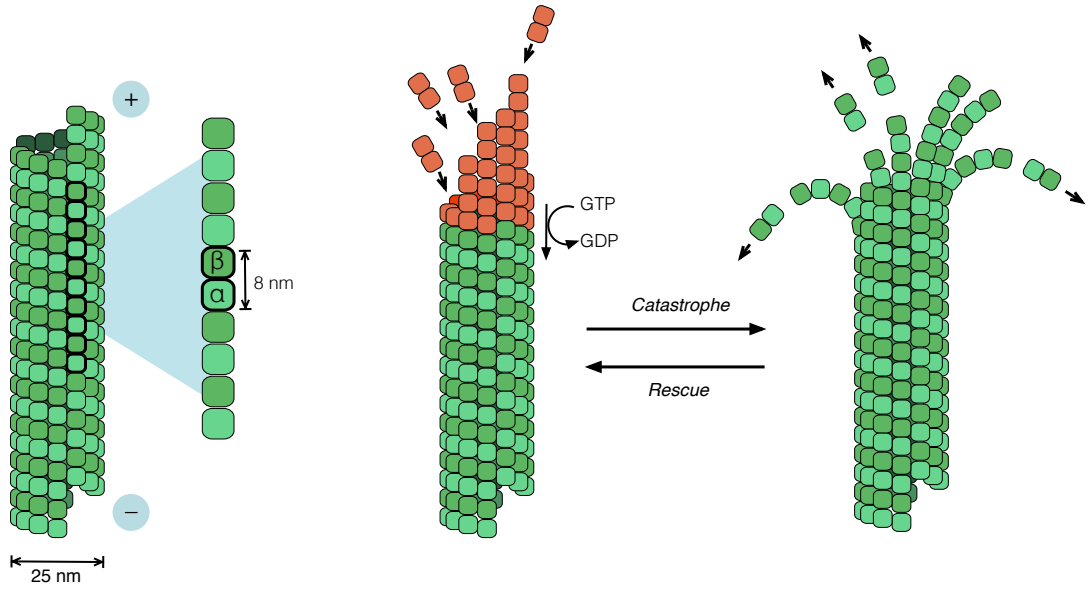

Figure 1.3: Structure of microtubules. This figure shows a cartoon representation of a section of a MT. Highlighted is the αβ-tubulin heterodimer, and how these combine in a head-to-tail conformation to form a single protofilament. Thirteen protofilaments associate laterally into a tube structure – the microtubule. GTP-tubulin heterodimers (orange) associate with the growing MT tip, with the GTP being hydrolysed to GDP as it is incorporated into the MT lattice. This 'GTP cap' prevents depolymerisation of the MT, but when this cap is lost MTs switch from growth to shrinkage (*catastrophe*), with protofilaments unfurling and peeling away from the lattice. When the GTP cap is recovered, the MT switches back from shrinkage to growth (*rescue*). This behaviour is termed 'dynamic instability'.

Bamburg et al., 1986). MTs also form the principal component of the mitotic spindle, enabling cells to segregate their genetic material. The many functions of MTs in the cell stem from their structure, and the characteristic behaviours which result from this (see Figure 1.3).

A single MT subunit is a heterodimer comprised of one α- and one β-tubulin. αβ-tubulin subunits polymerise in a head-to-tail manner to form protofilaments (Amos and Klug, 1974) which subsequently join laterally, curve, and seal into a tube along the MT seam (Mandelkow et al., 1986a; Mandelkow et al., 1986b). MTs can contain varying numbers of protofilaments, but MTs most commonly seen in the mitotic spindle contain 13 protofilaments (Evans et al., 1985). Assembly of MTs requires energy which is generated by the hydrolysis of GTP tubulin to GDP tubulin upon incorporation of the subunit into the MT lattice.

MTs are inherently polar macromolecules due to their αβ-tubulin subunits, and because β-tubulin is capable of hydrolysing GTP to GDP (Weisenberg et al., 1976), tubulin subunits are readily added to this MT tip. As a result, this is called the "plus-end", while the slower-growing α-tubulin-exposed tip is called the "minus-end".

These important features confer 'dynamic instability' to the MTs, allowing them to switch stochastically between phases of growth and shrinkage. The presence of a stabilising 'GTP cap', where the newly added GTP-tubulin has not yet been hydrolysed to GDP-tubulin, was postulated to influence whether a MT undergoes growth or shrinkage (Mitchison and Kirschner, 1984). When the GTP-tubulin cap is lost, GDP-tubulin is rapidly lost from the end of the MT – a process termed 'catastrophe'. When the cap is restored, polymerisation can resume – termed 'rescue'.

1.3.1 The metaphase mitotic spindle

When the mitotic spindle was first described in the early 1880s (Flemming, 1882; Wilson, 1925; Schrader, 1953.) it was clear that force was being generated along the spindle axis in order to segregate the sister chromatids, pulling them to the cell poles and ultimately being separated by cytokinesis. Today it is known that the mitotic

spindle is comprised of many MTs that, in concert with hundreds of MT-associated motor and non-motor proteins, generate the forces necessary to perform this vital cellular function. This study investigates the mitotic spindle at metaphase, so this will be the focus of the following sections.

1.3.1.1 Astral microtubules

Astral MTs (aMT) are so-named because they radiate in asters out from the centrosomes at the poles of the cell, as well as extending out towards the chromatin. These MTs act to position the mitotic spindle in the centre of the cell through forces exerted on the MT by the interaction of dynactin at specific sites of the cell cortex with dynein motors (Korden and Vale, 2009). aMTs anchor the centrosomes in position at the pole, acting as a brace for the generation of forces needed to separate the chomatids.

1.3.1.2 Interpolar microtubules

Interpolar MTs (ipMT), often referred to as spindle MTs or non-kinetochore MTs, extend out into the spindle from the centrosome, terminating at various distances from the cell pole, sometimes extending to the opposite pole (McDonald *et al.*, 1992, McIntosh and Landis, 1971). ipMTs originating from like poles run parallel to each other, and are able to interact with antiparallel MTs from the opposite pole. Although ipMTs interact, they do not form large bundles. At metaphase, bundles of 2 – 4 MTs can be found, increasing up to 6 MTs as the cell progresses to anaphase – eventually becoming the central spindle and ultimately the midbody as mitosis comes to a close (Mastronarde et al., 1993). The anti-parallel sliding activity and elongation of ipMTs contributes to the separation of centrosomes during anaphase B (McIntosh et al., 1979, Masuda et al., 1988, Hogan and Cande, 1990, Ding et al., 1993; Aist and Bayles, 1991; Saxton and McIntosh, 1987).

1.3.1.3 Kinetochore microtubules

Kinetochore MTs (kMT) are MTs which connect the sister chromatids to the cell poles via the kinetochore at the centromere of each sister. In mammalian cells, kMTs exist

in bundles of between 20-40 MTs (Rieder, 1982), depending on the diameter of the kinetochore to which they are attached. These bundles of kMTs are termed kinetochore fibres (K-fibres) and have a role in the capture of chromosomes, their congression to the metaphase plate, and segregation of sister chromatids during anaphase. Studies using EM to examine K-fibres identified some MTs in K-fibre bundles that run continuously from the pole to the kinetochore, suggesting that K-fibres are responsible for the transduction and propagation of force during anaphase to segregate the sister chromatids to their respective poles (McDonald et al., 1992; Witt et al., 1981; Church and Lin, 1982; Nicklas et al., 1982; Rieder, 1981). Recent work suggests that K-fibre bundles themselves may not all be directly connecting chromosomes to the pole, however, and that some K-fibres are connected to the pole via interaction with K-fibres of adjacent chromosomes (Sikirzhytski et al., 2014).

In the first instance, K-fibres form from chance encounters as aMTs radiating out from the centrosome are captured by kinetochores and are protected from depolymerisation (Zaytsev and Grishchuk, 2015; Review: Rieder 2005; Rieder and Borisy, 1981; Kirschner and Mitchison, 1986). Simultaneously, MTs are nucleated from unattached kinetochores which then continue to grow before being captured by aMTs and incorporated into the bipolar spindle array through the action of MT-associated motor proteins (Maiato et al., 2004, Khodjakov et al., 2003). These alternative spindle assembly pathways, acting together, result in the formation of K-fibres.

At metaphase when K-fibres are mature, kMTs exist in a state of poleward MT flux, regulating the spindle length and generating tension at kinetochores (Shimamoto, 2011). In MT flux tubulin subunits are incorporated into MT plus ends at the kinetochore, while simultaneously being lost from the MT minus ends which are anchored at the cell pole (Mitchison, 1989).

The force necessary to pull sister chromatids through the viscous cytoplasm is achieved through depolymerisation of kinetochore-associated MTs during anaphase. In fact, K-fibres are able to generate forces greatly surpassing the force actually needed to pull each sister, as demonstrated by needle manipulation experiments (Nicklas, 1983). One single depolymerising MT is thought to produce in the order of 50 pN of force (Grishchuk et al., 2005), with the force needed to overcome the viscous

drag on chromosomes itself being only tens of pico-Newtons (McIntosh et al., 2012). How depolymerising MTs maintain their association with kinetochores is still unresolved. In yeast, the Dam1 ring complex couples the disassembly of MT plus ends to the movement of chromosomes (Cheeseman et al., 2001). However, no homologue of this complex has yet been found in vertebrates. A study by McIntosh *et al.* using electron tomography identified thin fibrils emanating from the kinetochore and contacting protofilaments of kMTs, suggesting this type of connection, rather than a ring structure, could be responsible for maintaining kinetochore-MT attachment (McIntosh et al., 2008). One candidate for these connections is the Ska1 complex, a component of the human kinetochore that has been shown to form part of the kinetochore-MT interface and possess the ability to couple cargo to depolymerising MTs in vitro (Welburn et al., 2009). The exact mechanism cells use to execute this remains to be elucidated.

1.3.1.4 Additional spindle microtubules

In addition to the MTs that fall into the classes previously discussed, there are MTs present in the spindle which are not nucleated at the centrosomes or kinetochores and so do not conform to the definitions of aMTs, ipMTs or kMTs as described here. It is known that MTs can be nucleated within the spindle via existing MTs, significantly increasing the number of MTs present in the spindle (Goshima et al., 2008; Uehara et al., 2009). These MTs are then organised through the action of MAPs, contributing to the formation of a robust bipolar spindle (Burbank et al., 2007; Lecland and Luders, 2014). The augmin complex has been found to play an important role in intra-spindle MT nucleation, and is discussed further in the following section.

1.3.1.5 Pathways of mitotic spindle assembly

Early work proposed two models of spindle assembly. One model, termed “search and capture” proposed that MT growth and shrinkage from centrosomes is sufficient to capture kinetochores, stabilise kMTs, and result in the formation of a bipolar spindle (Kirschner and Mitchison, 1986). A second model – “self-assembly” or “self-organisation” – used observations that MTs could also be nucleated in the vicinity of mitotic chromatin, leading to spindle formation when coupled with the action of MT

motors, and centrosomes for spindle positioning (Karsenti et al., 1984; Steffen et al., 1986). This chromatin-mediated MT nucleation is dependent on a RanGTP gradient found in the cell, with the highest concentration being localised at chromatin. This gradient stimulates MT nucleation through the action of different proteins depending on cell type and species (Kalab and Heald, 2008; Terry et al., 2007; Goodman and Zheng, 2006; Clarke and Zhang, 2004). See Figure 1.4 for a diagram of factors contributing to spindle assembly.

It seems clear, however, that neither of these assembly pathways is the sole route of spindle formation and that coordination of multiple assembly pathways results in the formation of the mitotic spindle apparatus. Centrosomes are dispensable for generation of a functional spindle (Khodjakov et al., 2000; Megraw et al., 2001), and decreasing chromatin-mediated nucleation results in an increase in growth rate from aMTs (Hayward et al., 2014), demonstrating that alternate mechanisms can compensate for loss of another.

Another key player in spindle assembly is the augmin complex, which was demonstrated to be responsible for MT-dependent MT nucleation by recruiting γ-tubulin to existing MTs, increasing the density of MTs in the spindle (Goshima et al., 2007; Goshima et al., 2008; Uehara et al., 2009; Wainman et al., 2009). Recent studies in *Drosophila* syncytial embryos demonstrate the importance of this pathway, with chromatin-generated MTs and MT output from centrosomes both being delayed when augmin is inactivated (Hayward et al., 2014). Hayward *et al.* demonstrated that *Drosophila* syncytial embryos possess each of the discussed spindle assembly pathways and use them synergistically to form their spindle apparatus. The authors postulate that centrosomes lead the spindle assembly process due to their being exposed to αβ-tubulin and 'preprimed' for MT nucleation before NEBD.

Goshima *et al.* propose a model where initial kMTs generated centrosomally or via chromatin-mediated nucleation are important for commencing spindle assembly, and provide a template from which augmin can increase nucleation and therefore MT density in the spindle – contributing to K-fibre formation and capture of kinetochores (Goshima et al., 2008).

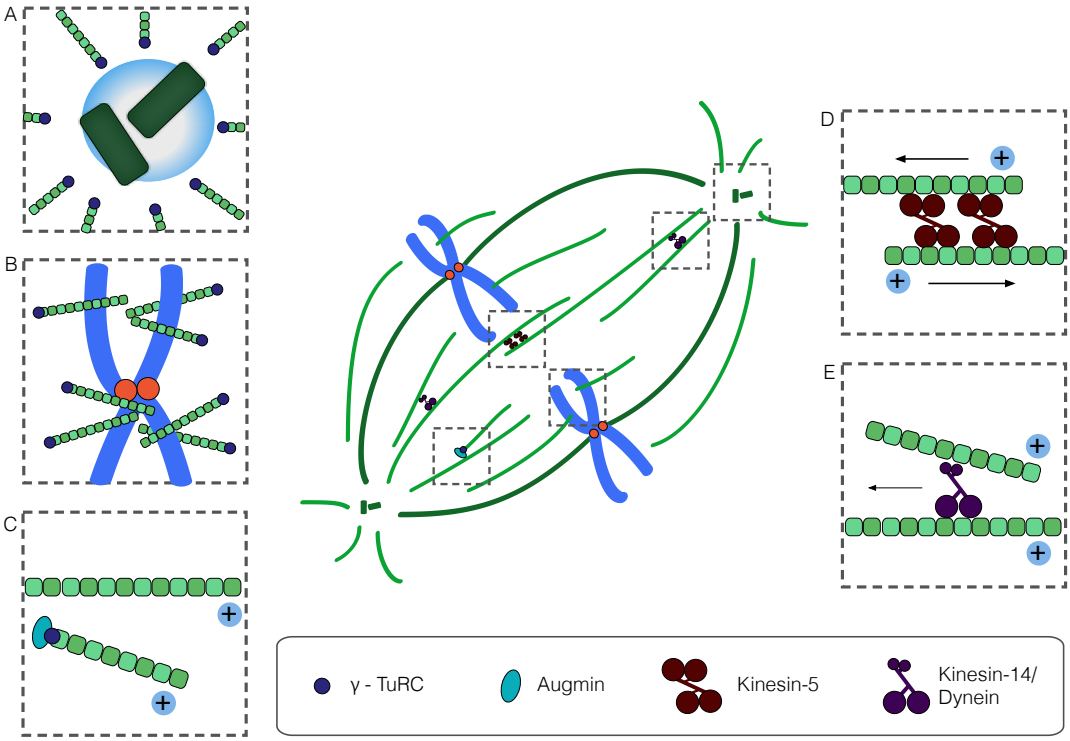

Figure 1.4: The mammalian mitotic spindle and its assembly. There are several mechanisms of spindle assembly and maintenance, each used to varying degrees by different species. Some of these mechanisms are highlighted in this cartoon representation of the mitotic spindle. Highlighted in **A** is the centrosome, comprising of two centrioles. Centrosomes reside at the poles of the cell and can nucleate MTs through the action of the γ-tubulin ring complex (γ-TuRC). The centrosomes nucleate MTs in asters which contact the cell cortex, maintaining spindle position, and MTs which explore the cytoplasm to capture chromosomes. **B** illustrates how MTs are also nucleated at chromatin, contributing to the building of the spindle. **C** highlights the augmin complex which, as the name suggests, augments the spindle by nucleating more MTs from existing MTs through recruitment of γ-TuRC. The spindle is also organised through the action of MT motor proteins. Kinesin-5 associates with anti-parallel MTs, contributing to this organisation through MT sliding via minus-end directed transport (**D**). Dynein and kinesin-14 act to focus the MTs at the poles through poleward, minus-end directed transport (**E**). Figure adapted from Wang et al., 2014.

1.3.1.6 Centrosomes

Centrosomes are often described as the major MT organising centre (MTOC) in many species. They have a unique structure, comprised of two MT-based barrel-shaped centrioles, arranged orthogonally to each other (Bobinnec et al., 1998; Bornens, 2002). An individual centriole has a cartwheel structure consisting of a central circular hub, from which nine 'spokes' radiate outwards. At the terminus of each spoke exists a MT 'blade' composed of a MT triplet. These triplet MT blades form the wall of the centriole cylinder (Marshall, 2001; Preble et al., 2000). Surrounding the two centrioles is a cloud-like matrix of proteins, referred to as the peri-centriolar matrix (PCM).

Centrosomes aid in the formation of the mitotic spindle by nucleating and anchoring new MTs in the peri-centriolar matrix (PCM), where the γ-tubulin ring complex (γ-TuRC) protects the MT minus end from depolymerisation (Moritz et al., 1995; Gould and Borisy, 1977; Pereira and Schiebel, 1997).

The centrosome duplication cycle is tightly coupled to the cell division cycle – when these two cycles are miscoordinated, supernumary centrioles can occur, which is a common feature of cancerous cells and results in aneuploidy (Godinho and Pellman, 2014; Nigg et al., 2014). New cells have one centrosome comprising two associated centrioles. In G1 phase, the centrioles become disengaged from each other, tethered loosely. In G1/S phase, a procentriole beings to be assembled perpendicular to each centriole, which continues to elongate as the cell progresses through G2 phase. As the cell prepares for mitosis, the original 'mother' centriole increases its MT nucleating capabilities through accumulation of additional PCM, before the tether between the mother centrioles release, and they are free to travel to opposite sides of the cell where they will form the spindle poles during mitosis (Fu et al., 2015).

Although centrosomes are important in many species, biological systems do exist in which a bipolar spindle is formed in the absence of centrosomes. For example, in meiosis of several species including mouse, *Drosophila* and *C. elegans* a bipolar spindle is formed without centrosomes (Radford et al., 2012; Szollozi et al., 1972; Theurkauf et al., 1992; Albertson and Thomson, 1993). Cell wall-encased plant cells are also known to organise their spindle in the absence of discrete MTOCs (Dhonukshe et al., 2006; Marc, 1997).

1.3.1.7 Kinetochores

The kinetochore is a large macromolecular protein assembly which acts as the site of attachment between the mitotic spindle and the chromosomes (Figure 1.5), required for their accurate segregation. In 1985, the first protein components of the kinetochore were characterised (Earnshaw and Rothfield, 1985), but today it is known that the kinetochore is a complex, dynamic machine functioning through the action of more than 100 different proteins (Cheeseman and Desai, 2008). Although it is clear that the kinetochore is a key player in accurate mitosis, there are some situations in which chromosomes are segregated independently of kinetochores (Muscat et al., 2015).

EM studies using conventional chemical fixation presented the structure of the kinetochore as being trilaminar – composed of three distinct domains – an inner plate associated with centromeric DNA, an electron-lucent middle plate, and an outer electron-dense plate to which spindle MTs bind (Jokelainen, 1967; Rieder, 1982; McEwen et al., 1993). However, more recent studies using optimised methods of fixation have demonstrated that the middle plate is exaggerated – an artefact of chemical fixation – and in fact the kinetochore comprises fibrous material organised into a thick mat, directly connected to centromeric DNA (McEwen et al., 1998).

Kinetochores are assembled on centromeric DNA as a result of a CENP-A-containing nucleosome upon which the rest of the kinetochore proteins are recruited (Cleveland et al., 2003; Musacchio and Hardwick, 2002). Throughout the cell cycle, a number of proteins are present at this centromeric DNA, comprising the CCAN – constitutive centromere associated network (Cheeseman and Desai, 2008) – which acts as a scaffold for the rapid recruitment of outer kinetochore proteins (Gascoigne and Cheeseman, 2013). These outer kinetochore proteins form connections with spindle MTs, with the Ndc80 complex being proposed to be responsible for forming stable interactions with these MTs. As previously discussed, the Ska1 complex is thought to play an important role in MT attachments during depolymerisation, and it is thought that Ska1 confers this ability to the Ndc80 complex (Schmidt et al., 2012).

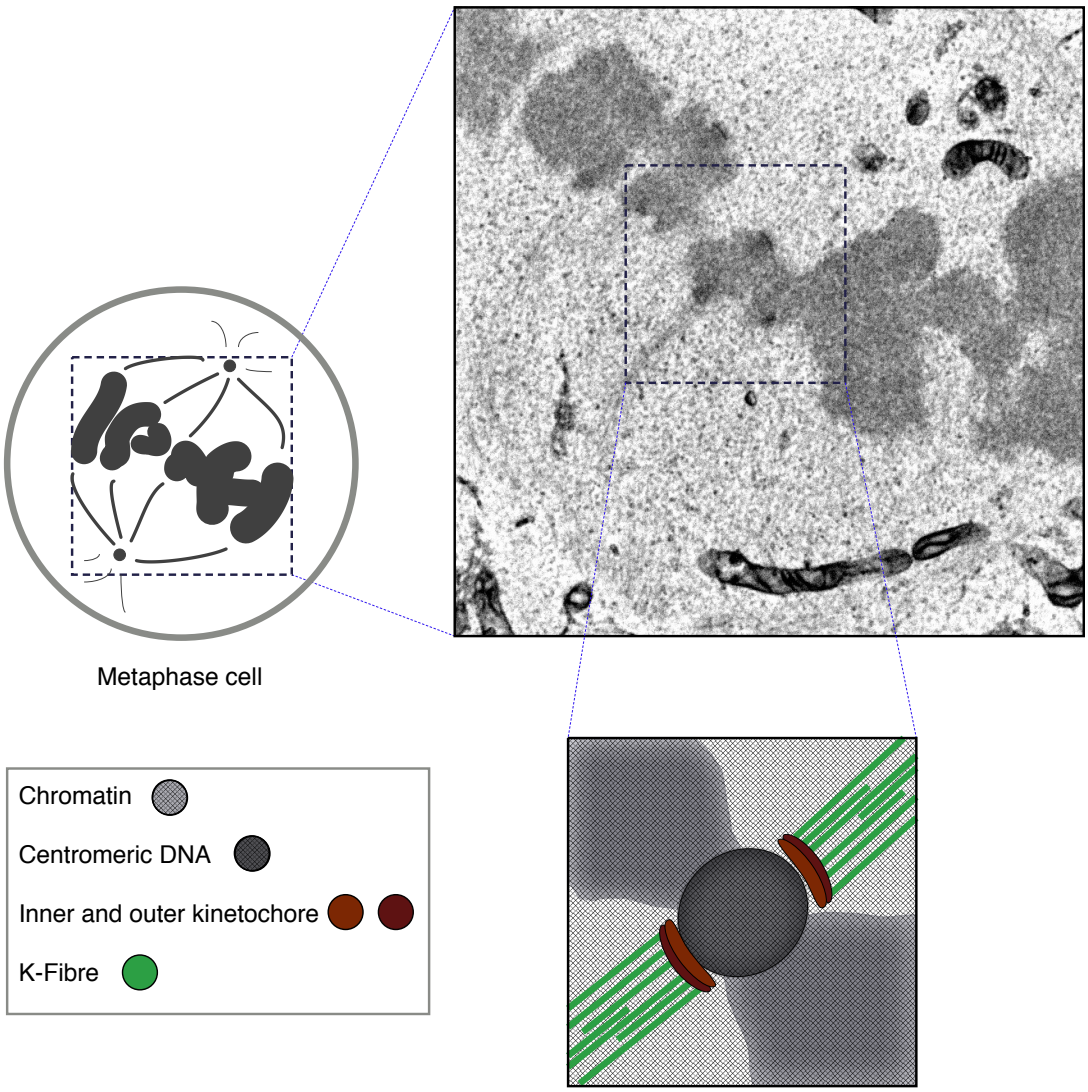

Figure 1.5: Kinetochore and K-fibres. This figure shows a metaphase cell by electron microscopy – with sister kinetochores and attached K-fibres highlighted. A cartoon representation of this area is shown, highlighting the inner and outer kinetochore, and kMTs stably attached. The mature spindle generates tension on sister kinetochores, detected by the spindle assembly checkpoint (SAC). Once the SAC has been satisfied, the two sister chromatids are separated and pulled to the cell poles by the K-fibres.

It is important that the kinetochore-MT interface is stable, so the connection can withstand the force generated by the spindle in order to segregate the DNA in anaphase. However, it is also necessary to possess a mechanism of correcting attachment errors, and preventing anaphase until all kinetochores are bioriented (sister kinetochores are attached to opposite spindle poles). Although geometric constraints associated with the back-to-back orientation of sister kinetochores does contribute to the prevention of incorrect attachments (Zaytsev and Grischuk, 2015), nevertheless, syntelic and merotelic attachments can occur. In these instances, both sister kinetochores are attached to the same pole, or a single sister kinetochore is attached to both poles, respectively. Without error correction, these situations could result in aneuploidy. Aurora B kinase plays an important role in correcting erroneous kinetochore-MT attachments (Biggins et al., 1999; Tanaka et al., 2002). It does this by inhibiting the action of a number of proteins involved in the kinetochore-MT interface – including the Dam1 complex, the Ndc80 complex, and the Ska1 complex (Cheeseman et al., 2002; Cheeseman et al., 2006; DeLuca et al., 2006; Chan et al., 2012; Schmidt et al., 2012). This results in the loss of incorrect attachments. Aurora B acts in a tension-selective manner – meaning only kinetochores with incorrect attachments are targeted, sparing bioriented kinetochores under tension from attachments via the spindle to both poles (Liu et al., 2009; Welburn et al., 2010).

1.3.1.8 The spindle matrix

The mitotic spindle has long been proposed to exist within the confines of an elastic, scaffold-like spindle matrix to overcome the inherent dynamic instability of MTs and aid in the organisation and stability of the spindle so chromosomes can be segregated. This spindle matrix was proposed over fifty years ago (Mazia, 1967) and although several studies provide some evidence to support the hypothesis, compelling evidence for such a structure in mammalian cells is lacking and so its existence is under some contention.

In *Drosophila*, there are several proteins that localise to the spindle region forming a spindle-like structure in mitosis (Walker et al., 2000; Rath et al., 2004; Qi et al., 2004; Qi et al., 2005). Depletion of some of these proteins (namely megator and chromator) results in mitotic defects characteristic of aberrant SAC activity, leading to the notion that the matrix may be a spatial regulator of mitosis (Lince-Faria et al., 2009; Ding et

al., 2009). This, coupled with the observation that regulators of mitosis, like cyclin B and Mad2, also accumulate in the spindle zone (Lince-Faria et al., 2009; Raff et al., 2002; Moutinho-Santor et al., 1999) lead to the notion that the spindle matrix is important for spindle assembly. However, only putative matrix proteins lamin B and megator have mammalian orthologues. Tpr (mammalian orthologue of megator) is a nuclear pore complex protein and although it has been shown to associate with spindles it is not enriched *in vivo* and this association depends on MTs (Lince-Faria et al., 2009; Schweizer et al., 2014).

Although evidence for an elastic spindle matrix consisting of a conglomeration of proteins has been presented, especially in the 'semi-open' mitosis of *Drosophila* embryos, it is still unclear whether these proteins truly form a spindle matrix, or whether their presence in the spindle region is due to an as yet unknown function (Schweizer et al., 2014), and so the spindle matrix remains elusive.

1.3.2 Known microtubule crosslinkers and candidate proteins

The mitotic spindle functions in concert with hundreds of MT-associated proteins (MAPs) which have roles in MT nucleation, polymerisation, stabilisation, chromosome congression and segregation, to name just a few. Some of these MAPs are capable of crosslinking MTs, and these crosslinkers have been visualised in the spindle since first being highlighted by EM in the late 1960s (Wilson, 1969). In this study, the author described these crosslinkers as electron-dense "bridges' connecting two MTs, and hypothesised that they functioned to maintain MT bundles in parallel conformation. In subsequent years, a number of other EM studies observed these bridges – illustrating their commonality within K-fibres throughout a range of different species, including humans (Wilson, 1969; Hepler et al., 1970; Tiwari et al., 1984; Bastmeyer and Fuge, 1986; Oakley and Heath, 1978).

The ideas that the bridges might provide resistance to shear, and contribute to the even transduction of force in the K-fibre were added to their proposed function in the spindle. EM allowed some characterisation of these crosslinkers – with authors noting that they tend to be 20-40 nm in length; approximately 3 nm width; occurring regularly along the MT lattice with 10, 20, 30 and 40 nm spacing; often perpendicular

to the longitudinal MT axis but sometimes emanating at angles or in a curved conformation (Hepler et al., 1970). Figure 1.5 summarises the types of bridges found in these classic EM studies, as well as some more recent studies.

Current technology in light microscopy precludes the resolution of single MTs in a K-fibre bundle. Using single chain antibody fragments against tubulin, Mikhaylova et al., were able to resolve single MTs from a small bundle, but their method is still limited by the point spread function of the microscope and would therefore be limited in the resolution of large K-fibre bundles (Mikhaylova et al., 2015). In addition to this, methods for accurately screening candidate bridge proteins are lacking at present. Immunogold labelling in electron microscopy studies allows for the labelling of candidate bridge proteins, but due to antibody size this labelling could be ambiguous when different populations of bridging proteins likely exist in close proximity within the spindle. The following sections describe known MAPs that represent molecular candidates for these observed inter-MT bridges.

1.3.2.1 Microtubule motor proteins

Many motor proteins exist in the cell, capable of crosslinking MTs and are known to do so to execute a variety of functions.

In mitosis, motors work in concert during bipolar spindle formation by crosslinking adjacent MTs and, through their plus- or minus-end directed motion act to focus the spindle poles (Goshima et al., 2005) and elongate the spindle by sliding of anti-parallel MTs – pushing apart the spindle poles during anaphase B (Brust-Mascher et al., 2004).

HSET is a MT minus-end directed kinesin initially noted to have a role in focussing minus ends thus contributing to spindle formation (Matthies et al., 1996; Endow and Komma 1996, 1997; Walczak et al., 1997). It has since been shown to crosslink and slide spindle MTs, contributing to both spindle length and its structural stability (Mountain et al., 1999; Cai et al., 2009). Significant cytoplasmic MT bundling is seen when the normal location of HSET is disrupted, emphasising its ability to crosslink and bundle MTs (Cai et al., 2009). In cells that utilise centrosomes for spindle assembly, the MT-focussing role of HSET is dispensable (Mountain et al., 1999), but

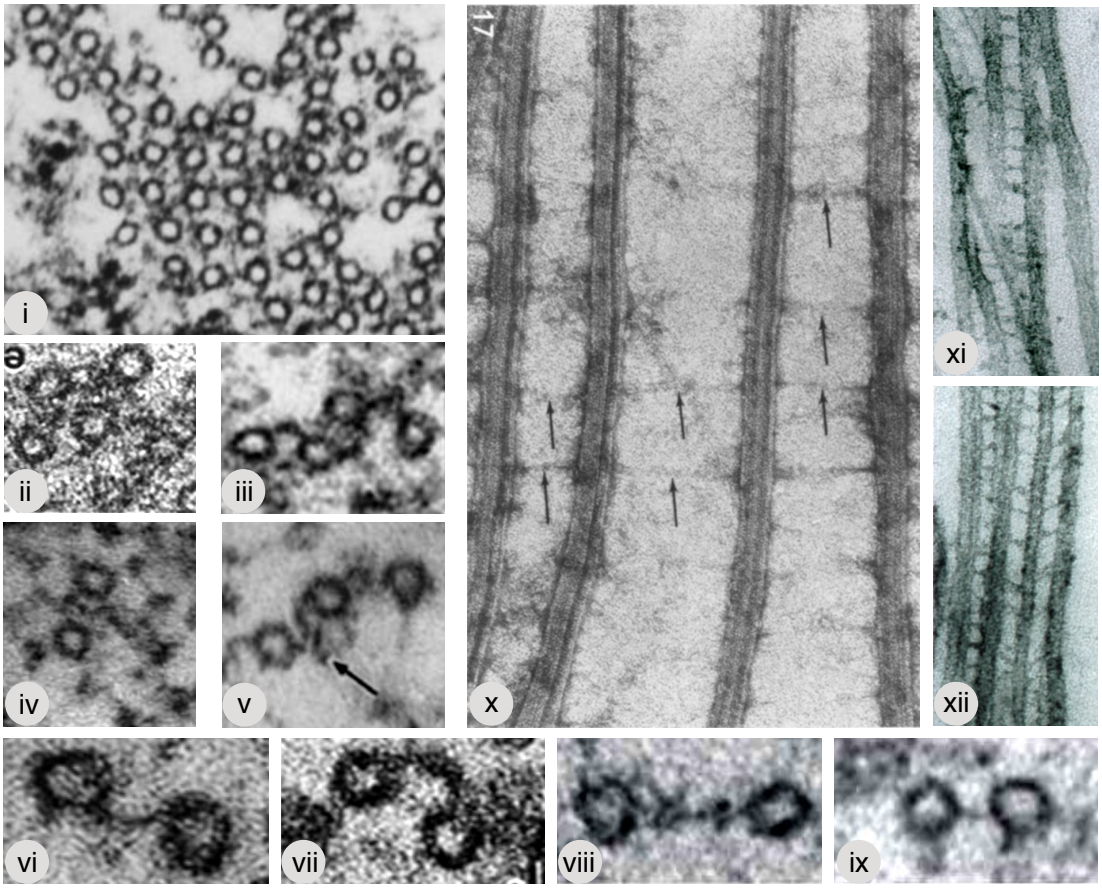

Figure 1.6: Inter-microtubule crosslinkers by electron microscopy. This figure shows a conglomeration of crosslinking structures that have been seen between MTs in previous EM studies. **i** to **v**: crosslinkers that appear quite filamentous, almost branching, although these structures are impossible to resolve in 2D images. **vi** to **ix** show more simple bridging structures connecting MT pairs. All of these MTs have been sectioned orthogonal to the MT axis. **x** to **xii**: bridging structures viewed longitudinally to the MT axis. Note that throughout these images, crosslinkers appear heterogeneous – with some appearing as simple 'struts', and some hinting at a more filamentous, branching morphology. These images have been gathered from a variety of classical, and more recent, EM studies. **i** shows crosslinking in the central spindle of *Diatoma vulgare* (McDonald et al., 1979); **ii, vi** and **vii**: bridges in the metaphase spindle of PtK1 cells (Brinkley and Cartwright, 1971); **iii** was taken in the mitotic spindle of algae (Wilson, 1969); **iv** and **v**: crosslinkers between interphase MTs in HeLa cells (Bhisey and Freed, 1971); **viii** and **x**: bridges between kMTs in metaphase HeLa cells (Booth et al., 2011); **x**: these bridges are also seen between cilia MTs (Warner, 1976); **xi** and **xii**: carrot MTs grown *in vitro*, crosslinked by MAP65 (Chan et al., 1999).

this function becomes important in cancer situations where cancer cells often possess supernumerary centrosomes. HSET allows cancer cells to cluster their centrosomes or acentrosomal MTOCs, controlling spindle multipolarity and avoiding cell death as a result (Kwon et al., 2008; Kleylein-Sohn et al., 2012). In fact, HSET over-expression is often seen in cancers that display centrosome amplification (Pannu et al., 2015).

1.3.2.2 Non-motor microtubule-associated proteins

Non-motor proteins are also known to crosslink spindle MTs, contributing to organisation through bundling activity, and structural stabilisation of MT arrays.

Fission yeast Ase1 (the homologue of mammalian PRC1, which is involved in central spindle assembly) has recently been implicated in MT organisation, with a reduction in Ase1 resulting in the spatial integrity of MT bundles being abrogated (Tikhonenko et al., 2015). This relates to its characterised role in stabilisation of antiparallel MT overlaps by effectively 'braking' kinesin-driven MT sliding. Ase1 does this by crosslinking along the length of antiparallel MTs, providing resistance to MT sliding in these bundles, allowing new, short MTs to continue to be positioned by sliding into these MT bundles (Braun et al., 2011, Jansen et al., 2007). In addition to Ase1, Mia1p (a fission yeast TACC protein) has also been shown to crosslink MTs, with a reduction in this bridge resulting in disassembly of MT bundles (Thadani et al., 2009). Cep169 is a centrosomal protein which has also been recently shown to crosslink MTs and form bundles (Mori et al., 2015).

Recent studies suggest that crosslinked MT networks have the ability to bear more stress (Lopez and Valentine, 2015) – suggesting an additional purpose in formation and stabilisation of MT bundles in the spindle.

There are several proteins known to be localised to the mitotic spindle.

One well characterised MT crosslinker is PRC1, a member of the MAP65 family of proteins. This protein is necessary for the formation of the central spindle during anaphase (Mollinari et al., 2002). During this time, PRC1 is recruited to central spindle MTs where it selectively crosslinks those MTs in an antiparallel orientation,

causing increased MT bundling in this region (Bieling et al., 2010; Gaillard et al., 2008; Janson et al., 2007; Loiodice., et al 2005). PRC1 is required to recruit other proteins necessary for forming the central spindle and midbody, including the kinesin Kif4, which is recruited to overlap zones by PRC1 and subsequently travels to the MT plus-ends to suppress MT dynamics (Kurasawa et al., 2004; Zhu and Jiang, 2005; Bieling et al., 2010).

NuMA is a MT crosslinking protein that, in concert with dynein, tethers MT minus-ends to the spindle pole (Merdes et al., 1996). Without NuMA, cells in prophase fail to form a functional spindle apparatus, and collapse of the spindle is observed when NuMA is depleted at metaphase (Yang and Snyder, 1992). This emphasises the important role this MT crosslinker plays in spindle maintenance. NuMA is also involved in positioning of the spindle as part of a complex with $G\alpha_i$ and LGN (a G-protein and modulator of G-protein signalling, respectively) which anchors dynein at the cell cortex, exerting force on the plus-ends of aMTs radiating out from the pole (Woodard et al., 2010; Kiyomitsu and Cheeseman 2012; Kotak et al., 2012; Zheng et al., 2013).

HURP (Hepatoma upregulated protein) was identified in 2003 as a protein enriched in G2/M phase and over-expressed in hepatocellular carcinoma (Tsou et al., 2003). A proteomic study of the HeLa spindle apparatus linked HURP to spindle MTs (Sauer et al., 2005) and it has since been characterised as localising to K-fibres in the vicinity of chromosomes in a RanGTP-dependent manner. In vitro, HURP binds to and bundles MTs, and this activity has been shown to stabilise K-fibres in mitosis (Sillje et al., 2006). When it is depleted from K-fibres, a delay in mitosis is seen with chromosome congression impaired (Sillje et al., 2006). More recent studies however, identify the kinesin Kif18A as an interaction partner of HURP and suggest that the role HURP plays in timely chromosome congression is through this interaction (Ye et al., 2011).

NuSAP (nuclear and spindle associated protein) is another MT-binding protein implicated in spindle organisation and stabilisation (Raemaekers et al., 2003). It has been shown to possess MT crosslinking capabilities with Ribbeck *et al.* showing that NuSAP can prevent MT depolymerisation and contribute to the formation of MT networks and bundles (Ribbeck et al., 2006). The authors also demonstrated longer

MTs and increased MT bundling when added at high levels to *Xenopus* egg extracts. NuSAP knockdown resulted in abnormal spindles coupled with chromosome segregation problems and defects in cytokinesis (Raemaekers et al., 2003), emphasising the importance of this crosslinker in mitosis.

The spindle localisation of the protein astrin was described in 2001 using immunofluorescence (Mack and Compton, 2001) and has since been demonstrated to have a role in proper spindle assembly and segregation of chromosomes (Gruber et al., 2002; Thein et al., 2007). Astrin is in complex with its binding partner, kinastrin. Together, astrin and kinastrin form a MT plus-end tracking complex needed for normal K-fibre formation (Dunsch et al., 2011). Astrin also has a domain structure very similar to that of motor proteins, albeit with very little sequence similarity (Gruber et al., 2002), which could potentially crosslink MTs.

TPX2 (targeting protein for Xklp2) is a MAP present on the spindle apparatus with important roles in regulating aurora A kinase by causing its activation and subsequent localisation to the spindle (Kufer et al., 2002; Bayliss et al., 2003; Eyers and Maller, 2004); the formation of kinetochore-proximal MTs (Tulu et al., 2006); and the regulation of Eg5 by binding to MTs and blocking the motility of the kinesin (Balchand et al., 2015). In addition to this, TPX2 has been shown to induce MT polymerisation and bundling (Schatz et al., 2003), and its depletion produces multipolar or short spindles in cells which subsequently fail to complete mitosis (Gruss et al., 2002; Garrett et al., 2002).

1.4 The TACC3-chTOG-clathrin inter-microtubule bridge

One recently identified inter-MT bridge within K-fibres is a complex of three proteins – TACC3, chTOG and clathrin – recruited to the spindle by Aurora A kinase phosphorylation of TACC3 (Booth et al., 2011, Cheeseman et al., 2011; Fu et al., 2010; Lin et al., 2010; Hubner et al., 2010). The following sections outline what is known about the function of these proteins individually, before describing the current understanding of the location and function of the TACC3-chTOG-clathrin complex.

1.4.1 TACC3

There are three proteins in the transforming acidic coiled-coil (TACC) protein family in humans – TACC1, TACC2 and TACC3 – all of which are concentrated in the centrosomal region during mitosis (Gergely et al., 2000a). The *Drosophila* homologue, D-TACC, was shown to be required for proper spindle function in early embryos with perturbation of this protein resulting in short centrosomal MTs and chromosome segregation failures (Gergely et al., 2000b). Similar observations were also seen in *Xenopus* with the depletion of maskin (the *Xenopus* homologue) causing smaller spindles containing fewer MTs (Peset et al., 2005). A role in spindle assembly was hypothesised as a result (O'Brien et al., 2005). Shortly after, TACC3 was reported to play an important role in mitosis in humans with depletion resulting in aberrant spindle structure and kinetochore-MT attachments, misaligned chromosomes, and ultimately resulted in cell death (Schneider et al., 2007). As mentioned previously, spindle localisation and MT nucleation ability of TACC3 is reliant upon phosphorylation of serine 558 by aurora A kinase (LeRoy et al., 2007; Kinoshita et al., 2005).

TACC3 interacts with chTOG, a MT polymerase, in order to regulate the behaviour of MTs, and this interaction is conserved in multiple species. D-TACC and Msps together influence centrosomal MT stability in *Drosophila* (Lee et al., 2001); maskin interacts with XMAP215 in *Xenopus* (O'Brien et al., 2005); Alp7 interacts with Alp14 in *S. pombe* (Sato et al., 2004); and TAC-1 couples with Zyg9 in *C. elegans* (Bellanger and Gonczy, 2003; Le Bot et al., 2003; Srayko et al., 2005).

The exact function of TACC3 and its homologues remains questionable. Evidence suggests that TACC3 influences MT stability, but the question of whether TACC3 influences MT dynamics themselves is contentious. Nwagbara *et al.* demonstrated that TACC3 can act as a MT plus-tip tracking protein, influencing the velocity of MT growth in *Xenopus* growth cones and other embryonic cells when it is over-expressed or depleted (Nwagbara et al., 2014). In contrast to this, Gutierrez-Caballero *et al.* did not detect any change in MT dynamics after TACC3 over-expression or depletion in RPE1 cells (Gutierrez-Caballero et al., 2014). In addition to this, the authors describe distinct pools of TACC3, in which it acts as a MT plus-tip tracking protein in complex with chTOG, and as part of the TACC3-chTOG-clathrin inter-MT bridge where binding

to MTs occurs in partnership with clathrin (Gutierrez-Caballero et al., 2014). This study also demonstrated that in human cells, TACC3 does not colocalise with centrosomes and it suggested that tip-tracking of growing MTs by TACC3-chTOG may explain its apparent localisation at this area.

Other roles for TACC3 have also been identified. For example, TACC3 is highly expressed in haematopoietic cells and has been hypothesised to regulate whether multipotent progenitor cells continue expansion of mature to erythroid cells (Garriga-Canut and Orkin, 2004; Sadek et al., 2003). TACC3 has also be shown to contribute to nuclear envelope structure in addition to TSC2 (Gomez-Baldo et al., 2010), and TACC proteins were shown to interact with histone acetyl-transferases (HATs), implicating them in transcription and suggesting that abnormal expression levels could affect gene regulation (Gangisetty et al., 2004).

1.4.2 chTOG

The XMAP215/Dis1 family of MT polymerases, of which chTOG is the human homologue, have been well characterised in a number of different species. These proteins act as a catalyst for the addition of tubulin heterodimers to the growing MT tip, accelerating MT growth. They do this via the action of TOG domains – conserved regions in the protein capable of binding tubulin subunits (Charrasse et al., 1998).

In vivo, chTOG localises to the spindle, centrosomes and at the kinetochore, with its depletion causing severely disorganised spindles in mitosis (Gergely et al., 2003), and short, less dynamic interphase MTs (Tournebize et al., 2000; Brittle and Ohkura 2005; Kawamura and Wasteneys 2008).

As discussed above, chTOG and its homologues interact with TACC3 homologues to assemble and organise the mitotic spindle. Like TACC3, evidence suggests different populations of chTOG exist during mitosis – one acting with TACC3 and clathrin as an inter-MT bridge, one in complex with TACC3 tip-tracking the MT plus-ends, and a population which localises to the centrosomes and kinetochores autonomously (Gutierrez-Caballero et al., 2014). The function of chTOG at kinetochores is unknown, although a recent study found that Alp14 (the *S. pombe* homologue) at the

kinetochore aids in their capture by the spindle (Tang et al., 2013, Kakui et al., 2013; Hsu and Toda, 2011; Garcia et al., 2001). In *S. pombe,* Alp7 is also at the kinetochore, whereas in human cells TACC3 is absent from this population of chTOG (Gutierrez-Caballero et al., 2014).

1.4.3 Clathrin

Clathrin is a protein with a unique, triskelion-shaped structure with each of its three legs comprising a light (23-27kDa) and a heavy (190kDa) chain (Kirchhausen and Harrison, 1981). Heavy chains exist in one isoform and comprise several functionally distinct regions. They are referred to as the "legs" of the clathrin molecule, and possess a globular β-propeller at their N-terminal domain which contains the binding site for endocytic adaptor proteins (Fotin et al., 2004). The distal and proximal regions of the leg are joined by a flexible "knee", with trimerisation of the three legs into the triskelion mediated by their C-terminal region. There are two isoforms of the clathrin light chain, and these randomly associate with the heavy chain via the proximal region of each leg (Brodsky et al., 1991; Ybe et al., 1998).

It is from its triskelion structure that clathrin's role in endocytosis stems – many triskelions come together forming a cage-like structure around an invaginating membrane in order to traffic cargo from one part of the cell to another. Endocytosis is used by the cell for many important functions, including uptake of nutrients and the regulation of surface receptor expression (Goldstein et al., 1985). Although the cell possesses several mechanisms of internalisation, clathrin is involved in the so-named "clathrin-mediated endocytosis" (CME). The role of clathrin in endocytosis has been the subject of many investigations, starting with Roth and Porter who used electron microscopy to describe the fundamentals of clathrin-coated pit (CCP) formation (Roth and Porter, 1964). CME occurs when endocytic adaptors (eg. AP-2) that are associated with the plasma membrane act to localise and recruit clathrin to the membrane resulting in the formation of CCPs. Conformational changes in the clathrin net of CCPs cause invagination of the membrane at this locus, and the GTPase dynamin is able to self-assemble into a helical structure at the neck of the deeply-invaginated CCP causing fission of the vesicle from the membrane (Robinson, 1994). Through this process, cargo bound to receptors at the plasma membrane surface

can be internalised. Once the vesicle and cargo are internalised, the clathrin lattice disassembles via the activity of uncoating enzymes. Uncoated vesicles are then free to fuse with one another forming an "early endosome". The acidic conditions with in the early endosome cause the release of ligands from their receptors which then pinch off in "sorting endosomes" and return to the plasma membrane via the cytoskeletal network.

1.4.3.1 Clathrin in mitosis

Although clathrin is important for endocytosis, much evidence has come to light in recent years regarding clathrin's "moonlighting" function during mitosis (Royle et al., 2005). Before its identification as part of the TACC3-chTOG-clathrin inter-MT bridge in K-fibres, its spindle localisation had been observed by several different groups using techniques including immunofluorescence and mass spectrometry (Maro et al., 1985; Okamoto et al., 2000; Sutherland et al., 2001; Mack and Compton, 2001). It was inferred that this observation was a result of clathrin-coated vesicles (CCVs) present in the spindle. However, adaptor proteins for these coated vesicles were not found to co-localise with clathrin in this region (Royle et al., 2005). Depletion of clathrin was shown to destabilise K-fibres leading to chromosome congression defects and prolonged mitosis, and this observation, coupled with the fact that clathrin was observed on K-fibres by both immunofluorescence and electron microscopy (Royle et al., 2005; Okamoto et al., 2000; Maro et al., 1985), led to the hypothesis that clathrin does have a functional role in the activity of the mitotic spindle. Several experiments using different mutants of clathrin that were able to function in mitosis but not endocytosis, and *vice versa*, demonstrated that these two important functions of clathrin are distinct from each other (Blixt and Royle, 2011; Hood and Royle, 2009; Royle and Lagnado, 2006; Hood et al., 2013). The hypothesis that clathrin may cross-bridge kMTs came as these integral studies into the presence of clathrin at the spindle identified the regions required for its localisation there – one region in the NTD and one in the ankle (Royle et al., 2005; Royle and Lagnado, 2006; Hood and Royle, 2009). These regions map to area at the distal portion of each clathrin leg, suggesting that the clathrin triskelion may crosslink kMTs. Clathrin legs were demonstrated by atomic force microscopy (AFM) to be approximately 2 nm in width and 52 nm in length (Jin and Nossal, 2000) – in agreement with observed inter-MT bridge characteristics.

1.4.4 The TACC3-chTOG-clathrin complex

Based on initial experiments linking clathrin to the stabilisation of K-fibres (Royle et al., 2005; Royle and Lagnado, 2006; Hood and Royle, 2009), and being responsible for mediating recruitment of TACC3 to the spindle (Fu et al., 2010; Hubner et al., 2010; Lin et al., 2010), questions arose about the nature of this complex, its function and its recruitment to the spindle.

Booth *et al.* confirmed the presence of this complex on the spindle using immunofluorescence and its purification from spindles (Booth et al., 2011). The authors then set out to investigate the presence of this complex bridging adjacent kMTs. This investigation utilised correlative light-electron microscopy (CLEM) and immunogold labelling to demonstrate that a proportion of crosslinkers contained clathrin, and after clathrin RNAi K-fibres contained fewer MTs coupled with a decrease in their cross-sectional area. The density of kMTs in these fibres was also reduced, indicating an impact on kMT organisation and spacing with the loss of clathrin from the spindle. By electron microscopy (EM) it could also be seen that a specific proportion of bridging structures were lost after depletion of clathrin, with a concomitant reduction in the number of bridges seen per unit length of MT. These observations led to the conclusion that the TACC3-chTOG-clathrin bridge comprises only one population of MT crosslinker in K-fibres – in control cells the authors observed at least three different populations of bridge based on their length and, after clathrin RNAi, they saw a significant reduction in the shortest of these bridges. Similar observations were noted upon TACC3 depletion, leading to the hypothesis that clathrin and TACC3 are responsible for MT crosslinking over short distances in K-fibres (Booth et al., 2011).

Although clathrin had previously been demonstrated to play a role in K-fibre stabilisation (Royle et al., 2005), the role of this TACC3-chTOG-clathrin complex is yet to be fully established. Cheeseman *et al.* sought to answer this question using Knock-sideways (KS) to rapidly reroute the complex during mitosis – overcoming some of the potential shortcomings of the slow RNAi method (Cheeseman et al., 2013). The authors demonstrated that re-routing of TACC3 away from the spindle using the KS method also resulted in the simultaneous removal of clathrin and chTOG from the spindle, but left other spindle proteins including HURP and Eg5 unaltered. Again, the

loss of this population of bridge was confirmed using CLEM. With TACC3 KS, cells exhibited different phenotypes depending on the exact time that the complex was removed - dissecting out different functions for these bridging structures during different stages of mitosis. Upon TACC3 rerouting at NEBD, the time spent in prometaphase was significantly increased and the cells' ability to congress their chromosomes was severely compromised. In mature spindles that had already congressed their chromosomes, TACC3 rerouting had the effect of delaying anaphase – due to decreased K-fibre tension as indicated by a decrease in inter-kinetochore distance and an increase in Mad2-positive kinetochores. In this case, no significant loss of kMTs was detected by CLEM. However, reduced dynamicity of both kinetochores and poles was noted (Cheeseman et al., 2013).

The study by Cheeseman *et al.* suggests multiple functions of inter-kMT bridges – from initial formation and maturation of functional K-fibres during prometaphase, to maintenance of K-fibre tension in the metaphase to anaphase transition.

In the studies outlined previously, the order of recruitment of each of the complex members was under contention, with reports suggesting that each protein was required for recruitment of the other to the spindle (Fu et al., 2010; Hubner et al., 2010; Lin et al., 2010; Booth et al., 2011). The exact interactions between these proteins and the requirements for their recruitment to the spindle were mapped in 2013 (Hood et al., 2013). Already known was the requirement of phosphorylation of TACC3 serine 558 by Aurora A for spindle binding (Kinoshita et al., 2005; LeRoy et al., 2007; Lin et al., 2010; Fu et al., 2010; Hubner et al., 2010; Booth et al., 2011; Cheeseman et al., 2011). The authors also found, using deletion mutants, that removal of the coiled-coil-containing TACC domain of TACC3 prevented binding to the spindle. They also found that the TACC domain alone is not sufficient for binding of TACC3 to the spindle. In addition to the TACC domain and pS558, a dileucine motif was also found to be essential for TACC3 recruitment to the spindle. During this investigation into spindle recruitment of TACC3 using deletion mutants, the authors noted that the spindle localisation of clathrin exactly mirrored that of TACC3 – when TACC3 binding was reduced, so was clathrin binding. Although the TACC domain was required for spindle binding, it was found to be dispensable for interaction with clathrin through *in vitro* experiments using purified proteins. This work led the authors to propose a model in which a "clathrin interaction domain" (CID), containing S558 and the

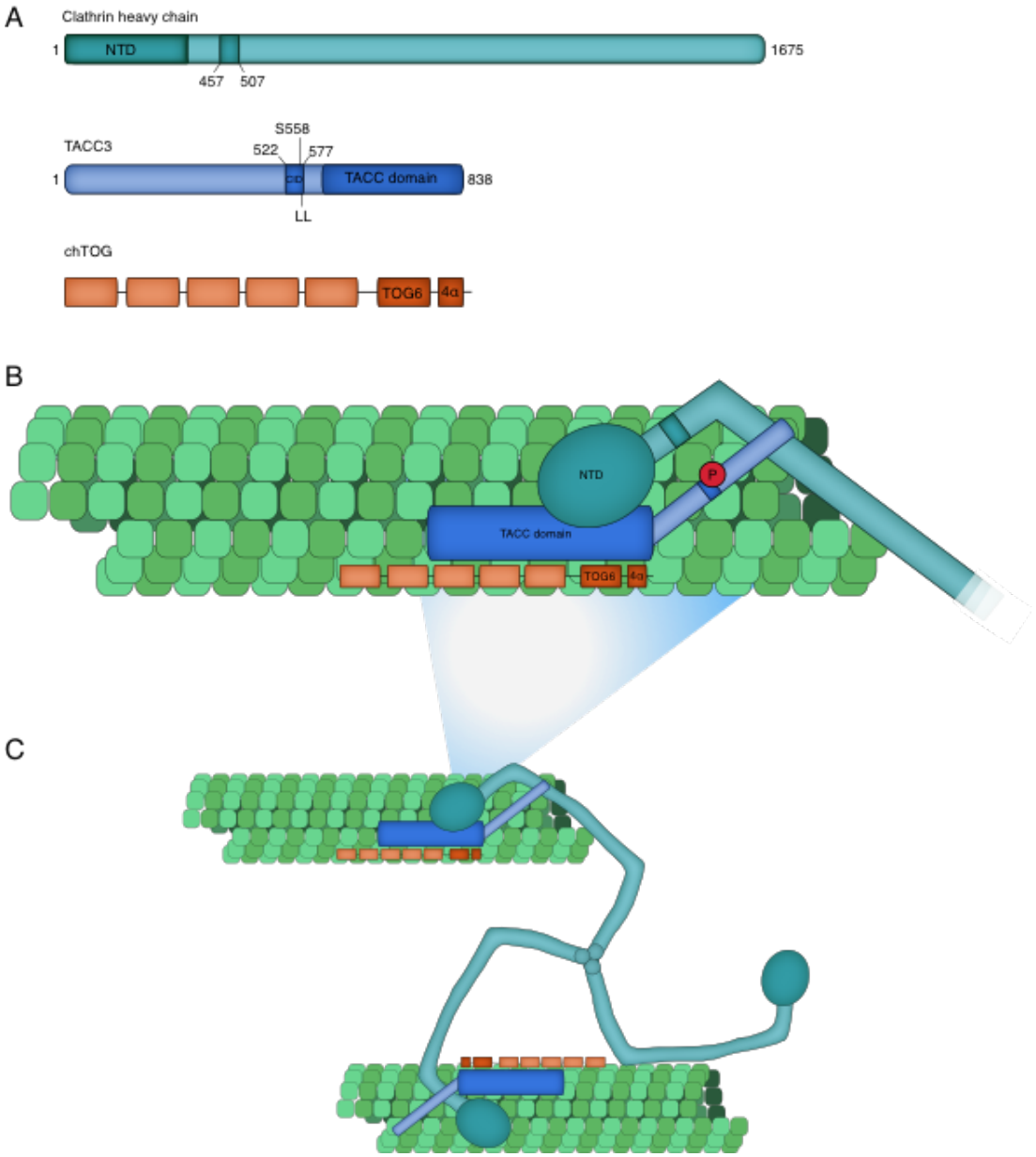

Figure 1.7: The TACC3-chTOG-clathrin inter-microtubule bridge. A: schematics of the individual proteins in this complex with the regions important for binding to each other, and MTs, highlighted. The clathrin interaction domain (CID) of TACC3 is highlighted which contains the dileucine motif and S558 residue which must be phosphorylated by Aurora A kinase, both needed for its interaction with clathrin. Clathrin binds TACC3 via residues in its ankle region, forming a MT interaction surface. This couples with clathrin's NTD and the TACC domain of TACC3 for full spindle binding. chTOG binds to TACC3 via its C-terminal region, containing its TOG6 and 4α domains. **B**: how these proteins might assemble on the MT lattice, and **C**: how this complex may bridge between two MTs.

dileucine motif, is required for the interaction with clathrin, and the TACC domain is required for MT binding. The authors also mapped the region of clathrin necessary for its recruitment to the spindle as two separate regions on clathrin heavy chain (CHC) – the ankle and at the NTD. Again, *in vitro* binding experiments showed that clathrin interacts with TACC3 via positive charges and hydrophobic pockets in its ankle region, and that the NTD plays no role in TACC3 binding. By light microscopy, a fusion protein containing the NTD of clathrin and the TACC domain of TACC3 was seen to mimic the localisation of both TACC3 and clathrin together. From this, a model was proposed where neither TACC3 nor clathrin can bind MTs alone, but coordination of a CID on TACC3 and the ankle domain of clathrin forms a MT binding surface which couples with the TACC domain and clathrin NTD to allow full binding to the spindle. The authors also established the region of interaction between TACC3 and chTOG to be between a break in the coiled-coil region of TACC3 and the C-terminal region of chTOG. By examining the spindle localisation of mutants incapable of binding chTOG, the authors established that chTOG is not the recruitment factor for the TACC3-chTOG-clathrin complex, and that the interaction of chTOG with TACC3 is in fact required for its localisation to the spindle. This meticulous experimentation established the mechanism of recruitment of this complex to the spindle, explaining why both TACC3 and clathrin had previously been observed to be necessary for spindle recruitment. Figure 1.7 illustrates the regions in these proteins that are important for spindle binding, and shows a speculative cartoon of how the complex may crossbridge MTs.

1.4.5 TACC3, chTOG and clathrin in cancer

Abnormal expression levels of TACC3, as well as its regulator aurora A kinase, have been identified in several types of cancer, including squamous cell carcinoma of the oesophagus (Huang et al., 2015), bladder cancer (Williams et al., 2013), lung cancer (Jung et al., 2006), and glioblastoma (Duncan et al., 2010). One genetic alteration in the region of the TACC3 gene on chromosome 4p16.3 results in the formation of a FGFR3-TACC3 gene fusion – present in several types of cancer. It is likely that ligand-independent dimerization and subsequent signalling may contribute to carcinogenesis (Singh et al., 2012), but the extent to which this abnormal fusion affects endogenous TACC3 and its spindle function is yet to be fully investigated.

TACC3 has also been shown to contribute to metastasis by promoting epithelial-to-mesenchymal transition in an EGFR-dependent mechanism (Ha et al., 2013).

As described by its nomenclature, chTOG was identified as being over-expressed in colonic and hepatic tumours (Charrasse et al., 1995). Due to this over-expression, the authors postulated that chTOG could be associated with the proliferative state of cells, and they noted that the chromosome locus of chTOG (11p11.2) is commonly implicated in neoplasia.

Clathrin is implicated in a variety of haematological and renal cancers by the presence of gene fusions involving ALK (Touriol et al., 2000; Cools et al., 2002; Gascoyne et al., 2003; Chikatsu et al., 2003; Gesk et al., 2005) and TFE3 (Argani et al., 2003; Kauffman et al., 2014). Experiments examining the role of these fusion proteins in cells found that CHC-ALK displays a similar distribution to wild type clathrin and is able to function normally in mitosis – suggesting that abnormal clathrin function is unlikely to have a role in carcinogenesis in these cancers. However, CHC-TFE3 is mislocalised and is unable to function in endocytosis, although it does appear to function normally in mitosis (Blixt and Royle, 2011).

1.5 Aims of the present study

There is no doubt that the mitotic spindle is highly complex, under the influence of many regulatory proteins and working in concert with an abundance of MAPs. It is clear that inter-MT crosslinkers have an important role in K-fibres within the spindle, with its proper function being abrogated when these crosslinking proteins are perturbed. It also seems clear that to examine kMT crosslinkers on the nanometer scale, in three dimensions, and in their native state within cells, requires technology to be optimised - pushing the limits of their achievable resolution.

The aim of the present study is to optimise light and electron microscopy techniques to provide information in greater detail on these crosslinking structures within K-fibres, and shed light on their function within the spindle.

Specifically, my project will focus on the following key questions:

1. What is the ultrastructural morphology of inter-MT crosslinkers in K-fibres?

2. How do these crosslinkers contribute to K-fibre function?

3. Can methods be further developed to better visualise K-fibre ultrastructure?

The protein complex discussed previously, namely the TACC3-chTOG-clathrin complex, is known to form kMT bridges, and individually these proteins are also all implicated in various cancers. This highlights the utility of this study in elucidating the structure and function of this complex in the spindle, and how the spindle could be adversely affected when these proteins are misregulated in a cancer situation. This in turn has the potential to lead to treatments for these particular types of cancer, or a method of specifically targeting cancer cells, in the future.

2. Materials and Methods

2.1 Cell biology

2.1.1 Reagents

Unless otherwise stated, cell culture reagents and plasticware were purchased from Sigma Aldrich (Poole, UK) and Corning (US), respectively. Culture medium and Oligofectamine were purchased from Invitrogen (Paisley, UK). GeneJuice was obtained from Novagen (distributed by Merck Chemicals Ltd, Nottingham, UK).

2.1.2 Cell Lines

HeLa cells, originating from human cervical carcinoma of the epithelium, were purchased from Health Protection Agency Cultures (Salisbury, UK; catalogue number: 93021013). HeLa cells capable of over-expressing TACC3 upon induction by doxycycline (Invitrogen, D9891) were obtained from previous work in the lab (Booth, 2011). They were produced from HeLa TetOn® cells (Clontech) which express the reverse tetracycline-controlled transactivator (rtTA); achieving a stable transfection with a plasmid expressing TACC3 under control of a tetracycline response element (TRE) producing an inducible gene expression system for this protein. Retinal Pigment Epithelial 1 (RPE1) cells were purchased from ATCC (US). Glioblastoma cell lines were kindly gifted by Heiko Wurdak (University of Leeds).

2.1.3 Cell Culture

Dulbecco's Modified Eagle Medium (DMEM) containing 10 % v/v foetal bovine serum (FBS) and 1 % v/v penicillin/streptomycin was used to culture cells, and they were maintained at 37 °C in a humidified 5 % CO_2 incubator.

The cell culture medium was further supplemented with G418 (300 µg/ml) for the HeLa TetOn® cells, and G418 and Hygromycin B (200 µg/ml) for the HeLa TetOn® cells stably transfected with the TACC3 plasmid.

Plastic 75cm^2 flasks were used to culture the cells to 80-100 % confluency, at which time the cells were passaged by removing the culture medium, washing with warm phosphate-buffered saline (PBS), adding Trypsin/EDTA and incubating until the cells became detached. At this point the cells were resuspended in the supplemented culture medium, and this solution was used to reseed the cells into a new flask at the required density.

RPE1 cells were cultured in F-12 DMEM supplemented with 10 % v/v FBS, 1 % v/v penicillin/streptomycin, 7.5% v/v sodium bicarbonate, and 2 mM L-Glutamine. Glioblastoma cell lines were cultured using Neurobasal® medium, supplemented with B27, N2, human fibroblast growth factor (FGF) (40 ng/ml) and human epidermal growth factor (EGF) (40 ng/ml).

Plastic 75cm^2 flasks were used to culture Glioblastoma cell lines, coated with poly-L-ornithine (10 mg/ml in sterile H_2O) and laminin (0.2 % v/v in PBS) solutions. To coat 75cm^2 flasks, 10 ml of poly-L-ornithine was incubated in the flask at RT for 1 h, before rinsing with sterile ddH_2O and adding 10 ml of laminin solution. The flasks containing laminin solution were incubated at room temperature overnight, then rinsed with PBS. At this point, the flasks could be used immediately, or stored at -20 °C until needed.

To passage Glioblastoma cell lines the culture medium was removed, and the cells were washed with 10 ml PBS before adding 1 ml Trypsin and incubating until the cells had become detached. Cells were then suspended in 4 ml Neurobasal medium and centrifuged at 300 *x g* for 5 min. The medium was then removed and the cell pellet was resuspended in fresh Neurobasal medium (with supplements) before seeding into new flasks.

2.1.4 Transfection of DNA plasmids

Cells were transfected using GeneJuice, according to manufacturer's instructions. To summarise this protocol, cells were seeded into a 6-well plate at between 50-80 % confluency, 24 hr prior to transfection. To perform the transfection, 3 µl of GeneJuice was added to 100 µl of OptiMEM, mixed, and incubated for 5 min at room temperature. 1 µg of DNA was added to the GeneJuice/OptiMEM mix and the solution was incubated at room temperature for a further 15 min. It was then added to a well containing 3 ml of fresh supplemented media and allowed to express for the required length of time.

2.2 Microscopy

2.2.1 Reagents

For light microscopy, glass slides and coverslips were purchased from Thermo Scientific (Leicestershire, UK). All other chemicals were purchased from Sigma Aldrich (Poole, UK) unless otherwise stated.

For TEM, all reagents were purchased from TAAB (Aldermaston, UK) unless otherwise stated.

2.2.2 Light Microscopy

2.2.2.1 Fixation and mounting

Routine fixation of cells for light microscopy was done at 37 °C using PTEMF – a paraformaldehyde (PFA)-based fixative containing Triton X100 (0.2 % v/v), PIPES (50 mM), EGTA (10 mM) and $MgCl_2$ (1 mM) which is optimal for preservation of microtubules (MTs). Cells were fixed for 15 min. Coverslips were mounted on glass slides using the mountant Mowiol, containing the fluorescent DNA stain 4',6-diamidino-2-phenylindole (DAPI). Slides were stored in the dark at 4 °C once imaged.

2.2.2.2 Immunofluorescence

After fixation, permeabilisation solution (0.5 % v/v Triton X-100 in PBS) was added for 10 min, before adding blocking solution (3 % BSA w/v, 5 % goat serum v/v, in PBS) for 1 h. This was then removed before adding the primary antibody, mixed in blocking solution to the required dilution, to the coverslips for 1-2 h. The coverslips were then washed twice for 5 min each in PBS, and the secondary antibody was added, again diluted in blocking solution, for a further 1-2 h. Following incubation with the secondary antibody, coverslips were washed three times in PBS, each for 5 min. The coverslips were then carefully washed once in ddH_2O, and mounted with Mowiol.

2.2.2.3 Fluorescence imaging

Fluorescence imaging was done using a Nikon Eclipse Ti-U microscope with standard filter sets for visualisation of DAPI, GFP, Alexa Fluor 568 and Alexa Fluor 633. Epifluorescence micrographs were acquired using a Photometrics (Arizona, US) camera, 20x air and 60x oil objectives, and NIS Elements acquisition software.

2.2.2.4 Cold treatment

Cold treatment of metaphase cells prior to fixation was done first by fluorescence imaging to determine correct mitotic stage, then the growth media was removed and replaced with ice-cold growth media for 10 min. The dish was also placed on ice during this time. After 10 min, the dish was removed from ice and the media replaced with fixative, as described in section 2.2.3.4.

2.2.2.5 Live cell imaging

Live cell imaging of mitotic progression was performed with the same Nikon Eclipse Ti-U microscope using a 37 °C temperature-controlled OKOlab Perspex chamber. The cells were maintained in CO_2-independent medium supplemented with 10 % FBS and 1 % v/v Penicillin/Streptomycin for the duration of the experiment. Brightfield

images were acquired sparingly, every tenth frame, to reduce cell damage as a result of light exposure.

2.2.3 Electron Microscopy

2.2.3.1 Preparation of Formvar-coated copper grids

Coated mesh grids were prepared using a Formvar solution made to 0.3 % w/v in chloroform. To ensure the grids were clean, they were first rinsed briefly in ethanol then acetone, covered, and allowed to dry before being coated. Only uniform films of Formvar were used to coat the grids to reduce any variation in stability and contrast on the TEM. Different types of grids were used, including those with a hexagonal support lattice (totalling 200, 100 and 75 hexagons) and with a 0.5 mm x 2 mm slot down the centre. For the slot grids, and the 75 hexagonal lattice grids, extra support was required and this was provided by coating with 0.5% w/v Formvar, and evaporating 3 nm carbon onto the surface using the Leica ACE 200 carbon coater.

2.2.3.2 Sample processing and resin embedding

For chemical fixation, cells were fixed using formaldehyde (0.5 %) and glutaraldehyde (3 %) in phosphate buffer designed to be at the correct osmotic strength (approximately 280 mOsm) to maintain cell morphology – using a recipe available from previous work in the lab (Booth et al., 2013). Fixation was performed for 1 h, the cells were washed in wash buffer (0.05 M phosphate buffer, 0.1 M sucrose; Booth et al., 2013) before being replaced with a small amount of 1 % v/v OsO_4 in ddH_2O for 1 h. Cells were washed twice in ddH_2O, then treated with 30 % v/v ethanol for 30 min before adding 0.5 % w/v uranyl acetate (UA) in 30 % v/v ethanol for 1 h. The cells were then dehydrated using graded ethanol solutions: 30 %, 50 %, 60 %, 70 %, 80 %, 90 % ethanol each for 10 min, followed by two 10 min ethanol steps. The samples were then embedded in Epon resin 812 prepared for medium hardness, as per manufacturer's instructions. This was done by preparing a fully homogenised solution with a 1:2 ratio of resin to ethanol and covering the cells with this mix for 20 min. The solution was subsequently replaced with a 1:1 resin/ethanol

mix, followed by 100 % resin, for 20 min each. Finally, the 100 % resin was replaced with fresh 100 % resin before being cured at 60 °C for 48-72 h.

A 350 μm^2 block face was trimmed around the area of interest using freshly prepared glass knives. Knives were made using the Leica Knifemaker KMR3. A Diatome (Switzerland) diamond knife was used to take thin sections (70-100 nm) from the area of interest, which were then mounted onto Formvar-coated mesh grids.

To increase the contrast of the sample, the sections were then post-stained using 4 % UA in 50 % ethanol for 7 min per grid, and subsequently with Reynolds' Lead Citrate (Reynolds., 1963), again for 7 min.

2.2.3.3 Correlative light-electron microscopy processing

For correlative light-electron microscopy (CLEM), cells were cultured on glass-bottomed, gridded dishes (MatTek corporation, Massachusetts, US). In the first instance, epifluorescent and brightfield images were taken of the cell of interest using a 20x air objective. These low magnification images were needed to produce a reference with a large enough field of view to include the surrounding cells with grid letters/numbers clearly visible. This was required so that the cell of interest could be relocated later in the process. Once these images were taken and the cells had been in fixative solution (as described in section 2.2.3.2) for 1 h, the cells were then washed and incubated in Wash Buffer containing 0.1 % Hoechst-33342 for 20 min, to stain the DNA. The cells were again rinsed in wash solution and returned to the microscope so the cell of interest could be imaged at a higher magnification using a 60x oil objective. These images of the chromosomes were needed to ensure that the cell of interest was at the correct stage of mitosis. Processing for EM then continued using the previously described protocol (section 2.2.3.2).

To process for longitudinal sections through the spindle, a small gelatine capsule filled with resin was placed over the area containing the cell of interest just prior to polymerisation of the resin at 60 °C. Once polymerised, the glass gridded portion of the dish was removed by briefly immersing the dish in LN_2 then prising it away from the resin and dish. The remaining plastic portion of the dish was then removed from

the resin using pliers. For longitudinal sectioning, the area of resin below the capsule was roughly trimmed using a razor blade to remove excess resin, and freshly made glass knives to trim a 350 µm square around the cell of interest, located using the original 20x LM images and the imprinted grid. A diamond knife and the Leica UC6 ultramicrotome were then used to take thin sections through the cell, usually at a 70 nm thickness, for examining on the TEM. Sections were retrieved from the knife water bath using Formvar-coated grids. See Figure 2.1.

For orthogonal sections through the spindle, the resin containing the cell of interest was re-trimmed using a junior hacksaw based on the axis of the metaphase plate, as determined from the 20x and 60x images taken on the light microscope. The resin was then rough trimmed and sectioned as for longitudinal sectioning. See Figure 2.1. Grids containing the sections were then post-stained as described previously (section 2.2.3.2).

2.2.3.4 3View® processing

The processing for SEM using the 3View® platform (Gatan, California, US) varied slightly from the previously described EM-processing protocols. This system of Serial Block Face Scanning Electron Microscopy (SBF-SEM) uses an automated version of an ultramicrotome stage which advances the sample of interest towards a scanning electron beam, cutting slices between scanning the surface of the sample to build a 3D volume of the entire sample. As with TEM, the system is limited by size – only small blocks with a face of a few mm^2 can be imaged. The resolution provided by SEM is also lower than that provided by TEM. However, the throughput for generation of 3D volume data using the 3View® system is much higher than that for TEM.

To prepare samples for the 3View®, the cells were again processed in a correlative manner to ensure only metaphase cells expressing the protein of interest were chosen, using the gridded MatTek dishes, but extra steps were needed in order to maximise staining of the ultrastructural components of the cell. Firstly, the formaldehyde and glutaraldehyde fixative solution was prepared using a phosphate buffer, with 0.1% tannic acid and 3% sucrose. The protocol also contained two OsO_4 steps – the first was a 1 h reduced osmium step where 2 % OsO_4 was prepared in 1.5 % potassium ferrocyanide solution, again in phosphate buffer. This was followed

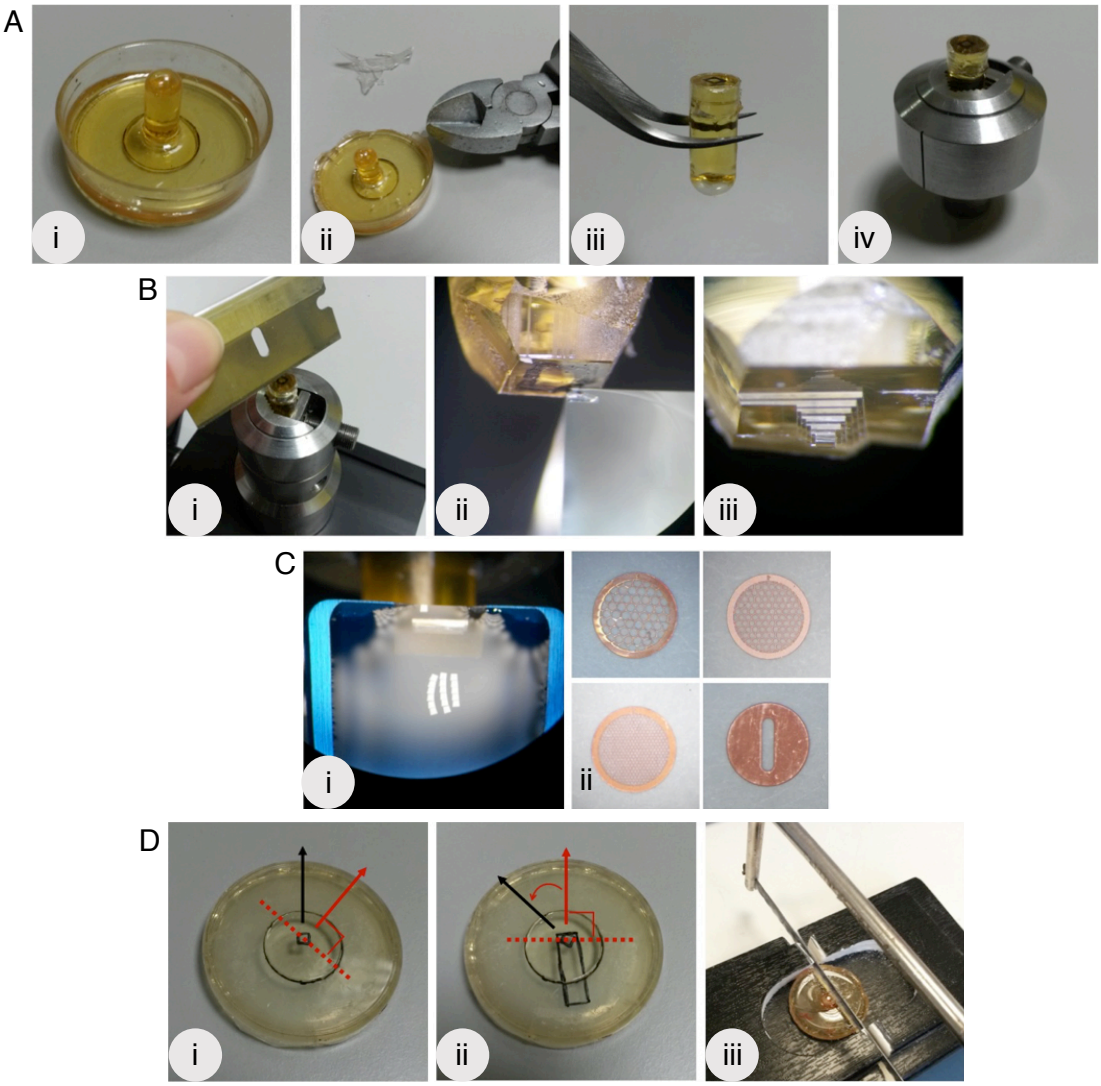

Figure 2.1: CLEM processing with chemical fixation. This figure illustrates EM processing for chemical fixation/CLEM samples. **A**: the process of rough trimming of the sample resulting in extraction of the resin capsule containing the cell of interest. **i**: MatTek CLEM dish with polymerised resin with a gelatine capsule placed over the cell of interest. Pliers and a razor blade were used to remove the plastic dish and gridded glass coverslip from the resin (**ii**). Pliers were used to remove excess resin leaving only the capsule (**iii**); the cell area was marked; and the capsule was mounted in the microtome chuck ready for trimming and sectioning (**iv**). **B**: fine trimming of the capsule prior to sectioning. Razor blades were used to trim around the marked area of interest (**i**) and fresh glass knives were used to trim a 350 µm square around the cell of interest, and excess resin from the periphery to avoid catching the diamond knife (**ii** and **iii**). A diamond knife was used to cut thin sections from the new block face. For serial sections, the block face was trimmed into a trapezium shape so the sections could be orientated in the TEM (**Ci**). Sections were mounted on a variety of copper grids (**Cii**). **D**: the process of rough trimming for orthogonal samples. The orientation of the metaphase plate is noted (marked in red dotted line), giving the necessary direction of sectioning (red arrow), shown in **Di** and **ii**. A new block is marked that would allow sectioning in this direction, which is then cut from the resin using a junior hacksaw (**Diii**).

by five 3 min ddH_2O washes before 0.1 % thiocarbohydrazide (TCH) was added for 30 min as a mordant. After the water wash steps were repeated, a second OsO_4 step (2 % in ddH_2O) was applied for 30 m. The cells were again washed in water as before, then stained overnight using 1 % UA in ddH_2O at 4 °C. The following day the water washes were repeated before incubating with lead aspartate at 60°C for 30 min. The cells were then dehydrated, again using graded ethanol as described previously (section 2.2.3.2).

For 3View® processing, the cells were infiltrated using TAAB Epon 812 Hard premixed resin kit. Once the resin was fully polymerised, the plastic dish and gridded glass coverslip were removed and the area of interest was found, as described previously (section 2.2.3.2). This area was then excised using a junior hacksaw and razor blades to leave an approximately 2 mm^3 piece of resin containing the cell. This cube of resin was super-glued onto special steel pins which fit into the chuck of the 3View® platform (Agar Scientific, Essex, UK). As described previously, the area around the cell was fine-trimmed using fresh glass knives, leaving as little resin as possible around the cell of interest to reduce interference produced by charging of the resin surface during SEM imaging. This produced an approximately 100 μm^2 block face. Due to the design of the 3View® stage and ultramicrotome, the majority of the 2 mm^3 block needed to be trimmed away to avoid excess resin catching on the knife blade or holder. This produced an extremely delicate block face so special care was needed to prevent damage during manipulation.

Once trimmed, the block was coated with a silver paint using an eyelash, before a 15 nm gold/palladium coating was evaporated onto the block surface, again to reduce surface charging (Quorum Technologies, East Sussex, UK).

Once dry, the pin/block was mounted into the 3View® stage and aligned manually with the knife-edge. When aligned, the 3View® was allowed to cut/image the block surface, with 100 nm slices, initially adjusting the contrast and magnification to optimum for that particular block, before leaving the platform to run until the cell was fully sectioned and imaged. A 768x768 image, 60 nm sections, 60 µs pixel dwell time, 2.1 keV, and 21000x magnification was found to be optimal for imaging of the spindle zone. These conditions needed to be fine-tuned for the individual sample,

and were a compromise between reduced levels of sample charging, magnification and resolution.

2.2.3.5 High pressure freezing

High pressure freezing (HPF) was performed using the EMPACT2 and the HPM100 machines (Leica). Sample preparation for both machines was similar. All tools and solutions were kept at 37 °C prior to use. Post-freezing, all tools used for manipulation of samples were pre-cooled to –90 °C. The method of HPF of mitotic cells involves the freezing of a cell pellet. Cells were grown in T75 culture flasks to 50-60 % confluency, and then synchronised using 2 mM thymidine for 16 h, to arrest the cells in the S-phase. They were then 'released' by washing three times with PBS and then replacing with fresh DMEM. 6 h post-release from thymidine, 9 µM RO-3306 was added to arrest the cells at the G_2/M-phase transition. The cells were then released, again by washing three times in PBS, and fresh DMEM was added. After approximately 30 min, allowing the cells time to move through mitosis and create an enriched population at metaphase, a mitotic shake-off was performed. The culture medium was then centrifuged at 300 x g for 2 min, and the supernatant was discarded. The cell pellet was re-suspended in approximately 10 µl DMEM supplemented with 20% FBS, as a cryoprotectant. The samples from the pellet were pipetted into either 100 µm or 200 µm deep membrane carriers (Leica) for the EMPACT2, or Type A and B carriers for the HPM100, before being frozen and subsequently dispensed into LN_2. See Figure 2.2 for detail on process of freezing using the HPM100, and Figure 2.3 for timescales involved in the freezing protocol. Correlative HPF is possible using 1.5 mm diameter sapphire disks as the cell substrate. However, due to the low throughput of this method, it was not used to generate any of the results presented in this thesis.

2.2.3.6 Freeze substitution

A freeze substitution (FS) medium of 0.5 % v/v UA, 1 % OsO_4 v/v, 5 % H_2O dissolved in acetone was used to fix and dehydrate the samples, over a specified temperature ramp using the Leica AFS2 FS unit. Cells were brought to room temperature over 67 h via the following protocol: 27 h at –90 °C; a temperature ramp from –90 °C to –60 °C over 15 h, 8 h at –60 °C; –60 °C to –30 °C over 15 h; 1 h at –30 °C; –30 °C to 4 °C

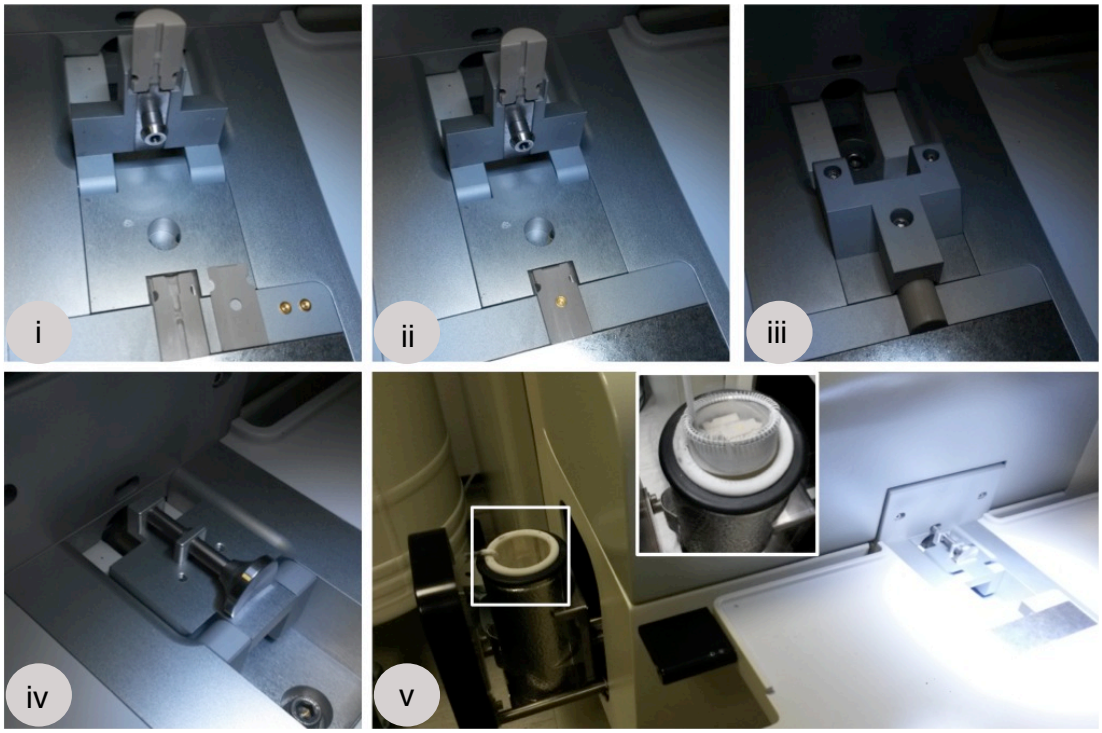
i
ii
iii
iv
v

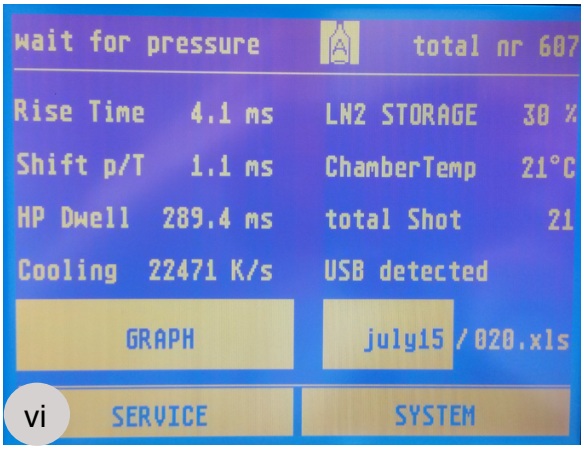
wait for pressure
total nr 607
Rise Time 4.1 ms
LN2 STORAGE 30 %
Shift p/T 1.1 ms
ChamberTemp 21°C
HP Dwell 289.4 ms
total Shot 21
Cooling 22471 K/s
USB detected
GRAPH
july15 / 020.xls
vi
SERVICE
SYSTEM


vii

Figure 2.2: HPF/FS using the HPM100 and AFS2. This figure illustrates the workflow of HPF. Parts **i** to **v**: the capsule assembly prior to freezing – the individual components of the system were clipped into place on the HPM100, the assembly was closed (**iii**) and pushed into the freezer (**iv**). Once frozen, the entire capsule of individual components was ejected into LN_2 contained in a small dewar in the machine. This is shown pulled out of the machine in (**v**) and a closer view of the basket containing the freezing components in LN_2 (inset). **vi**: the display of the HPM100 post-freezing, showing the cooling rate. Cooling of 20 000 K/s is optimal for this machine. Once frozen, the samples were transferred to the chamber of the Leica AFS2, cooled to –90 °C - (**vii**), and chamber (inset). Once the freeze substitution programme was finished, the samples were resin-infiltrated, polymerised, and were ready for sectioning.

over 1 h; then the cells were transferred from the AFS2 chamber to the fume hood to reach room temperature. Once at room temperature, the FS medium was removed and the samples were washed in acetone three times, for 5 min each. They were then infiltrated in Epon 812 resin by first incubating for 30 min with a 1:1 resin/acetone mix. Finally, the samples were incubated at room temperature with 100 % resin for 30 min, before replacing with fresh 100 % resin and allowing to polymerise for 48-72 h at 60 °C. A graphic representation of steps in this protocol and their associated timings is shown in Figure 2.2.

2.2.3.7 Imaging

TEM imaging was done using the FEI Tecnai G2 Spirit BioTWIN electron microscope at 120kV. AnalySIS acquisition software was used to acquire electron micrographs at various magnifications from 750x to 135000x (Soft Imaging System, Olympus). The same software was used to acquire MIA images, where multiple high magnification images were taken, then stitched together by the software to produce a high-resolution overview of a large region of interest. For tomographic reconstructions, TIA software (TEM Imaging and Analysis, FEI) was used to take the required tilt series of images, from +50 ° tilt through to -50 ° tilt, in 1 ° steps. The IMOD etomo package (Mastronarde, 1997) was used to produce the final tomogram from the tilt series of images.

2.3 Experimental set-up

HPF/FS and electron tomography experiments were done using the HeLa TetOn® stable cell line, induced to over-express GFP-TACC3 using doxycycline, in addition to HeLa TetOn® 'parental' cells as a control.

Chemical fixation experiments for examination by SBF-SEM and TEM were done with a number of different conditions. These include: 'parental' TetOn® HeLa cells, transiently transfected with GFP only as a control; the inducible GFP-TACC3 HeLa TetOn® stable cell line; and 'parental' TetOn® HeLa cells, transiently transfected with pBrain-GFP-TACC3(S558A)KDP-shTACC3 construct. This plasmid allows for the expression of a GFP-tagged, knock-down proof (KDP) TACC3 mutant, S558A –

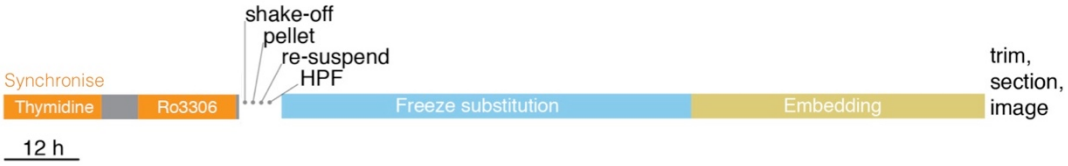

Figure 2.3: HPF experiment timescales. This figure shows a schematic of the protocol of processing for EM using HPF/FS. Cells were synchronised over two days using thymidine (2 mM) and RO-3306 (9 μM), before a mitotic shake-off was performed. Cells were harvested, centrifuged, and the cell pellet was re-suspended in DMEM pre-heated to 37 °C, supplemented with 20 % FBS as a cryoprotectant. The cells were frozen, 1-2 μl at a time, using the Leica HPM100. From thymidine addition to trimming of resin blocks was approximately 8 days.

where the serine normally phosphorylated by Aurora A for TACC3-chTOG-clathrin complex formation and spindle localisation is mutated to alanine. Simultaneously, a short hairpin RNA is expressed for the knockdown of endogenous TACC3. The pBrain plasmids contain a H1 promoter for expression of shRNA targeting the protein of interest, as well as a CMV promoter for re-expression of the RNAi-refractory protein, tagged with a fluorescent reporter, and the construct used in this study was available from previous work in the Royle lab. Using this experimental set-up, I was able to investigate cells with endogenous TACC3 levels, over-expressingTACC3, and cells which had only a form of TACC3 incapable of forming the TACC3-chTOG-clathrin bridge.

In addition to these HeLa cell lines, 5 Glioblastoma cell lines were chemically fixed and processed for SBF-SEM and TEM. The cell lines, gifted by Heiko Wurdak (Leeds), were from Glioblastoma samples and each over-express TACC3 to different extents. The information known about these cell lines is summarised in Table 1.

These chemical fixation experiments were performed using the modified fixation protocol for enhanced staining, described in section 2.2.3.4.

2.4 Three-dimensional segmentation and rendering

All 3D segmentation and surface rendering was performed using Amira software (Visualization Sciences Group, FEI). Tomograms were converted from .rec files produced by etomo to .tif files before loading into Amira. The voxel size in nm^3 was entered upon loading of the file into Amira.

2.4.1 Microtubule segmentation in tomograms

2.4.1.1 Manual microtubule segmentation

Orthogonally-sectioned MTs were identified, by eye, by electron density in the Segmentation Editor in the middle orthoslice of the tomogram and traced individually throughout all slices using a Wacom Bamboo tablet.

Lab nomenclature	WHO classification	TACC3 expr. level rank
GBM 4	N/A	=2
GBM 11	GBM IV. Gliosarcoma	=2
GBM 13	GBM IV.	5
GBM 14	GBM IV. Giant cell Glioblastoma	1
GBM 20	GBM IV.	4

Table 1: Glioblastoma cell lines. 5 cell lines were examined and processed for TEM and SBF-SEM: GBM4, GBM11, GBM13, GBM14 and GBM20. They were all sourced from different Glioblastoma samples. Tumour samples were graded according to the World Health Organisation classification for tumours of the central nervous system (from I to IV, increasing in aggressiveness). All Glioblastomas are graded IV, some Glioblastomas are further classified into Gliosarcomas and Giant Cell Glioblastoma, based on their histological morphology. GBM4 is an older cell line, whose origins are not known. These cell lines over-express TACC3 to different levels (given a rank, 1 being the highest, 5 the lowest). All information in the table was provided by the Wurdak Lab.

2.4.1.2 Interpolation-aided microtubule segmentation

To detect lengths of MT automatically, MTs were first identified and manually segmented in the first, middle and last orthoslice of the tomogram. Then the interpolation function of the Amira segmentation editor was used to detect the rest of the MT length throughout the tomogram volume. Although this method is significantly quicker and less labour-intensive, it was found to be less accurate in tracing MTs than manual segmentation, so manual segmentation was used.

2.4.2 K-fibre mesh segmentation in tomograms

2.4.2.1 Manual mesh segmentation

To manually segment interconnecting material between kMTs, the Wacom tablet was used to trace electron dense material making contact with MTs. This was done throughout each slice of the tomogram.

2.4.2.2 Semi-automated mesh segmentation

To segment the mesh in a semi-automatic way, the mean pixel intensity of the MTs was outputted using the *material statistics* function of Amira. This value was used to threshold the tomogram, excluding any material with a pixel value more than (and therefore less electron dense) this value. The *magic wand tool* was then used to select thresholded pixels making contact with the MTs. Amira then detected any thresholded pixels with values less than or equal to the mean MT pixel intensity that were making contact with the selection, throughout the tomogram. Using this method, any interconnecting material making contact with the MTs throughout the volume of the tomogram that was more or equally electron dense than the MTs was selected.

2.4.3 3D rendering of 3View® volume stacks

MTs in 3View® volume stacks were segmented manually in Amira by tracing all the MTs visible in each orthoslice throughout the entire volume, this segmentation was

rendered to generate a 3D surface. In addition, where kinetochores and centrioles were visible, these were also manually segmented. The *Material Statistics* function of Amira was used to generate the volume data for the rendered MTs.

2.5 Data collection and analysis

In longitudinal sections, K-fibres were defined as bundles of MTs contacting both the kinetochore and the pole. In orthogonal sections, K-fibre bundles were defined using an 80 nm boundary around each MT; 80 nm being the longest observed bridge structure in previous work (Booth et al., 2011). Each MT that was contained within the 80 nm boundary was counted as being part of the K-fibre. Reconstructions of ipMTs in metaphase cells show bundles of 2-6 MTs (Mastronarde et al., 1993), so to ensure that ipMTs were excluded from the study the analysis was restricted to bundles of 10 MTs or more.

Analysis was performed collaboratively with Stephen Royle using IgorPro (Wavemetrics). Custom-written procedure files for IgorPro were written by Stephen Royle, available at *https://github.com/quantixed/TomogramAnalysis.* All box plots show the median, 75th and 25th percentile, and whiskers show 90th and 10th percentile.

2.5.1 Orthogonal analysis of K-fibres

2.5.1.1 Microtubule packing analysis

To analyse MT packing within K-fibres, ImageJ was used to collect the coordinates of the centre of each MT. At this stage, each MT in the fibre was assigned a number that corresponded to its associated Cartesian coordinate, so that a map of MTs could be created and individual MTs could be referred to consistently in separate analyses. From the MT coordinates, the average distance between MTs and the distance to the nearest MT neighbour was calculated. This was done in Microsoft Excel using Pythagoras' Theorem. 3D coordinate sets of the x and y coordinate and nearest neighbour distance were used to generate heat maps by Voronoi interpolation using

IgorPro. To find the area of each K-fibre, the area within a convex hull surrounding the MTs was calculated.

2.5.1.2 Microtubule trajectory analysis

To analyse the trajectories of kMTs from electron tomograms, 3D coordinates for each MT in the fibres (at the top and the bottom of the tomogram) were gathered and recorded using ImageJ. IgorPro was then used to compile these coordinates into individual matrices. From this, farthest point clustering was used to calculate the centre of the bundle, and the distance from this point to each MT was recorded. Due to unavoidable variation in K-fibre axes relative to the plane of sectioning, the bundles needed to be normalised. This was achieved using IgorPro by multiplying the MTs by rotation matrices:

$$R = R_z(\alpha)R_y(\beta)R_x(\gamma),$$

for (in radians) $0 \leq \alpha \leq 2\pi, 0 \leq \beta \leq \pi/2, \gamma = 0$ in $180/\pi$ increments.

The bundle could then be rotated in space to the point at which most of the MT vectors point towards the zenith. The spherical coordinates, given by:

$$R = \sqrt{x^2 + y^2 + z^2},$$

$$\theta = cos^{-1}\left(\frac{z}{\sqrt{x^2 + y^2 + z^2}}\right),$$

$$\varphi = tan^{-1}\left(\frac{y}{x}\right)$$

were then used for plotting and analysing trajectories.

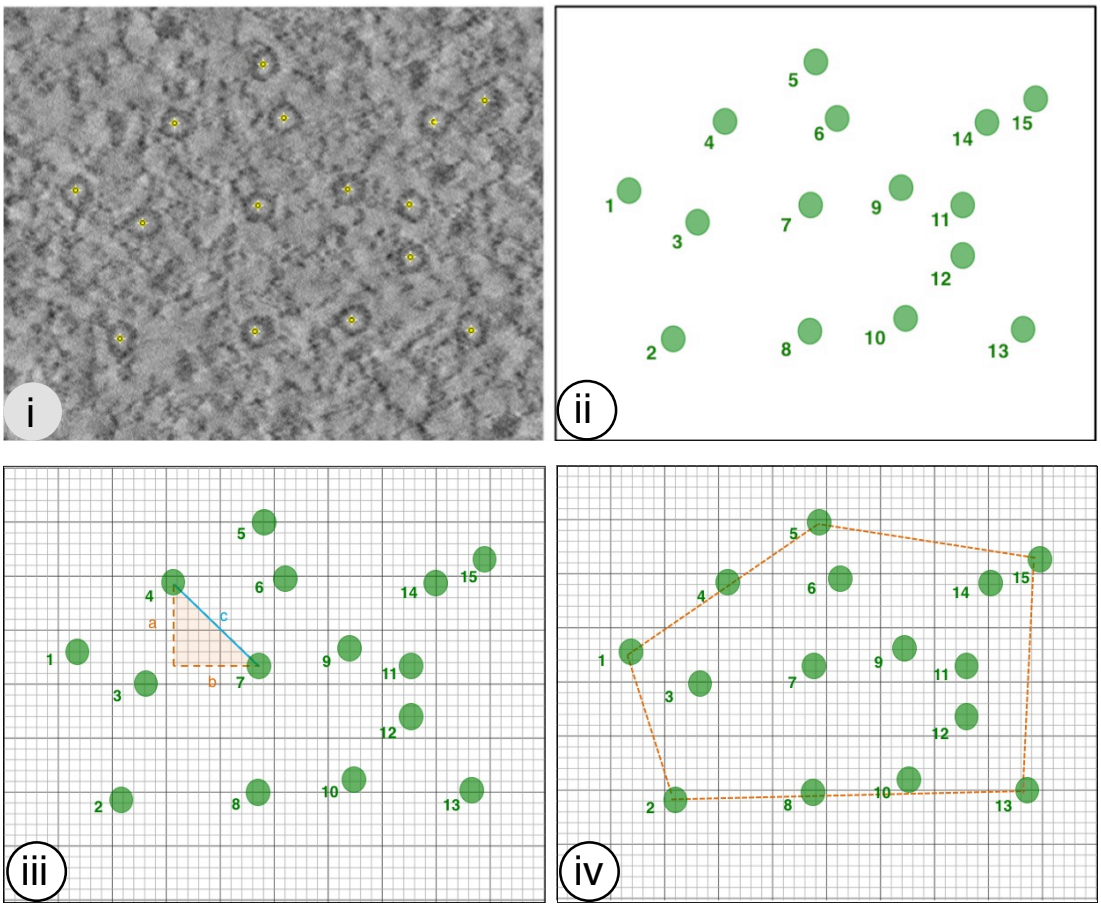
i
ii
iii
iv
v
z
r
θ
y
ϕ
x

Figure 2.4: Analysis of kinetochore microtubule organisation. This figure shows an example tomogram with the MTs annotated to produce the MT map used throughout the analyses. **i**: an orthoslice from the original tomogram, with the MT centre points marked in yellow – these represent the x and y coordinate positions that were collected for the MTs. **ii**: representation of the MT map associated with the tomogram in **i**. **iii**: how the distances between MTs were calculated using Pythagoras' Theorem. **iv**: the convex hull (orange) for this K-fibre, which was used to calculate its area. **v**: a graphical representation of the 3D coordinate system used to analyse MT trajectories within K-fibres (analysis done using IgorPro with custom-written procedures (Stephen Royle)).

2.5.2 3D segmentation measurements

The MTs and mesh of each K-fibre in tomograms were rendered as described in sections 2.3.1.1 and 2.3.2.1, using Amira software.

2.5.2.1 Microtubule/mesh volume measurement

Once the MTs and mesh in K-fibres were segmented, the *material statistics* function of Amira was used to output the volume in nm^3 of both materials. The proportion of mesh per MT was then calculated from these values – normalised to the number of MTs in each K-fibre.

2.5.2.2 Inter-microtubule bridge measurement

To identify different classes of bridge (bipolar, tripolar and quadrupolar) and to analyse the volumes of each, the bridges were individually selected in the Amira Segmentation Editor, and a new material was created for each. The position of the bridges within the fibre and the MTs they make contact with were analysed by recording the MT numbers from the corresponding map described previously (section 2.4.1.1). The *material statistics* function was used to give volume data (nm^3) for each of the bridges.

2.5.2.3 Microtubule attachment quantification

To further analyse the K-fibre mesh and the connectivity within fibres, the coordinate sets were supplemented with chain membership data. “Chains” were defined as MTs continuously connected by bridges in an unbroken group. Producing membership data involved assigning a value to each MT in the fibre based on the size of the chain to which they belonged. For example, all single MTs that were not connected to any others were assigned a value of 1; all MTs belonging to a chain of 3 were assigned a value of 3, etc. This was then used to analyse the connectivity of the K-fibres, and to address the question of whether branched MTs were more or less likely to have more neighbours than single MTs.

2.5.2.4 Contact point visualisation

Visualisation of the mesh/MT footprints was done using Amira. This was done by creating a duplicate surface with the MTs rendered in a different colour, then using the *patch visualisation* function of Amira to add/remove patches between materials as needed.

3. Kinetochore fibres contain a network of microtubule connectors – the mesh

3.1 Introduction

Kinetochore fibres (K-fibres) of the mitotic spindle are bundles of MTs which are able to act as coherent units in order to segregate the replicated chromosomes into two daughter nuclei (Rieder, 1981., Spurck et al., 1997). These K-fibres are focussed at their termini at the spindle pole and at the kinetochore to help them perform this vital function (McEwen et al., 1997, Sikirzhytski et al., 2014). Moreover, many classic EM studies have demonstrated the presence of inter-MT bridges between K-fibre MTs which exist throughout the fibres (McDonald et al., 1992, Mastronarde et al., 1993,). Are these crosslinkers holding them together throughout the entirety of their length? Inter-MT bridges have been the subject of many investigations and have been shown to possess a variety of morphological characteristics beyond the simple two-dimensional bridge that was initially described (Booth et al., 2011). The bridging structures have been proposed to confer stability to K-fibres (Hepler et al., 1970, Rieder, 1982, Witt et al., 1981), but the ultrastructural and molecular basis for this hypothesis is yet to be fully established.

A method is currently lacking which enables the morphology of these bridges within K-fibres to be characterised fully in three dimensions, which would have the potential to shed light on their function within the spindle. Thus far, 3D studies have investigated bridging fibrils emanating from MTs, but this was restricted to the connection to the kinetochore (Dong et al., 2007, McIntosh et al., 2008); and although initial investigations have begun to characterise the network of proteins in K-fibres in 3D (Booth, 2011), more work is needed to optimise the methods used to characterise these bridges fully.

Electron microscopy is a method with the potential to address this problem. High Pressure Freezing (HPF) is a relatively novel EM technique which preserves ultrastructural cellular components in a life-like state. This method, combined with

electron tomography to gain volume data, and 3D segmentation and rendering to visualise this data, has the potential to allow detailed characterisation of the ultrastructural morphology of K-fibres.

3.2 Aims

The aims of this chapter are:

1. To apply High Pressure Freezing and Freeze Substitution methods for examination of mitotic cells by Transmission Electron Microscopy and Electron Tomography.

2. To qualitatively and quantitatively characterise the ultrastructural morphology of kinetochore fibres in two- and three-dimensions.

3. To examine kinetochore fibre ultrastructural morphology in different cell types.

3.3 Results

3.3.1 Inter-microtubule connectors in K-fibres are bridges in 2D and a "mesh" in 3D.

Mitotic cells were processed by HPF/FS for EM and metaphase cells were examined by TEM. In 2D electron micrographs of K-fibres taken either longitudinal or orthogonal to the spindle axis, the canonical 2D bridging structures could be seen between kMTs (Figure 3.1, A and B).

However, when tilt series of orthogonal K-fibres were gathered, the resulting tomographic reconstructions showed a more filamentous network existing between the kMTs and throughout the volume of the tomogram (Figure 3.2i, ii). 3D segmentation and rendering of the kMTs and material in direct contact with them revealed this network of proteins, and it was termed the K-fibre "mesh".

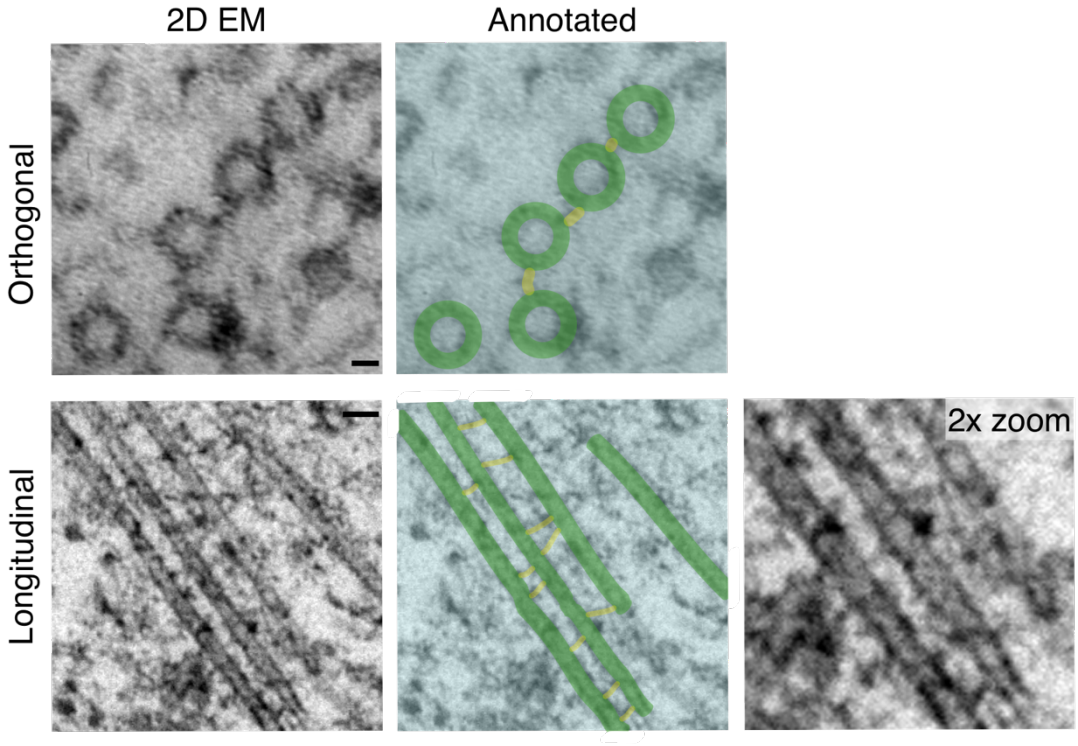

Figure 3.1. Inter-microtubule connectors are bridges in 2D. 2D electron micrographs of inter-MT bridges within K-fibres, taken either orthogonally or longitudinally to the spindle axis. Sections were produced from high pressure frozen samples. **A**: kMTs sectioned orthogonally; **B**: kMTs sectioned longitudinally. Bridges can be seen to form simple bipolar 'struts' between MTs, with varying lengths, tilt angles relative to the MT, and periodicity along the length of the MTs. Scale bar = 10 nm in orthogonal micrograph; 50 nm in longitudinal micrograph.

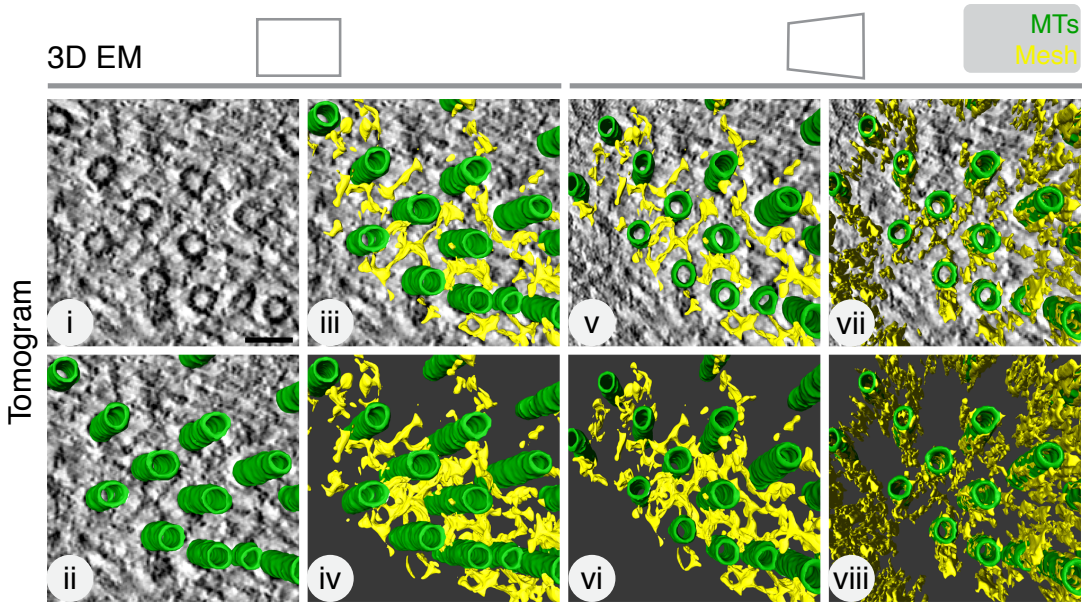

Figure 3.2: Inter-microtubule connectors are a mesh in 3D. Single orthoslice of a tomogram of kMTs, with and without 3D rendered MTs and mesh. **i**: A single tomogram orthoslice, with MTs and filamentous material visible between MTs. **ii**: MTs manually segmented and rendered throughout the volume of the tomogram. **iii**: Initial method of manually segmenting the connecting material. **iv**: As previous, with orthoslice removed. **v**: As **iii** and **iv**, but the camera angle is rotated to align with the MT lumens. **vi**: As previous, with the orthoslice removed. **vii**. Automated method of segmenting and rendering the mesh. **viii**. As previous, with orthoslice removed. For scale, the diameter of a MT is 25 nm. Seven K-fibres were rendered using the automated method, from three different cells, from two separate experiments. Scale bar = 50 nm.

Initial attempts to segment this mesh manually proved subjective (Figure 3.2iii-vi), so an automated method of detection was developed in order to segment this material without bias, as described in Materials and Methods (Figure 3.2vii, viii). This enabled quantitative characterisation of the mesh.

3.3.2 The mesh is major component of kinetochore fibres.

Tomograms of K-fibres from cells at metaphase cells were segmented using Amira. It was then possible to extract volume data from these segmentations in order to quantify the relative proportion of the mesh to the MTs within the fibre (Figure 3.3, A and B). As a result of this quantification, the mesh was found to be a major constituent of K-fibres, comprising a higher proportion of the fibre volume than the MTs themselves. This fact suggests that the mesh is playing an integral role in K-fibre function, supporting the hypothesis that connections between kMTs contribute to fibre stability. The MT volume was calculated both including and excluding the volume of the MT lumen – to understand the contribution of the actual MT volume, and the volume occupied by the MT as a whole within the K-fibre slice (Figure 3.3B).

3.3.3 The ultrastructural morphology of the mesh is heterogeneous, and contains bipolar, tripolar and quadrupolar connectors.

Once tomograms of the K-fibres and mesh had been segmented and rendered in 3D, the different types of connectors were closely examined and recorded in terms of morphology, bridging distance between MTs, and volume. This investigation revealed that individual connectors within the mesh belonged to one of three different classes of connector – bipolar, tripolar and quadrupolar (Figure 3.4A). These classes were defined as an individual unit connecting two, three, or four MTs for bipolar, tripolar and quadrupolar, respectively. No quintrupolar connections were observed.

To dissect whether these tripolar and quadrupolar connectors were multimeric assemblies of a single protein subunit, the volume of each connector was extracted

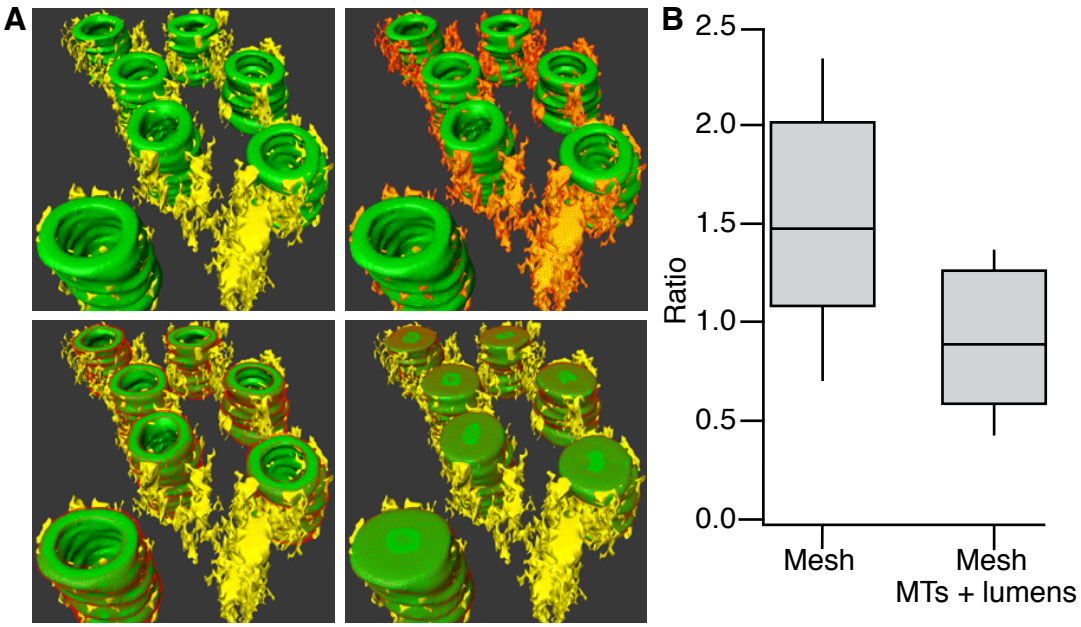

Figure 3.3: The mesh is major component of kinetochore fibres. Quantification of volumes of kMTs and mesh from segmented tomograms. **A** illustrates the volumes measured in Amira. Red matrix indicates the volume that was measured – mesh, MTs, and MTs including their lumen. **B**: Box plots of the ratio of mesh to MT volume, including and excluding the MT lumen. Box plots show the median, 75th and 25th percentile, and whiskers show 90th and 10th percentile. MT and mesh volume quantified from seven K-fibres from three different cells, from two separate experiments.

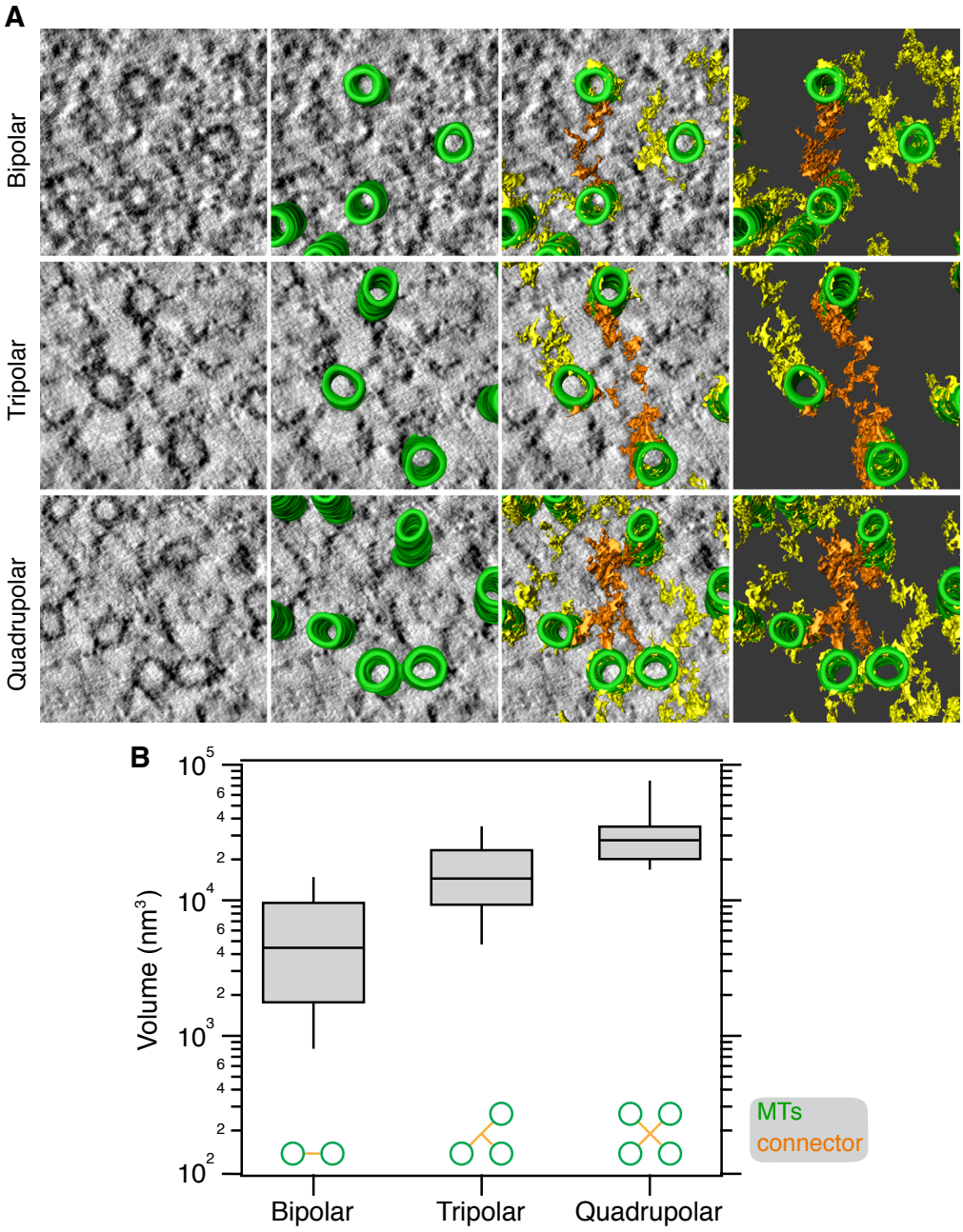

Figure 3.4: The ultrastructural morphology of the mesh is heterogeneous. 3D segmentation and rendering of representative examples of the different classes of connector identified, and quantification of the contribution of each class to the mesh. MTs are rendered in green. **A**: example of a bipolar, tripolar and quadrupolar connector, shown in orange, within the mesh, shown in yellow. **B**: box plots of the volume in nm^3 of each different class of connector within the mesh from multiple tomograms. Crosslinkers quantified from seven K-fibres from three different cells, from two separate experiments.

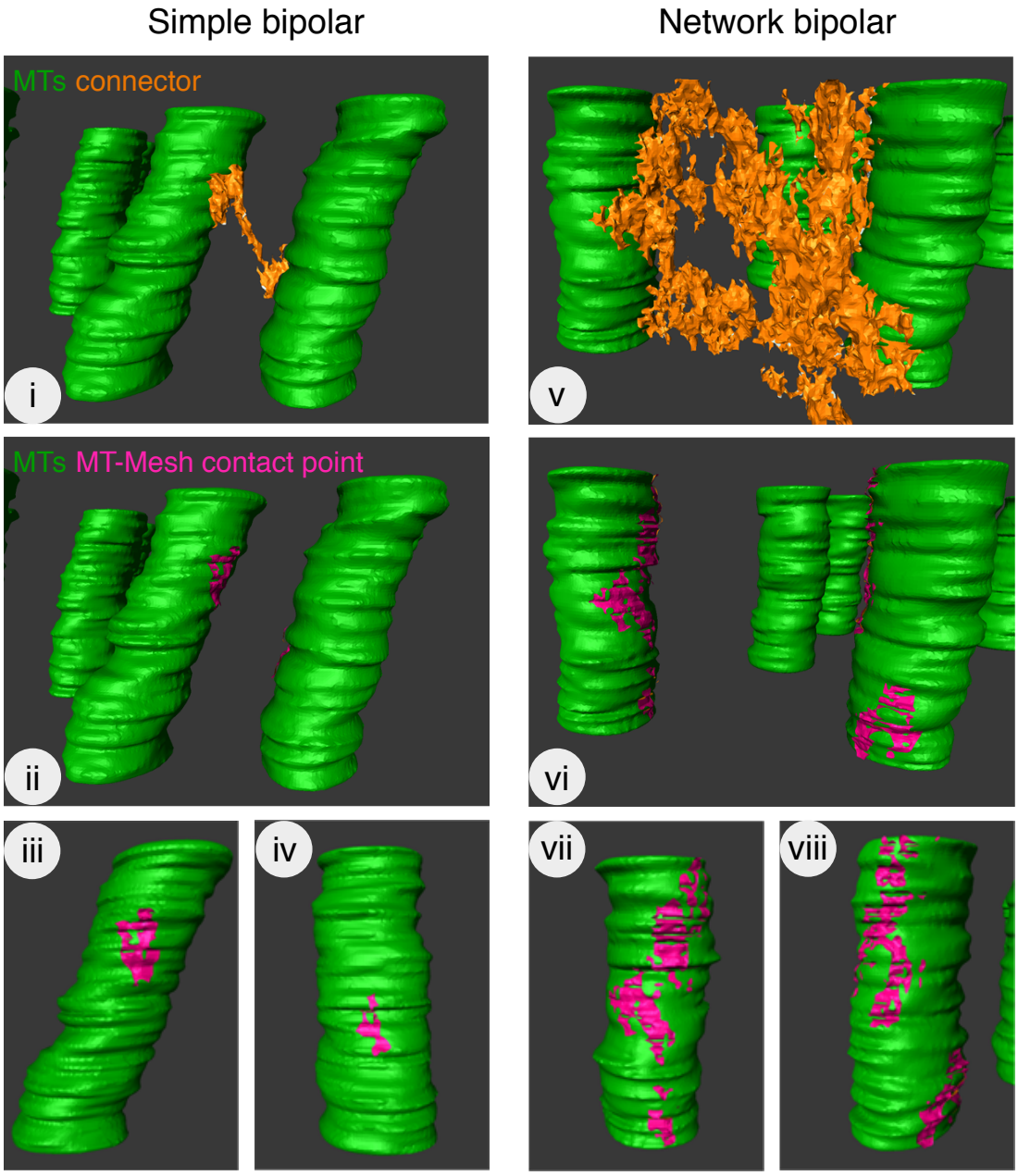

Figure 3.5: individual connectors of the same class are also highly heterogeneous. 3D reconstructions of connected kMTs. Example connector exhibiting a simple bipolar structure is shown in **i**. In **ii** the connector has been removed to show the contact point between the MT and the connector – the footprint. **iii** and **iv**: the bridged MTs, rotated to view the footprint face-on. **v** shows an example of a bipolar connector with a complex connection to the MT, contacting in multiple places along the length. Again, **vi**: the footprints with the connector removed; **vii** and **viii**: the MTs face-on for optimal visualisation of the MT-mesh contact points. In these 3D reconstructions, the entirety of the mesh is not shown, to make the individual connector more easily visible. Crosslinkers quantified from seven K-fibres from three different cells, from two separate experiments.

using Amira (Figure 3.4B). The mean volume determined for each class of connector did not scale with the number of MTs bridged, suggesting that many proteins are involved in the K-fibre mesh. Further support for this comes from the observation that individual connectors of the same class were also highly heterogeneous (Figure 3.5). 3D reconstructions of connectors within the same class were compared to one another and their morphology was found to vary significantly. The 'footprints' of the connectors on the MTs were examined and these contact points were also found to be morphologically heterogeneous (Figure 3.5ii-iv, vi-viii). Different connectors were seen to contact a MT at the same axial position (Figure 3.3A, 3.4A), arguing against the hypothesis that there is a 'preferred' location on the MTs where proteins of the mesh are able to bind.

3.3.4 HPF/FS is needed for optimal mesh preservation.

After detailed characterisation of the K-fibre and mesh ultrastructure, 3D segmentation and rendering was performed on K-fibre tomograms acquired from chemically-fixed samples to determine if the same information could be gained from using the chemical fixation method, which has a higher throughput than HPF. However, segmentation and rendering of chemically fixed tomograms revealed the lack of preservation of mesh proteins (Figure 3.6). It is well documented that aldehyde fixation shows decreased preservation of fine subcellular structures. This result suggests that the complex ultrastructure of K-fibres cannot be optimally preserved using chemical fixation, therefore only HPF has been used in this study to characterise the mesh.

3.3.5 The mesh is K-fibre- rather than spindle-specific.

To establish whether the mesh is K-fibre-specific – existing between kMTs rather than the area between K-fibres – several segmentation methods were used. Firstly, the area around kMTs was segmented alone (Figure 3.7A). This produced amorphous, dense material, which differed from that detected between kMTs.

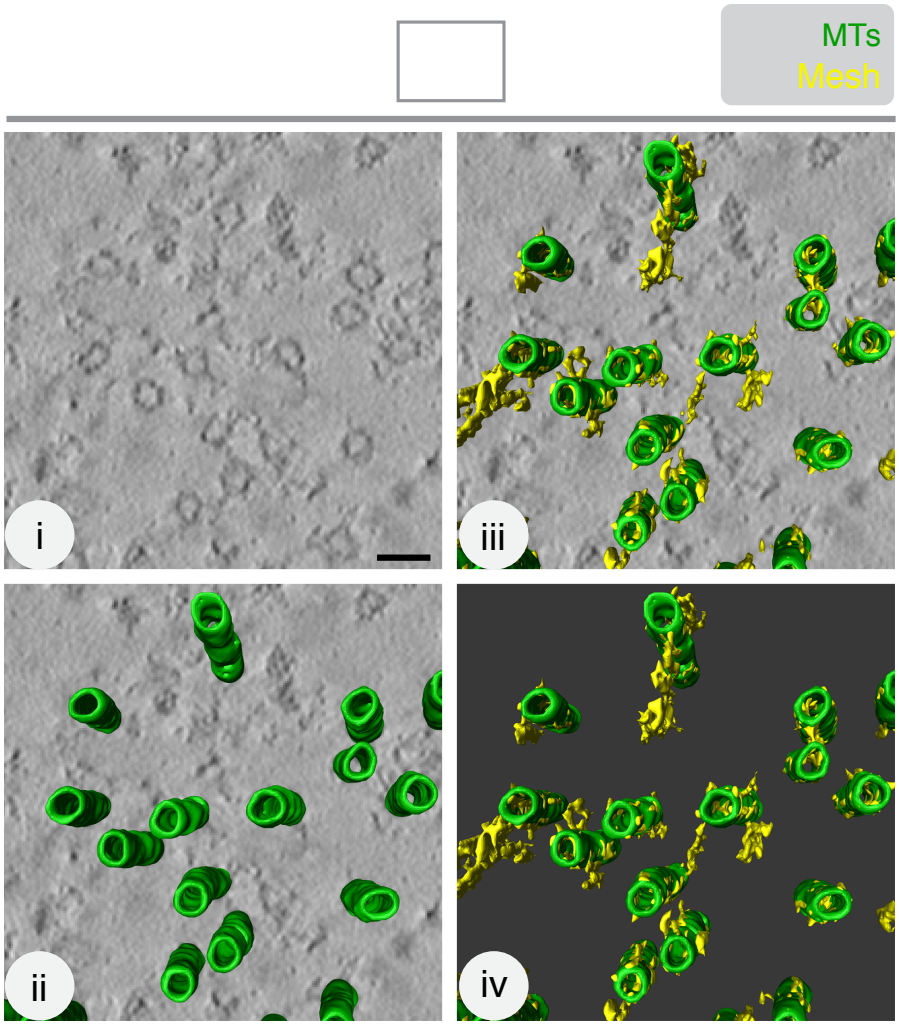

Figure 3.6: HPF/FS is needed for optimal mesh preservation. Orthoslice from a tomogram taken of a K-fibre from a chemically-fixed sample (**i**), with MTs (**ii**) and mesh (**iii**) segmented and rendered in 3D. The tomogram is removed in **iv**. Some mesh can be detected after chemical fixation (yellow), but it is significantly less well preserved. Scale bar = 50 nm.

Secondly, segmented kMTs were transposed into an area of the tomogram where there were no MTs or organelles, and then a 'pseudo-mesh' was segmented with the same automated method of segmentation used previously. The material that was detected appeared similarly amorphous and large areas of density frequently passed through the MT lumen (Figure 3.7B). These investigations demonstrated that the mesh is specific to K-fibres and exists between kMTs. No evidence was found to suggest the mesh exists between K-fibres – that is, MTs in adjacent K-fibres.

3.3.6 The mesh is a major component of kinetochore fibres in multiple cell types.

To exclude the possibility that the mesh is a structure seen only in HeLa cells, the same investigations were performed using RPE1 cells - which are diploid. RPE1 cells were synchronised, pelleted and HPF was performed, as previously, and metaphase cells were identified by TEM. Tilt series were taken of K-fibres, and tomograms generated. 3D segmentation and rendering using Amira, revealed the mesh within K-fibres (Figure 3.8). The mesh in RPE1 K-fibres appears to share the same characteristics as those seen in HeLa cells, supporting the notion that the mesh is a genuine novel spindle component, and is not something that is specific to HeLa cells.

3.4 Discussion

HPF and FS have been shown here to provide superior preservation of the ultrastructural features of K-fibres, improving on the fixation and subsequent visualisation of kMT-associated proteins provided by routine chemical fixation and alcohol dehydration. Many classic EM studies have investigated inter-kMT bridges in order to characterise their morphologies and frequency within the K-fibre. These studies have revealed the presence of different classes and sizes of bridges within K-fibres, and have provided information about their relative frequencies in the fibre (Hepler et al., 1970; Rieder, 1982; Witt et al., 1981; Booth et al., 2011). However, comparing the structural information provided by both methods of EM processing,

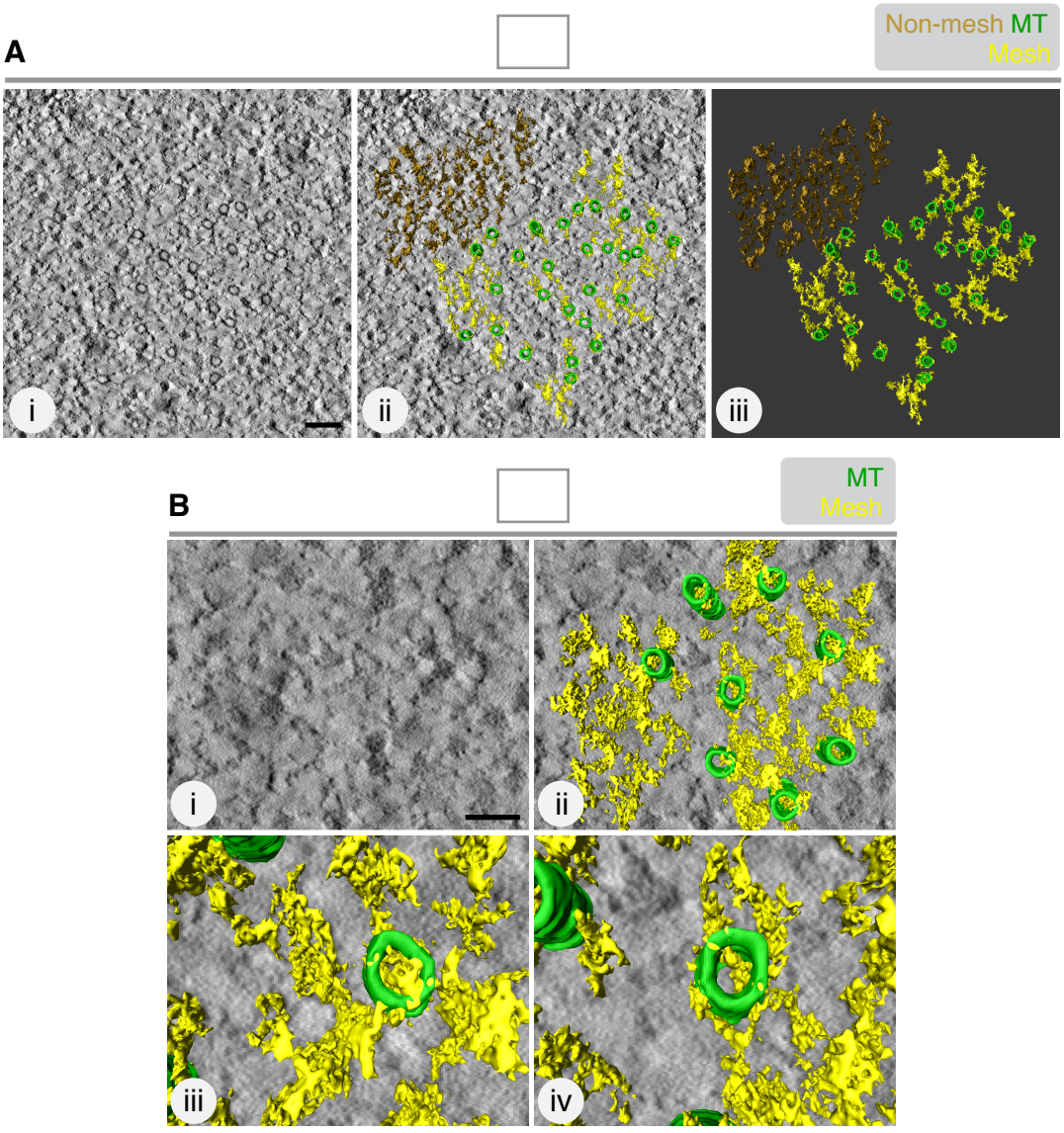

Figure 3.7: The mesh is K-fibre- rather than spindle-specific. **A**: The area outside of the K-fibre was segmented with the same method used to segment the mesh (shown in bronze). The detected material appeared amorphous and more dense than material detected within the K-fibre. **i** is the original tomogram; **ii**: rendered kMTs and mesh; and the tomogram is removed in **iii**. **B**: kMTs were transposed to a MT-free zone and a 'pseudo-mesh' was segmented, again using the same method of segmentation. This material also did not appear to correlate with the K-fibre mesh, as detected material formed large aggregates and penetrated the MT lumen. **i** is the area of the original tomogram to where the MTs were transposed. **ii**: rendered MTs transposed to this area. **iii** and **iv**: close-ups of MTs with 'pseudomesh' aggregates and presence within the lumen. Scale bar in **A** = 100 nm; **B** = 50 nm. The surrounding material was examined in seven K-fibre tomograms from three different cells, from two separate experiments.

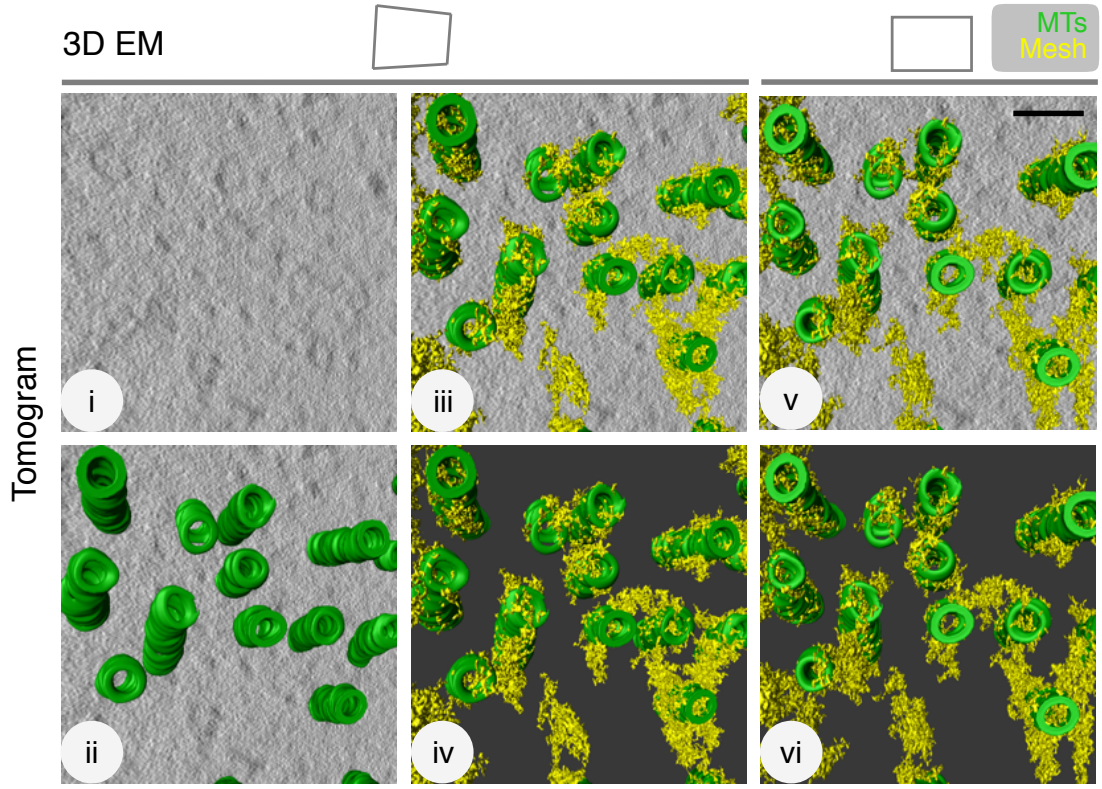

Figure 3.8: Mesh is present in RPE1 cells. Electron tomograms were taken of metaphase RPE1 cells, and segmented and reconstructed using Amira. Mesh between kMTs was seen to possess the same characteristics as seen in HeLa cells. **i**:an orthoslice from the original tomogram; **ii**: rendered MTs; **iii** and **iv**: rendered mesh, with and without the tomogram orthoslice. **v** and **vi**: the same segmentation, rotated to align the MT axis to view the surface face-on. Two K-fibres examined from two cells, from one experiment. Scale bar = 50 nm.

it can be seen that HPF/FS, in conjunction with electron tomography, provides a wealth of information that is lost or inaccessible when only 2D EM is used. 3D segmentation of this volume data is shown to be an ideal method of visualising this structural information and quantifying ultrastructural features, and has led here to the identification and characterisation of the 'mesh' – a novel component of the mitotic spindle architecture. Using this method, it was possible to identify different types of connectors within the mesh, and their respective volumes. Previous studies have shown that it is more than attachment to both the pole and kinetochore that maintains the stability and coherence of K-fibres. Laser ablation experiments have shown that 'stubs' persist after severing of K-fibres at their mid-point (Elting et al., 2014; Spurck et al., 1997, Chen and Zhang, 2004), and my work suggests that the mesh could be responsible for maintaining the observed structural integrity of the kMT bundle.

Inter-kMT bridges have been proposed to play a role in stabilisation of the K-fibre, enabling the fibres to act as coherent units within the spindle (Witt et al., 1981). The mitotic spindle is capable of generating a large amount of force for the purpose of pulling sister chromatids through the cytoplasm into two new cells (Nicklas, 1983), and inter-kMT bridges have been proposed to contribute to the uniform transduction of forces throughout the K-fibre to aid in this purpose. Recent work has also dissected the differing temporal roles for some of these bridges throughout mitosis – showing their importance for maintaining K-fibre tension and satisfaction of the SAC, and critical for K-fibre maturation during prometaphase (Cheeseman et al., 2013). The mesh characterised in this chapter is likely implicated in these proposed roles in providing support for the kMTs along their length. The mesh can be seen to encompass kMTs, which suggests it may also have an additional role in organisation of kMTs with K-fibres. This idea will be investigated further in subsequent chapters.

The spindle matrix is a proposed ensemble of macromolecules enveloping the mitotic spindle and permeating throughout in a lattice-like structure providing a scaffold as the chromosomes are segregated (Pickett-Heaps et al., 1984), and has been the subject of several studies since its proposal. The spindle apparatus of several organisms has been shown to be embedded in a proteinaceous matrix (Chang et al., 2004; Ma et al., 2009; Johansen et al., 2011; Schweizer et al., 2014), but it is as-yet unclear whether these proteins are simply located in the spindle region as a result of a specialised mitotic function, or whether they do truly work co-

operatively as a spindle matrix (Schweizer et al. 2014). Only one of the putative matrix proteins identified in *Drosophila* has a mammalian orthologue, and this orthologue does not localise to the spindle region (Lince-Faria et al., 2009). Immunofluorescence investigations performed in the Royle lab established that members of the TACC3-chTOG-clathrin complex do not persist in the spindle after depolymerisation of spindle MTs using nocodazole (Cristina Gutierrez-Caballero. (Appendix: Nixon et al., 2015 – Author response image 1)). As such, the K-fibre mesh does not appear to correlate with a spindle matrix as it has been described thus far. The spindle structure identified here is kMT-associated, exists within K-fibres rather than between them, and does not persist in the spindle region in the absence of K-fibres

What is the purpose of the K-fibre mesh? Although potential roles of the mesh have been proposed, direct investigation of its function is an important next step in characterising this novel cellular structure. This chapter has outlined important first steps in describing the mesh, but further work is needed to determine if the mesh is important in conferring stability to K-fibres and holding them together.

4. Manipulating the mesh influences kinetochore fibre organisation

4.1 Introduction

The MTs of the mitotic spindle functions in concert with a vast array of MAPs (Sauer et al., 2005). As previously discussed, some of these MAPs have been proposed to crosslink kMTs and confer stability to K-fibres. The optimisation of electron microscopy techniques has enabled us to examine cellular ultrastructure, preserved in a life-like state. This has allowed for the characterisation of the mesh – a three-dimensional network of crosslinking proteins within K-fibres – where only hints at this more complex structure had been observed previously (Wilson, 1969; Warner, 1976).

From previous studies it was established that the TACC3-chTOG-clathrin complex has a role within the mesh, and it was observed that when TACC3 was over-expressed on the spindle, the other complex members are equally increased on the spindle (Booth et al., 2011).

With this in mind, it is now possible to utilise HPF, electron tomography and 3D reconstruction in order to examine the effect that manipulating levels of the TACC3-chTOG-clathrin complex in the spindle has on kMTs and K-fibre ultrastructure. This investigation could shed light on the contribution of the TACC3-chTOG-clathrin complex to the mesh, and the role of the mesh in the function of the spindle apparatus in mitosis.

4.2 Aims

The aims of this chapter include the following:

1. Using manipulation of TACC3 levels, investigate how the organisation of kinetochore fibres is affected by increased mesh.

2. Investigate changes to kinetochore fibre morphology upon TACC3 over-expression using segmentation and 3D rendering.

3. Explore possible functions of the mesh and the TACC3-chTOG-clathrin complex by examining any changes in K-fibre structure after TACC3 over-expression.

4.3 Results

4.3.1 Increasing the mesh by over-expressing TACC3 leads to bigger K-fibres with more microtubules.

GFP-TACC3-expressing mitotic cells were gathered and processed for EM by HPF (as described in Materials and Methods). Electron tomograms were reconstructed from tilt series taken of areas of metaphase K-fibres (orthogonal to the spindle axis). Coordinates of the individual MTs in the K-fibres were used to calculate the K-fibre area, number of kMTs in each fibre, and how close they were to one another. This data was gathered for control HeLa cells and compared to that gathered for TACC3 over-expressing cells (Figure 4.1). After TACC3 over-expression, the number of MTs present in the K-fibres increased significantly. The cross-sectional area of the K-fibres also increased in comparison to controls, but the overall density of the MTs in the fibre remained equivalent to control cells. From these observations it appeared that with TACC3 over-expression, K-fibres simply scaled up in size – there are more MTs in a bigger area, with equivalent spacing to control cells. This suggested that increasing the quantity of protein in the mesh had the effect of recruiting more MTs to the K-fibres. However, qualitatively it appeared that MT spacing within the TACC3

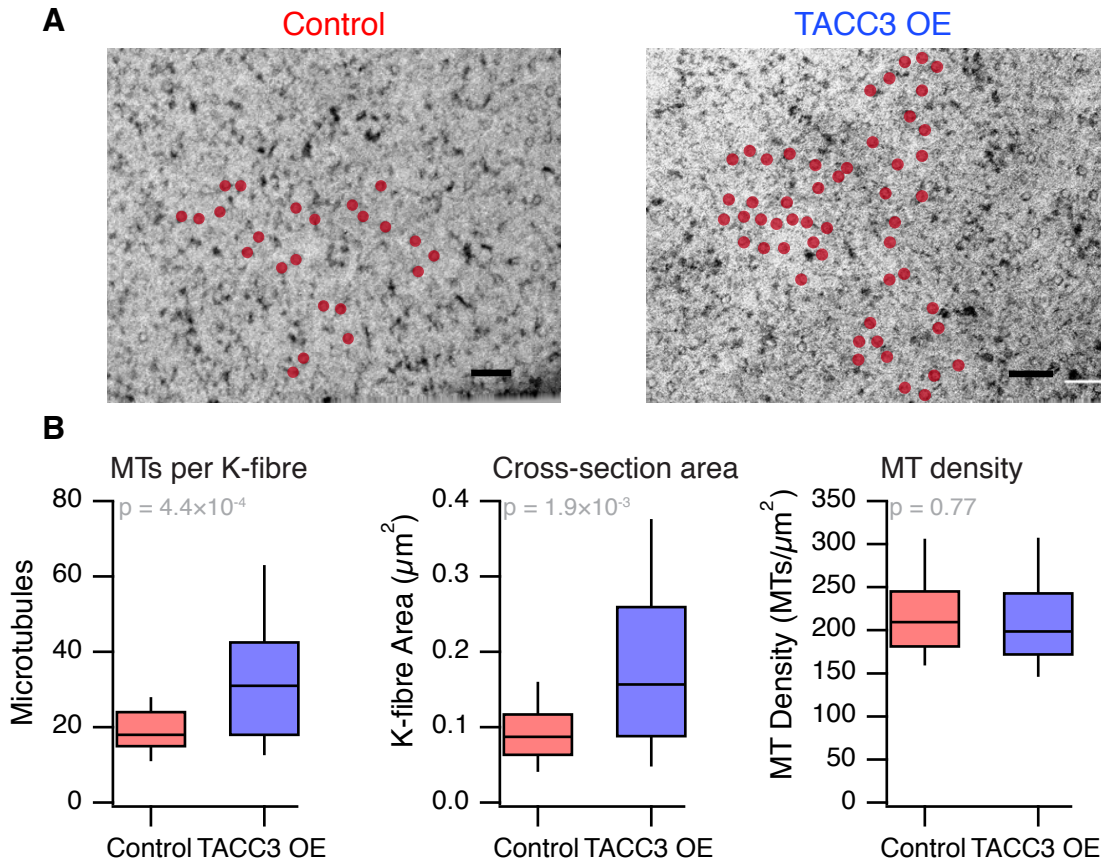

Figure 4.1: Over-expressing TACC3 leads to bigger K-fibres with more microtubules. A: Orthoslices from representative control and TACC3 over-expressing tomograms. Scale bar = 100 nm. **B**: The increase in number of MTs and K-fibre area after TACC3 over-expression. Box plots show the quantification of number of MTs per K-fibre, K-fibre cross-sectional area (μm^2) and MT density within the fibres. Number of MTs and the area of K-fibres increased after TACC3 over-expression, but MT density showed no significant difference between conditions. p values from Welch's t-test are shown. Control K-fibres = 26 (from three cells, from two experiments). TACC3 OE K-fibres = 37 (from two cells, from two experiments).

over-expressing fibres did differ from control fibres, so this was investigated further.

4.3.2 Increased mesh within kinetochore fibres results in a change in local kinetochore microtubule density.

As discussed in the previous section, the overall density of kMTs was unchanged after TACC3 over-expression, but upon examination of tomograms it appeared that the local clustering of kMTs was affected as there appeared to be a greater quantity of smaller clusters within the fibres (Figure 4.2A). To investigate the local packing of MTs within K-fibres, spatial maps were created using the Cartesian coordinate position of individual MTs. The distance of each MT from its nearest neighbouring MT, as well as the number of MTs within bridging distance (80 nm) was calculated from this data (Figure 4.2B). From the resulting maps it was clear that there was a much higher proportion of small clusters of two, three and four MTs in K-fibres of TACC3 over-expressing cells compared to controls (Figure 4.2Bi) and MTs were more likely to have more MTs within bridging distance after TACC3 over-expression (Figure 4.2Bii). When looking at the distance of the nearest neighbouring MT for each MT in the fibres, this distance was smaller after TACC3 over-expression. This suggests that the mesh has a role in kMT spacing, and this spacing is affected by increasing a component of the mesh. Inducing the presence of more TACC3-chTOG-clathrin bridging MTs had the effect of bringing kMTs closer to each other, suggesting that the mesh is capable of influencing the packing of MTs within fibres and may therefore help the K-fibre to act as a coherent unit with even transduction of force throughout the fibres from the kinetochore to the pole.

4.3.3 Kinetochore microtubule interconnectivity is increased with TACC3 over-expression.

From the previous investigations, it was clear that MT packing was influenced by TACC3 over-expression, suspected to be as a result of more TACC3-chTOG-clathrin bridging complexes and thus more inter-connectivity within the fibre. To

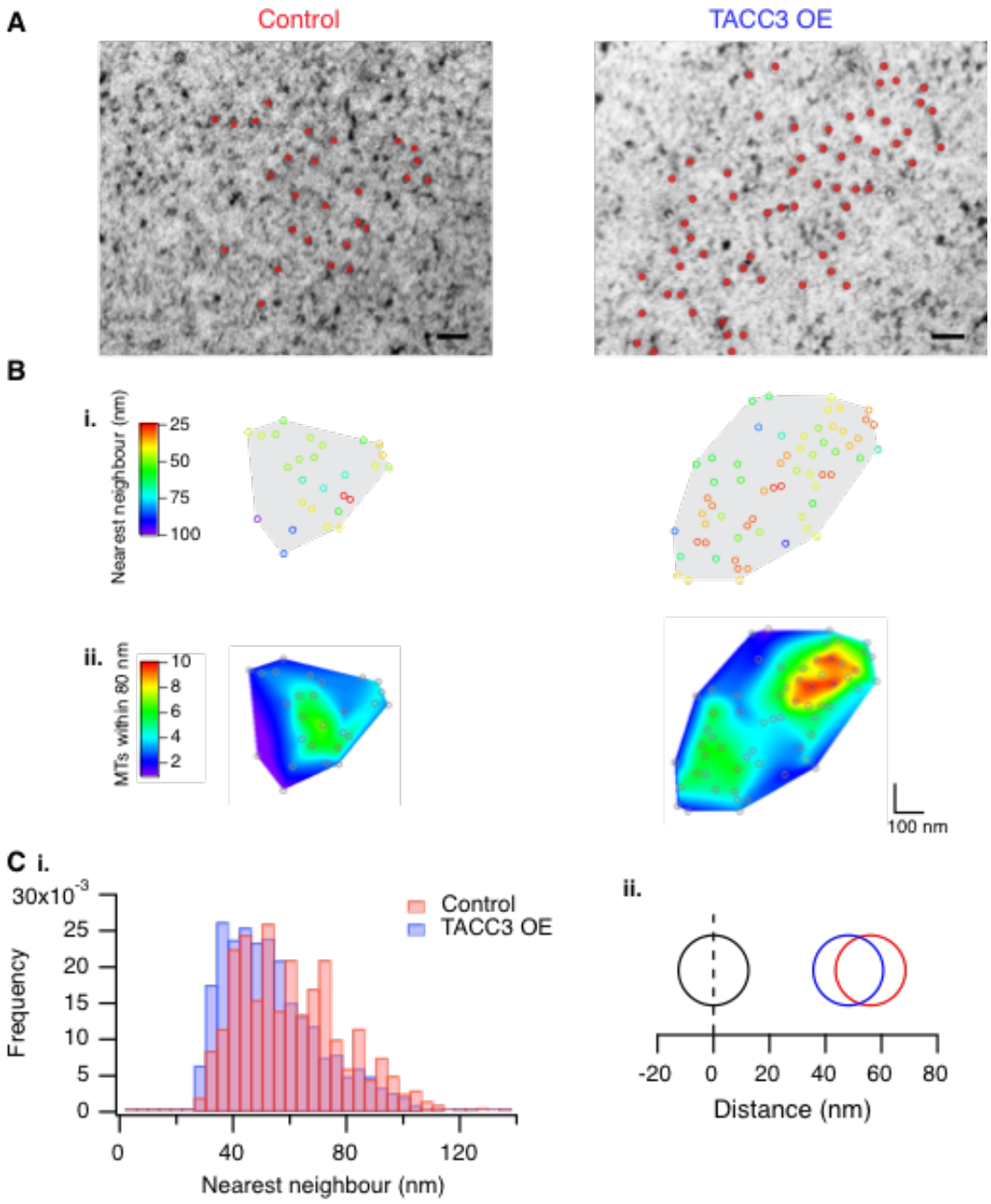

Figure 4.2: Increased mesh within kinetochore fibres results in a change in local kinetochore microtubule density. Clustering of MTs within K-fibres and how this is affected by TACC3 over-expression. **A**: orthoslices from control and TACC3 over-expressing K-fibre tomograms, with MTs annotated. Qualitatively, more small clusters of MTs could be seen after TACC3 over-expression. Scale bar = 100 nm. **B**: spatial maps of the MTs in the above tomograms, colour coded based on the proximity of each MT's nearest neighbour (**i**) and the number of neighbours within 80 nm of each MT (**ii**). **Ci:** histogram showing the frequency of distances to the nearest neighbour for each MT – after TACC3 over-expression, more MTs are in closer proximity. **Cii**: graphical representation of the median distance between MTs in control fibres, showing how much this distance decreases after TACC3 over-expression. Control = 26 K-fibres (N_{MTs} = 500); TACC3 = 37 K-fibres (N_{MTs} = 1344).

test this hypothesis, the connectivity of kMTs from control *versus* TACC3 over-expressing fibres was examined. 3D reconstructions of K-fibres and associated mesh were carefully inspected, and MTs that were connected by uninterrupted mesh density were recorded – to test whether MTs were directly connected to each other in more instances in TACC3 over-expressing cells. To make comparisons with control fibres, a measure of inter-connectivity was established by counting the number of MTs joined together in one continuous "chain" – one MT connected by mesh to another, which may then be connected to a number of other MTs etc. Careful inspection of 3D reconstructions made it possible to identify which MTs were directly connected to another via mesh, and gather data on the number and size of continuous chains within the fibres. In fibres from TACC3 over-expressing cells, the chain sizes were much greater, containing double the amount of MTs than those in control cells (Figure 4.3A) demonstrating that over-expression of TACC3 results in K-fibres becoming much more inter-connected. The contributions of bipolar, tripolar and quadrupolar connectors to the mesh in control and TACC3 over-expressing K-fibres were examined (Figure 4.3B) demonstrating that in both conditions, bipolar connectors were most prominent.

To investigate if these connected regions correlated with the areas of tighter MT packing described in the previous section, spatial maps of the K-fibres were annotated with the position of connectors seen in 3D reconstructions and compared to heat maps of the number of MTs within 80 nm of each individual MT. In TACC3 over-expressing cells, the clustered areas within K-fibres appeared to show some correlation with the areas containing larger chains of MTs (Figure 4.4A). This suggested that MTs could be more clustered as a result of being more inter-connected, so this hypothesis was investigated further.

Figure 4.5 shows the relationship between MT proximity and chain membership – to investigate whether MTs that belonged to a chain were more likely to be more closely clustered together. This analysis showed that after TACC3 over-expression, MTs belonging to a chain were indeed more likely to have more neighbours in close proximity than unchained MTs. This relationship was not seen in control fibres, where chained MTs and single MTs had similar numbers of neighbours. This result suggests that the mesh may play an influential role in kMT spacing within K-fibres, with more mesh pulling MTs closer together.

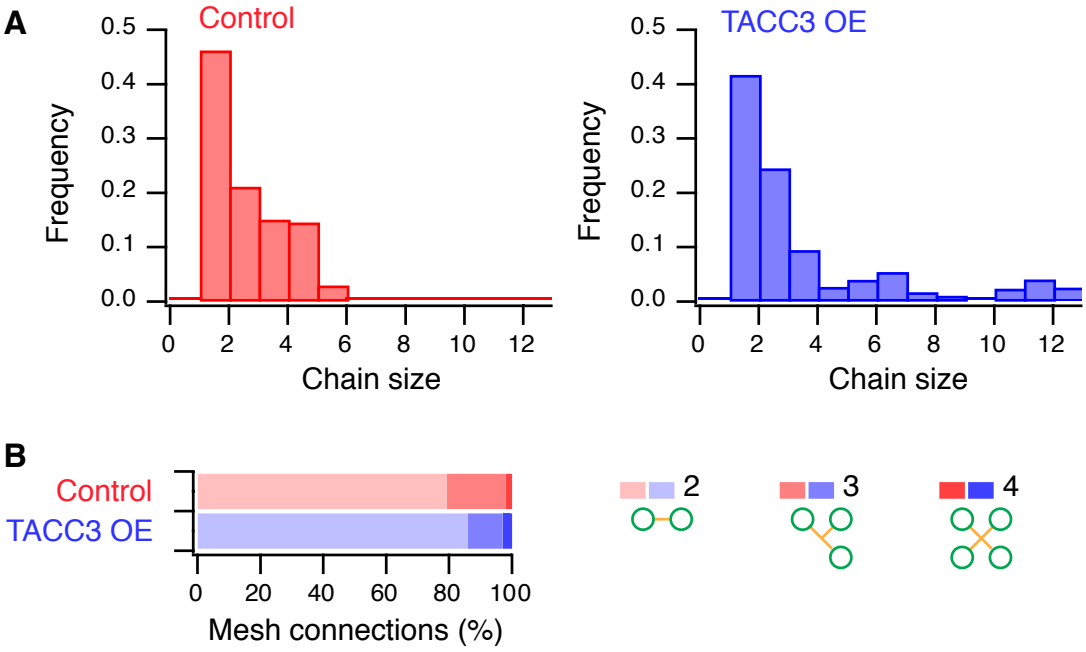

Figure 4.3: Kinetochore microtubule interconnectivity is increased with TACC3 over-expression. The plots show the increase in interconnected kMTs after TACC3 over-expression. **A**: the frequency of different chain sizes in control and TACC3 over-expressing K-fibres. Additional populations of larger chain sizes are present with over-expression of TACC3 (analysis refers to the MTs that are seen to be connected in a single tomogram of approximately 70 nm in thickness). **B**: a quantification of the contribution of each class of connector to the chains. In both conditions, the majority of connectors were bipolar. Crosslinkers quantified from 7 K-fibres from three different cells, from two separate experiments (controls) and 15 K-fibres from three different cells, from two separate experiments (TACC3 over-expression).

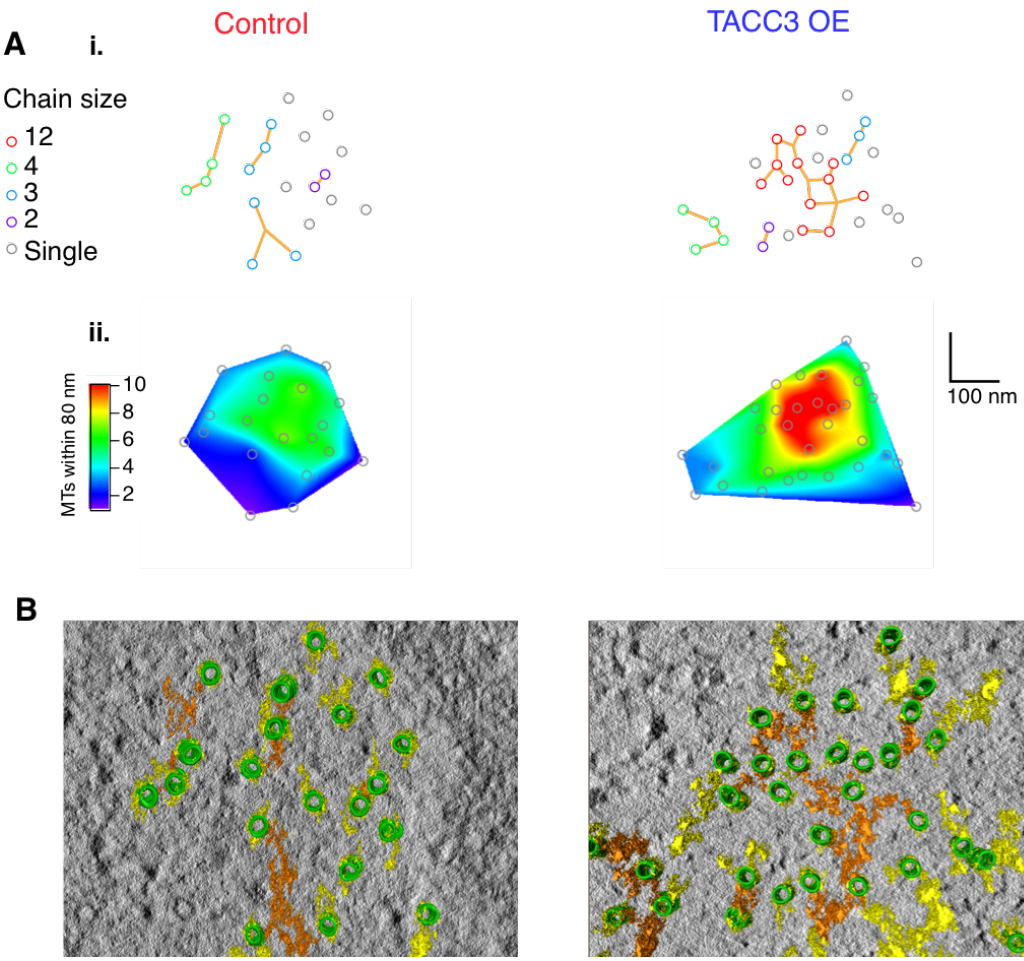

Figure 4.4: Comparison of microtubule connectivity and proximity. Was the increase in MT packing caused by increased interconnectivity after TACC3 over-expression? **Ai:** representative spatial maps of K-fibres from control and TACC3 over-expressing samples with the chains in those fibres annotated. Comparing annotated spatial maps to heat maps generated as in Figure 4.2 (**Aii**), it appeared that there was some over-lap between the more clustered areas and the areas with large chains in the TACC3 over-expressing fibre. **B**: orthoslices from control and TACC3 over-expressing K-fibre tomograms, overlaid with 3D reconstructions of the kMTs and mesh. The mesh connections that were found to directly contact another MT are annotated in orange. Crosslinkers quantified from 7 K-fibres from three different cells, from two separate experiments (controls) and 15 K-fibres from three different cells, from two separate experiments (TACC3 over-expression).

4.3.4 Over-expression of TACC3 influences microtubule trajectories within K-fibres.

To investigate the hypothesis that the mesh is influential in the K-fibre and plays an active role in kMT positioning, tomograms of K-fibres were used to examine the trajectories of the kMTs within them. Upon examination of 3D reconstructions, MTs which seemed to travel in a direction different from the other MTs in the fibre were seen (Figure 4.6A). To examine this quantitatively, the coordinates from the first and the last slice of the tomogram were recorded for each MT to produce a vector in 3D for the trajectory of each MT in the fibre. These were normalised to the overall K-fibre trajectory and the deviations of the vectors from this trajectory were analysed (see Materials and Methods). The polar angles of kMTs in TACC3 over-expressing fibres were often significantly greater than those seen in control fibres (Figure 4.6B,C), suggesting that more MTs in the TACC3 over-expressing fibres deviated from the overall K-fibre trajectory. This could be visualised most easily by setting an XY plane at an arbitrary distance in z (100 nm) and looking at the scatter of all MT vectors starting at the origin as they intersected this plane (Figure 4.6C).

To examine where in the fibre these deviating MTs were, the polar and azimuthal angles of the MTs were plotted relative to distance from the centre of the K-fibre (Figure 4.6D). In control fibres, the MTs that deviated slightly from the K-fibre trajectory had a tendency to be at the periphery of the fibre. However, for TACC3 over-expressing fibres, the MTs deviating from parallel were distributed at all distances from the K-fibre centre.

The results outlined in this section suggest that the mesh is playing an active role in the positioning of MTs within K-fibres. Over-expression of TACC3 caused the kMTs to become less parallel, suggesting higher than normal levels of mesh results in MTs being more interconnected and pulled from their normal trajectory.

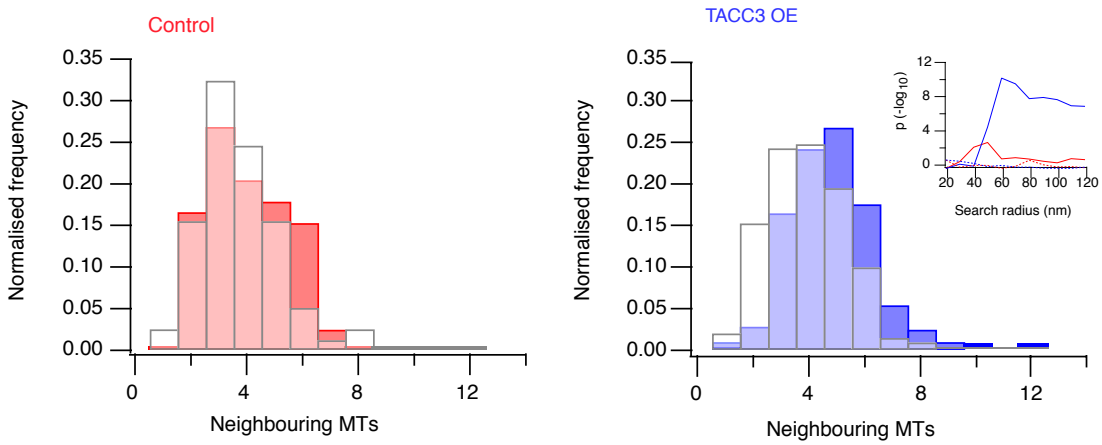

Figure 4.5: Microtubules belonging to a chain are more likely to have more neighbours in close proximity than unchained microtubules. Histograms show the frequency of MTs with a specific number of neighbours within 100 nm (MT centre-to-centre distance), both for single MTs that do not form part of a chain (white) and for MTs that are part of a chain (red/blue). In control samples, single MTs have similar numbers of neighbours as unchained MTs, but in TACC3 over-expressing fibres, chained MTs are significantly more likely to have more neighbours than unchained MTs. Inset shows the p-value ($-\log^{10}$) for comparisons made at a variety of search radii (from 20 nm to 120 nm centre-to-centre), with the dotted line representing the same comparison after the data was randomised.

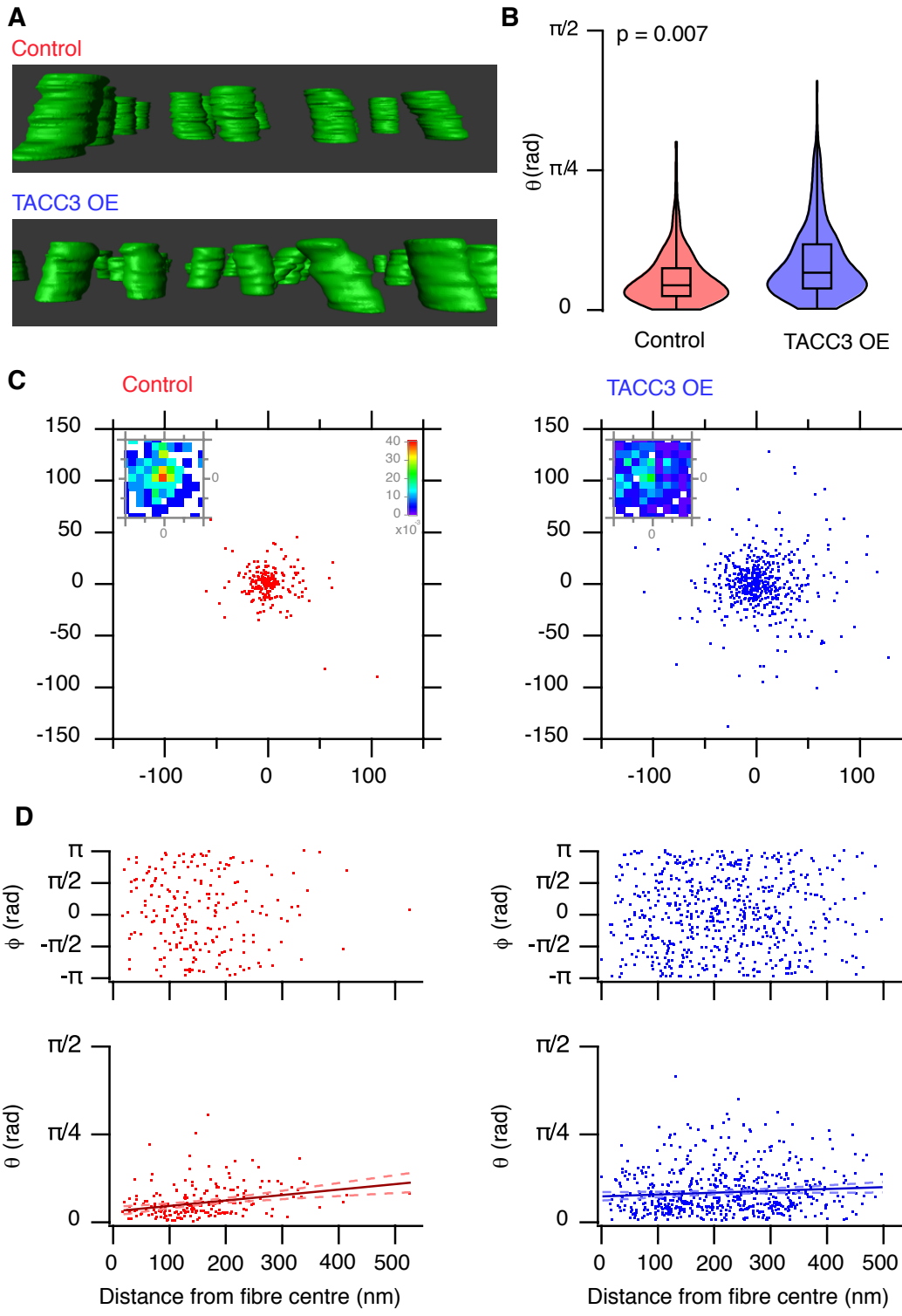
A
Control
TACC3 OE
B
p = 0.007
θ (rad)
π/2
π/4
0
Control
TACC3 OE
C
Control
TACC3 OE
150
100
50
0
-50
-100
-150
-100
0
100
40
30
20
10
0
x10
D
ϕ (rad)
π
π/2
0
-π/2
-π
θ (rad)
π/4
0
100
200
300
400
500
Distance from fibre centre (nm)

Figure 4.6: Over-expression of TACC3 influences microtubule trajectories within K-fibres. Shows analysis of kMT trajectories in control fibres *versus* TACC3 over-expressing fibres. **A**: 3D reconstructions of representative tomograms from control fibres and fibres over-expressing TACC3 – kMTs that appeared to deviate from the parallel trajectory of the K-fibre were seen upon rendering of the 3D surface. **B**: the increase in polar angle demonstrated by kMTs from TACC3 over-expressing fibres (radians). To visualise this more clearly, plots were produced showing the intersection of the MT vectors (normalised to begin at a common origin - 0, 0, 0) through a plane at a z-distance of 100 nm above the origin. Insets show a normalised 2D histogram of the coordinates cropped to a 40x40 square centred at 0, 0, 100, to account for the difference in number of MT between the two conditions (**C**). **D**: phi and theta angles plotted as a function of distance from the K-fibre centre – showing that the MTs deviating the most from parallel in control fibres tended to be around the periphery, while deviating MTs in TACC3 over-expressing fibres were distributed throughout the fibre. N_{fibres} = 12-15.

4.4 Discussion

HPF combined with electron tomography and 3D reconstruction have been used here to examine K-fibre ultrastructure when the mesh is altered. Previous work demonstrated that when TACC3 is over-expressed, more of the other TACC3-chTOG-clathrin complex members are similarly over-expressed at the spindle. This over-expression of TACC3 was utilised to examine the effects of manipulating mesh levels on K-fibre and kMT structure and organisation.

Quantification from electron tomograms of MTs within K-fibres from control and TACC3 over-expressing HeLa cells allowed for the comparison of K-fibre cross-sectional area, and the number of MTs within them. By EM, the number of MTs within K-fibres was significantly increased after TACC3 over-expression, which was coupled with an increase in K-fibre area – suggesting that additional mesh results in increasing recruitment or retention of kMTs within the fibre. Although the density of MTs within the fibres was not significantly altered after TACC3 over-expression, heat maps of MT position in K-fibres revealed areas within TACC3 over-expressing fibres that were more densely-packed, indicating that mesh influences the structural organisation within K-fibres. Segmentation and 3D rendering of these electron tomograms allowed for the characterisation of changes to K-fibre ultrastructure in relation to the presence of mesh within them. 3D volume data generated from the tomograms demonstrated that, after TACC3 over-expression, kMTs were more connected to others within the fibre. In these cells, K-fibres contained chains of up to 12 MTs – more than double the chain size seen in controls. This again implicates the mesh in an organisational role within K-fibres. When this fact is coupled with the observation that interconnected MTs are in closer proximity to each other than non-connected ones, it is likely that the mesh influences spacing within K-fibres.

The possibility that the mesh is passive, and only encapsulates MTs that already exist in close proximity, remains open. However, further experimentation performed in the Royle lab, and results presented in this chapter, argue that the mesh is more influential with regards to MT spacing within K-fibres. *In vitro* experimentation using pre-assembled taxol-stabilised MTs, plus complex member proteins, demonstrated that the TACC3-containing complex is capable of bundling MTs (Fiona Hood; Nixon et al., 2015 (Appendix)). Furthermore, using electron tomography of TACC3 over-

expressing K-fibres, the loss of the normal parallel trajectory of kMTs was seen, with many more MTs deviating from this trajectory. These deviating MTs are seen throughout the K-fibre, again supporting the hypothesis that the mesh is influencing spacing and organisation of kMTs within fibres. The results in this chapter suggest that the TACC3-chTOG-clathrin complex effectively pulls kMTs closer together by favouring close spacing between MTs, but not that it actively pulls kMTs together in a process requiring energy. In this way, the mesh is actively supporting K-fibres and holding them together along their length.

If the mesh is responsible for organisation and spacing within K-fibres, why does more mesh result in more deviating kMTs, rather than making the fibre 'more parallel'? Previous studies into MT crosslinkers within the spindle (Booth et al., 2011) suggest that the mesh is not comprised of the TACC3-chTOG-clathrin complex alone. Over-expressing only one component of the mesh would result in an imbalance, and could explain the non-uniform changes in spacing and trajectory. Previous studies that utilised CLEM to examine inter-MT bridges found that there were at least three populations of connectors within K-fibres, and that the shortest of these was lost after TACC3 depletion (Booth et al., 2011). Increasing the mesh component that has the shortest bridging distance would lead to the results presented in this chapter – abrogated spacing and skewed trajectories.

It is clear that the normal ultrastructural characteristics of K-fibres are altered when levels of the TACC3-chTOG-clathrin complex are altered, but does this have any effect during mitosis? Live cell imaging experiments performed in the Royle lab of HeLa cells over-expressing TACC3 demonstrate that mitotic progression is reduced in this condition (Cristina Gutierrez-Caballero; Nixon et al., 2015 (Appendix)). The time taken to congress chromosomes to the metaphase plate is significantly increased after TACC3 over-expression, as is the time taken to initiate anaphase. This phenotype is also seen upon TACC3 depletion (Lin et al., 2010; Booth et al., 2011; Cheeseman et al., 2013), and suggests that mitosis is sensitive to TACC3 levels. Based on the changes to K-fibre ultrastructure after TACC3 over-expression presented in this chapter, this sensitivity to TACC3 level likely stems from its role in the K-fibre mesh: have too much of the complex and the kMTs are over-stabilised and lose their parallel trajectory, too little of the complex and the mesh cannot organise or stabilise K-fibres adequately. Bakhoum *et al.* describe hyper-stabilisation

of kMTs in cancer cells when compared to normal RPE1 cells (Bakhoum et al., 2009) and show that these hyper-stable attachments result in a loss of ability to correct erroneous couplings between spindle and chromosome – contributing to CIN (chromosomal instability). Aurora A kinase is over-expressed in a number of cancers (Nikonova et al., 2013), and is responsible for recruiting the TACC3-chTOG-clathrin complex to the spindle (LeRoy et al., 2007; Hood et al., 2013). Indeed, over-expression of all complex members is associated with different cancer types. The results presented in this chapter open up the possibility that hyper-stabilisation resulting from TACC3-chTOG-clathrin over-expression could contribute to cancer initiation or propagation.

Recent work established a pool of TACC3 in complex with chTOG at MT plus-ends within the spindle (Gutierrez-Caballero et al., 2015). Although homologues of TACC3 and chTOG are known to have a role in the polymerisation of MTs (Gard and Kirschner, 1987; Tournebize et al., 2000), it is not clear whether the TACC3-chTOG complex influences MT dynamics in mammalian cells, with some studies reporting modest increases in growth velocity after TACC3 over-expression (Nwagbara et al., 2014) and some studies reporting none (Gutierrez-Caballero et al., 2014). Further work in necessary to delineate the contribution of individual pools of TACC3 to the mitotic spindle assembly and maintenance.

Kinetochore cross-sectional area has been documented previously, in some cases being directly measured in electron micrographs (McEwen et al., 1998b). Kinetochore area is variable, depending on the chromosome to which it belongs (Brinkley et al., 1984; Peretti et al., 1986; Cherry and Johnston, 1987). However, after TACC3 over-expression, K-fibre area is significantly increased in comparison to controls, with the mean value exceeding the majority of values recorded in previous studies. Although MT density is increased locally within TACC3 over-expressing K-fibres, the overall MT density is similar to controls. Furthermore, immunofluorescence experiments were performed to detect tubulin intensity in proximity to kinetochores before and after cold treatment to depolymerise non-kMTs. This demonstrated higher tubulin near kinetochores in TACC3 over-expressing cells in comparison to controls, but that this increase in tubulin fluorescence intensity is lost after cold treatment (Cristina Gutierrez-Caballero; Nixon et al., 2015 (Appendix)). Figure 4.7 shows a model, proposed from these results, which may explain the presence of additional

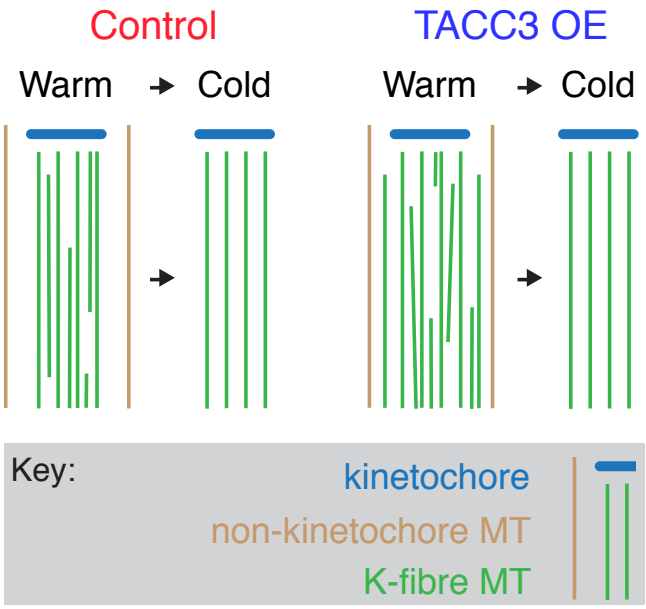

Figure 4.7: Model of K-fibre enlargement after TACC3 over-expression. Graphic representation of K-fibres and peripheral MTs in control and TACC3 over-expressing cells, before and after cold treatment to depolymerise non-kMTs. After TACC3 over-expression, there is an increase in MTs within K-fibres, but these are not stably attached to the kinetochore and are lost after cold treatment, resulting in equivalent numbers of kMTs in both conditions.

MTs in K-fibres of TACC3 over-expressing cells – despite the fibre exceeding the cross-sectional area of documented kinetochore size, and accounting for the loss of these extra MTs after cold treatment. The results presented in this chapter suggest that endowing K-fibres with more mesh results in extra, “passenger” MTs to become part of the K-fibre – MTs that would not belong to the K-fibre unit but have become linked to the fibre through additional crosslinking protein complexes. These MTs would not terminate at the kinetochore, but could cease before reaching the chromatin, or continue to polymerise, bypassing the point of attachment at the kinetochore, contributing to the lack of organisation within the spindle. The model postulates that ‘passenger’ MTs become encapsulated within the K-fibre and these MTs are now interconnected with, and indistinguishable using LM and EM from, K-fibre MTs that would have existed with endogenous TACC3 levels. To establish whether this is the situation that exists in reality, a method is required that would allow whole K-fibres, ideally the entire spindle, to be visualised on the scale of individual MTs in order to establish what these extra MTs are doing and where they are going.

5. Serial Block Face-SEM can be used in conjunction with TEM to provide a more complete picture of spindle architecture

5.1 Introduction

In Chapters 3 and 4 I used HPF, electron tomography and 3D rendering to examine the ultrastructure of K-fibres in unprecedented detail, and this yielded the characterisation of the K-fibre mesh. While this method has provided the best preservation and given the greatest resolution required to examine the mesh, there are some drawbacks to the method. The orientation of the cells in the frozen pellet is random and this makes the likelihood of sectioning precisely orthogonally or precisely longitudinally to the spindle axis rare. As such, the throughput for this method is relatively low compared with conventional chemical fixation. In addition to this, there are obstacles to reconstructing the entire length of a K-fibre using this method, including technical limitations in mounting and imaging the entirety of the same K-fibre in serial sections, as well as loss of information associated with joining serial tomograms.

A technique with the potential to address these shortcomings is Serial Block Face Scanning Electron Microscopy (SBF-SEM). As the name suggests, this equipment scans the surface of a block and records the information gained from the scatter of electrons, before using an automated diamond knife to slice away the surface that was previously scanned. The block is continually scanned and sliced to produce a 3D volume of the contents of the original resin block. This technique has been used successfully to investigate a number of large-scale cellular features, including neuronal circuits in the brains of mice (Holcomb et al., 2013; Mikula and Denk, 2015); podocytes (Ichimura et al., 2015); and skeletal muscle extra-cellular matrix (Gillies et al., 2014). Although SEM cannot achieve the resolution of TEM, the utility of SEM in these studies is clear - providing information normally inaccessible using light microscopy or TEM. However, Jones *et al.* reconstructed the *Xenopus* mitotic spindle using SBF-SEM in order to visualise centriole pairs, but they were unable to resolve

spindle MTs in their images (Jones et al., 2014). If SBF-SEM could be used to examine spindle ultrastructure, this could shed light on K-fibre morphology and the role of spindle associated proteins in building and maintaining this structure. Can the technical limitations of the SBF-SEM system be pushed in order to visualise single MTs? The capability of the technique to achieve MT-level resolution is as yet untested.

Analysis in Chapter 4 demonstrated that over-expression of TACC3 has deleterious effects on K-fibres and progression through mitosis. Glioblastoma is an aggressive astrocytoma with a poor prognosis, and these tumours often over-express TACC3. Studies of mitosis and spindle morphology using electron microscopy could determine if over-expression of TACC3 in Glioblastoma has any consequences in a clinical setting, and will be investigated in this chapter. In addition to this, TACC3 has been shown to exist in different complexes within the cell – forming part of the TACC3-chTOG-clathrin kMT bridge, but also forming a complex with chTOG alone where it tracks the plus-ends of MTs (Gutierrez-Caballero et al., 2014; Nwagbara et al., 2014). There is evidence both for and against this TACC3-chTOG complex possessing the ability to alter MT dynamics, but this chapter will attempt to determine the contribution of these different pools of TACC3 to K-fibre structure.

5.2 Aims

The aims of this chapter are to:

1. Optimise the SBF- SEM system coupled with 3D reconstruction for visualising spindle architecture.

2. Use SBF-SEM to characterise spindle changes after TACC3 over-expression.

3. Use this system to characterise spindle changes after removal of the TACC3-chTOG-clathrin bridge from K-fibres.

4. Determine if there are any abnormalities in Glioblastoma cell lines which could be associated with their over-expression of TACC3.

5.3 Results

5.3.1 Spindle microtubules can be visualised using SBF-SEM.

Parental TetOn® HeLa cells were imaged by LM, then immobilised using the altered chemical fixation protocol for enhanced staining (described in Materials and Methods). They were then embedded in resin and prepared for loading onto the 3View® SBF-SEM system. Optimisation of SEM imaging resulted in establishing conditions which provided resolution sufficient to see nanometre-scale structures, in an area encompassing the spindle zone.

Figure 5.1 shows the result of this optimisation – bundles of MTs in the spindle are clearly visible running from the pole to the chromatin. The majority of biological studies that utilise SBF-SEM, do so to examine structures on the scale of hundreds of micrometres, and the ability of the system to image microtubules in the spindle was unknown. As demonstrated in Figure 5.1, this is indeed possible with the correct conditions for fixation and imaging. From this, the possibility of reconstructing the entire spindle using 3D rendering software was investigated.

5.3.2 3D reconstruction of SBF-SEM volumes show complete spindle architecture.

The stacks produced by the 3View® system of the spindle volume were loaded into Amira, and the MTs visible in each slice of the stack were manually segmented throughout the entire volume of the spindle. From this segmentation, a 3D surface was generated, allowing the visualisation of the mitotic spindle (Figure 5.2). From this it was possible to view the architecture of the spindle - discerning K-fibres and ipMTs. In some instances, kinetochores were also visible (Figure 5.3).

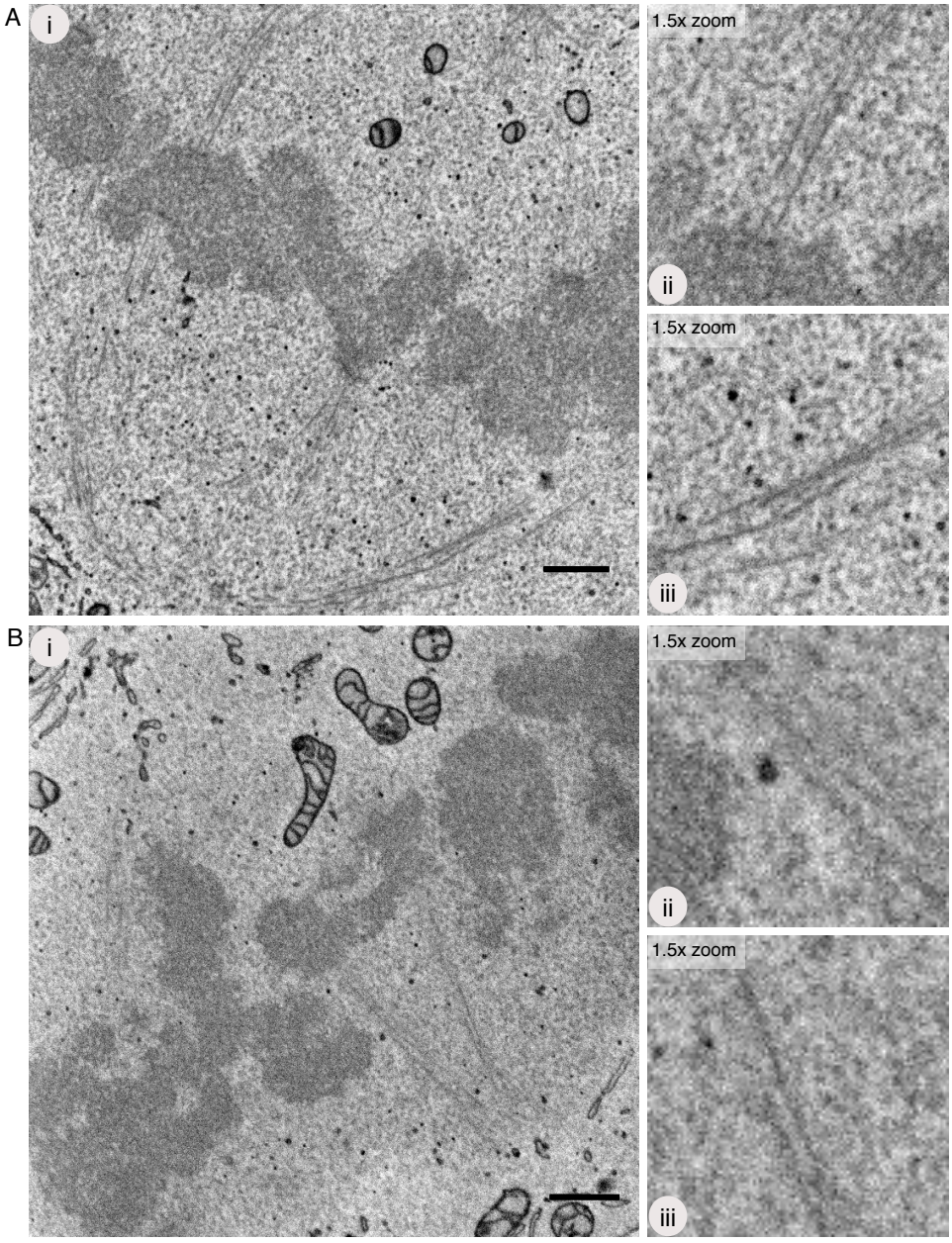

Figure 5.1: Spindle microtubules can be visualised using SBF-SEM. Ai and **Bi**: orthoslice from SBF-SEM of control HeLa cells at metaphase, longitudinal to the spindle axis, focussing on the spindle zone. The chromatin in seen aligned at the equator, diagonally across the orthoslice. K-fibres are visible spanning the distance from the poles to the chromatin. **Aii** and **iii**: zoomed regions from the orthoslice in **A**. **Bi** same region from a different control cell, again with close-ups of MTs in **ii** and **iii**. Scale bar in **Ai** and **Bi** is 1 µm. SEM Magnification: 21,000x. kMTs visible in 28 cells, from 2 separate experiments.

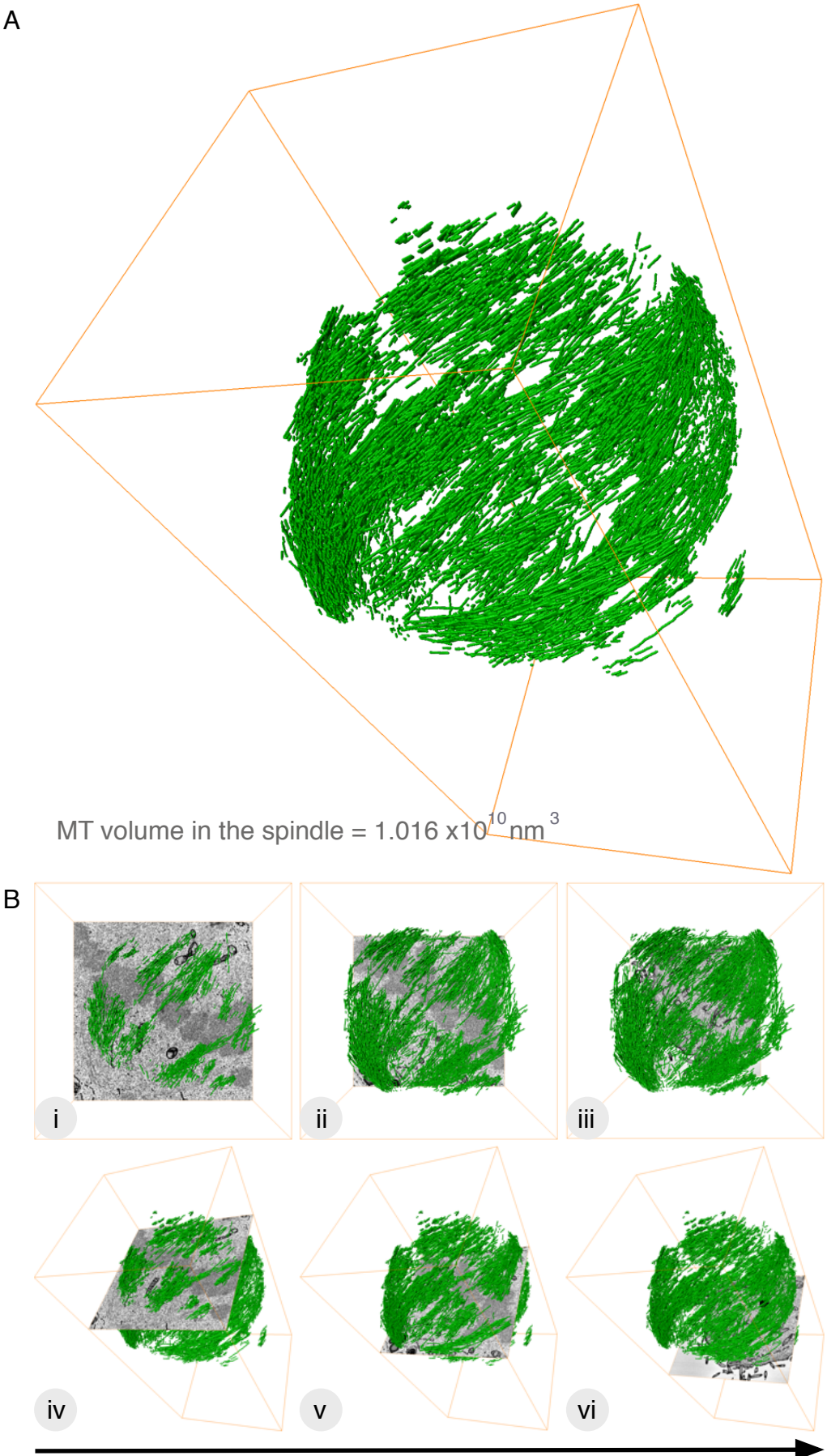
A
MT volume in the spindle = 1.016 x10^10 nm^3
B
i
ii
iii
iv
v
vi
Slice number

Figure 5.2: 3D reconstruction of SBF-SEM volumes show complete spindle architecture. A: 3D reconstruction of the entire MT volume of a GFP control HeLa cell, using Amira. The bounding box of the volume is shown in orange, for orientation, and demarcates the SBF-SEM block volume. The volume of the 3D rendered spindle is shown in nm^3. **Bi-iii**: sequential orthoslices through the SBF-SEM volume, with 3D rendering, in plan view. Individual K-fibres can be distinguished in the rendered volume. **iv-vi**: the same sequential orthoslices as **Bi-iii**, viewed at an angle. Spindle MTs of two control cells were rendered.

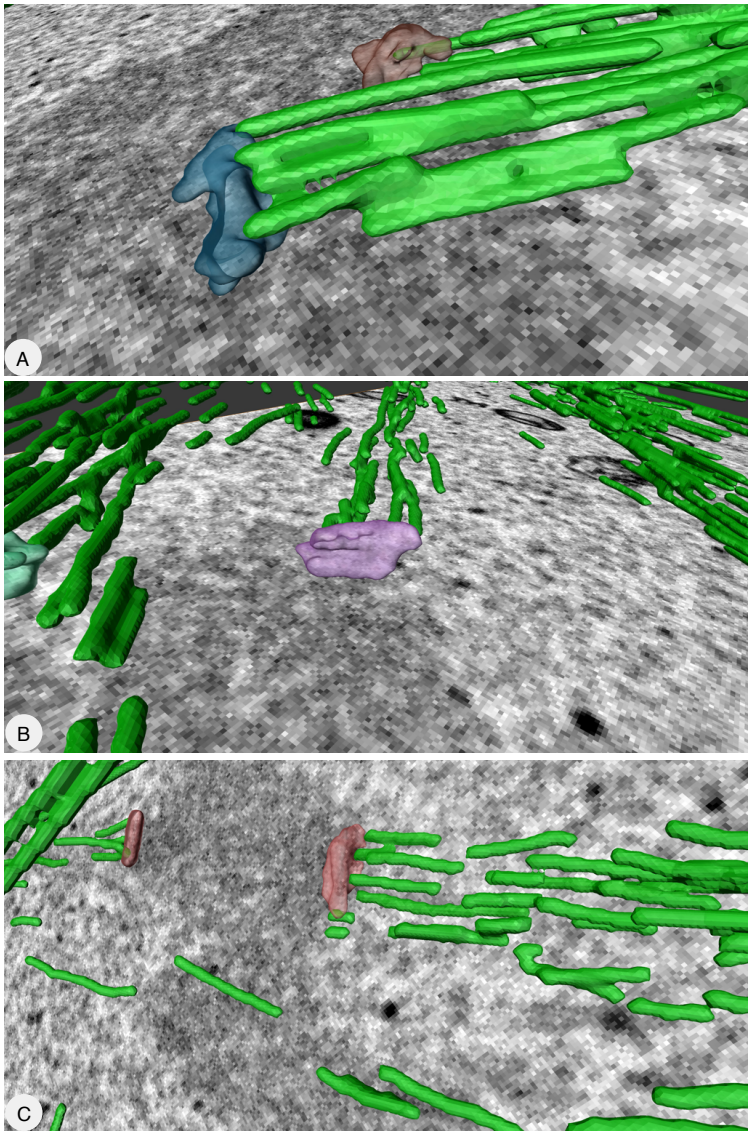

Figure 5.3. Kinetochores are visible in SBF-SEM volumes: This figure shows snapshots of areas in the SBF-SEM volume where kinetochores, and kMTs attaching to kinetochores, could be distinguished. Kinetochores are segmented and rendered in different colours, MTs in green. The third panel shows putative sister kinetochores on either side of the chromatin visible in the orthoslice.

5.3.3 TACC3 over-expressing K-fibres are merged in the body of the spindle, but become distinct at the kinetochore.

It was concluded that SBF-SEM in combination with 3D rendering could offer the resolution needed to visualise MTs - on a large enough scale to shed light on how the spindle architecture is altered after TACC3 over-expression.

HeLa cells over-expressing TACC3, at metaphase, were chemically fixed and prepared for SBF-SEM, imaged and the volume of the spindle reconstructed using Amira. Qualitatively, the spindle region appeared populated with more MTs than was seen in control HeLa cells (Figure 5.4). SBF-SEM volumes were produced for 4 TACC3 over-expressing metaphase cells, from two separate experiments, although only one of these was rendered in 3D.

Upon closer inspection of the visible K-fibres, some MTs appeared to belong to a large bundle away from the kinetochore, only becoming distinct as they terminate at the kinetochore (Figure 5.4, 5.5), suggesting that over-expression of the TACC3-chTOG-clathrin component of the mesh is causing fibres to become merged in the body of the spindle, only resolving into two separate fibres at their plus-ends.

To determine whether this merging was solely responsible for the increased MT number and K-fibre area seen in Chapter 4, the volume was measured of MTs in both the control HeLa cell and the TACC3 over-expressing HeLa cell. The volume of MTs in the TACC3 over-expressing cell was slightly increased (Figure 5.2, Figure 5.4), suggesting that more of the mesh complex does result in more MTs overall within the spindle, but that altered spacing is also likely to be contributing to this perceived difference.

After cold treatment of metaphase HeLa cells, no difference in tubulin intensity adjacent to kinetochores between control and TACC3 over-expressing HeLas could be detected by immunofluorescence (Cristina Gutierrez-Caballero; Nixon et al., 2015 (Appendix)). Could any difference be detected using SBF-SEM? Metaphase cells were cold-treated and prepared for the 3View® system, and then the spindle was segmented and rendered into 3D. SBF-SEM volumes were produced for 3 cold-treated TACC3 over-expressing metaphase cells, from two separate experiments,

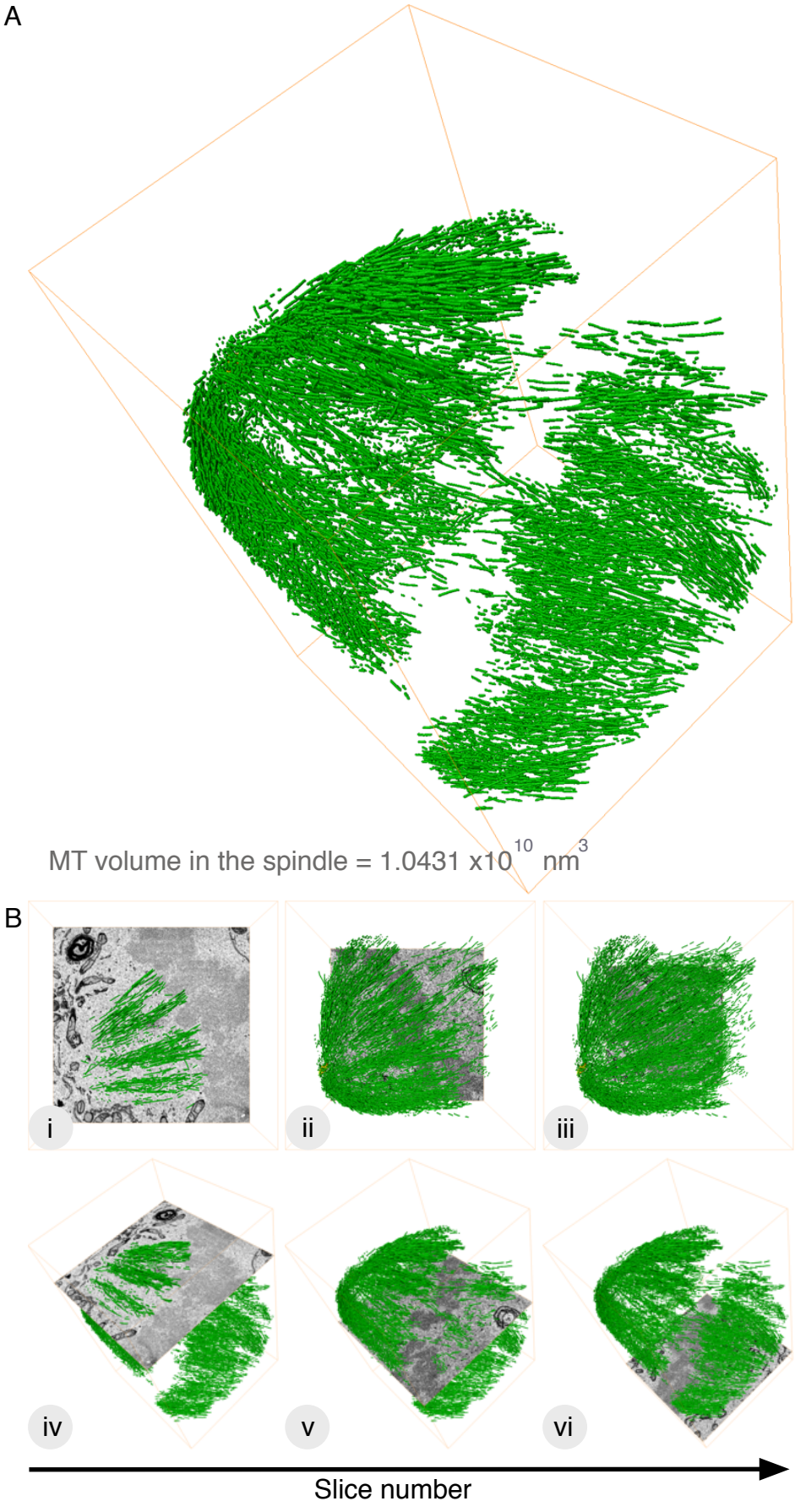
A
MT volume in the spindle = 1.0431 x10 10 nm 3
B
i
ii
iii
iv
v
vi
Slice number

Figure 5.4: TACC3 over-expressing HeLa cells have more microtubules in their spindle. A: 3D reconstruction of the entire MT volume of a GFP-TACC3 over-expressing HeLa cell, using Amira. A bounding box is shown in orange for orientation, demarcating the SBF-SEM volume. The volume of the 3D rendered spindle is shown in nm^3, and is increased compared to that of control HeLa cells (Figure 5.2). **Bi-iii**: sequential orthoslices through the SBF-SEM volume, with 3D rendering, in plan view. Qualitatively, K-fibre bundles appear larger in the cell than in the control. **iv-vi**: the same sequential orthoslices as **Bi-iii**, viewed at an angle. Spindle MTs of one TACC3 over-expressing cell was rendered.

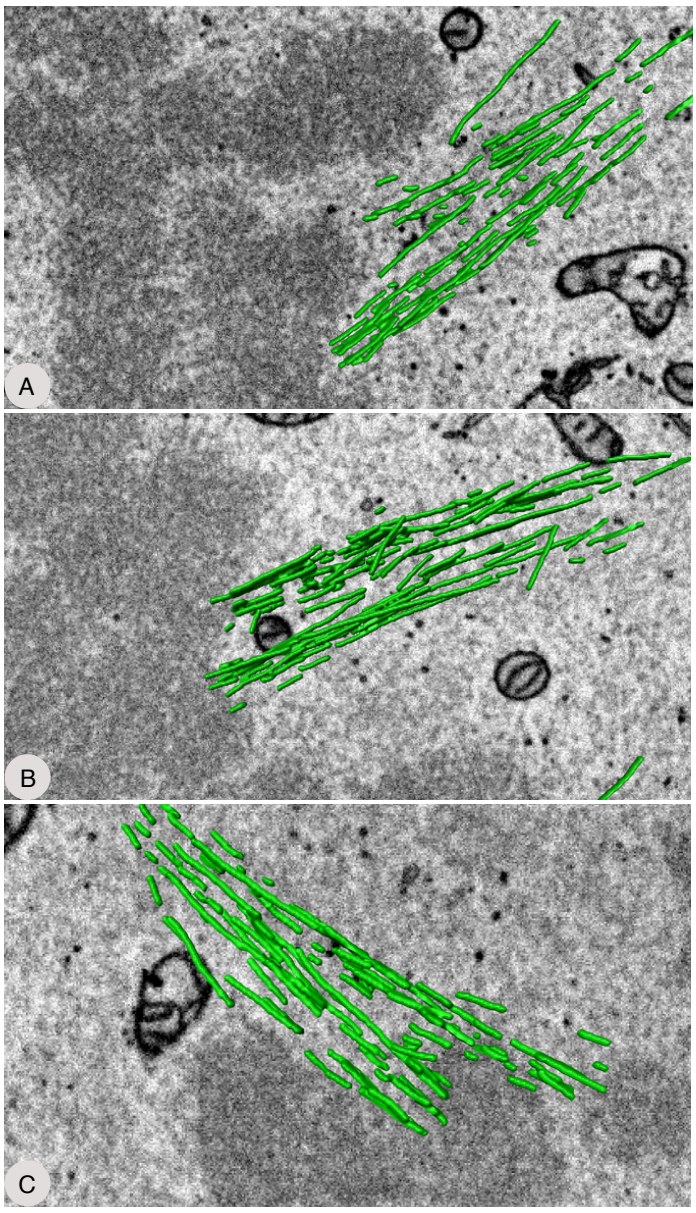

Figure 5.5: K-fibres are merged in the body of the spindle, becoming distinct at the kinetochore. A, B and **C**: Orthoslices of SBF-SEM volumes with rendered K-fibres, showing examples from TACC3 over-expressing HeLa cells where large fibres appear merged in the body of the spindle, closer to the pole, but split apart as they terminate at the chromatin.

A

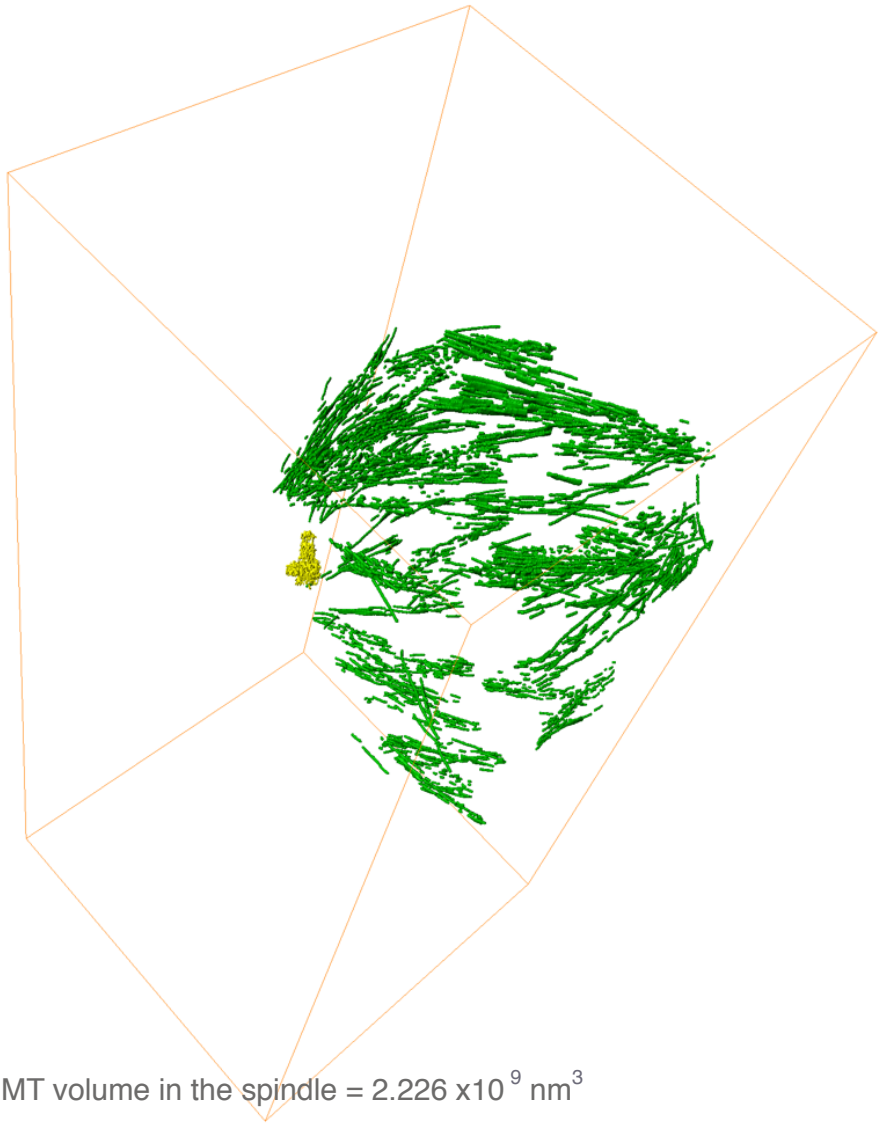

MT volume in the spindle = 2.226 x10 ^{9} nm^{3}

B

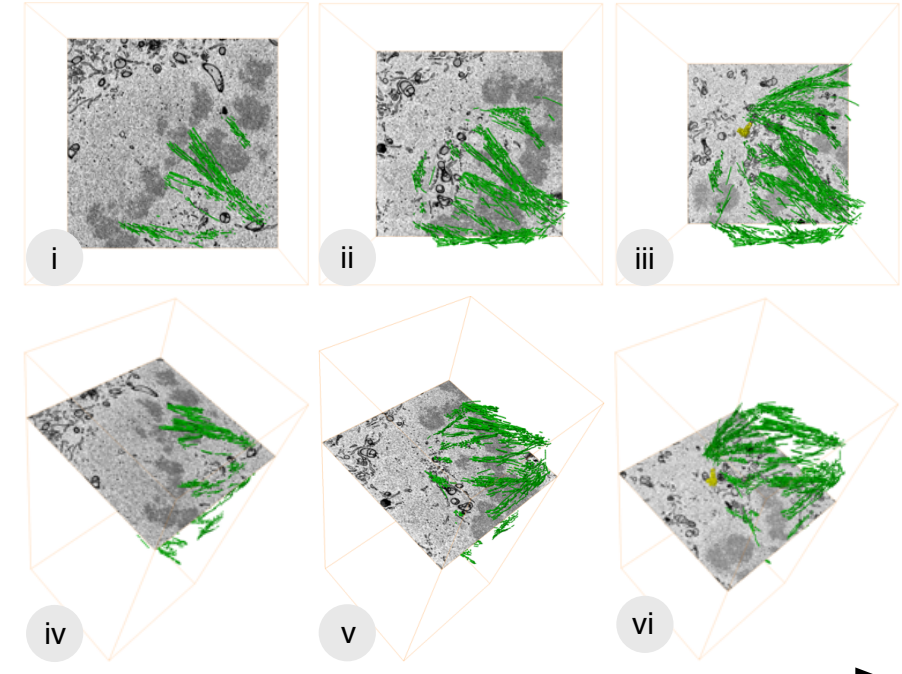

C

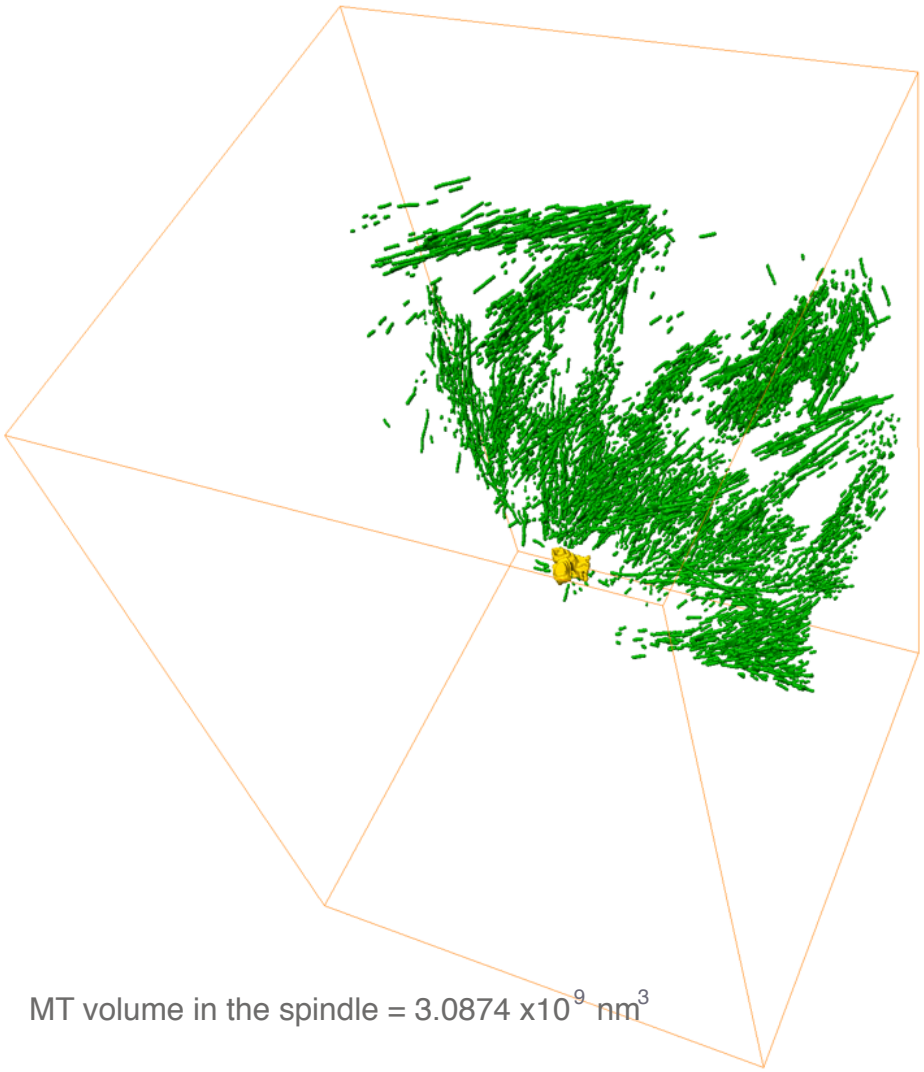
MT volume in the spindle = 3.0874 x10 9 nm3

D

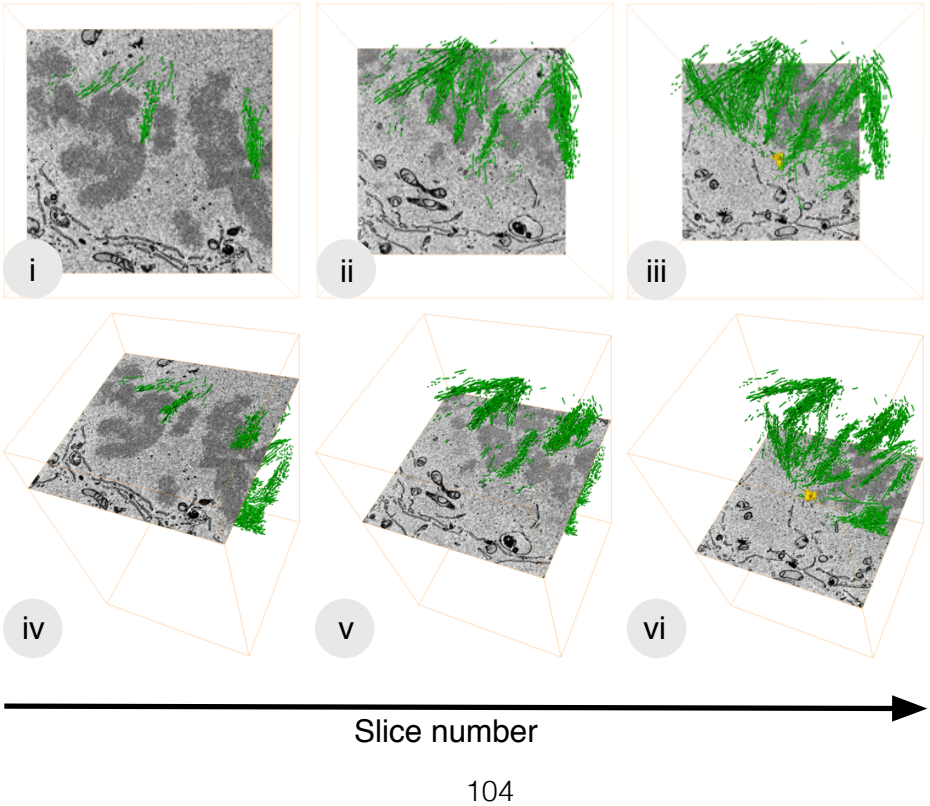
i
ii
iii
iv
v
vi
Slice number

Figure 5.6: Cold treated cells over-expressing TACC3 contain more microtubules than control cells. A: 3D reconstruction of the entire MT volume of a cold-treated control HeLa cell, using Amira. A bounding box is shown in orange for orientation, demarcating the SBF-SEM volume. **Bi-iii**: sequential orthoslices through the SBF-SEM volume, with 3D rendering, in plan view. **iv-vi**: the same sequential orthoslices as **Bi-iii**, viewed at an angle. **C** and **D**: the same as **A/B**, for a cold treated TACC3 over-expressing HeLa cell. The volumes of the 3D rendered spindles are shown in nm^3, and is increased in the TACC3 over-expressing cells compared to the control. Spindle MTs of one cold treated control cell and one TACC3 over-expressing cell were rendered.

although only one of these was rendered in 3D. The volume of MTs detected in the 3D segmentation of the GFP-TACC3 cell was greater than the volume in the control HeLa (Figure 5.6) suggesting that more of the mesh complex may be causing more MTs to become included in K-fibres and become stably-attached to kinetochores, although light microscopy does not provide the resolution required to detect this phenotype.

5.3.4 TEM analysis of K-fibres close to the kinetochore shows smaller differences between Control and TACC3 over-expressing K-fibres.

As outlined in the Materials and Methods chapter, the electron micrographs and tomograms were collected of K-fibres at least 1 μm away from the kinetochore, to avoid including the proteins which attach kMTs to the kinetochore in our analysis of the mesh. Using SBF-SEM, merged K-fibres were seen away from the kinetochore, which appeared to separate as they terminate. If electron tomograms were taken of K-fibres closer to the kinetochore, could this phenotype be detected using TEM? Metaphase cells chemically-fixed using the protocol for SBF-SEM were instead trimmed and sectioned for imaging by TEM. Tomograms of K-fibres close to the kinetochore were gathered and analysed, as in Chapter 4, to investigate the differences between control and TACC3 over-expressing K-fibres closer to the chromatin. Analysis of mesh and connections between kMTs was not repeated due to the proximity to the kinetochore, and the fact that chemical fixation would be unlikely to preserve such fine structures (as seen in Chapter 3, Figure 3.6).

This analysis demonstrated that, after TACC3 over-expression, kMT number and area showed an increase (Figure 5.7A), although this increase was less marked than was seen in the previous chapter. This is consistent with the observations from 3D reconstruction of SBF-SEM volumes that the spindle contains more MTs, and that these large K-fibres do appear to branch off from each other as they reach the kinetochore.

A decrease in the overall kMT density within the K-fibres was detected after TACC3 over-expression (Figure 5.7A), although this analysis does not provide information regarding the local packing of MTs within the fibres. To examine this, heat maps were again produced, showing distances to the nearest MT neighbour, and the number

of neighbours within bridging distance (80 nm) (Figure 5.7C). This demonstrated differences in MT packing between controls and TACC3 over-expressing K-fibres, with control fibres tending to have a small cluster of MTs at their centre, and TACC3 fibres containing multiple clusters. As with the analysis in Chapter 4, having more of the TACC3-chTOG-clathrin complex appears to affect the spacing of MTs within K-fibres, even in close proximity to the kinetochore.

As seen in Figure 5.6, using SBF-SEM, an increase in kMTs is maintained after cold treatment of TACC3 over-expressing cells when compared to controls – a change that could not be detected by immunofluorescence. Figure 5.8 shows analysis of MT number, K-fibre area and MT density in control cells compared to TACC3 over-expressing cells, after cold treatment, using TEM. This analysis shows that the same phenotype is maintained – after cold treatment, the MT number and K-fibre area in TACC3 over-expressing K-fibres is greater than in control fibres. Bigger fibres with larger clusters of MTs are still seen in TACC3 over-expressing fibres, as seen in the heatmaps in (Figure 5.8C).

Analysis of MT trajectories in control and TACC3 over-expressing fibres close to the kinetochore shows only slight differences between conditions, with the distribution of theta angles remaining largely similar (Figure 5.9). After cold treatment, this phenotype becomes more marked, with more of the remaining MTs deviating from parallel in TACC3 over-expressing fibres than controls (Figure 5.10). This again suggests that more TACC3 causes more MTs to deviate from their parallel trajectory, possibly due to its role in the TACC3-chTOG-clathrin complex, and this phenotype is still detectable in close proximity to the kinetochore in cold-treated cells. As with the analysis of Chapter 4, the deviating MTs showed a tendency to be present at the periphery of the K-fibres in control cells, both before and after cold treatment (Figure 5.9Ci and Figure 5.10Ci). This pattern was mirrored in TACC3 over-expressing fibres fixed at 37 °C, but in cold-treated fibres over-expressing TACC3, the deviating MTs were present throughout the entire fibre (Figure 5.9Cii and Figure 5.10Cii).

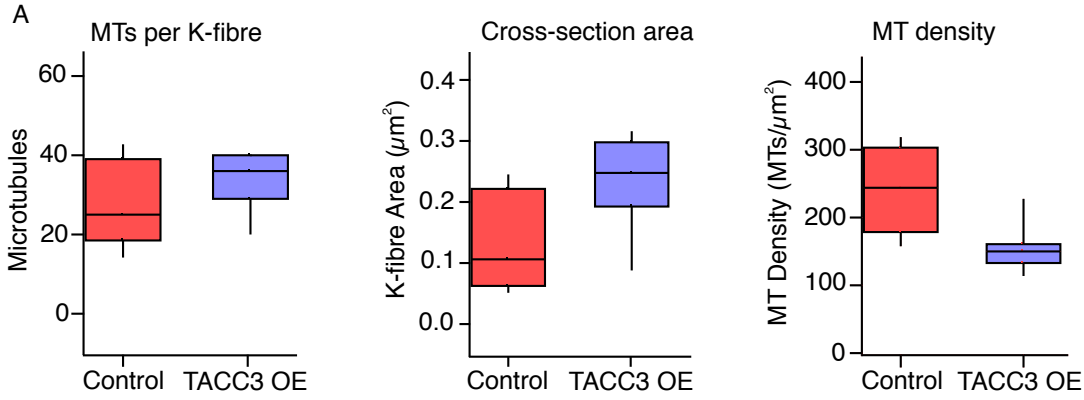
A
MTs per K-fibre
Microtubules
60
40
20
0
Control
TACC3 OE
Cross-section area
K-fibre Area (μm²)
0.4
0.3
0.2
0.1
0.0
Control
TACC3 OE
MT density
MT Density (MTs/μm²)
400
300
200
100
0
Control
TACC3 OE

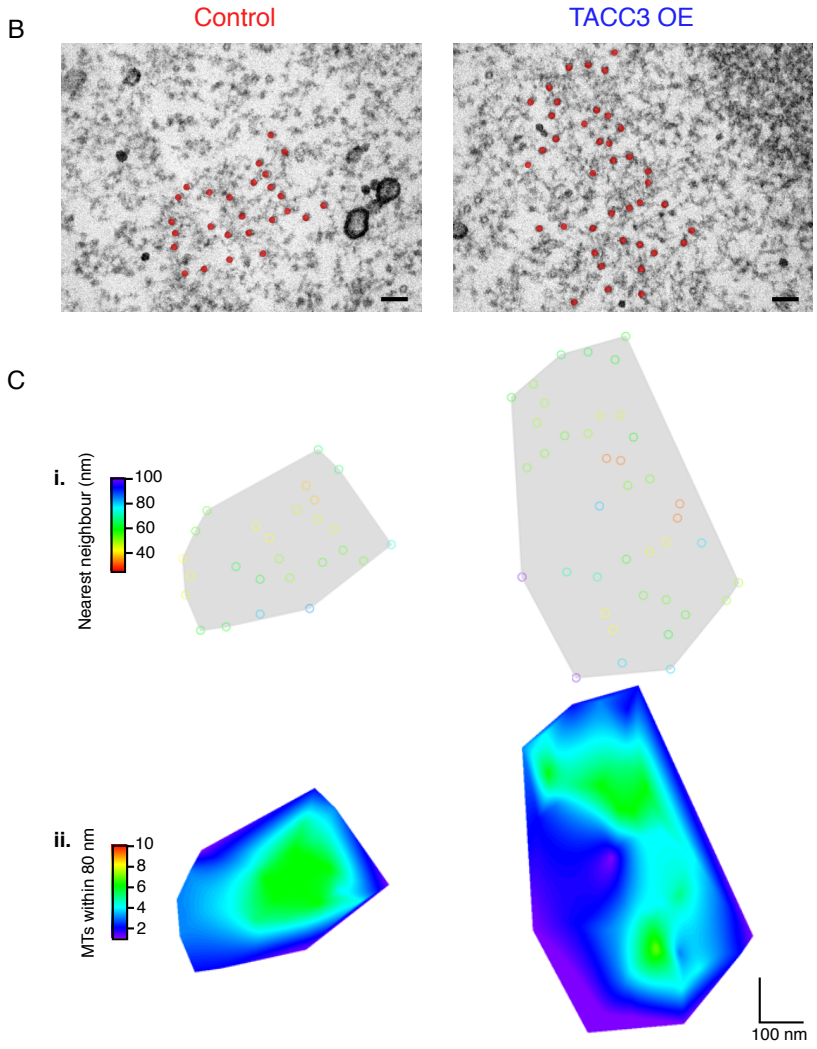
B
Control
TACC3 OE
C
i.
Nearest neighbour (nm)
100
80
60
40
ii.
MTs within 80 nm
10
8
6
4
2
100 nm

Figure 5.7: TEM analysis of K-fibres close to the kinetochore shows smaller differences between control and TACC3 over-expressing K-fibres. A: Box plots showing the number of MTs per K-fibre, K-fibre cross-sectional area, and MT density in control and TACC3 over-expressing fibres, from tomograms taken close to the chromatin. **B**: orthoslices from representative control and TACC3 over-expressing fibres, with MTs annotated in red. Scale bar = 100 nm. **Ci**: spatial maps of the same K-fibres, demonstrating the distance from each MT to its nearest neighbouring MT; **Cii**: heatmaps showing the number of other MTs within bridging distance of each kMT. The same phenotype is observed in this analysis as in Chapter 4, but the differences are less marked. K-fibres are still larger, with more clustered areas within them. Analysis from two cells per condition, fixed in two experiments (control K-fibres = 18; TACC3 over-expression K-fibres = 9).

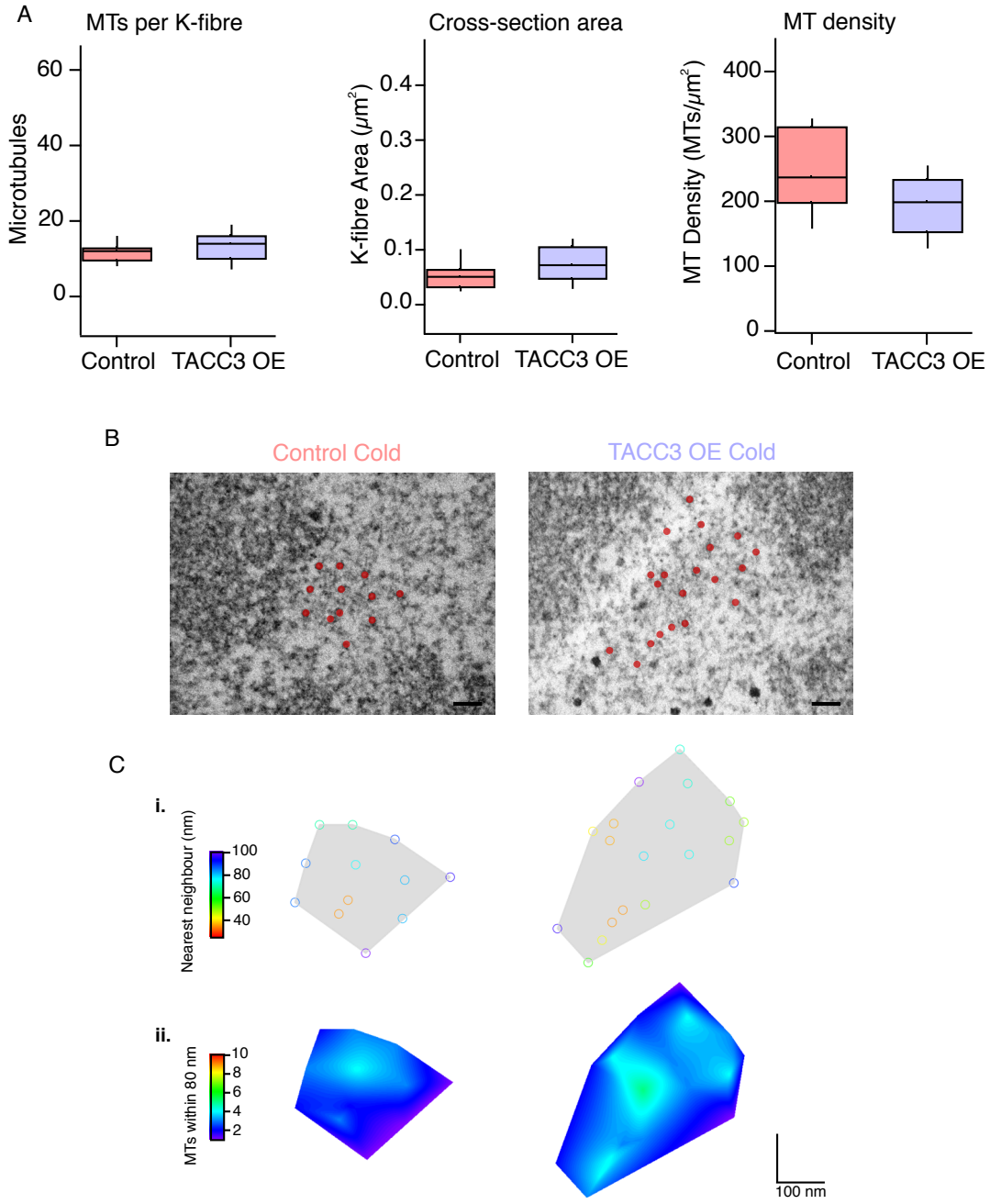

Figure 5.8: TEM analysis of control and TACC3 over-expressing fibres after cold treatment. **A**: Box plots showing the number of MTs per K-fibre, K-fibre cross-sectional area, and MT density in control and TACC3 over-expressing fibres in cold treated cells, from tomograms taken close to the chromatin. **B**: orthoslices from representative control and TACC3 over-expressing fibres, with MTs annotated in red. Scale bar = 100 nm. **Ci**: spatial maps of the same K-fibres, demonstrating the distance from each MT to its nearest neighbouring MT; **Cii**: heatmaps showing the number of other MTs within bridging distance of each kMT. The phenotype seen in cells fixed after cold treatment mirrors that of cells fixed without cold treatment. K-fibres are still generally larger with more MTs and contain more areas of closer packing. Analysis from two cells per condition, fixed in two experiments (control K-fibres = 8; TACC3 over-expression K-fibres = 12).

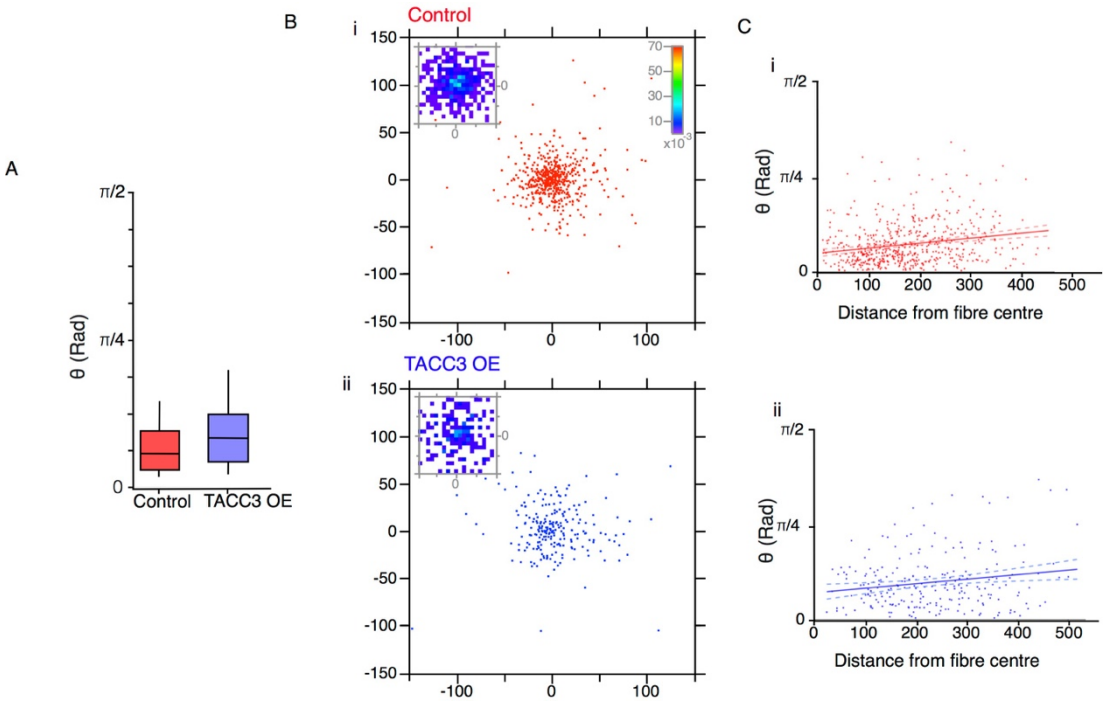

Figure 5.9: Kinetochore microtubule trajectories in control and TACC3 over-expressing fibres close to the chromatin. A: Box plots of theta angles show that there is a slight increase in TACC3 over-expressing cells, but to a lesser extent when examined close to the chromatin. **Bi** and **ii**: representation of MT vectors, starting at the Cartesian coordinate position 0, 0, 0, crossing an arbitrary z-plane (set at 100 nm) to visualise more easily the parallelness of MT trajectories, in controls and TACC3 over-expressing fibres respectively. The insets show a 2D histogram of the coordinates, cropped to a 40 x 40 nm square centred at 0, 0, 100, to account for differences in MT number and make any differences more easily visible. The difference in TACC3 over-expressing cells is less marked. **Ci** and **ii**: theta angles of trajectories plotted as a function of distance from the fibre centre shows a weak tendency for deviating MTs to be at the periphery of the K-fibre. Line of best fit is shown with 95% confidence bands (dashed line), r^2 = 0.15 (control), and 0.22 (TACC3 overexpression). Analysis from two cells per condition, fixed in two experiments (control K-fibres = 18; TACC3 over-expression K-fibres = 9).

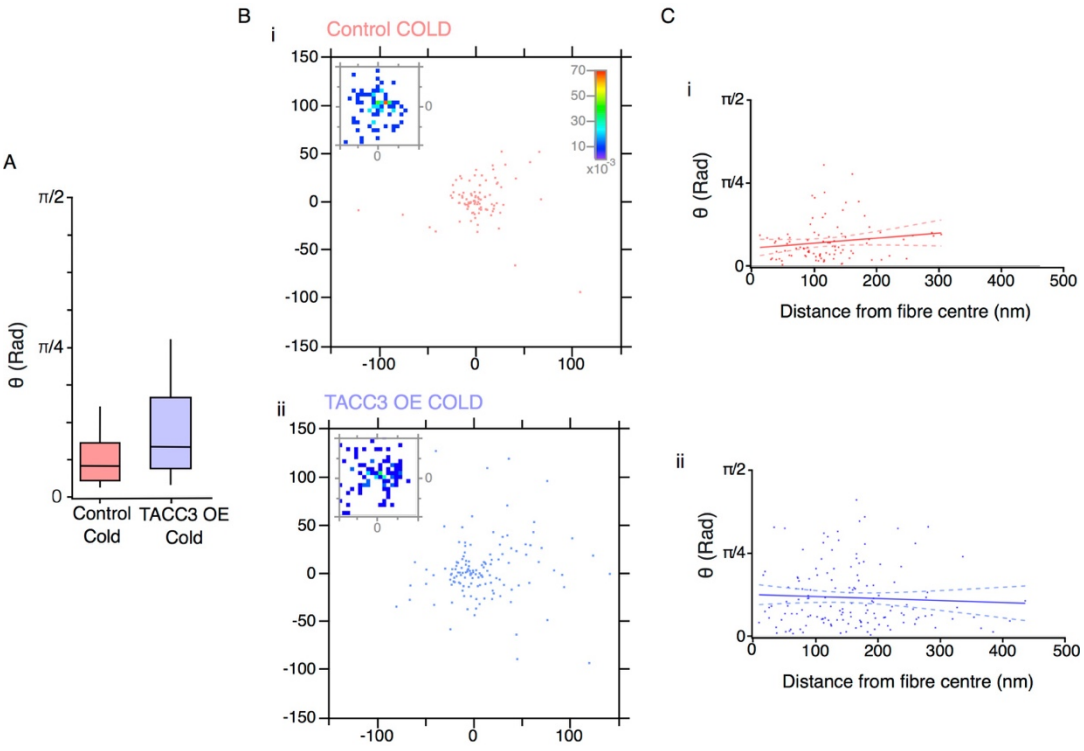

Figure 5.10: Kinetochore microtubule trajectories in control and TACC3 over-expressing fibres close to the chromatin, after cold treatment. A: Box plots of theta angles show that there is an increase in TACC3 over-expressing cells, but to a lesser extent when examined close to the chromatin. **Bi** and **ii**: representation of MT vectors, starting at the Cartesian coordinate position 0, 0, 0, crossing an arbitrary z-plane (set at 100 nm) to visualise more easily the parallelness of MT trajectories, in cold-treated controls and TACC3 over-expressing fibres respectively. Again, the insets show a 2D histogram of the coordinates, cropped to a 40 x 40 nm square centred at 0, 0, 100, to account for differences in MT number and make any differences more easily visible. **Ci** and **ii**: theta angles of trajectories plotted as a function of distance from the fibre centre (in control and TACC3 over-expressing fibres, respectively) shows a weak tendency for deviating MTs to be at the periphery of the K-fibre. After cold treatment, the deviating MTs in TACC3 over-expressing cells are distributed throughout the whole K-fibre. Line of best fit is shown with 95% confidence bands (dashed line), r^2 = 0.16 (control), and 0.40 (TACC3 overexpression). Analysis from two cells per condition, fixed in two experiments (control K-fibres = 8; TACC3 over-expression K-fibres = 12).

5.3.5 TEM and SBF-SEM demonstrate that K-fibres in TACC3 mutant S558A contain fewer microtubules and are disorganised.

Since TEM and SBF-SEM proved useful methods for the visualisation of spindle ultrastructure, these methods were then used to further characterise the role of TACC3 in the spindle. The methods were utilised to investigate the effect on HeLa cells of removing endogenous TACC3, and re-expressing TACC3 that is unable to function as part of the TACC3-chTOG-clathrin complex - see Materials and Methods. Briefly, a non-phosphorylatable “S558A” TACC3 mutant was expressed in cells, simultaneously depleted of wild type TACC3. These cells were subsequently processed using the SBF-SEM chemical fixation protocol for both the 3View® and TEM in order to examine the effects on the cell of having no TACC3-chTOG-clathrin crosslinker.

SBF-SEM volumes were produced for three S558A-mutant metaphase cells, from two separate experiments, although only one of these was rendered in 3D. Equally, SBF-SEM volumes were produced for 3 cold-treated S558A-mutant metaphase cells, from two separate experiments, again with one being rendered in 3D. Segmentation and reconstruction of the spindle of the S558A mutant cells using Amira demonstrated that there appeared to be fewer MTs present in the volume of the spindle when compared to control cells (Figure 5.11). Measurement of the MT 3D volume confirmed that it was decreased. This suggested that the mesh has a role in recruitment or retention of MTs in the spindle,

Closer examination of the 3D reconstruction revealed that some K-fibres seemed to be disorganised, with MTs from one bundle sometimes traversing to join another bundle (Figure 5.12). Also noted was the size of the K-fibres, which appeared more variable – some appeared to be large fibres, similar to those seen in TACC3 over-expressing cells; and some appeared to be smaller than controls (Figure 5.11). These observations supported the notion that the TACC3-chTOG-clathrin mesh complex has a role in organisation of the spindle and K-fibres within them.

This was analysed further with the TEM, taking tomograms of K-fibres in S558A mutant cells. There was an increase in the number of MTs per K-fibre and the K-fibre area when compared to controls, but the density of kMTs was reduced (Figure 5.13).

Although these differences were not found to be statistically significant, they highlight tendencies of K-fibres in these cells to be abnormal, and these observations were supported by the information gained using SBF-SEM. Again, these two techniques, when used in combination, were providing a clearer picture of the ultrastructure of the spindle – with nanometre-scale changes within K-fibres being detected by TEM, and gross spindle changes observed using the 3View® system.

Analysis of the spacing of kMTs from electron tomograms shows marked changes when compared to controls (Figure 5.13C). These K-fibres appear to have more clustered areas accompanied by increased distances between peripheral MTs. These fibres show a similar level of disorganisation as seen in TACC3 over-expressing fibres.

However, when this analysis was repeated on cold-treated metaphase cells, fewer MTs were retained when compared to both TACC3 over-expressing cells and controls (Figures 5.8 and Figure 5.13). This suggests that without the TACC3-chTOG-clathrin bridge, K-fibres are less stable.

Significant deviations in kMTs trajectory were not detected in S558A mutants fixed at 37 °C. The distribution of theta angles slightly increased after cold treatment, but not to the same magnitude that was seen in TACC3 over-expressing cells (Figure 5.10 and Figure 5.14).

A

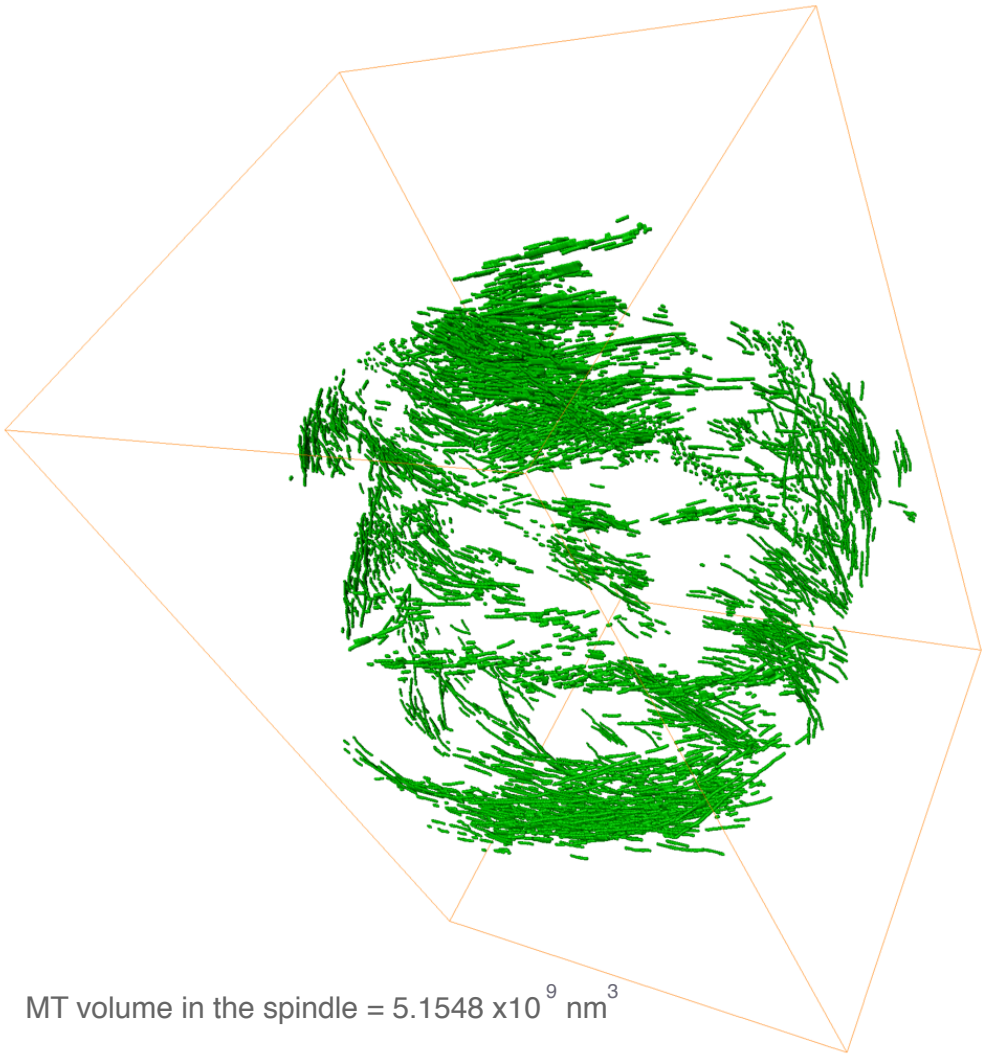
MT volume in the spindle = 5.1548 x10 9 nm3

B

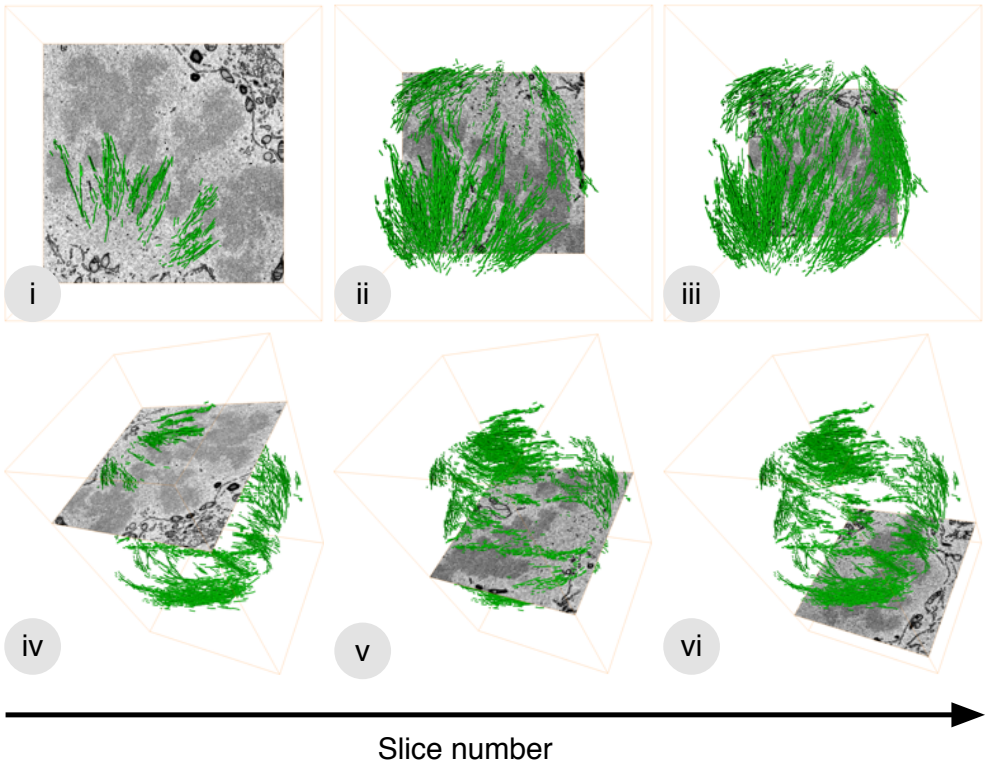
i
ii
iii
iv
v
vi
Slice number

C

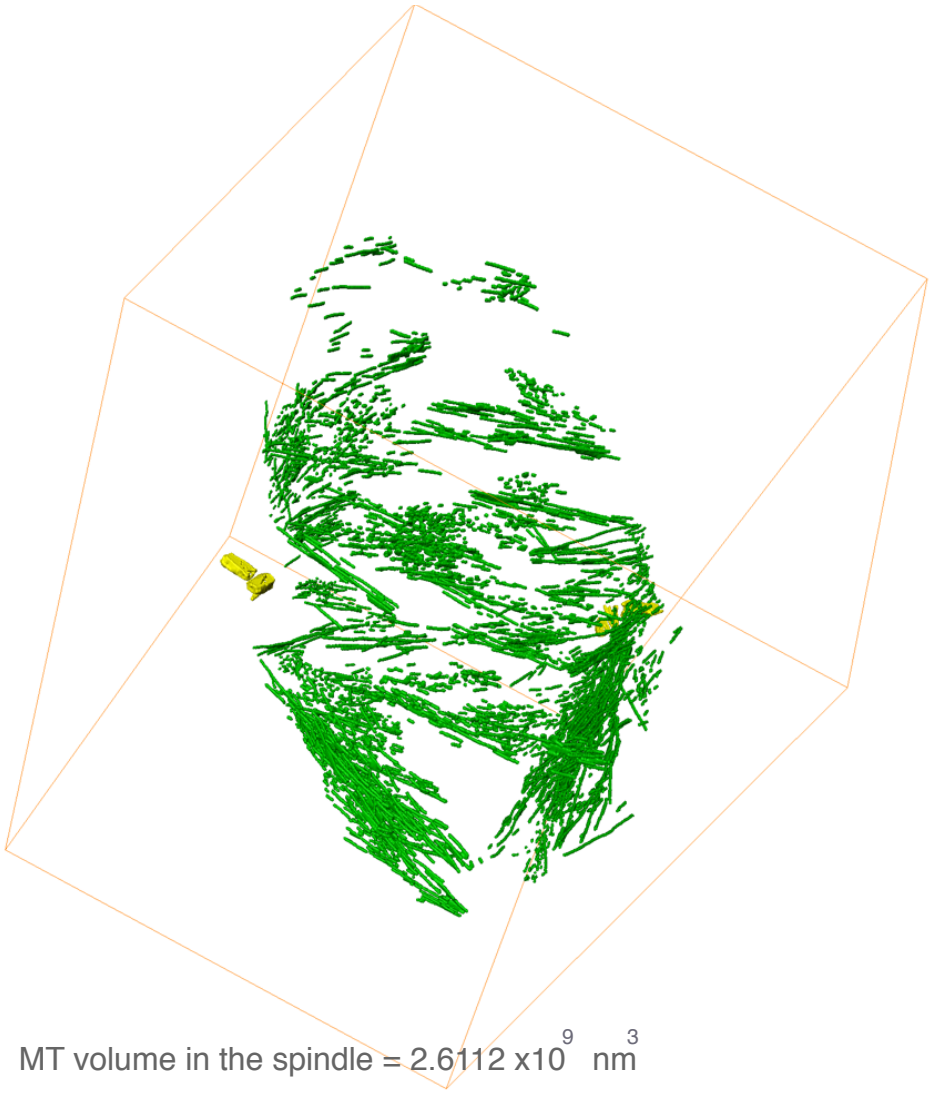

MT volume in the spindle = 2.6112 x10^{9} nm^{3}

D

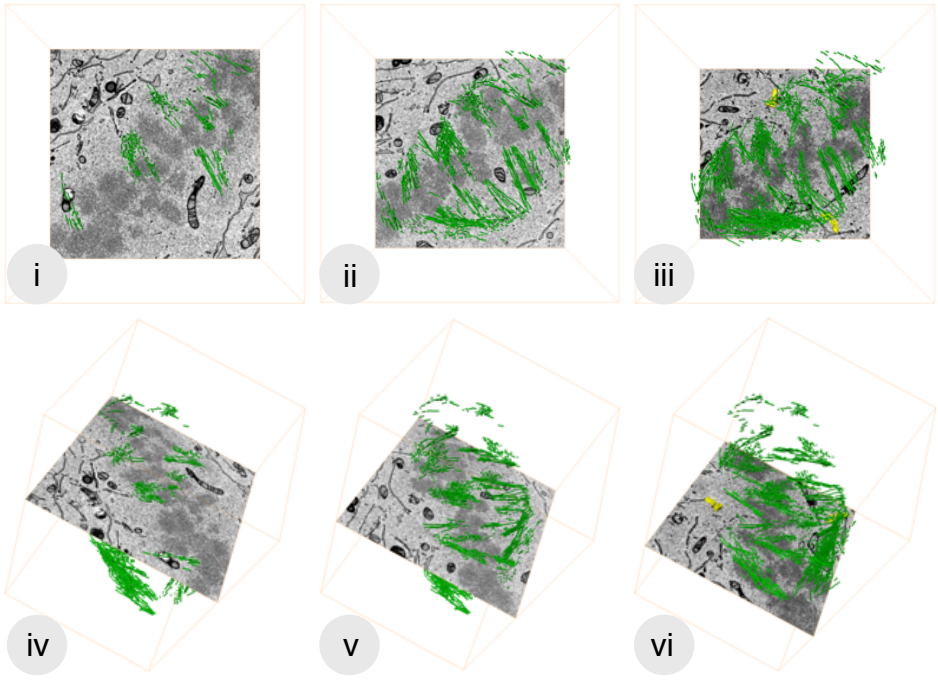

Figure 5.11: The spindle in TACC3 mutant S558A contains fewer microtubules. **A**: 3D reconstruction of the entire MT volume of a cell expressing the S558A TACC3 mutant, using Amira. A bounding box is shown in orange for orientation, demarcating the SBF-SEM volume. The volume of the 3D rendered spindle is shown in nm^3, and is decreased compared to that of control HeLa cells (Figure 5.2). **Bi-iii**: sequential orthoslices through the SBF-SEM volume, with 3D rendering, in plan view. **iv-vi**: the same sequential orthoslices as **Bi-iii**, viewed at an angle. There are fewer MTs present in the spindle as a whole and fibre bundles show a range of sizes. **C** and **D**: same as **A** and **B**, but showing 3D reconstruction of a cell expressing the S558A TACC3 mutant, after cold treatment. The volume of MTs in the spindle reverts back to similar levels to control HeLa cells. The spindle MTs of one 37 °C and one cold-treatment condition cell were rendered.

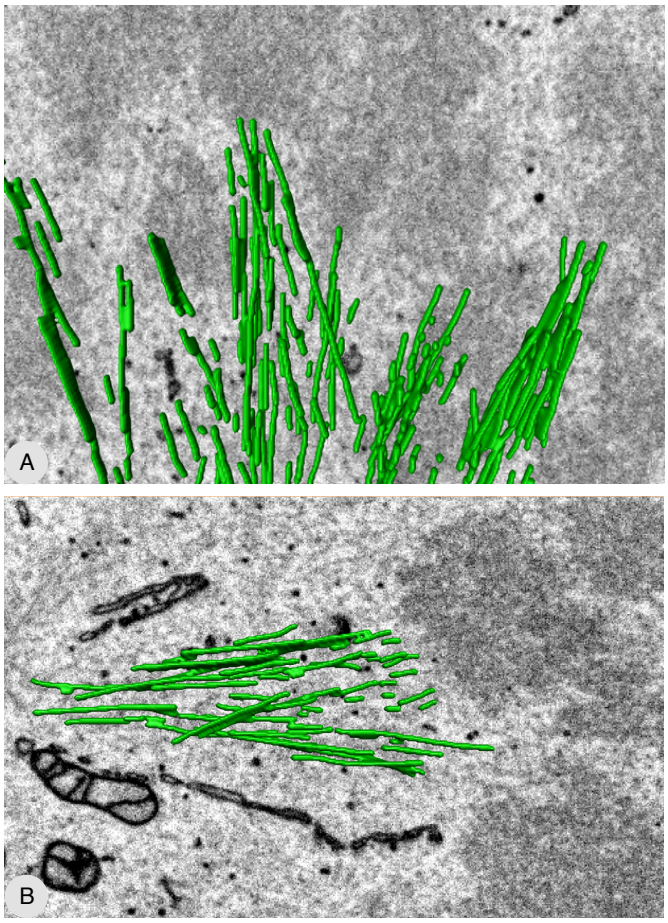

Figure 5.12: K-fibres are more disorganised in S558A mutant cells. Orthoslices from SBF-SEM volumes, with MTs rendered. **A** and **B**: examples of K-fibres where MTs appear to cross from one fibre to another.

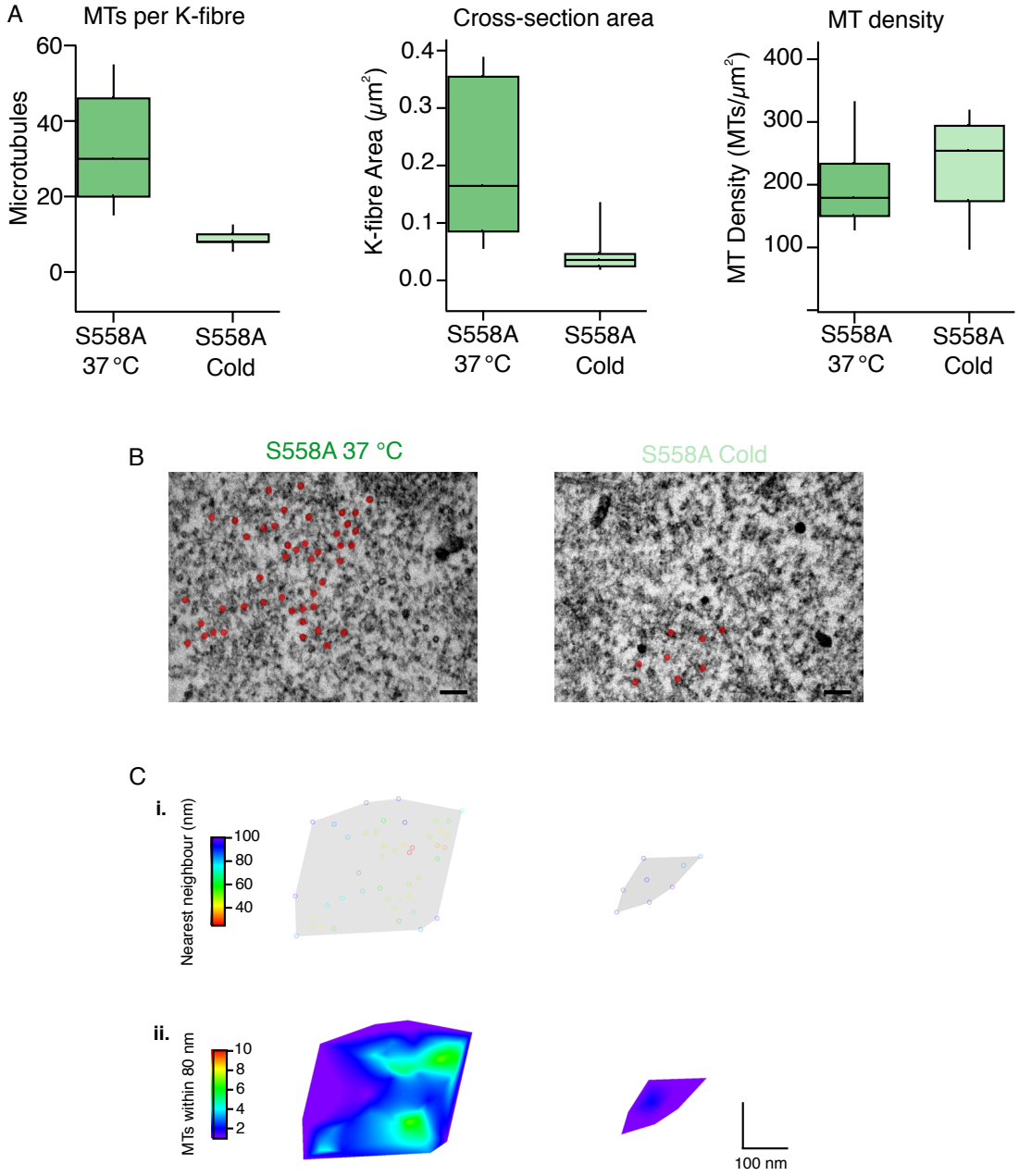

Figure 5.13: TEM analysis of K-fibres in S558A mutant cells, with and without cold treatment. A: Box plots showing the number of MTs per K-fibre, K-fibre cross-sectional area, and MT density in S558A mutant cells, with and without cold treatment, from tomograms taken close to the chromatin. **B**: orthoslices from representative 37 °C and cold treated fibres, with MTs annotated in red. Scale bar = 100 nm. **Ci**: spatial maps of the same K-fibres, demonstrating the distance from each MT to its nearest neighbouring MT; **Cii**: heatmaps showing the number of other MTs within bridging distance of each kMT. The number of MTs and the K-fibre area reflects the phenotype seen in the SBF-SEM segmentation – that K-fibres are variable in size, with some large fibres as well as small ones. MT packing is also altered, with clusters and increased spacing visible within the fibres in the heatmaps. Analysis from two cells per condition, fixed in two experiments (37 °C K-fibres = 14; cold-treated K-fibres = 9).

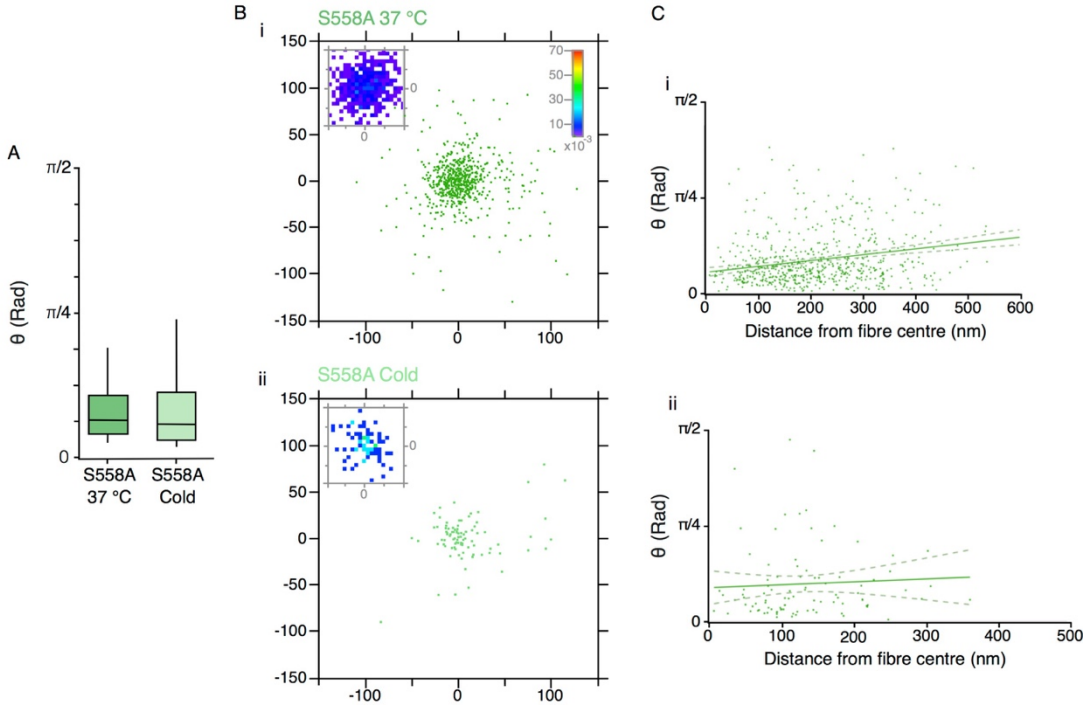

Figure 5.14: Trajectories of kinetochore microtubules in S558A mutant cells, with and without cold treatment. A: Box plots of theta angles show that there is no significant increase in MT deviancy when compared to controls (Figure 5.9). **Bi** and **ii**: representation of MT vectors, starting at the Cartesian coordinate position 0, 0, 0, crossing an arbitrary z-plane (set at 100 nm) to visualise more easily the parallelness of MT trajectories, in S558A mutant cells with and without cold treatment, respectively. The insets show a 2D histogram of the coordinates, cropped to a 40 x 40 nm square centred at 0, 0, 100, to account for differences in MT number and make any differences more easily visible. **Ci** and **ii**: theta angles of trajectories plotted as a function of distance from the fibre centre (with and without cold treatment, respectively) shows a tendency for deviating MTs to be at the periphery of the K-fibre. After cold treatment, the deviating MTs appear to be distributed throughout the whole K-fibre. Line of best fit is shown with 95% confidence bands (dashed line), r^2 = 0.17 (37 °C), and 0.27 (cold). Analysis from two cells per condition, fixed in two experiments (37 °C K-fibres = 14; cold-treated K-fibres = 9).

5.3.6 Glioblastoma cells progress through mitosis more slowly than HeLa cells.

Glioblastoma (GBM) is an aggressive cancer of the astrocytes of the central nervous system. Focal gains on the long arm of chromosome 4 have been frequently identified in a subset of GBMs, and this region contains several genes including the gene for TACC3 (Duncan et al., 2010). GBM cell lines (gifted by Heiko Wurdak, Leeds) which over-express TACC3 were investigated to determine if these cells are subject to the same spindle abnormalities seen in the TACC3 over-expressing HeLa cells used in this study thus far.

Do the spindle features seen by TEM and SBF-SEM correlate with affected mitosis in Glioblastoma-derived cells? LCI was used to examine the mitotic progression of GBM cells (Figure 5.15). When compared to HeLa cells, GBM cells take longer to progress through mitosis, with the transition from prometaphase to metaphase causing the delay. This could suggest that these cells have difficulty forming a bipolar spindle and congressing their chromosomes, possibly as a result of hyper-stabilisation of K-fibres through TACC3 over-expression.

5.3.7 TEM and SBF-SEM demonstrate that Glioblastoma cells have larger K-fibres with more microtubules.

Do GBM cells have any abnormalities in their spindle, which could explain the delay in mitosis? GBM cells were imaged by LM at metaphase, then subsequently fixed and processed for SBF-SEM and TEM. SBF-SEM volumes were produced for each of the GBM cell lines, both with and without cold-treatment (totaling 9 cells). 3D segmentation and rendering of the MT volume of the GBM11 cells demonstrated that the spindle in these cells appear to contain many more MTs than TACC3 over-expressing HeLa cells (Figure 5.4 and Figure 5.16). K-fibres are not easily discernable from the rest of the spindle in the reconstruction.

TEM analysis from tomograms of K-fibres in GBM cells supports this observation: the number of MTs per K-fibre and the K-fibre cross-sectional area almost twice that seen in control HeLas (Figure 5.17A). The overall density of MTs within K-fibres appears consistent with controls – however, maps showing nearest neighbouring

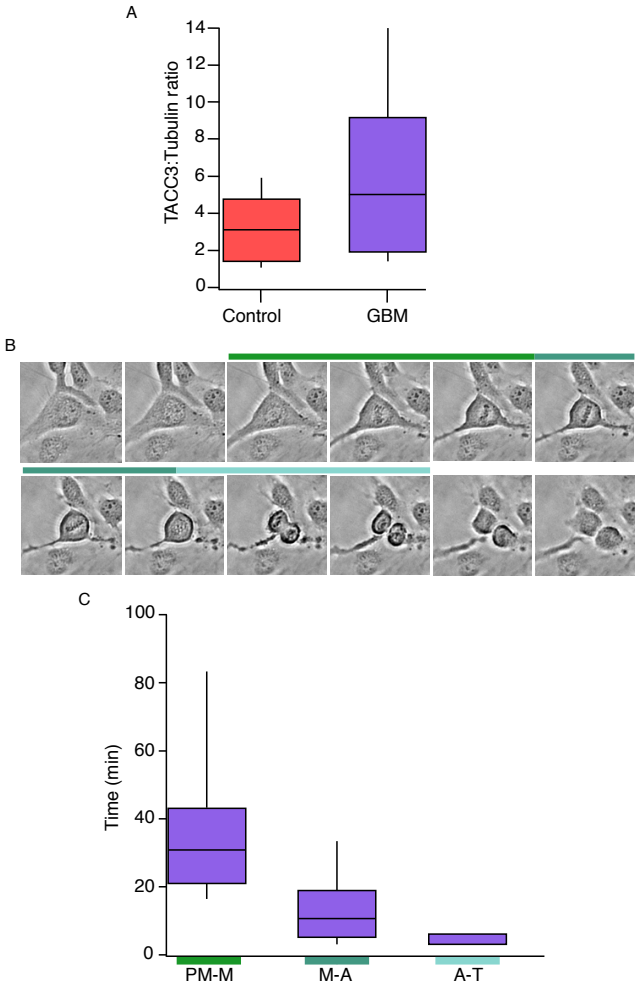

Figure 5.15: Mitosis is delayed in GBM cells. A: the ratio of TACC3 to tubulin on the spindle of control HeLa and GBM metaphase cells, calculated from IF images. The amount of TACC3 on the spindle in GBM cells is increased compared to HeLa cells. **B**: example brightfield images of a live-cell imaging (LCI) experiment to quantify mitotic progression of GBM cells. **C**: quantification of the timescales of different stages of mitosis in LCI of GBM cells. The different stages are highlighted in **B** and **C.** Due to the lack of a suitable control for this highly transformed cell line, GBMs were compared to control HeLas – also transformed.

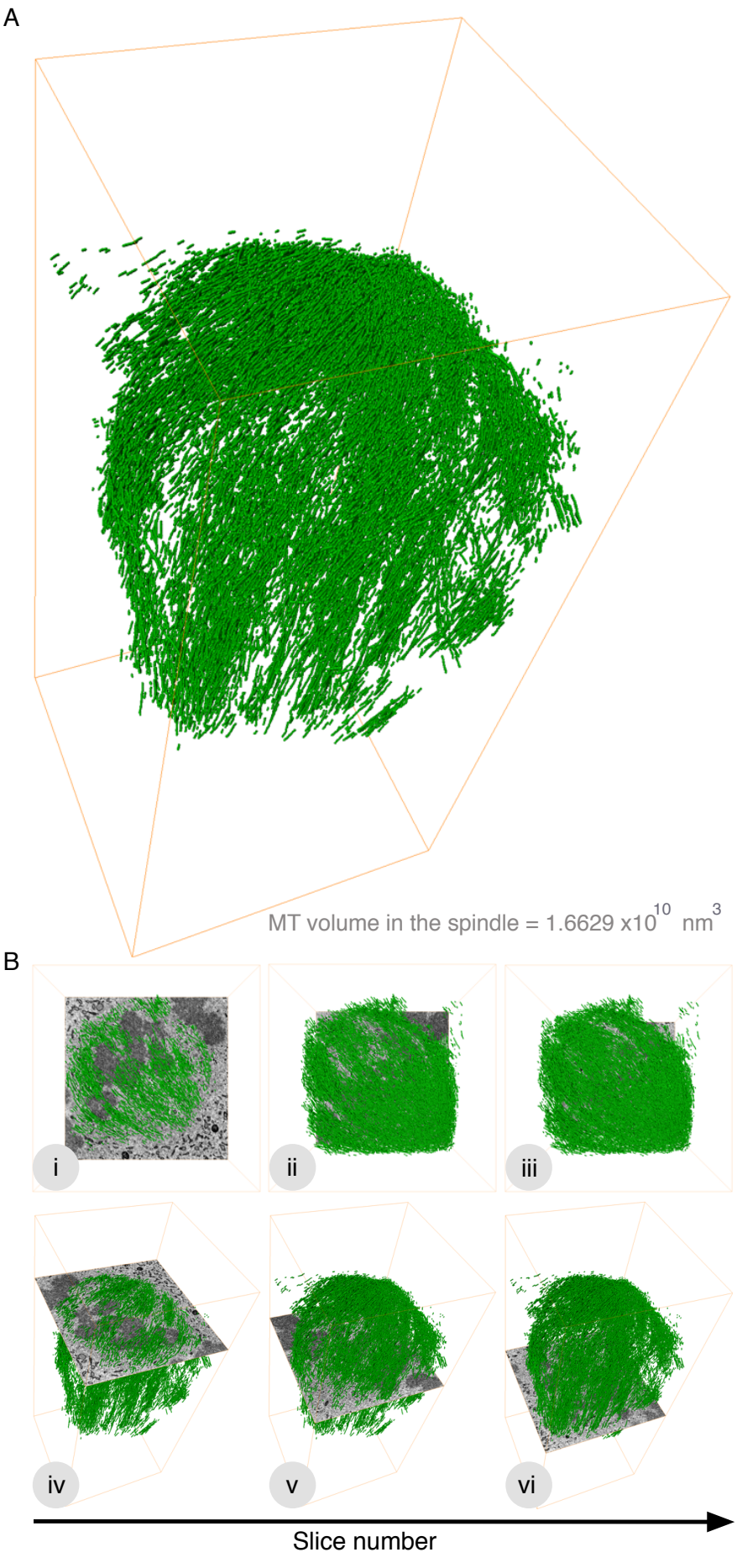
A
MT volume in the spindle = 1.6629 x10^10 nm^3
B
i
ii
iii
iv
v
vi
Slice number

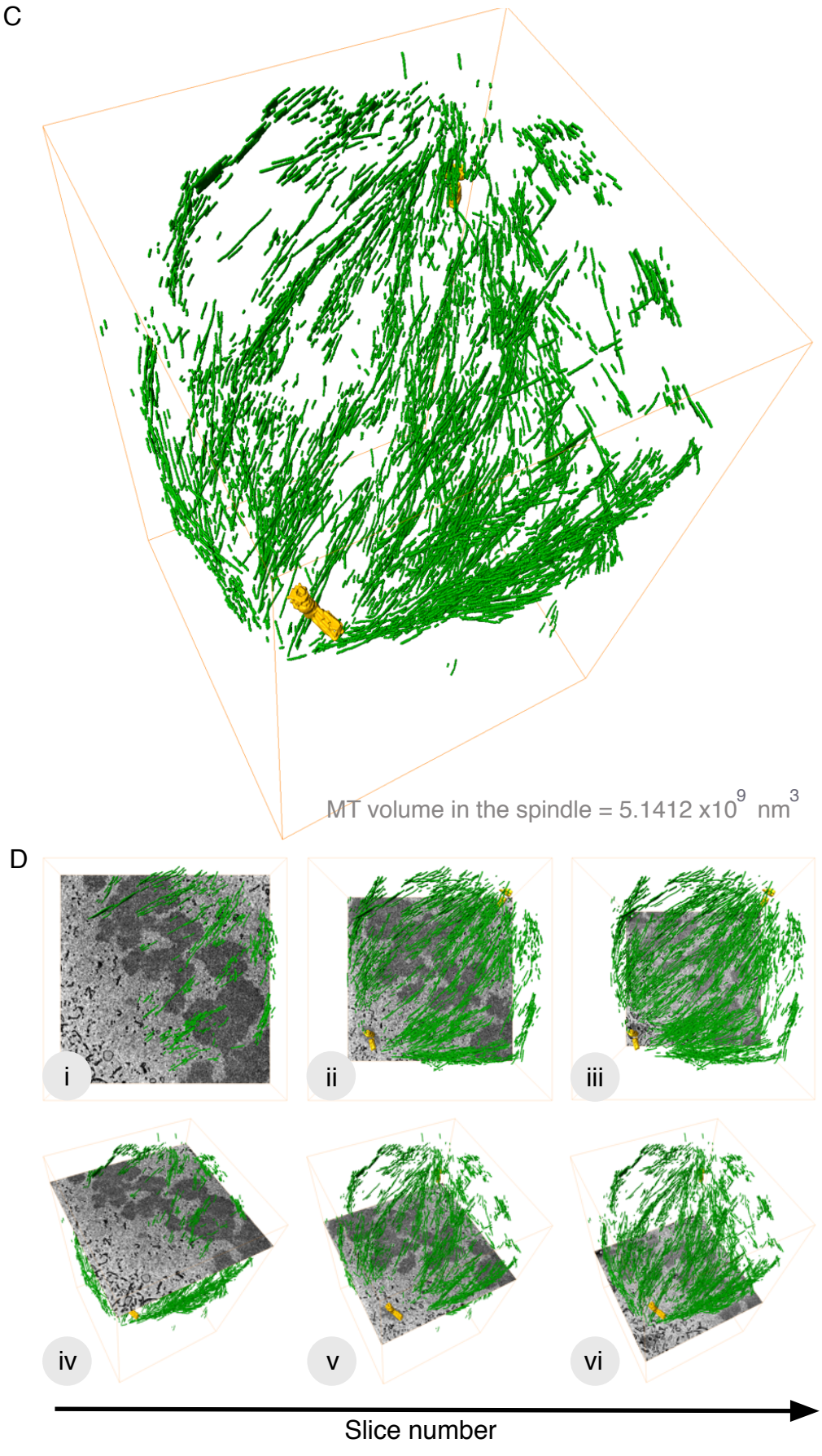
C
MT volume in the spindle = 5.1412 x10^9 nm^3
D
i
ii
iii
iv
v
vi
Slice number

Figure 5.16: By SBF-SEM, GBM mitotic spindle contains more microtubules than control and TACC3 over-expressing HeLa cells, with and without cold treatment. A: 3D reconstruction of the entire MT volume of a GBM cell, using Amira. A bounding box is shown in orange for orientation, demarcating the SBF-SEM volume. The volume of the 3D rendered spindle is shown in nm^3, and is increased compared to both control and TACC3 over-expressing HeLa cells (Figure 5.2). **Bi-iii**: sequential orthoslices through the SBF-SEM volume, with 3D rendering, in plan view. **iv-vi**: the same sequential orthoslices as **Bi-iii**, viewed at an angle. **C** and **D**: same as **A** and **B**, but showing 3D reconstruction of a GBM cell, after cold treatment. The volume of MTs in the spindle after cold treatment is almost double that of control HeLas. The spindle MTs of one 37 °C and one cold-treatment condition cell were rendered.

MTs and the number of MTs within bridging distance clearly demonstrate large areas where MTs are closely clustered (Figure 5.17C). When metaphase GBM cells are cold-treated before fixation, the organisation and morphology of K-fibres becomes similar to that seen in cold-treated control HeLa cells. This observation is at odds with the 3D segmentation of the cold-treated GBM cell, which retains a larger proportion of its spindle MTs as seen qualitatively from the 3D reconstruction as well as the value generated for the MT 3D volume, which is double the value determined for the cold-treated control HeLa (Figure 5.16C). It is possible that the orientation of the majority of K-fibres was altered after cold treatment, due to partial collapse of the spindle for example, resulting in the kMTs being invisible by TEM in the plane of sectioning (orthogonal to the spindle axis). This again highlights the utility of SBF-SEM for examining spindle ultrastructure, as TEM alone would not show the full extent of the morphology of the spindle in this case.

Of the K-fibres that were visible by TEM, trajectories were analysed as previously. Figure 5.18 shows that the distribution of theta angles of the MT vectors was almost identical to that seen in control HeLa fibres – when fixed at both 37 °C and after cold treatment. This suggests that any changes in the organisation and spacing within the fibres of GBM cells are more uniform than those seen in TACC3 over-expressing HeLa cells, with kMTs remaining parallel despite over-expression of TACC3.

Table 2 shows a summary of both TEM and SBF-SEM analysis for all conditions investigated in this chapter, for comparison. While the results presented here show some interesting differences between conditions, it must be stated that 3D segmentation was performed on a limited dataset and further work is necessary to fully establish the phenotypes detected here.

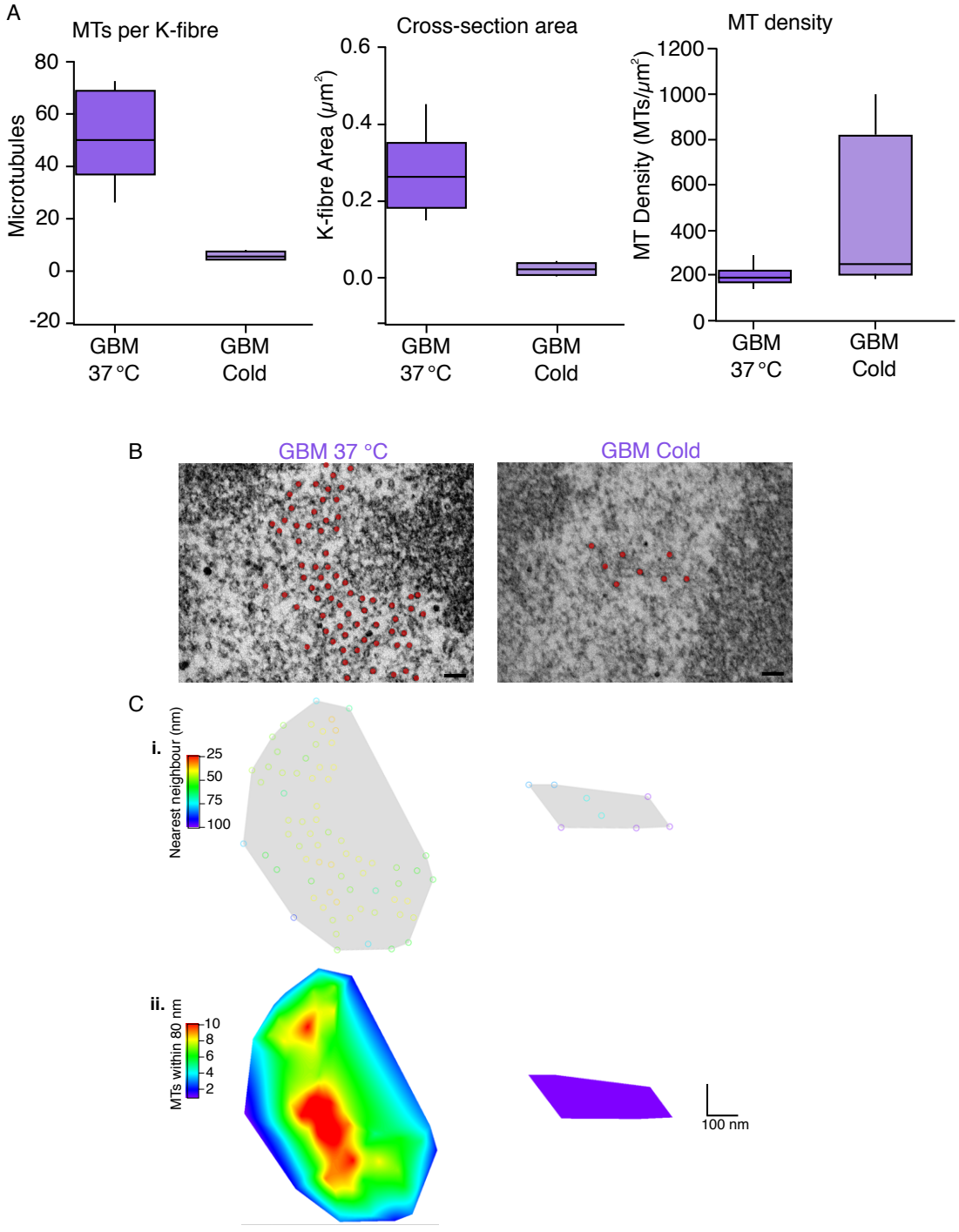
A
MTs per K-fibre
Microtubules
80
60
40
20
0
-20
GBM 37 °C
GBM Cold
Cross-section area
K-fibre Area (μm²)
0.6
0.4
0.2
0.0
GBM 37 °C
GBM Cold
MT density
MT Density (MTs/μm²)
1200
1000
800
600
400
200
0
GBM 37 °C
GBM Cold
B
GBM 37 °C
GBM Cold
C
i.
Nearest neighbour (nm)
25
50
75
100
ii.
MTs within 80 nm
10
8
6
4
2
100 nm

Figure 5.17: TEM analysis of GBM K-fibres, with and without cold treatment. A: Box plots showing the number of MTs per K-fibre, K-fibre cross-sectional area, and MT density in GBM cells, with and without cold treatment, from tomograms taken close to the chromatin. **B**: orthoslices from representative 37 °C and cold treated fibres, with MTs annotated in red. Scale bar = 100 nm. **Ci**: spatial maps of the same K-fibres, demonstrating the distance from each MT to its nearest neighbouring MT; **Cii**: heatmaps showing the number of other MTs within bridging distance of each kMT. The number of MTs and the K-fibre area reflects the phenotype seen in the SBF-SEM segmentation – that K-fibres are much larger and kMTs are more closely packed. TEM analysis of GBM cells after cold treatment shows that K-fibres revert back to levels similar to that seen in control HeLas. The extra MTs in the SBF-SEM reconstruction are not detected by TEM this close to the kinetochore. Analysis from one cell per condition, fixed in one experiment (37 °C K-fibres = 10; cold-treated K-fibres = 4).

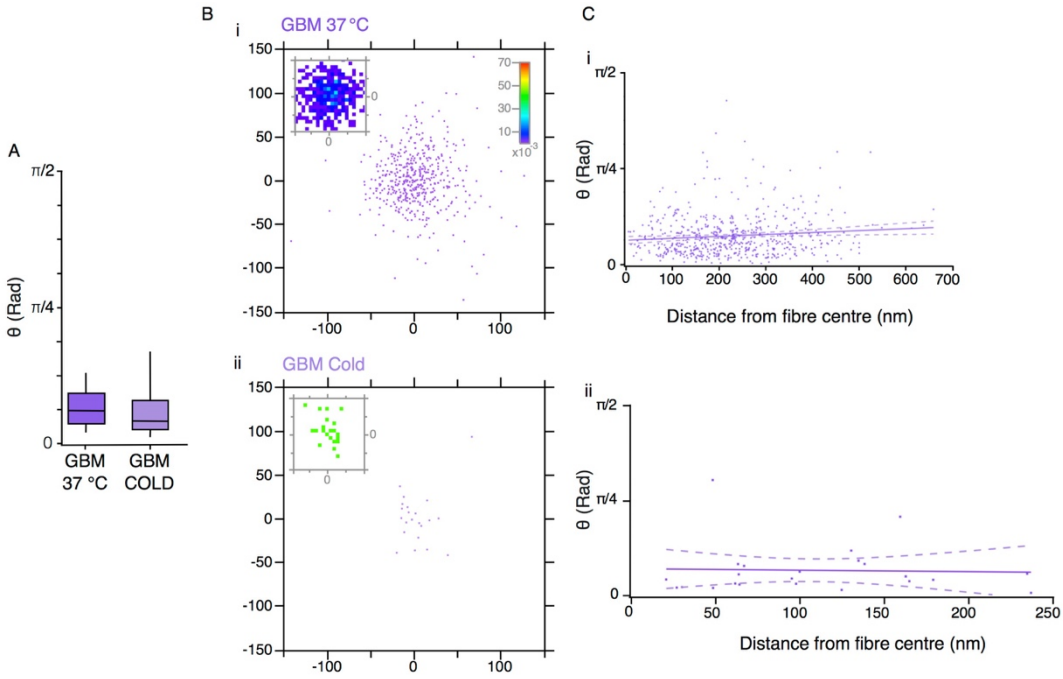

Figure 5.18: Trajectories of kinetochore microtubules in GBM cells, with and without cold treatment. A: Box plots of theta angles show that there is no significant increase in MT deviancy when compared to control HeLas (Figure 5.9). **Bi** and **ii**: representation of MT vectors, starting at the Cartesian coordinate position 0, 0, 0, crossing an arbitrary z-plane (set at 100 nm) to visualise more easily the parallelness of MT trajectories, in GBM cells with and without cold treatment, respectively. The insets show a 2D histogram of the coordinates, cropped to a 40 x 40 nm square centred at 0, 0, 100, to account for differences in MT number and make any differences more easily visible. **Ci** and **ii**: theta angles of trajectories plotted as a function of distance from the fibre centre (with and without cold treatment, respectively) shows a tendency for deviating MTs to be at the periphery of the K-fibre. Line of best fit is shown with 95% confidence bands (dashed line), r^2 = 0.20 (37 °C), and 0.22 (cold). After cold treatment, the deviating MTs appear to be distributed throughout the whole K-fibre. In both conditions, no significant deviation from parallel was detected, suggesting that the level of TACC3 over-expression in these cells is not causing the same abnormalities as seen in TACC3 over-expressing HeLa cells. Analysis from one cell per condition, fixed in one experiment (37 °C K-fibres = 10; cold-treated K-fibres = 4).

Condition	Spindle MT Vol. (nm^3)	MTs per fibre	K-fibre area (μm^2)	MT density (MTs/μm^2)	Theta angle (degrees)
Control	1.0196×10^{10}	25(18.50-39)	0.11(0.06-0.22)	243.78(178.56-303.05)	10.47(5.50-17.69)
Control *Cold*	2.2262×10^{9}	12(9.50-12.75)	0.05(0.03-0.06)	236.79(197.55-314.01)	9.77(5.06-16.42)
TACC3 over-expr.	1.0431×10^{10}	36(29-40)	0.24(0.19-0.30)	150(132.92-160.76)	15.38(8.07-22.80)
TACC3 over-expr. *Cold*	3.0874×10^{9}	14(10-16)	0.07(0.04-0.10)	198.59(152.53-232.98)	15.52(8.68-30.58)
S558A mutant	5.1548×10^{9}	30(20-46)	0.16(0.09-0.35)	178.96(149.89-233.22)	11.84(7.33-19.83)
S558A mutant *Cold*	2.6112×10^{9}	8(8-10)	0.03(0.02-0.05)	253.99(173.60-293.67)	10.64(5.23-20.69)
Glioblastoma	1.6629×10^{10}	50(37-69)	0.26(0.18-0.35)	189.74(164.01-220.76)	11.23(6.87-17.01)
Glioblastoma *Cold*	5.1412×10^{9}	5.5(4.25-7.50)	0.02(0.01-0.04)	246.39(197.26-821.21)	7.78(4.90-14.74)

Table 2: Summary of analyses. SBF-SEM (spindle MT volume) and TEM (number of MTs per K-fibre, K-fibre area, MT density and MT trajectory angles) analysis is summarised in this table for comparison between conditions. For all values except the spindle MT volume, the median is shown, with the interquartile range in brackets.

5.4 Discussion

This chapter has demonstrated that SBF-SEM using the 3View® system can be utilised in order to visualise spindle MTs. Optimisation of fixation, staining, resin embedding and SEM imaging parameters allowed for this visualisation, and meant that the spindle MT volume could be segmented and rendered in 3D – providing a picture of the entire spindle.

SBF-SEM has been used here to complement TEM analysis providing additional information to that given by electron tomography. The previous chapter proposed a model in which TACC3 over-expressing cells had larger K-fibres than controls, but that extra kMTs were not stably attached to the kinetochore as they appeared by IF to be lost after cold treatment of the cell, and these extra MTs simply surrounded the K-fibre – becoming 'enmeshed' as a result of too much TACC3-chTOG-clathrin. In this chapter, this model could be updated with the information provided by 3D rendering of SBF-SEM volumes (Figure 5.19). With this method, large K-fibres were seen to be merged together, splitting as they reach the chromatin. In addition to this, fewer MTs were lost from the spindle after cold treatment of metaphase cells over-expressing TACC3 than in controls, suggesting that more TACC3-chTOG-clathrin does in fact increase the amount of MTs stably attached to the kinetochore, or protected in another way from depolymerisation. This prompted investigation of K-fibres by TEM analysis closer to the chromatin, with and without cold treatment, to determine if this phenotype is supported by TEM analysis also. Analysis of electron tomograms of K-fibres closer to the kinetochore did detect these changes – larger K-fibres and altered spacing with and without cold treatment – albeit to a lesser extent than the phenotype seen in the previous chapter where the analysis was performed more than a micrometre away from the kinetochore. TEM analysis from both chapters, coupled with observations from SBF-SEM volume rendering, supports a picture where more TACC3-chTOG-clathrin results in more MTs not just within the spindle as a whole, but specifically within K-fibres, supporting the notion that more mesh within K-fibres results in hyper-stabilisation. This offers an explanation for the defects seen in progression through mitosis in cells over-expressing TACC3. Both SBF-SEM and TEM tomography were used in conjunction to investigate the effect of expressing TACC3 which was unable to form the TACC3-chTOG-clathrin complex – to further characterise the role of TACC3 in the spindle. TACC3 has a function at the

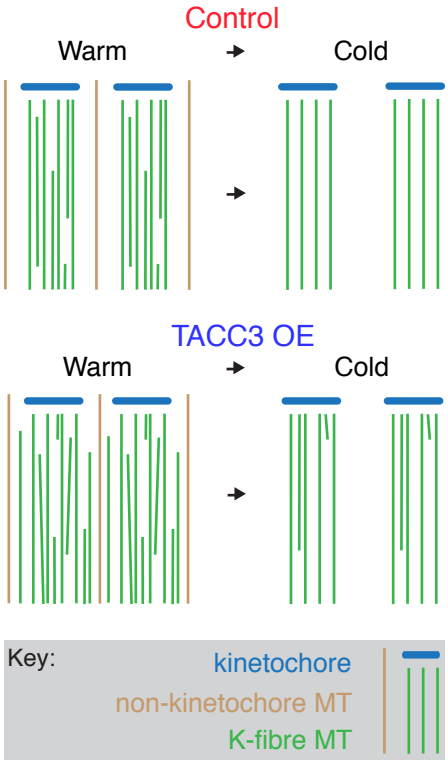

Figure 5.19: New model of K-fibre alteration after TACC3 over-expression. From SBF-SEM and TEM analysis, evidence suggests that more kMTs are protected from depolymerisation, possibly by being stably attached to the kinetochore, after TACC3 over-expression. 3D volume examination suggests this by showing large, merged K-fibres before cold treatment, and extra MTs present in the spindle after cold treatment. TEM analysis also suggests this, with large K-fibres and increased clustering seen after TACC3 over-expression. The phenotype is less marked closer to the kinetochore, but is still present.

plus-tips of MTs, in a complex with chTOG, independent of its role in the TACC3-chTOG-clathrin kMT bridge (Gutierrez-Caballero et al., 2014). Although the function of this TACC3-chTOG complex in mammalian cells is not fully established, some studies suggest that it is capable of altering MT dynamics (Nwagbara et al., 2014). It was important to investigate the role of these different pools of TACC3 in producing the phenotypes seen thus far – could they be a result of direct alteration of MT dynamics by the TACC3-chTOG complex at plus-tips, rather than alteration of the mesh? This chapter demonstrates that when cells only expressed a form of TACC3 which was unable to bind as part of the TACC3-chTOG-clathrin complex, K-fibres did appear more disorganised. Fibres were markedly different sizes; kMTs were seen to cross over from one fibre to another; and MT spacing was also altered. The disorganisation observed in these cells is similar to the disorganisation observed in TACC3 over-expressing cells, suggesting again a non-uniform alteration in the mesh components being the responsible factor – in this case loss of the shorter TACC3-chTOG-clathrin bridge. In contrast to TACC3 over-expressing cells however, S558A mutant cells had one important difference which was that they lost more spindle MTs after cold treatment suggesting that these fibres are less stable rather than hyper-stabilised. It would be interesting to repeat the tomography further away from the chromatin in these cells, as it is likely that a more severe phenotype could be detected in an area away from the kinetochore, where the kMT plus-ends have become focussed in the same orientation.

A glioblastoma (GBM) cell line was also investigated using SBF-SEM and electron tomography, as these cells are known to possess multiple copies of the TACC3 gene. GBM cells were found to reach metaphase more slowly, at a level similar to that seen in TACC3 over-expressing HeLa cells. Are there any spindle abnormalities which could explain this delay, detectable by EM? This chapter demonstrates that GBM cells contain many more MTs in their spindle than control HeLa cells, and more than TACC3 over-expressing HeLa cells. This was visible by both rendering of SBF-SEM volumes and by electron tomography. In these cells, MT spacing was markedly altered, with kMTs being more clustered than those seen in control and TACC3 over-expressing HeLa cells. This is again indicative of K-fibres possessing too much TACC3-chTOG-clathrin in their mesh. However, in these cells, it appeared that the trajectories of the kMTs were not altered, with the distribution of theta angles of the MTs being equivalent to those seen in control fibres. One possibility is that because

this analysis was done near the chromatin, any deviating MTs in the body of the K-fibre would be unlikely to be detected so close to the kinetochore as the ends of the MTs would presumably be stably attached to the kinetochore and all in the same orientation. However, large clusters were still detected at this distance which suggests the possibility that over-expression of TACC3 in these cells is resulting in the dominant component of the mesh becoming the short TACC3-chTOG-clathrin complex - replacing other, longer bridges between kMTs where there is now no available space to bind. This would explain increased clustering without abrogation of kMT trajectories. This is an intriguing possibility that could be investigated further in the future. HPF of mitotic GBM cells for the purpose of rendering the mesh in these cells has the potential to shed light on this question. The role of bridges within K-fibres has been proposed to contribute to their stability, and evidence for this has been shown in this thesis. It is known that there are other bridging proteins within K-fibres, not only the TACC3-chTOG-clathrin complex – so what is the purpose of multiple populations of crosslinkers? The fact that GBM cells lose an equivalent proportion of their kMTs after cold-treatment as control and TACC3 over-expressing HeLa cells (despite their trajectory to the kinetochore being unaltered) points to the possibility that it is not only the number of uniform bridging proteins present, but the combination of different proteins is also important. The insights into the ultrastructure of GBM K-fibres has the potential to be important in a clinical context. However, the lack of a suitable control for this cell type does limit the conclusions which can be drawn from this work.

The observations presented in this chapter represent an important step in the ambition to examine the full spindle structure of human cells at EM-level resolution. However, there are several experiments which are needed to support what our initial results suggest, increase confidence in these conclusions, and investigate further the role of TACC3 in the spindle. The following section outlines this future work. Performing SBF-SEM on cells where endogenous TACC3 has been knocked down, combined with TEM analysis, would shed light on how TACC3 is utilised by the cell in order to build a functional spindle. Cheeseman *et al.* utilised knock-sideways (KS) of TACC3 to determine that TACC3 was of vital importance in the prometaphase to metaphase transition, with many cells failing to reach metaphase after TACC3 KS at NEBD (Cheeseman et al., 2013). TACC3 KS at metaphase caused a delay in anaphase onset due to loss of the tension in K-fibres. It would be interesting to

examine the whole spindle using SBF-SEM after TACC3 KS to observe the effects on spindle structure and volume in this situation. In an attempt to delineate the roles of the different pools of TACC3 in the spindle, the structure of the spindle of cells expressing an S558A mutant of TACC3 was examined by SBF-SEM and TEM. This mutant is unable to bind spindle MTs as part of the TACC3-chTOG-clathrin complex, but is able to function in its plus-tip tracking role in complex with chTOG only (Gutierrez-Caballero et al., 2014). The construct used in this experiment knocked down endogenous TACC3 and re-expressed the mutant at endogenous levels to examine how the spindle is built when the TACC3-chTOG-clathrin complex is not bridging kMTs. It would also be interesting to examine this mutant over-expressed in cells with normal wild-type TACC3 levels – this would allow us to examine the possibility that the abundance of MTs seen after wild-type TACC3 over-expression is due to a potential MT polymerisation function of TACC3, rather than having excess mesh complex. Similar experiments using a TACC3 mutant unable to perform its tip-tracking function with chTOG but able to bind the spindle in the TACC3-chTOG-clathrin complex would aid in further characterisation of the different roles of TACC3 in building the spindle. Only one GBM cells line was examined using SBF-SEM and TEM in this chapter (GBM11). Similar analysis of the other four GBM cell lines received from the Wurdak lab could potentially shed light on the contribution of TACC3 to the spindle, as they are each over-expressing TACC3 but to a different degree. Correlation of spindle features with TACC3 level may offer an explanation of the mitotic defects characteristic of Glioblastoma. Finally, numerous repeats of the experiment presented in this chapter and the potential future work outlined in this discussion would be needed to provide confidence in the observations and the accuracy and utility of the methods as a whole.

From the work presented in this chapter it is clear that SBF-SEM is powerful technique for studying cellular ultrastructure. It has been used here to examine the global structure of K-fibres to supplement the local information provided by TEM – the techniques together providing a more complete picture of the spindle as a whole. The optimisation performed in this chapter has demonstrated the potential of these techniques in many different studies. For example, in some cases kinetochores were clearly visible, implicating this method in the study of attachment errors resulting in chromosome missegregation, for instance. The resolution of SEM is lower than that of TEM, and while we may not be able to determine with certainty that every MT in

the 3View® images are single MTs, work in this thesis has shown that SBF-SEM does provide a picture of the entire spindle on a nanometre scale, as well as doing this on timescales much shorter than TEM analysis. Both techniques require a significant amount of time and expertise, but the result of TEM tomography and reconstruction results in the production of a relatively small 3D EM dataset. Optimisation of SBF-SEM has opened up the possibility that large volumes can be examined at the nanometre scale, at a fraction of the time and labour-intensity, and increased numbers for the conditions studied in this chapter would provide further confidence in our observations.

6. General discussion

This thesis has demonstrated the use of novel techniques in electron microscopy in the detailed study of the mitotic spindle. Previous work in the Royle lab delineating the presence of the TACC3-chTOG-clathin complex on the spindle and its roles throughout the different stages of mitosis demonstrated that this complex was indeed an important component of the spindle (Booth et al., 2011; Cheeseman et al., 2013; Hood et al., 2013). When components of the complex were depleted, K-fibres lacked MTs and cells struggled to congress their chromosomes (Booth et al., 2011; Cheeseman et al., 2013; Royle et al., 2005). Detailed structural characterisation of K-fibres untaken in this thesis has offered an explanation of what this complex is doing within the spindle, and why cells are sensitive to the levels of its constituent proteins.

The work outlined in this thesis is the first in-depth characterisation of a novel sub-cellular structure - the mesh - and its role within K-fibres. The mesh has been shown to be a significant component of K-fibres, only being fully revealed with the use of High Pressure Freezing, electron tomography and 3D reconstruction. Through manipulation of TACC3 levels on the spindle, the mesh has been shown to crosslink kMTs in a complex, three-dimensional network, capable of bridging multiple MTs to effect their proper spacing and organisation within the K-fibre unit. This sheds light on how K-fibres form, and how they are able to function as a coherent unit – cooperating to congress and segregate chromosomes. When levels of the mesh are manipulated, the regular spacing within K-fibres is abrogated, causing more MTs to be incorporated into the fibre with areas of tighter packing between them. When more of one mesh constituent is over-expressed, this results in non-uniform changes to K-fibre spacing, with areas of clustering. This is evidence that the mesh acts to bundle MTs by favouring close spacing.

This thesis also outlines a new method of examining spindle ultrastructure on a large scale while maintaining high resolution using SBF-SEM. By pushing this system to the limit of its capability, individual K-fibres could be examined in the context of the whole spindle apparatus. This method was useful in investigating the effects of manipulating TACC3, by over-expression or expression of the S558A mutant, to

determine its role by examining the whole spindle in detail. Through this, I have demonstrated the potential of SBF-SEM for investigating the role of spindle proteins, by examining the effects of their manipulation on the morphology and ultrastructure of the whole spindle in high resolution. Work currently underway in the Royle lab to assign electron density to putative mesh components will further enhance the utility of this method in examining the role of MAPs in the spindle. From the results presented here, it seems clear that this technique could aid in the study of mitosis in many additional ways. An exclusion zone around the spindle was observed by Schweizer *et al.* which was hypothesised to to aid in the formation of the spindle and segregation of chromosomes by excluding large, obstructive organelles from the spindle region and confining mitotic regulators to this area (Schweizer et al., 2015). However, during the course of this study, organelles including large mitochondria as well as membranous networks have been observed occupying space within the spindle envelope. SBF-SEM combined with 3D rendering could shed further light on on the characteristics of this envelope – for example, do mitochondria within the spindle zone have a purpose in being there, for generating energy for motor proteins in the spindle perhaps? The optimisation of CLEM, combined with SBF-SEM and 3D rendering techniques in this thesis opens up many possibilities for researchers studying mitosis, potentially bridging the gap between the light and the electron microscope.

Each of the constituent proteins of the TACC3-chTOG-clathrin complex has been implicated in cancer situations. Fusions of CHC-TFE3 are present in renal and haematological cancers (Argani et al., 2003); chTOG, as the name implies, is over-expressed in cancers of the colon and liver (Charasse et al., 1995); and TACC3 expression levels are abrogated in lung and bladder cancers, amongst several others (Jung et al., 2006; Williams et al., 2013). TACC3 in particular has been the subject of a number of studies which make the targeting of this protein a potential form of cancer therapy. In several instances, degradation of TACC3 has been shown to selectively induce apoptosis of cancer cells, with normal tissues unaffected (Ohoka et al., 2014; Yao et al., 2012) implicating TACC3 as a potential chemotherapeutic target. Aurora A kinase is also commonly upregulated in many malignancies, over-riding the SAC and causing the cell to enter anaphase in an uncontrolled manner (Anand et al., 2003). TACC3 has been shown in the present study to cause delays in mitosis when its level on the spindle is increased or

decreased, as a result of disorganised K-fibres that are hyper-stabilised, or not stable enough. A situation where concomitant over-expression of Aurora A and TACC3 could contribute to aneuploidy and carcinogenesis as a result of defective spindle assembly and SAC satisfaction is easily imagined. Glioblastoma cells were also examined in this study, and although the contribution of TACC3 over-expression to cancer propagation in these tumours is not yet established, this electron microscopy analysis has demonstrated that there are spindle abnormalities which could abrogate mitotic defects in these cells. Our work offers an important insight into the function of TACC3 within K-fibres, contributing to our knowledge of the role this protein plays in the development of cancer.

7. Appendix

7.1: The mesh is a network of microtubule connectors that stabilises individual kinetochore fibres of the mitotic spindle

eLIFE elifesciences.org

RESEARCH ARTICLE

The mesh is a network of microtubule connectors that stabilizes individual kinetochore fibers of the mitotic spindle

Faye M Nixon[1,2], Cristina Gutiérrez-Caballero[1], Fiona E Hood[2], Daniel G Booth[2†], Ian A Prior[2], Stephen J Royle[1*]

[1]Division of Biomedical Cell Biology, Warwick Medical School, Coventry, United Kingdom; [2]Department of Cellular and Molecular Physiology, Institute of Translational Medicine, University of Liverpool, Liverpool, United Kingdom

Abstract Kinetochore fibers (K-fibers) of the mitotic spindle are force-generating units that power chromosome movement during mitosis. K-fibers are composed of many microtubules that are held together throughout their length. Here, we show, using 3D electron microscopy, that K-fiber microtubules (MTs) are connected by a network of MT connectors. We term this network 'the mesh'. The K-fiber mesh is made of linked multipolar connectors. Each connector has up to four struts, so that a single connector can link up to four MTs. Molecular manipulation of the mesh by overexpression of TACC3 causes disorganization of the K-fiber MTs. Optimal stabilization of K-fibers by the mesh is required for normal progression through mitosis. We propose that the mesh stabilizes K-fibers by pulling MTs together and thereby maintaining the integrity of the fiber. Our work thus identifies the K-fiber meshwork of linked multipolar connectors as a key integrator and determinant of K-fiber structure and function.

DOI: 10.7554/eLife.07635.001

***For correspondence:** s.j.royle@warwick.ac.uk

Present address: †Wellcome Trust Centre for Cell Biolog, University of Edinburgh, Edinburgh, United Kingdom

Competing interests: The authors declare that no competing interests exist.

Funding: See page 18

Received: 20 March 2015
Accepted: 18 June 2015
Published: 19 June 2015

Reviewing editor: Anna Akhmanova, Utrecht University, Netherlands

Introduction

Accurate mitosis is essential to eukaryotic life. It requires the correct assembly of a bipolar array of microtubules (MTs) into a mitotic spindle which, in concert with hundreds of different motors and non-motor proteins, segregates the duplicated sister chromatids to the two daughter cells. Many of the chromosome movements in mitosis are governed by the kinetochore fibers (K-fibers) of the spindle apparatus. In human cells, K-fibers are bundles of 20–40 parallel MTs that typically run from the kinetochore to the spindle pole (***McDonald et al., 1992***; ***Mastronarde et al., 1993***; ***McEwen et al., 1997***; ***Booth et al., 2011***; ***Sikirzhytski et al., 2014***). K-fibers can be thought of as coherent units: their constituent MTs are held together throughout their length, as well as being focused at either end (***Rieder, 1981***; ***Spurck et al., 1997***). The coherence of the K-fiber is thought to be crucial for accurate chromosome segregation in mitosis. However, the ultrastructural and molecular basis of K-fiber coherence is not well understood.

Lateral MT connectors are important for the function of MT arrays, such as K-fibers, in cells (***Brangwynne et al., 2006***; ***Ward et al., 2014***). Classic electron microscopy (EM) studies uncovered the presence of electron density between MTs of the K-fibers (***Wilson, 1969***; ***Hepler et al., 1970***; ***Witt et al., 1981***; ***Bastmeyer and Fuge, 1986***). These inter-MT bridges appear as bipolar struts laterally connecting two MTs in 2D electron micrographs. The bridges are typically ~5 nm thick and range from 6–20 nm in length. The morphology of bridges is heterogeneous, and they are likely composed of a variety of proteins (***Booth et al., 2011***). The mitotic spindle is an ensemble of hundreds of MT-associated proteins (***Sauer et al., 2005***), some of which are candidates for inter-MT bridges (***Manning and Compton, 2008***). The number of inter-MT bridges scales with the number of

eLife digest Before a cell divides, its genetic material must be copied and then equally distributed between the newly formed daughter cells. In the cells of plants, animals, and fungi, a structure known as the spindle pulls the two copies of the chromosomes apart. The spindle is made up of a network of long, protein filaments called microtubules, and the bundles of microtubules that attach to the chromosomes are referred to as 'K-fibers'.

K-fibers are organized in a way that provides strength. These bundles of microtubules are held together throughout their entire length and, in 2011, it was suggested that a group of proteins including one called TACC3 could cross-link adjacent microtubules within K-fibers. However, it remained unclear how these proteins achieved this.

Now, Nixon et al.—including several of the researchers involved in the 2011 work—have used a technique called 3D electron tomography to analyze what holds the K-fibers together in human cells. This analysis revealed struts or connectors that hold together adjacent microtubules within K-fibers. These connectors can vary in size and a single connector can link up to four microtubules. This means that, in a three-dimensional view, the connectors appear as a 'mesh' between the microtubules in the bundle.

Nixon et al. then increased the levels of the TACC3 protein and found that the K-fibers became disorganized. The spacing of the microtubules with the K-fibers was reduced so that they were more tightly packed than normal. These observations suggest that 'the mesh' influences the microtubule spacing within a K-fiber.

Nixon et al. analyzed how disorganized K-fibers affected dividing cells and found that it took longer for the chromosomes to move to the newly forming daughter cells. This suggests that cells must maintain optimal levels of TACC3 to ensure that the K-fibers can effectively separate the chromosomes. Further work is needed to identify the other proteins and molecules that make up the mesh.

DOI: 10.7554/eLife.07635.002

MTs and also with the number of paired MTs in a bundle (***Bastmeyer and Fuge, 1986***), and it was proposed that it is the inter-MT bridges that hold K-fiber MTs together (***Witt et al., 1981***). The connection between the kinetochore and K-fiber MTs has been studied by 3D-EM (***Dong et al., 2007***; ***McIntosh et al., 2008***). However, a similar 3D investigation of inter-MT connections away from the kinetochore has not been reported.

One molecular candidate for inter-MT bridges in K-fibers is TACC3–ch-TOG–clathrin. The assembly of this complex is regulated by phosphorylation of TACC3 at serine 558 by Aurora-A kinase (***Fu et al., 2010***; ***Hubner et al., 2010***; ***Lin et al., 2010***; ***Booth et al., 2011***). This allows two domains from TACC3 and clathrin to come together in space, making a single, composite MT interaction surface (***Booth et al., 2011***; ***Cheeseman et al., 2011***; ***Hood et al., 2013***). Previous work showed that this complex is necessary for K-fiber stabilization (***Royle et al., 2005***; ***Booth et al., 2011***; ***Cheeseman et al., 2013***) and that the complex forms a distinct class of short inter-MT bridges (***Booth et al., 2011***).

In this study, we set out to examine the 3D ultrastructure of K-fiber inter-MT bridges. Surprisingly, we found that inter-MT bridges are not simply bipolar connections between two MTs but are a network of interconnected struts that contact multiple MTs. We term this structure 'the mesh'. This novel subcellular structure positions MTs within the K-fiber and is required for normal mitosis.

Results

Inter-MT connectors in K-fibers are 'bridges' in 2D and a 'mesh' in 3D

Inter-MT bridges were first described in 2D electron micrographs as faintly stained fine threads projecting from the surface of the tubules (***Hepler et al., 1970***). For example, 2D views of inter-MT bridges connecting adjacent MTs within a K-fiber are shown in ***Figure 1A***. The morphology of inter-MT bridges is heterogeneous (***Booth et al., 2011***), as noted in the original report (***Hepler et al., 1970***). In order to examine the morphology of bridges in more detail, we used electron tomography of sections taken from mitotic HeLa cells fixed by high-pressure freezing/freeze substitution (HPF/FS). This gave a 3D view of the K-fiber MTs and the material that connected them (***Figure 1B***, ***Video 1***). Careful examination of the

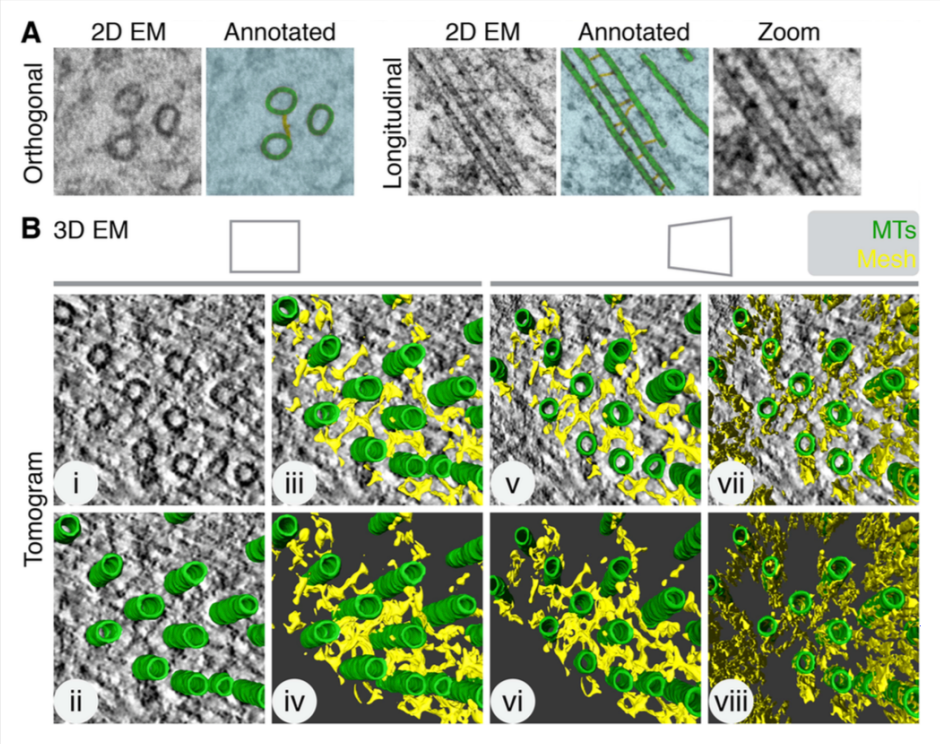

Figure 1. Intermicrotubule connectors in K-fibers are 'bridges' in 2D and a 'mesh' in 3D. (**A**) 2D views of inter-MT bridges in sections taken orthogonally or longitudinally to the spindle axis. In the annotated version, MTs (green) and inter-MT bridges (yellow) are shown on a blue background. Zoom of longitudinal section is a 2× expansion of the lower part of the 2D EM view. (**B**) Orthoslice of a tomogram generated from a tilt series of a single section through a K-fiber preserved using HPF/FS (**i**). Overlaid is a hand-rendered 3D representation of MTs (green) (**ii**) and associated mesh (yellow) (**iii**). The model is shown alone (**iv**). For (**v**–**viii**), the tomogram is tilted to show the MT axis. In **v** and **vi**, the overlay and model are shown. In **vii** and **viii**, the same view is shown but with the mesh detected by the automated segmentation method. Note that sections taken >1 μm away from the kinetochore are shown in this and all subsequent figures. Tomogram thickness, 45.6 nm. For scale, MTs are 25 nm in diameter.

DOI: 10.7554/eLife.07635.003

The following figure supplements are available for figure 1:

Figure supplement 1. The mesh is visible, but not well preserved, in chemically-fixed K-fibers.

DOI: 10.7554/eLife.07635.004

Figure supplement 2. The mesh is associated with K-fiber MTs.

DOI: 10.7554/eLife.07635.005

tomograms revealed that inter-MT bridges are not just simple bipolar struts connecting two adjacent MTs: they are interconnected and can contact multiple MTs within the K-fiber. This network of inter-MT connectors is best illustrated by rendering the densities seen in the tomogram and visualizing the resultant computer model (***Figure 1B***). We term the interconnecting material 'the mesh'.

To obtain an unbiased view of the mesh, we developed a semi-automated segmentation method for 3D model building (***Figure 1B***, ***Video 1***). This method was used for all subsequent quantification.

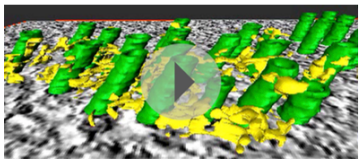

Video 1. Example of the K-fiber mesh from a normal HeLa cell at metaphase. Tomogram of a K-fiber. The mesh (yellow) is shown by manual rendering and by automated rendering. MTs (green) were rendered by hand. All segmentation was smoothed in Amira.
DOI: 10.7554/eLife.07635.006

We found that mesh preservation was superior using HPF/FS compared with chemical fixation (***Figure 1—figure supplement 1***). Moreover, the mesh was associated with K-fiber MTs. In contrast, segmentation of non-K-fiber areas resulted in distinct, particulate density and translating MTs to a non-K-fiber area meant that globular density, which passed through the MTs, was detected (***Figure 1—figure supplement 2***).

Ultrastructural morphology of the mesh

Having established a detection method, we next explored the anatomy of this novel subcellular structure. Three types of connectors within the mesh could be distinguished in these 3D models. Bipolar, tripolar, or quadrupolar connectors could be selected using the criterion of uninterrupted density that connects two, three, or four MTs, respectively (***Figure 2A***). These connectors were highly heterogeneous in size. Where the volumes of individual connectors could be determined easily, we found that bipolar, tripolar, and quadrupolar connectors had mean volumes of 6689, 17,370, and 32,376 nm^3, respectively (***Figure 2B***). Therefore, there is not a linear relationship between the number of struts in a connector and the connector volume. The volume of mesh within each fiber was, on average, equivalent to the volume of MTs that it encapsulates and larger than the volume of MT walls alone (***Figure 2C***). This observation establishes that the mesh is a major component of every K-fiber.

We next examined the contacts made between the mesh and MTs to determine if there were preferred locations on the MT for mesh attachment, for example, on the seams of MTs. We found that mesh-MT contacts were highly heterogeneous (***Figure 2D***). For example, a crosslink between two MTs could be a simple bipolar strut with a small footprint on both connected MTs, or at the other extreme, the crosslink could be a network of multiple-linked struts, with large mesh contact areas on both MT surfaces. These larger, composite footprints extended for some distance along both linked MTs, but these were not confined to a co-axial line on the MT wall. Moreover, several mesh connectors could contact the same MT at the same axial position (e.g., ***Figure 1B***), which further argues that the mesh has no preference for the MT seam.

Manipulating the mesh influences K-fiber organization

Previous work indicated that one component of the mesh is a complex of TACC3–ch-TOG–clathrin whose assembly is regulated by Aurora-A kinase (***Booth et al., 2011***; ***Hood et al., 2013***). Moreover, the amount of this complex on K-fibers can be increased simply by overexpressing TACC3 (***Booth et al., 2011***). In order to experimentally manipulate the mesh, we, therefore, made a stable inducible HeLa cell line where GFP-TACC3 could be overexpressed in a controlled manner (***Figure 3—figure supplement 1***). The most obvious effect of this manipulation was to alter MT organization. K-fibers in cells expressing GFP-TACC3 had more MTs per fiber, and the cross-sectional area that those MTs occupied was larger, compared to fibers in control uninduced HeLa cells (***Figure 3A***). The MT density was similar between the two groups suggesting that the fiber area scaled with the number of MTs (***Figure 3A***).

To look in more detail at MT packing within a K-fiber, we analyzed the distance from each MT to its nearest neighbor, and the number of neighboring MTs found within 80 nm. Both analyses showed that *local* MT packing density within the fiber had increased substantially in TACC3 overexpressing cells compared to uninduced controls (***Figure 3B***), although the fibers themselves were larger overall. A simple manifestation of this tighter local packing was the increased frequency of doublet and triplet MTs within TACC3 overexpressing K-fibers (***Figure 3B***). The median distance to the nearest neighboring MT had decreased from 56.1 to 48.1 nm (***Figure 3C***), a change in edge-to-edge proximity from 31.1 to 23.1 nm. This means that in TACC3 overexpressing cells, the average nearest neighboring MT is less than the width of one MT away. Because the overexpression of TACC3 alters the MT packing within the K-fiber, these experiments suggested to us that the mesh might influence

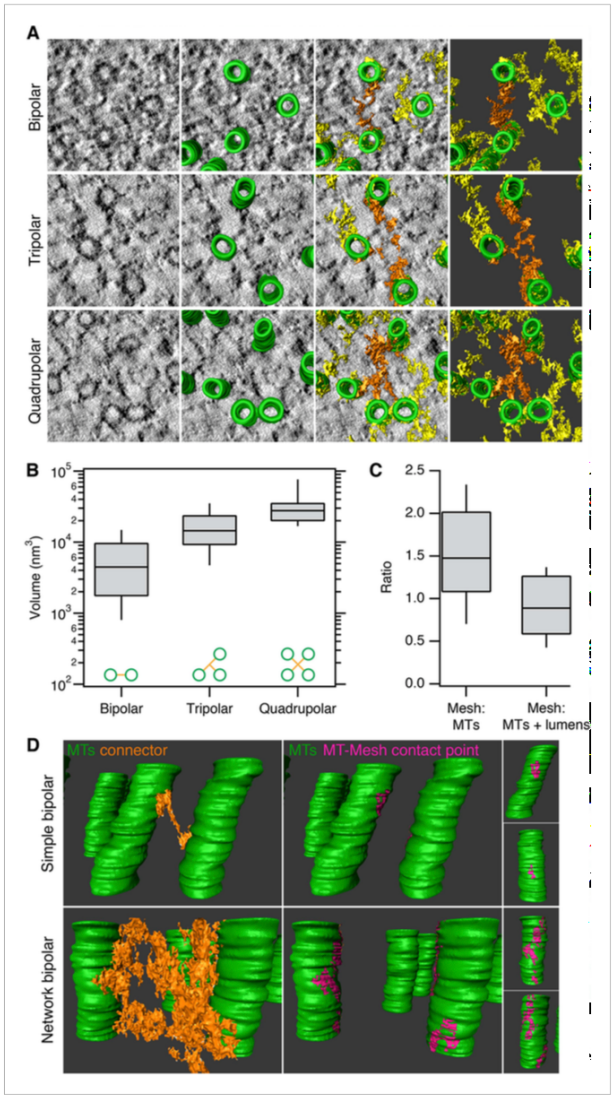

Figure 2. Inter-MT linkages are defined connectors with heterogeneous MT-mesh contacts. (**A**) Examples of bipolar, tripolar, and quadrupolar connectors within the mesh. Single orthoslices from tomograms showing examples of different connectors. MTs are hand-rendered (green), mesh is automatically detected (yellow, see 'Materials and methods'), and example connectors are highlighted orange. Tomogram thickness, 51.3 nm (bipolar) and

Figure 2. continued on next page

Figure 2. Continued

35.2 nm (tripolar and quadrupolar). (**B**) Box plots to show the volume of bipolar, tripolar, and quadrupolar connectors within the mesh from multiple tomograms. (**C**) Box plot to show the ratio of the volume of mesh relative to MTs (walls only) or MTs + lumens ('filled-in' MTs). Box plots show the median, 75th and 25th percentile, and whiskers show 90th and 10th percentile. (**D**) Heterogeneity of contacts between mesh and MTs. Two pairs of MTs are shown with a simple bipolar connector (above) or with a more complex connection (below). MTs (green) are shown with a single component of the mesh (orange). The contact points between the selected mesh and the MTs are shown in pink. Note the extensive mesh-MT contacts in the lower example. Tomogram thickness, 66.4 nm (simple) 64.8 nm (network). For scale, MTs are 25 nm in diameter.

DOI: 10.7554/eLife.07635.007

MT spacing within the K-fiber. We return to the hypothesis that the mesh has an important role in MT spacing below.

Are the additional MTs in TACC3 overexpressing K-fibers stably attached to the kinetochore? To address this question, we used a 3D confocal microscopy assay of tubulin staining in the vicinity of kinetochores (***Cheeseman et al., 2013***). In agreement with the EM analysis, we detected a higher tubulin signal in cells expressing GFP-TACC3 compared to those expressing GFP alone. Following cold treatment, the tubulin intensity in the vicinity of kinetochores was reduced to comparable levels in both conditions, suggesting that the additional MTs in TACC3 overexpressing K-fibers are attached by mesh to the rest of the K-fiber but were not stably attached to the kinetochore (***Figure 3D***).

Overexpression of TACC3 also increased the volume of mesh between K-fiber MTs in a tomogram to 5.2 ± 1.0 × 10^6 nm^3 (mean ± s.e.m.). This corresponds to 9.1 ± 0.01% of the fiber volume in the tomogram, whereas control mesh was 5.7 ± 0.01%. This change is somewhat difficult to interpret because of the significant increase in the number of MTs per fiber and the tighter local packing. More MTs per fiber might push up the volume of mesh, but the closer proximity of MTs limits the space available for mesh to be present.

Overexpression of TACC3 increases MT interconnectivity in K-fibers

One defining characteristic of the mesh is that it connects multiple MTs within K-fibers. This interconnectivity means that a MT that is contacted by the mesh is connected to one or more MTs and each of these, in turn, may be connected to one or more MTs and so on. We defined these connected MTs as 'chains'. In uninduced cells, chain sizes were small, containing at most 6 MTs (***Figure 4A***). By contrast, cells overexpressing TACC3 had chains containing up to 12 MTs (***Figure 4A***), suggesting that the MTs were more interconnected as a result of TACC3 overexpression. Although MTs in TACC3 overexpressing K-fibers were more interconnected, the constitution of the connectors within the mesh was not noticeably altered (***Figure 4B***). In both conditions, the mesh was composed of a predominance of bipolar connectors and similar proportions of tripolar and quadrupolar connectors (***Figure 4B***).

We next wondered if the larger chains in TACC3 overexpressing cells were the result of the tighter local MT packing. Accordingly, we constructed 2D MT maps, where each MT's chain membership was displayed, and we compared these to the heat maps of local packing as previously described (***Figure 4C***). The entire dataset was analyzed computationally in order to test the idea that chain membership depended on MT proximity. For each MT, we calculated the number of neighboring MTs within a given search radius and compared these values for single ('unchained') MTs and those that were part of a chain (***Figure 4D***). This analysis showed that in controls, the single MTs and chained MTs had similar numbers of neighbors, that is, meshed MTs were not more likely to be in tightly packed regions of the fiber. However, in the TACC3 overexpressing fibers, the MTs that were part of a chain had significantly more neighbors than single MTs (***Figure 4D***), this pattern was seen for search radii >50 nm and was not seen if the dataset was randomized (***Figure 4D***, inset, see 'Materials and methods'). The closer proximity of chained MTs vs single MTs indicates that the mesh influences MT positioning, effectively pulling them closer together. An alternative possibility is that the mesh is passive and only encapsulates MTs if they are in close proximity. However, this possibility is less likely because MTs in control fibers exhibit no difference in their proximity relative to their chain status.

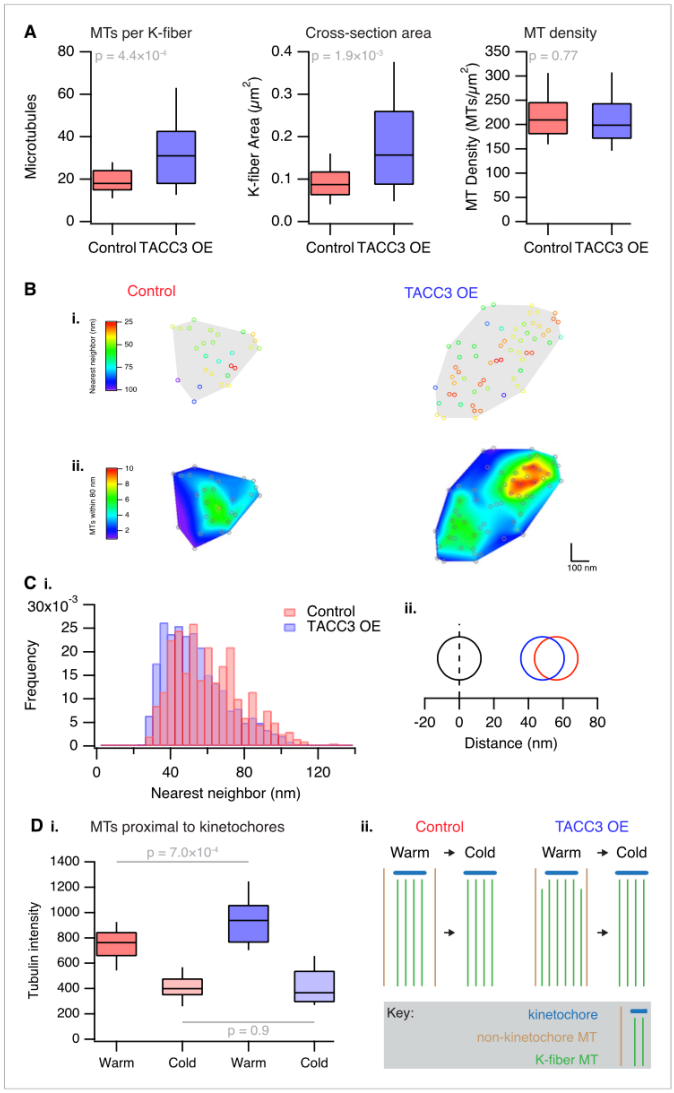

Figure 3. Analysis of MT packing within a K-fiber. (**A**) Box plots showing the number of MTs per K-fiber, the cross-sectional K-fiber area, and the density of MTs in the K-fiber. N_{fiber} = 26 (control), 37 (TACC3 OE). Box plots show the median, 75th and 25th percentile, and whiskers show 90th and 10th percentile. p values from Welch's t-test are shown. (**B**) Spatial maps of MTs (circles) in a representative K-fiber from a control (left) or TACC3 overexpressing cell

Figure 3. continued on next page

Figure 3. Continued

(right) color-coded to show (**i**) the distance to the nearest neighbor or (**ii**) overlaid on a heatmap to show the number of MTs within 105 nm (center-to-center distance), 80 nm (edge-to-edge distance). (**C**) Histogram to show the frequency of distances to the nearest neighboring MT (**i**). A representation of the change in average (median) MT spacing to the nearest neighboring MT that is caused by TACC3 overexpression (**ii**). N_{MTs} = 500–1324. (**D**) Analysis of tubulin intensity in the vicinity of kinetochores by confocal microscopy. Box plot to show the distribution of median values per cell of tubulin intensities in a sphere surrounding the kinetochore (**i**). Box plots show the median, 75th and 25th percentile, and whiskers show 90th and 10th percentile. p values from one-way Anova with Tukey's *post hoc* test are shown. N_{cell} = 20–25, $N_{kinetochore}$ = 2823–3533. Schematic diagram of the changes in K-fibers induced by TACC3 overexpression (**ii**). K-fibers are thicker because MTs that are not stably attached to the kinetochore are recruited to the K-fiber bundle.

DOI: 10.7554/eLife.07635.008

The following figure supplement is available for figure 3:

Figure supplement 1. Inducible expression of GFP-TACC3 in HeLa cells to alter the composition of mesh.

DOI: 10.7554/eLife.07635.009

Bundling of MTs by mesh components

The two possibilities for mesh stabilization of K-fibers are shown in (***Figure 5A***). To test the possibility that the mesh can influence MT positioning in K-fibers, we turned to an in vitro assay. Fluorescently labeled MTs assembled in vitro and stabilized with taxol were incubated with proteins, and any effect on MT bundling was observed by light or EM. To reconstitute the mesh component containing TACC3, a protein mixture comprising clathrin, TACC3, ch-TOG, and GTSE1 was prepared and phosphorylated by Aurora-A kinase (see 'Materials and methods'). As a positive control, we used PRC1, which is known to bundle MTs (***Mollinari et al., 2002***). As a negative control, we used an equivalent amount of GST and MBP-His_6 protein as in the test condition, phosphorylated by Aurora-A kinase. Thick bundles of MTs could be seen by fluorescence microscopy for the TACC3-containing complex and for PRC1 but not for the negative control (***Figure 5B***). These images indicated specific bundling activity for the TACC3 complex.

To look in more detail at the bundled MTs, we analyzed the control, PRC1, and TACC3 complex conditions by EM. In the PRC1 and TACC3 complex conditions, pairs of MTs were interconnected by short electron dense connectors (***Figure 5C***). In control conditions, MTs were randomly oriented, but on occasions when they were in close proximity, no density was seen.

These MT-bundling experiments were complicated by the purification of several large proteins (***Figure 5—figure supplement 1***). As an alternative source, we immunoprecipitated protein complexes, which contained clathrin and TACC3 directly from mitotic spindle of HeLa cells at metaphase (***Figure 5—figure supplement 2A,B***). We observed bundling of Taxol-stabilized MTs in vitro, using this complex specifically (***Figure 5—figure supplement 2C***).

Together these experiments indicate that the TACC3 complex can crosslink MTs and drive the recruitment of stabilized MTs into bundles. They are not compatible with a passive role for the mesh in responding to MT positioning. In the context of the K-fiber, this suggests a role for the mesh in maintaining fiber integrity by tethering MTs together and influencing MT positioning.

Overexpression of TACC3 influences MT trajectories within K-fibers

To look further for any evidence of a role for the mesh in MT positioning, we examined the trajectories of MTs within each fiber. K-fibers are bundles of parallel MTs, and we sought to characterize how parallel the MTs are and to test if this is altered by TACC3 overexpression. Deviations from parallel would suggest that the mesh tethers MTs closer together and interferes with their trajectory. Qualitatively, we could see that MTs in TACC3 overexpressing K-fibers were more disorganized (***Figure 6A***, ***Video 2*** and ***Video 3***). To measure parallelism more rigorously and to allow comparison of multiple K-fibers, we used several computational approaches (described in 'Materials and methods'), which allowed us to normalize the 3D trajectory of each fiber and then examine the deviation of MT trajectories from this vector. K-fibers in cells overexpressing TACC3 had a higher proportion of MTs that deviate from parallel. They frequently had significantly larger polar angles compared to MTs in K-fibers from control cells (***Figure 6B,C***). The deviation of MTs from a completely

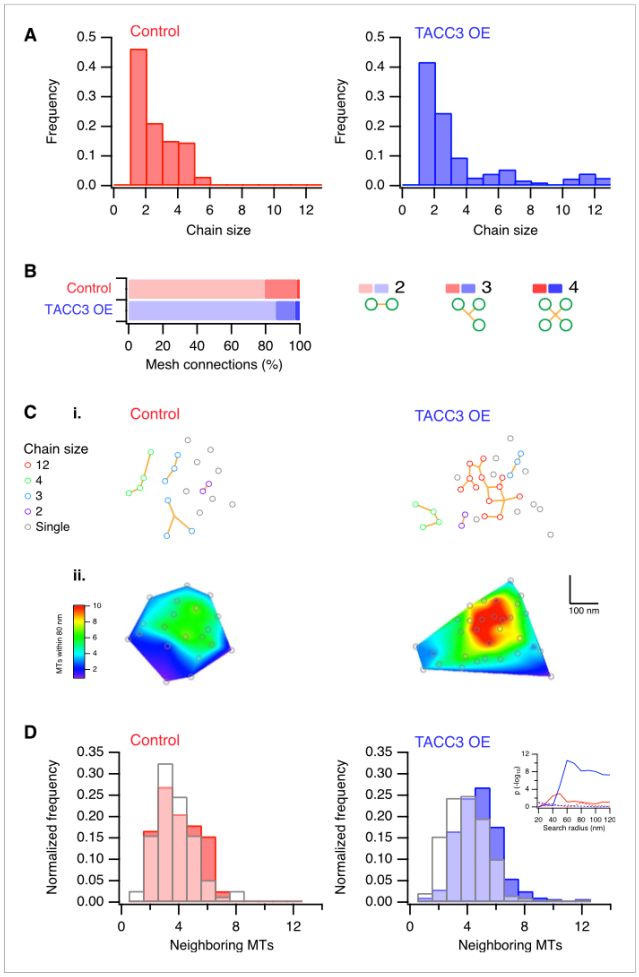

Figure 4. Analysis of MTs captured by mesh, their connectivity, and proximity. (**A**) Histogram to show frequency of MT chain sizes detected in single section tomograms. MT chains are collections of MTs that are connected by mesh within a section. Note that single MTs do not feature. (**B**) Bar chart to show the proportion of mesh that is bipolar, tripolar, and tetrapolar, as a percentage of total mesh connections. (**C**) Analysis of MT connectivity and proximity. (**i**) Spatial maps of MTs (circles) in a representative K-fiber from a control (left) or TACC3 overexpressing cell (right). Chains of MTs are shown in color, gray circles show MTs that are not detectably connected to other MTs by mesh. Orange lines represent the mesh connections schematically (see ***Figure 4—figure supplement 1***). (**ii**) Spatial maps are shown overlaid on heatmaps for the same fibers to show the number of MTs within 105 nm (center-to-center distance), 80 nm (edge-to-edge distance). Note that single (unchained) MTs are attached to the mesh, but that the MT to which they are attached is outside of the section. Tomogram thickness, 43.6 nm (Control),

Figure 4. continued on next page

Figure 4. Continued

28.8 nm (TACC3 OE). (**D**) Histogram to show frequency of MTs with a given number of neighboring MTs within 100 nm (center-to-center distance). MTs connected to others by mesh are shown in color, and single MTs are shown in white. Inset shows the p-value for comparisons calculated using search radii from 20 nm to 120 nm (center-to-center distance). Dotted lines show the same analysis following randomization of the chain membership data.

DOI: 10.7554/eLife.07635.010

The following figure supplement is available for figure 4:

Figure supplement 1. Examples of MTs chains and associated mesh.

DOI: 10.7554/eLife.07635.011

parallel condition is easier to visualize, by examining the Cartesian intersection coordinates of each MT vector with an x-y plane at a given distance (z) from a common origin (see 'Materials and methods'). These scatter plots show that MTs in TACC3 overexpressing cells deviate further from parallel than those in control cells (***Figure 6D***). The fraction of MT vectors intersecting this plane at radial distances of <10 nm from the center is 0.39 and 0.18 in control and TACC3 overexpressing cells, respectively. In other words, there are half as many parallel MTs after TACC3 overexpression.

Where are these deviant MTs? If they resided towards the periphery of the fiber, they may represent 'extra MTs', perhaps non-kinetochore MTs, that became enmeshed in the fiber when TACC3 was overexpressed. Alternatively, if the deviant MTs are throughout the fiber, this could be evidence for a role of the mesh in influencing MT spacing and packing within the fiber. To assess this, we plotted the polar and azimuthal angles as a function of distance from the K-fiber center (***Figure 6E***). These plots show that deviant MTs in TACC3 overexpressing cells are distributed at all distances from the center of the fiber. In controls, there was a weak tendency for deviant MTs to be at the fiber periphery, but the overall extent of trajectory deviancy was lower than in TACC3 overexpressing cells (***Figure 6C,E***). The lack of relation between distance from the fiber center and the deviancy from the fiber trajectory of MTs in fibers from TACC3 overexpressing cells indicates that the mesh plays an influential role in organizing MTs *within* the fiber. Together our results show that the change in composition of the mesh, caused by TACC3 overexpression, results in tighter local packing of MTs, more interconnectivity and disruption of the parallel organization of MTs within a K-fiber.

Mitotic problems associated with TACC3 overexpression

What are the functional consequences of the ultrastructural changes in MT organization *within* K-fibers? To address this question, we used live-cell imaging of our stable inducible cells expressing H2B-mCherry, growing asynchronously and compared mitotic progression in cells, where GFP-TACC3 expression was induced vs not induced. ***Figure 7*** shows that TACC3 overexpression increases the time taken for cells to congress all chromosomes to the metaphase plate (prometaphase-to-metaphase). In addition, the time from last chromosome alignment to the onset of anaphase (metaphase-to-anaphase) is also longer (***Figure 7***). No change was seen in the duration of anaphase (anaphase-to-telophase). Interestingly, these changes in mitotic progression are similar to those seen following depletion of TACC3 (***Lin et al., 2010***; ***Cheeseman et al., 2013***) (***Figure 7—figure supplement 1***). We conclude from these experiments that mitosis is sensitive to the levels of TACC3 and that this sensitivity correlates to changes in MT organization within the K-fiber.

Discussion

In this paper, we described the mesh: a network of MT connectors in K-fibers. We showed that the mesh is comprised of different connector types and is a major component of the K-fiber. Overexpression of TACC3 alters the mesh and changes the trajectory of MTs within the fiber, indicating that the mesh is a determinant of K-fiber structural integrity. This manipulation causes defects in mitosis and establishes that TACC3 levels at the spindle must be regulated for optimal mitosis.

Since the first EM studies of mitotic spindles, it has been clear that K-fiber MTs are held together throughout their length, presumably to function as a integrated unit (***Hepler et al., 1970***; ***Rieder, 1981***; ***Witt et al., 1981***). The importance of inter-MT connections along the length of the K-fiber was

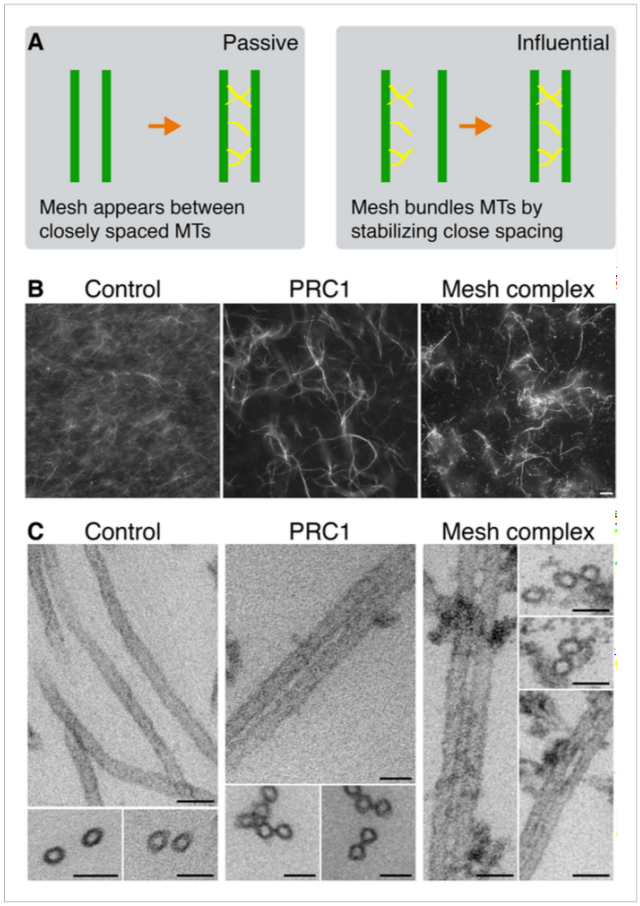

Figure 5. Bundling of MTs in vitro by mesh components. (**A**) Cartoon to illustrate two potential models for mesh function. In the passive model (left), MT distances are set by some other factor, and the mesh fills in the gaps to connect MTs. In the influential model (right), the mesh bundles MTs by favoring close spacing, this in turn influences MT spacing. (**B**) Representative fluorescence micrographs of rhodamine-labeled MTs incubated with the indicated proteins. Control (210 nM MBP-His_6, 100 nM GST), PRC1 (2 μM His_6-PRC1), and Mesh complex (10 nM MBP-ch-TOG-His_6, 100 nM clathrin, 100 nM GST-TACC3-His_6, 100 nM MBP-GTSE1-His_6), all phosphorylated by TPX2(1–43)/Aurora-A. Scale bar, 10 μm. (**C**) Representative electron micrographs of MTs incubated with the indicated proteins as described in **A**. Pelleted material was chemically fixed, embedded in resin, sectioned, and imaged. Scale bar, 50 nm.

DOI: 10.7554/eLife.07635.012

The following figure supplements are available for figure 5:

Figure supplement 1. MT bundling using purified components.

DOI: 10.7554/eLife.07635.013

Figure supplement 2. MT bundling using mesh complex immunoisolated from mitotic HeLa cells.

DOI: 10.7554/eLife.07635.014

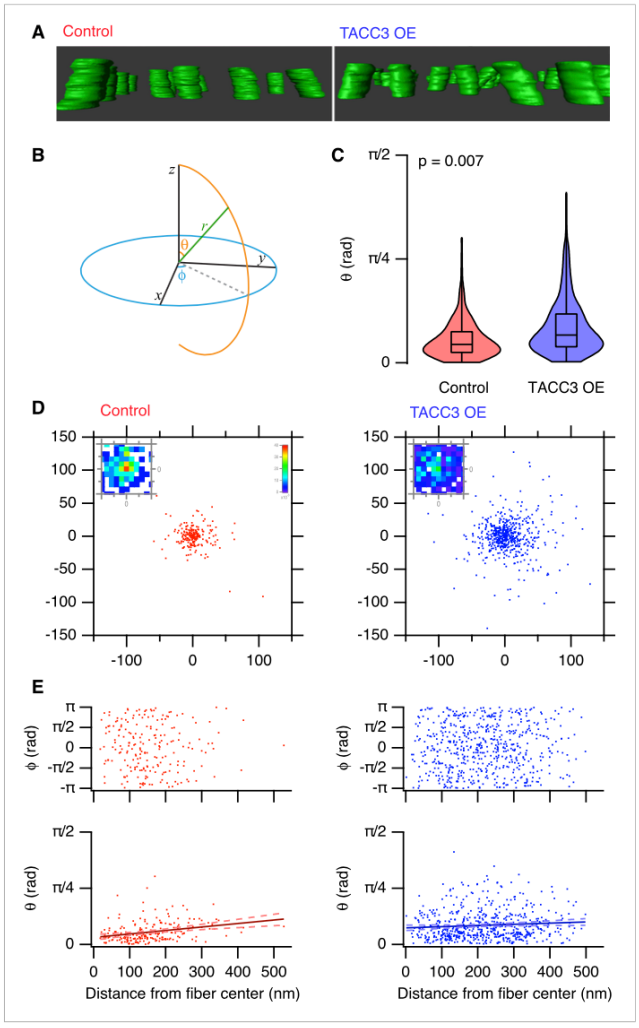

Figure 6. Analysis of MT trajectories within a K-fiber. (**A**) Representative 'side views' of rendered MTs in single tomograms of individual K-fibers from control (left, red, ***Video 2***) or TACC3 OE (right, blue, ***Video 3***) cells. Tomogram thickness, 66.4 nm (Control) trimmed to 34.2 nm, 34.2 nm (TACC3 OE). For scale, MTs are 25 nm in diameter. (**B**) *Aide memoire* of the spherical coordinate system. Trajectories of MTs (green line) in K-fibers were defined and normalized via Euler's rotation (see 'Materials and methods') such that the overall trajectory of all fibers pointed to the zenith. Measurements of polar angle (θ) and azimuthal angle (φ) were made from the normalized sets and are presented in **C**–**E**. (**C**) Violin plots of the polar angles for MTs in K-fibers from control and TACC3

Figure 6. continued on next page

Figure 6. Continued

overexpressing cells. Box plots show the median, 75th and 25th percentile, and whiskers show the minimum and maximum. Violins show a kernel density estimate of the data and are trimmed to the minima and maxima. Comparison of the median MT angle from each K-fiber Wilcoxon Rank Sum Test, $p = 0.007$, $N_{fiber} = 12–15$. (**D**) Illustration of the deviation of MTs from the fiber axis caused by TACC3 overexpression. Cartesian coordinates of the intersection of individual MT vectors that start from a common origin (0, 0, 0), with an x-y plane at z = 100 nm. To account for the difference in number of MTs, the insets show a normalized 2D histogram of these coordinates cropped to a 40 x 40 nm square centered at 0, 0, 100. (**E**) Plots of azimuthal angle (above) and polar angle (below) as a function of distance from the fiber center (defined as described in the 'Materials and methods'). Line of best fit is shown with 95% confidence bands (dashed line), $r^2 = 0.07$ (control), and 0.007 (TACC3 overexpression).

DOI: 10.7554/eLife.07635.015

demonstrated by severing K-fibers at their midpoint (***Spurck et al., 1997***). This resulted in two K-fiber stubs attached to the pole and kinetochore. The stubs do not immediately collapse but instead maintain their structural integrity. Our work identifying the mesh suggests that it is the structure that holds MTs together. This makes sense structurally, but there is a possibility that the mesh is passive and simply connects MTs in the fiber, wherever they may be. However, our work points to a role for the mesh in influencing MT position within the K-fiber. The evidence for this is: first, in K-fibers overexpressing TACC3, interconnected MTs are closer together than those not contacted by mesh. Second, a complex containing TACC3 was able to bundle MTs in vitro. Third, mesh in TACC3 overexpressing fibers pulls MTs out of alignment. In this way, the mesh plays an active role in MT positioning in K-fibers by favoring inter-MT interactions of defined distances. An extension of this is that the mesh can actively pull MTs together, in an energy-consuming process. We have no evidence for this intriguing possibility, which is compatible with our findings.

It seems counterintuitive that overexpression of a mesh component results in skewed MTs; shouldn't it make the MTs in the fiber 'more parallel'? However, it is likely that the mesh is made of other proteins, besides the TACC3–ch-TOG–clathrin complex, for example, CHD4, HURP/DLGAP5, and HSET/KIFC1 (***Mountain et al., 1999***; ***Sharp et al., 1999***; ***Koffa et al., 2006***; ***Yokoyama et al., 2013***). We favor the idea that because we have increased only one component of the mesh experimentally and not others, we do not see uniform changes in spacing and packing. This seems plausible as previous analysis determined TACC3–ch-TOG–clathrin was the shortest crosslinks in K-fibers (***Booth et al., 2011***), and so an imbalance of connector sizes in the mesh is predicted to skew MT trajectories.

The spindle matrix was originally proposed as a microtrabecular lattice that assists the motors and MTs of the mitotic spindle during chromosome movement (***Pickett-Heaps et al., 1982***). The existence

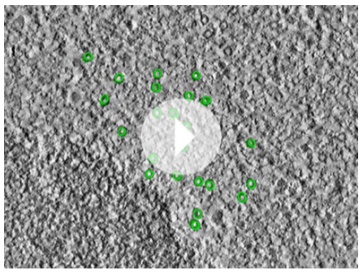

Video 2. Example of MT organization in a K-fiber from a control cell. Tomogram of a K-fiber. MTs (green) were rendered by hand. All segmentation was smoothed in Amira.

DOI: 10.7554/eLife.07635.016

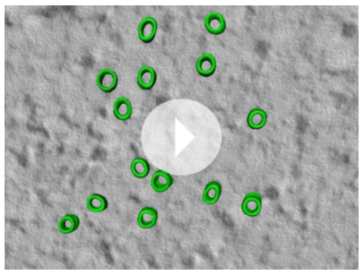

Video 3. Example of MT organization in a K-fiber from a GFP-TACC3 expressing cell. Tomogram of a K-fiber. MTs (green) were rendered by hand. Pale green is used to highlight two highly deviant MTs. All segmentation was smoothed in Amira.

DOI: 10.7554/eLife.07635.017

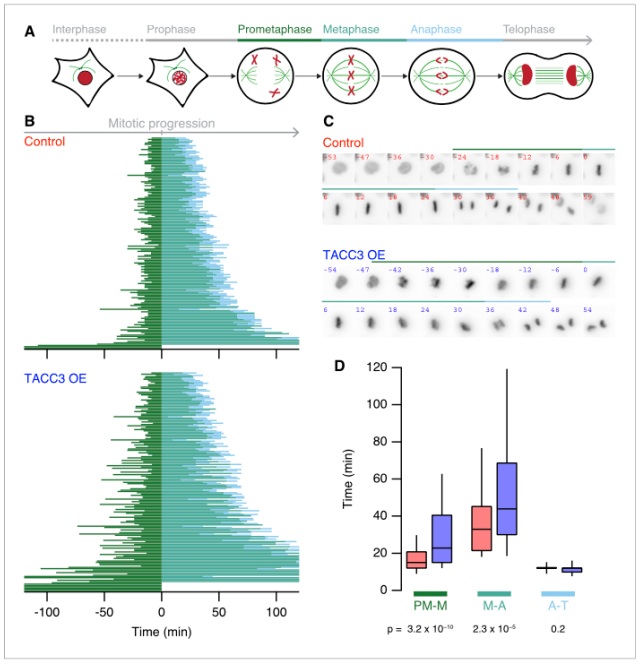

Figure 7. Mitotic consequences of TACC3 overexpression. (**A**) Cartoon representation of the stages of mitosis captured in live-cell imaging experiments. Cells expressing H2B-mCherry were staged as indicated with the transition to prometaphase marked by nuclear envelope breakdown; transition to metaphase marked by alignment of the last chromosome to the metaphase plate; to anaphase marked by first sign of chromosome segregation and transition to telophase marked by decondensation of H2B-mCherry. These events allowed us to assign prometaphase-to-metaphase (PM-M, dark green), metaphase-to-anaphase (M-A, light green), and anaphase-to-telophase (A-T, light blue). (**B**) Mitotic stage duration for individual cells. Time taken to go from prometaphase-to-metaphase (PM-M), metaphase-to-anaphase (M-A), or anaphase-to-telophase (A-T) is shown for control (red, above) or GFP-TACC3 overexpressing (blue, below) cells expressing H2B-mCherry. Each line represents a single cell. The time when the last chromosome aligned was set as 0 (metaphase). Cells that did not achieve metaphase halt at 0. Note that the time axis is truncated to show a 4 hr window centered on metaphase. N_{cell} = 163–169, N_{exp} = 4. (**C**) Still images of example cells from live-cell imaging experiments to determine mitotic progression. Detection of H2B-mCherry is shown on an inverted grayscale. Time in min is shown and the colored bars represent the staging, as in **A** and **B**. (**D**) Box plots to summarize mitotic progression experiments. Time taken to go from prometaphase-to-metaphase (PM-M), metaphase-to-anaphase (M-A), or anaphase-to-telophase (A-T) is shown for control (red) or GFP-TACC3 overexpressing (blue) cells. Whiskers show 90th and 10th percentiles.

DOI: 10.7554/eLife.07635.018

The following figure supplement is available for figure 7:

Figure supplement 1. Mitotic consequences of TACC3 depletion.

DOI: 10.7554/eLife.07635.019

of the matrix has been elusive, although several large macromolecular complexes have been proposed as matrix components (***Pickett-Heaps et al., 1984***; ***Chang et al., 2004***; ***Ma et al., 2009***; ***Johansen et al., 2011***; ***Schweizer et al., 2014***). Although superficially similar, we do not think that the K-fiber mesh is the ultrastructural correlate of the spindle matrix. The mesh that we have observed

exists between MTs within K-fibers (rather than between K-fibers) and is most likely composed of MT-associated proteins that function on K-fiber MTs. Most models of the spindle matrix envisage an elastic milieu that encompasses the entire spindle, yet it is independent of the MTs (**Scholey et al., 2001**; **Yao et al., 2012**). Despite this, micromanipulation experiments have left open the possibility that an anisotropic matrix could exist along K-fibers (**Gatlin et al., 2010**), and this would be compatible with our observations. The K-fiber mesh is in agreement with theoretical and experimental work showing that lateral MT connectors are important for MT arrays to sustain physical forces in cells (**Brangwynne et al., 2006**).

We used overexpression of TACC3 as our primary tool to manipulate the mesh. Progression through mitosis is slower under these conditions due to problems in chromosome congression and satisfying the spindle assembly checkpoint. Interestingly, a similar phenotype is observed when TACC3 is depleted from the spindle (**Lin et al., 2010**; **Booth et al., 2011**; **Cheeseman et al., 2013**). This indicates that mitosis is sensitive to TACC3 levels. We propose that this sensitivity reflects the robustness of the K-fibers. Too little TACC3–ch-TOG–clathrin and the mesh cannot strengthen the fibers adequately too much, and the MTs within the fibers become less parallel and oversupported. Previous work has suggested that hyperstabilization of K-fibers is counter-productive, leading to errors in mitosis (**Bakhoum et al., 2009**). TACC3 levels are altered in several human cancers, for example, ovarian, non-small cell lung cancer, and bladder (**Schmidt et al., 2010**), and fusions between TACC3 and FGFR3 are reported in glioblastoma and bladder cancer (**Singh et al., 2012**; **Williams et al., 2013**). Moreover, the amount of TACC3–ch-TOG–clathrin at the spindle is limited by the availability of phosphorylated TACC3 (**LeRoy et al., 2007**; **Hood et al., 2013**), and since Aurora-A kinase is amplified or upregulated in a wide range of cancers (**Nikonova et al., 2013**), it is possible that hyperstabilization of K-fibers occurs in these cells. Under any of these conditions, erroneous mitosis leading to aneuploidy may contribute to cancer initiation or progression. While we favor the idea that normal mitosis requires optimal K-fiber stabilization by the mesh, it must be noted that TACC3 has at least one additional function in mitosis (**Gutiérrez-Caballero et al., 2015**), and future work will seek to delineate the role of TACC3 in the mesh vs at the MT plus-ends.

Identifying and locating proteins within the mesh is the next challenge. Potentially, 3D views of K-fibers in situ will allow us to dock molecular structures of mesh components as has been achieved for other cellular systems (**Lucic et al., 2013**). Methods to unambiguously assign specific electron density to a particular protein will enable us to achieve this, and efforts are currently underway in our lab to do this.

Materials and methods

Cell Biology

HeLa cells (HPA/ECACC #93021013) were maintained in Dulbecco's Modified Eagle's Medium (DMEM) plus 10% fetal bovine serum (FBS) and 100 U/ml penicillin/streptomycin, in a humidified incubator at 37˚C and 5% CO_2.

For TACC3 overexpression, HeLa Tet-On cells (Clontech) were used to inducibly express GFP-TACC3. HeLa Tet-On cells were maintained in full DMEM with 300 µg/ml G418, and HeLa Tet-On cells with stably integrated pTRE2hyg-GFP-TACC3(KDP) plasmid were maintained with 300 µg/ml G418 and 200 µg/ml Hygromycin B. Expression of GFP-TACC3 was induced with 0.5 µg/ml doxycycline, 24 hr before analysis (EM analysis or mitotic progression experiments). For TACC3 knockdown, cells were transfected with plasmids to co-express GFP and shRNA using GeneJuice according to the manufacturer's instructions 2 days before imaging.

For immunofluorescence, HeLa cells on coverslips transfected to express GFP or GFP-TACC3 were either kept at 37˚C or cold-treated for 5 min then fixed with ice-cold methanol for 10 min. Cells were then blocked (PBS with 5% BSA and 5% goat serum) before immunostaining with rabbit anti-alpha-tubulin (Thermo, PA5-19489, 1:500) and mouse anti-CENPA (Abcam, ab13939, 1:500) and Alexa568/Alexa633-conjugated secondary antibodies.

For EM analysis, cells were synchronized using 2 mM thymidine block for 16 hr, release for 6 hr, followed by 9 µM RO-3306 for 16 hr (see ***Figure 3—figure supplement 1***). After 30–40 min release, mitotic cells were collected by shake-off and centrifugation at 300×*g* for 2 min at 37˚C and resuspended in DMEM containing 20% FBS. Cell synchronization was necessary to harvest sufficient numbers of cells for our analysis. Similar results were obtained with cells synchronized using

nocodazole, and with no synchronization, using a correlative light-EM approach, where a single cell was targeted for freezing.

Molecular biology

For inducible expression, GFP-TACC3KDP (**Booth et al., 2011**) was inserted into pTRE2hyg vector at *Nhe*I and *Not*I sites. Plasmids for expression of GST-TACC3-His_6 and GST-TPX2(1–43) were available from previous work (**Hood et al., 2013**). To make MBP-ch-TOG-His_6, the coding sequence of full-length human ch-TOG was amplified by PCR to add *Bam*HI and *Eag*I sites before subcloning into pMALPreHis vector. For MBP-GTSE1-His_6, the coding sequence of human G-2 and S-phase expressed 1 was amplified from an IMAGE clone (4138532) to add *Eco*RI and *Bam*HI sites. For His_6-PRC1, the coding sequence of human Protein Regulator of Cytokinesis 1 was amplified from an IMAGE clone (2958690) and inserted into pRSETB at *Nhe*I and *Eco*RI sites. Plasmids to co-express GFP with shRNA targeting GL2 or TACC3 (pBrain-GFP-shGL2 and pBrain-GFP-shTACC3) were available from previous work (**Booth et al., 2011**; **Lopez-Murcia et al., 2014**).

Protein biochemistry

Clathrin was purified from rat liver as described previously (**Hood et al., 2013**; **Lopez-Murcia et al., 2014**). Recombinant human Aurora-A kinase was purchased from EMD Millipore. Reagents for in vitro MT assembly were from Cytoskeleton Inc. All proteins were purified from BL21pLysS bacteria as described previously (**Hood et al., 2013**).

For in vitro MT bundling experiments, the following conditions were used: Control (210 nM MBP-His_6, 100 nM GST), PRC1 (2 μM His_6-PRC1), and Mesh Complex (10 nM MBP-ch-TOG-His_6, 100 nM clathrin, 100 nM GST-TACC3-His_6, 100 nM MBP-GTSE1-His_6), and visualized by fluorescence microscopy and EM. Concentrations refer to the final concentration with MTs. Proteins were incubated at 30˚C for 90 min to allow for phosphorylation by TPX2(1–43)/Aurora-A, 2 μg/ml each. MTs were polymerized from 100 μM tubulin (1:10 labeled to unlabeled) in general tubulin buffer (80 mM K-Pipes, 2 mM $MgCl_2$, 0.5 mM EGTA, pH 7.0) with 1 mM GTP and 6% glycerol for 15 min at 37˚C. Diluted 1:20 in general tubulin buffer supplemented with 10 μM taxol (paclitaxel, Sigma) and 1 mM GTP, incubated for a further 5 min at 37˚C. To 92.4 μl of protein mixture, 69.9 μl of MTs were added and incubated at RT for 10 min. Then 7.25 μl of this was fixed with glutaraldehyde in BRB80 (1.45 μl; 0.1% final), then diluted with 10 μl 70% glycerol/BRB80. 6 μl was spotted onto glass slides, overlaid with a cover slip, and sealed with nail varnish. The remainder was split into two and spun for 90 min RT 21,000×*g* and the pellets fixed in 1% glutaraldehyde for 2 hr RT, followed by post-fixing with 3% glutaraldehyde, 15 min RT. Following three washes in PBS, samples were osmicated in 1% osmium tetroxide, 1 hr RT, washed in PBS (3 × 20 min), then dH_2O (2 × 20 min), and into 30% ethanol for 20 min. Samples were incubated in 0.5% uranyl acetate in 30% ethanol for 40 min. Samples were dehydrated and infused with resin and cured at 60˚C for 2 days. Sections were cut and visualized by transmission EM. The MT bundling assay by fluorescence microscopy alone was carried out more than five times. The experiment where the same samples were visualized by fluorescence microscopy and EM was performed twice using different protein preparations.

Immunopurification of the mesh complex was as described previously (**Booth et al., 2011**). Beads from this procedure were used directly for MT-bundling experiments as described above.

Light microscopy

For the mitotic progression assays, 6.8×10^4 cells/ml were seeded in 12 well plates and transfected with H2B-mCherry. GFP-TACC3 expression was induced the day after transfection. 24 hr later, the cells were imaged on a Nikon Ti epifluorescence microscope with 40× ELWD objective (0.6 NA) and a Coolsnap Myo camera (Photometrics) for 14 hr using NIS Elements AR software; H2B-mCherry was imaged once every 3 min, and GFP-TACC3 monitored once every 30 min. Cells were kept at 37˚C, in supplemented CO_2-independent medium containing doxycycline (0.5 μg/ml) for cells with GFP-TACC3 induction. Light intensity and exposure were minimized to avoid light-induced cell damage. Analysis of mitotic staging was by manual inspection of videos, with automated time look-up. The same microscope was used to assay the bundling of fluorescent MTs.

For analysis of MTs in the proximity of kinetochores, a similar method to that previously described was used (**Cheeseman et al., 2013**). Briefly, confocal imaging was performed on a spinning disc

confocal system (Ultraview Vox, Perkin Elmer) using a 100× ~1.4 NA oil immersion objective lens with a Hamamatsu C10600-10B ORCA-R2 camera. Fixed cells expressing GFP or GFP-TACC3, stained as described above, were excited at 488 nm, 561 nm, 405 nm, and 640 nm, and z-sections were taken every 0.25 μm. OME-TIFF image stacks were transferred to IMARIS (Bitplane) and subjected to spot detection in the CREST/CENP-A channel with a minimal spot size of 0.58 μm to detect kinetochores. Spots that were not properly assigned (~5%) were corrected manually. The mean pixel densities in this sphere were background subtracted, and the median intensity per cell was found using IgorPro.

Electron microscopy

HPF was performed using either EM PACT2 or EM HPM100 (Leica Microsystems). Mitotic cells were transferred to 100 μm-depth membrane carriers or Type A 100 μm-depth carriers for the EM PACT2 or EM HPM100, respectively. Once frozen, carriers were transferred in liquid nitrogen to the EM AFS2 (Leica Microsystems) FS machine, which was precooled to −90˚C. Carriers were immersed in a FS medium of 1% osmium tetroxide, 0.5% uranyl acetate, and 5% H_2O in acetone. Cells were brought to RT over 67 hr: 27 hr at −90˚C; ramp to −60˚C over 15 hr; 8 hr at −60˚C; ramp to −30˚C over 15 hr; 1 hr at −30˚C; ramp to 4˚C over 1 hr; cells were taken to the fume hood to reach RT. Cells were embedded in epoxy resin (TAAB) and polymerized at 60˚C for 48 hr. Sections (70 nm) were cut using an EM UC6 (Leica Microsystems) and post-stained using uranyl acetate and Reynold's lead citrate. Sections were imaged using the FEI Tecnai G2 Spirit BioTWIN microscope at 100 kV. Putative K-fibers were identified as bundles of more than 10 MTs in sections taken orthogonal to the spindle axis. K-fibers were imaged 1 μm away from the kinetochore, so as not to include any kinetochore-MT linkages (***Dong et al., 2007***). Each tilt series was taken using TIA software (TEM imaging and Analysis, FEI) from +50˚ to −50˚ in 1˚ steps. The IMOD etomo package was used to generate tomograms from these tilt series (***Mastronarde, 1997***). Tomogram thickness ranged from 28.8 to 66.4 nm.

Data analysis

For visualization, 3D rendering of tomograms was done in Amira 5.6.0 (Visualization Sciences Group, FEI) using a combination of manual and automated detection. Each MT was rendered individually by hand, and then any 3D density connecting the MTs was automatically detected throughout the volume of the tomogram, using the average gray value of the MTs as an initial threshold for segmentation. The space between MTs in a K-fiber is less granular than the surrounding cytoplasm, which improves mesh detection. This unbiased method superseded our initial attempts at hand-rendering the mesh and allowed for unbiased quantification and visualization of the mesh. Note that measurements are taken from the unsmoothed segmentation maps. The segmentation method detects unbroken density connected to MTs. However, after smoothing for visualization, breaks in the mesh appear. In Amira, MTs were smoothed using unconstrained smoothing, and the mesh was rendered with smooth surface (50 iterations, 0.6 lambda). Hand-rendered mesh in ***Figure 1B*** was smoothed with constrained smoothing and then smooth surface generated (20 iterations, 0.6 lambda).

In longitudinal sections, K-fibers were defined as bundles of MTs contacting both the kinetochore and the pole (***McDonald et al., 1992***; ***Booth et al., 2013***). In orthogonal sections, K-fiber bundles were defined as collections of 10 or more MTs, using an 80 nm boundary around each MT (105 nm from the MT center). This distance corresponds to the longest inter-MT bridges visualized previously by 2D EM (***Booth et al., 2011***).

For analysis of MT packing, coordinates of each MT at the midpoint of the tomogram were collected, and the area of a convex hull that enclosed the coordinates was found. The distance to the nearest neighboring MT and the number of MTs within 80 nm (105 nm from the MT center) were calculated. Heat maps were generated by Voronoi interpolation of 3D coordinate sets that comprised the x-y coordinates together with the number of MTs within 80 nm in the z dimension.

To analyze the mesh connections and MT chaining, individual connections in rendered tomograms were classified and recorded together with the chain sizes for each K-fiber. Coordinate sets were supplemented with chain membership data. This was used for an automated comparison of the number of neighboring MTs within a given search radius, comparing chained vs single MTs. The analysis was performed from 20 to 120 nm, and non-parametric Wilcoxon–Mann–Whitney two-sample rank test used to test the hypothesis that there was no difference in the number of neighboring MTs. Chain membership data were then randomized and the analysis repeated. Note that chain membership is

probabilistic and is a function of tomogram thickness and mesh density/MT interconnectivity. 'Single MTs' are those that are not detected to be attached to another but are likely to be attached to other MTs in a subsequent slab of K-fiber.

For analysis of MT trajectories, 3D coordinates for each MT at the bottom and top of the tomogram were logged in ImageJ and fed into IgorPro. Custom-written procedures ran through the following steps. First, coordinates were compiled into individual MT matrices. Second, the center of the bundle was found using farthest-point clustering, and then the distance of each MT from this point was calculated. Third, the fiber direction was 'normalized', that is, rotated through 3D space so that most MTs pointed towards the zenith. This was necessary because of the variability in the axes of different K-fibers relative to sectioning and the resultant tomograms. To do normalization, all MTs were multiplied by rotation matrices

$$R = R_z(\alpha)R_y(\beta)R_x(\gamma),$$

for (in radians) $0 \leq \alpha \leq 2\pi$, $0 \leq \beta \leq \pi/2$, $\gamma = 0$ in $180/\pi$ increments. The Cartesian distance of the orthogonal projection of each MT on the reference plane after rotation was summed, to find the rotation that produced the minimum value. The spherical coordinates, given by

$$r = \sqrt{x^2 + y^2 + z^2},$$

$$\theta = \cos^{-1}\left(\frac{z}{\sqrt{x^2 + y^2 + z^2}}\right),$$

$$\varphi = \tan^{-1}\left(\frac{y}{x}\right),$$

of the MTs set at optimal rotation, were used for plotting. Fourth, a 2D plot to visualize the degree of MT deviancy was generated. To do this, the point at which each 3D MT vector starting at the origin intersects an x-y plane that was set arbitrarily at z = 100 nm was calculated and plotted. Note that the even radial dispersal in ***Figure 6D*** and the even spread of azimuthal angles in ***Figure 6E*** show that capture of tilt series was randomized, and the data set has no bias towards a particular trajectory. Several other strategies were explored to analyze deviations in trajectory vs the fiber axis. These were: examining the variance in trajectory angles, pairwise comparison of all MTs in the bundle, and comparison to a reference MT that represented the fiber axis, using spherical rotation and rotating by an average value. These produced similar results, however, the one described here was the most robust and represents our best method for this kind of spatial statistical analysis. The computer code used in the main analysis pipeline can be found as a ***Source code 1***.

Images were cropped in Photoshop, and figures were assembled in Illustrator CS5.1. IgorPro 6.36 (Wavemetrics) was used for all analysis and plotting.

Acknowledgements

We thank Tom Honnor and Julia Brettschneider, members of the Royle lab and Anne Straube for critical discussion. We also thank Alison Beckett, Sam Williams, and Liam Cheeseman for technical help and Rob Cross for commenting on the manuscript. This work was supported by a project grant from North West Cancer Research (CR928) and by a Senior Cancer Research Fellowship from Cancer Research UK (C25425/A15182) to SJR.

Additional information

Funding

Funder	Grant reference	Author
Cancer Research UK (CRUK)	C25425/A15182	Cristina Gutiérrez-Caballero, Stephen J Royle
North West Cancer Research Fund (NWCR)	CR928	Faye M Nixon, Stephen J Royle

The funders had no role in study design, data collection and interpretation, or the decision to submit the work for publication.

Author contributions

FMN, Performed all 3D-EM analysis, tomography and rendering, Acquisition of data, Analysis and interpretation of data, Drafting or revising the article; CG-C, Performed the mitotic progression experiments, Acquisition of data, Analysis and interpretation of data; FEH, Performed the in vitro MT experiments, Acquisition of data; DGB, Made the initial observation of 'the mesh' and made cell lines that were essential for the study, Acquisition of data, Contributed unpublished essential data or reagents; IAP, Co-supervised electron microscopy work, Analysis and interpretation of data; SJR, Designed the study, wrote computer code for data analysis, assembled the figures and wrote the paper, Conception and design, Analysis and interpretation of data, Drafting or revising the article

Author ORCIDs

Stephen J Royle, http://orcid.org/0000-0001-8927-6967

Additional files

Supplementary file

• Source code 1. Custom written code in IgorPro 6.36 (Wavemetrics) was used for all analysis and plotting.

DOI: 10.7554/eLife.07635.020

References

Bakhoum SF, Genovese G, Compton DA. 2009. Deviant kinetochore microtubule dynamics underlie chromosomal instability. *Current Biology* **19**:1937–1942. doi: 10.1016/j.cub.2009.09.055.

Bastmeyer M, Fuge H. 1986. The distribution of intermicrotubular bridges in meiotic spindles of the crane fly. *Chromosoma* **94**:419–424. doi: 10.1007/BF00328643.

Booth DG, Cheeseman LP, Prior IA, Royle SJ. 2013. Studying kinetochore-fiber ultrastructure using correlative light-electron microscopy. *Methods in Cell Biology* **115**:327–342. doi: 10.1016/B978-0-12-407757-7.00020-7.

Booth DG, Hood FE, Prior IA, Royle SJ. 2011. A TACC3/ch-TOG/clathrin complex stabilises kinetochore fibres by inter-microtubule bridging. *The EMBO Journal* **30**:906–919. doi: 10.1038/emboj.2011.15.

Brangwynne CP, MacKintosh FC, Kumar S, Geisse NA, Talbot J, Mahadevan L, Parker KK, Ingber DE, Weitz DA. 2006. Microtubules can bear enhanced compressive loads in living cells because of lateral reinforcement. *The Journal of Cell Biology* **173**:733–741. doi: 10.1083/jcb.200601060.

Chang P, Jacobson MK, Mitchison TJ. 2004. Poly(ADP-ribose) is required for spindle assembly and structure. *Nature* **432**:645–649. doi: 10.1038/nature03061.

Cheeseman LP, Booth DG, Hood FE, Prior IA, Royle SJ. 2011. Aurora A kinase activity is required for localization of TACC3/ch-TOG/clathrin inter-microtubule bridges. *Communicative & Integrative Biology* **4**:409–412. doi: 10.4161/cib.4.4.15250.

Cheeseman LP, Harry EF, McAinsh AD, Prior IA, Royle SJ. 2013. Specific removal of TACC3-ch-TOG-clathrin at metaphase deregulates kinetochore fiber tension. *Journal of Cell Science* **126**:2102–2113. doi: 10.1242/jcs.124834.

Dong Y, Vanden Beldt KJ, Meng X, Khodjakov A, McEwen BF. 2007. The outer plate in vertebrate kinetochores is a flexible network with multiple microtubule interactions. *Nature Cell Biology* **9**:516–522. doi: 10.1038/ncb1576.

Fu W, Tao W, Zheng P, Fu J, Bian M, Jiang Q, Clarke PR, Zhang C. 2010. Clathrin recruits phosphorylated TACC3 to spindle poles for bipolar spindle assembly and chromosome alignment. *Journal of Cell Science* **123**:3645–3651. doi: 10.1242/jcs.075911.

Gatlin JC, Matov A, Danuser G, Mitchison TJ, Salmon ED. 2010. Directly probing the mechanical properties of the spindle and its matrix. *The Journal of Cell Biology* **188**:481–489. doi: 10.1083/jcb.200907110.

Gutiérrez-Caballero C, Burgess SG, Bayliss R, Royle SJ. 2015. TACC3-ch-TOG track the growing tips of microtubules independently of clathrin and Aurora-A phosphorylation. *Biology Open* **4**:170–179. doi: 10.1242/bio.201410843.

Hepler PK, McIntosh JR, Cleland S. 1970. Intermicrotubule bridges in mitotic spindle apparatus. *The Journal of Cell Biology* **45**:438–444. doi: 10.1083/jcb.45.2.438.

Hood FE, Williams SJ, Burgess SG, Richards MW, Roth D, Straube A, Pfuhl M, Bayliss R, Royle SJ. 2013. Coordination of adjacent domains mediates TACC3-ch-TOG-clathrin assembly and mitotic spindle binding. *The Journal of Cell Biology* **202**:463–478. doi: 10.1083/jcb.201211127.

Hubner NC, Bird AW, Cox J, Splettstoesser B, Bandilla P, Poser I, Hyman A, Mann M. 2010. Quantitative proteomics combined with BAC TransgeneOmics reveals in vivo protein interactions. *The Journal of Cell Biology* **189**:739–754. doi: 10.1083/jcb.200911091.

Johansen KM, Forer A, Yao C, Girton J, Johansen J. 2011. Do nuclear envelope and intranuclear proteins reorganize during mitosis to form an elastic, hydrogel-like spindle matrix? *Chromosome Research* **19**:345–365. doi: 10.1007/s10577-011-9187-6.

Koffa MD, Casanova CM, Santarella R, Kocher T, Wilm M, Mattaj IW. 2006. HURP is part of a Ran-dependent complex involved in spindle formation. *Current Biology* **16**:743–754. doi: 10.1016/j.cub.2006.03.056.
LeRoy PJ, Hunter JJ, Hoar KM, Burke KE, Shinde V, Ruan J, Bowman D, Galvin K, Ecsedy JA. 2007. Localization of human TACC3 to mitotic spindles is mediated by phosphorylation on Ser558 by Aurora A: a novel pharmacodynamic method for measuring Aurora A activity. *Cancer Research* **67**:5362–5370. doi: 10.1158/0008-5472.CAN-07-0122.
Lin CH, Hu CK, Shih HM. 2010. Clathrin heavy chain mediates TACC3 targeting to mitotic spindles to ensure spindle stability. *The Journal of Cell Biology* **189**:1097–1105. doi: 10.1083/jcb.200911120.
Lopez-Murcia FJ, Royle SJ, Llobet A. 2014. Presynaptic clathrin levels are a limiting factor for synaptic transmission. *The Journal of Neuroscience* **34**:8618–8629. doi: 10.1523/JNEUROSCI.5081-13.2014.
Lucic V, Rigort A, Baumeister W. 2013. Cryo-electron tomography: the challenge of doing structural biology in situ. *The Journal of Cell Biology* **202**:407–419. doi: 10.1083/jcb.201304193.
Ma L, Tsai MY, Wang S, Lu B, Chen R, Iii JR, Zhu X, Zheng Y. 2009. Requirement for Nudel and dynein for assembly of the lamin B spindle matrix. *Nature Cell Biology* **11**:247–256. doi: 10.1038/ncb1832.
Manning AL, Compton DA. 2008. Structural and regulatory roles of nonmotor spindle proteins. *Current Opinion in Cell Biology* **20**:101–106. doi: 10.1016/j.ceb.2007.11.004.
Mastronarde DN. 1997. Dual-axis tomography: an approach with alignment methods that preserve resolution. *Journal of Structural Biology* **120**:343–352. doi: 10.1006/jsbi.1997.3919.
Mastronarde DN, McDonald KL, Ding R, McIntosh JR. 1993. Interpolar spindle microtubules in PTK cells. *The Journal of Cell Biology* **123**:1475–1489. doi: 10.1083/jcb.123.6.1475.
McDonald KL, O'Toole ET, Mastronarde DN, McIntosh JR. 1992. Kinetochore microtubules in PTK cells. *The Journal of Cell Biology* **118**:369–383. doi: 10.1083/jcb.118.2.369.
McEwen BF, Heagle AB, Cassels GO, Buttle KF, Rieder CL. 1997. Kinetochore fiber maturation in PtK1 cells and its implications for the mechanisms of chromosome congression and anaphase onset. *The Journal of Cell Biology* **137**:1567–1580. doi: 10.1083/jcb.137.7.1567.
McIntosh JR, Grishchuk EL, Morphew MK, Efremov AK, Zhudenkov K, Volkov VA, Cheeseman IM, Desai A, Mastronarde DN, Ataullakhanov FI. 2008. Fibrils connect microtubule tips with kinetochores: a mechanism to couple tubulin dynamics to chromosome motion. *Cell* **135**:322–333. doi: 10.1016/j.cell.2008.08.038.
Mollinari C, Kleman JP, Jiang W, Schoehn G, Hunter T, Margolis RL. 2002. PRC1 is a microtubule binding and bundling protein essential to maintain the mitotic spindle midzone. *The Journal of Cell Biology* **157**:1175–1186. doi: 10.1083/jcb.200111052.
Mountain V, Simerly C, Howard L, Ando A, Schatten G, Compton DA. 1999. The kinesin-related protein, HSET, opposes the activity of Eg5 and cross-links microtubules in the mammalian mitotic spindle. *The Journal of Cell Biology* **147**:351–366. doi: 10.1083/jcb.147.2.351.
Nikonova AS, Astsaturov I, Serebriiskii IG, Dunbrack RL Jr, Golemis EA. 2013. Aurora A kinase (AURKA) in normal and pathological cell division. *Cellular and Molecular Life Sciences* **70**:661–687. doi: 10.1007/s00018-012-1073-7.
Pickett-Heaps J, Spurck T, Tippit D. 1984. Chromosome motion and the spindle matrix. *The Journal of Cell Biology* **99**:137s–143s. doi: 10.1083/jcb.99.1.137s.
Pickett-Heaps JD, Tippit DH, Porter KR. 1982. Rethinking mitosis. *Cell* **29**:729–744. doi: 10.1016/0092-8674(82)90435-4.
Rieder CL. 1981. The structure of the cold-stable kinetochore fiber in metaphase PtK1 cells. *Chromosoma* **84**:145–158. doi: 10.1007/BF00293368.
Royle SJ, Bright NA, Lagnado L. 2005. Clathrin is required for the function of the mitotic spindle. *Nature* **434**:1152–1157. doi: 10.1038/nature03502.
Sauer G, Korner R, Hanisch A, Ries A, Nigg EA, Sillje HH. 2005. Proteome analysis of the human mitotic spindle. *Molecular & Cellular Proteomics* **4**:35–43. doi: 10.1074/mcp.M400158-MCP200.
Schmidt S, Schneider L, Essmann F, Cirstea IC, Kuck F, Kletke A, Janicke RU, Wiek C, Hanenberg H, Ahmadian MR, Schulze-Osthoff K, Nurnberg B, Piekorz RP. 2010. The centrosomal protein TACC3 controls paclitaxel sensitivity by modulating a premature senescence program. *Oncogene* **29**:6184–6192. doi: 10.1038/onc.2010.354.
Scholey JM, Rogers GC, Sharp DJ. 2001. Mitosis, microtubules, and the matrix. *The Journal of Cell Biology* **154**:261–266. doi: 10.1083/jcb.200101097.
Schweizer N, Weiss M, Maiato H. 2014. The dynamic spindle matrix. *Current Opinion in Cell Biology* **28**:1–7. doi: 10.1016/j.ceb.2014.01.002.
Sharp DJ, McDonald KL, Brown HM, Matthies HJ, Walczak C, Vale RD, Mitchison TJ, Scholey JM. 1999. The bipolar kinesin, KLP61F, cross-links microtubules within interpolar microtubule bundles of *Drosophila* embryonic mitotic spindles. *The Journal of Cell Biology* **144**:125–138. doi: 10.1083/jcb.144.1.125.
Sikirzhytski V, Magidson V, Steinman JB, He J, Le Berre M, Tikhonenko I, Ault JG, McEwen BF, Chen JK, Sui H, Piel M, Kapoor TM, Khodjakov A. 2014. Direct kinetochore-spindle pole connections are not required for chromosome segregation. *The Journal of Cell Biology* **206**:231–243. doi: 10.1083/jcb.201401090.
Singh D, Chan JM, Zoppoli P, Niola F, Sullivan R, Castano A, Liu EM, Reichel J, Porrati P, Pellegatta S, Qiu K, Gao Z, Ceccarelli M, Riccardi R, Brat DJ, Guha A, Aldape K, Golfinos JG, Zagzag D, Mikkelsen T, Finocchiaro G, Lasorella A, Rabadan R, Iavarone A. 2012. Transforming fusions of FGFR and TACC genes in human glioblastoma. *Science* **337**:1231–1235. doi: 10.1126/science.1220834.
Spurck T, Forer A, Pickett-Heaps J. 1997. Ultraviolet microbeam irradiations of epithelial and spermatocyte spindles suggest that forces act on the kinetochore fibre and are not generated by its disassembly. *Cell Motility and the Cytoskeleton* **36**:136–148. doi: 10.1002/(SICI)1097-0169(1997)36:2<136::AID-CM4>3.0.CO;2-7.

Ward JJ, Roque H, Antony C, Nedelec F. 2014. Mechanical design principles of a mitotic spindle. *eLife* **3**:e03398. doi: 10.7554/eLife.03398.
Williams SV, Hurst CD, Knowles MA. 2013. Oncogenic FGFR3 gene fusions in bladder cancer. *Human Molecular Genetics* **22**:795–803. doi: 10.1093/hmg/dds486.
Wilson HJ. 1969. Arms and bridges on microtubules in the mitotic apparatus. *The Journal of Cell Biology* **40**: 854–859. doi: 10.1083/jcb.40.3.854.
Witt PL, Ris H, Borisy GG. 1981. Structure of kinetochore fibers: microtubule continuity and inter-microtubule bridges. *Chromosoma* **83**:523–540. doi: 10.1007/BF00328277.
Yao C, Rath U, Maiato H, Sharp D, Girton J, Johansen KM, Johansen J. 2012. A nuclear-derived proteinaceous matrix embeds the microtubule spindle apparatus during mitosis. *Molecular Biology of the Cell* **23**:3532–3541. doi: 10.1091/mbc.E12-06-0429.
Yokoyama H, Nakos K, Santarella-Mellwig R, Rybina S, Krijgsveld J, Koffa MD, Mattaj IW. 2013. CHD4 is a RanGTP-dependent MAP that stabilizes microtubules and regulates bipolar spindle formation. *Current Biology* **23**: 2443–2451. doi: 10.1016/j.cub.2013.09.062.

Figure 1: ***Figure Supplement 1***

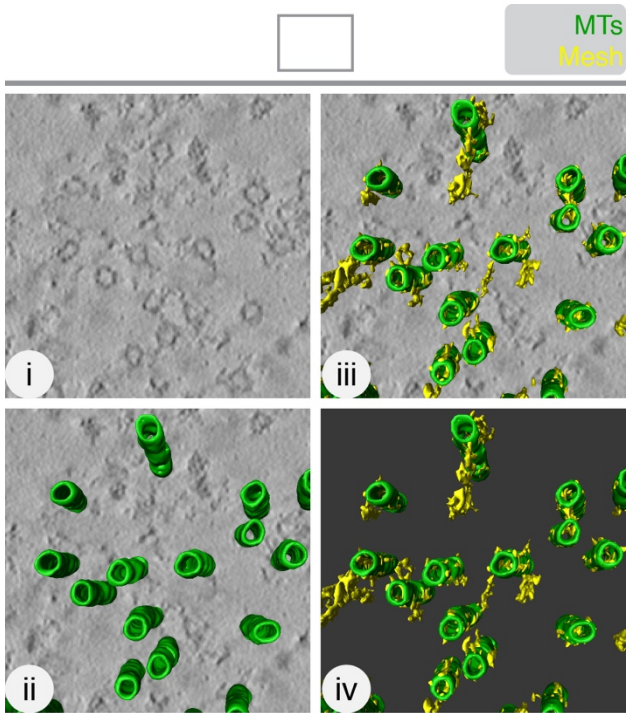

The mesh is visible, but not well preserved, in chemically-fixed K-fibers.

Orthoslice of a tomogram generated from a tilt series of a single section through a K-fiber fixed with glutaraldehyde (**i**). Overlaid is a hand-rendered 3D representation of MTs (green) (**ii**) and mesh segmented by automated detection (yellow) (**iii**). The model is shown alone (**iv**). Tomogram thickness, 51.3 nm. For scale, MTs are 25 nm in diameter.

Figure 1: ***Figure Supplement 2***

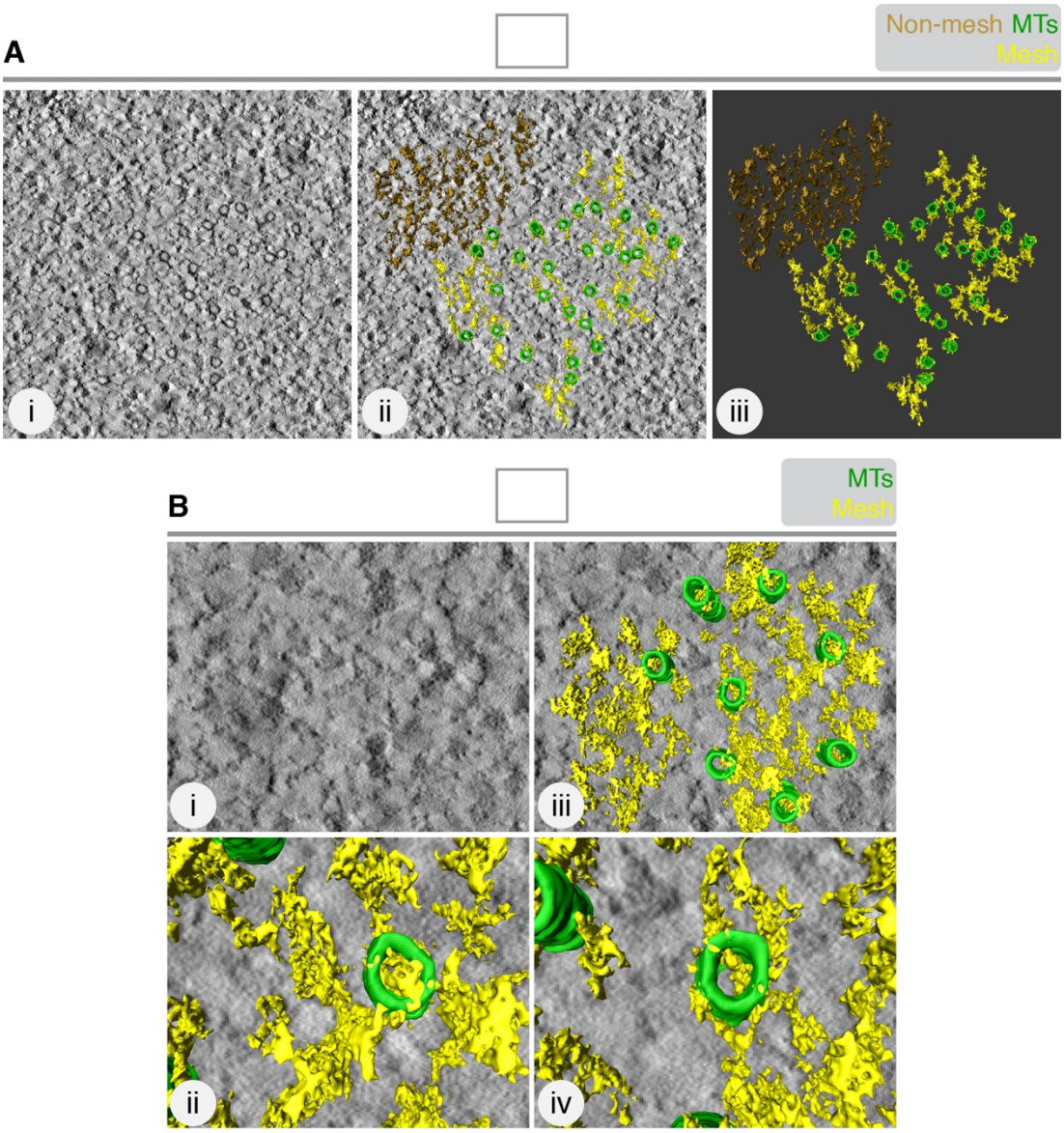

The mesh is associated with K-fiber MTs.

A: 3D rendering of 'non-mesh' (brown) in a tomogram of a single K-fiber. Single orthoslice (**i**), with added rendering (MTs, green; mesh, yellow) (**ii**) and model alone (iii), is shown. Rendering the mesh involves segmenting density that is attached to the MTs. Here, density to the upper right of the K-fiber was rendered, although it was not touching MTs. The result is a particulate 3D structure that is dissimilar to the K-fiber mesh. **B**: Translation of MT map from the tomogram in **A**, to the upper right corner. Mesh detection was performed as described in 'Materials and methods'. Single orthoslice view (**i**), with added rendering (MTs, green; mesh, yellow) (**ii**). Zoomed views of two MTs and associated 'pseudo-mesh' are shown in (**iii** and **iv**). Note that the mesh passes through the MTs and is more particulate than the K-fiber mesh. Tomogram thickness, 35.2 nm.

Figure 3: ***Figure Supplement 1***

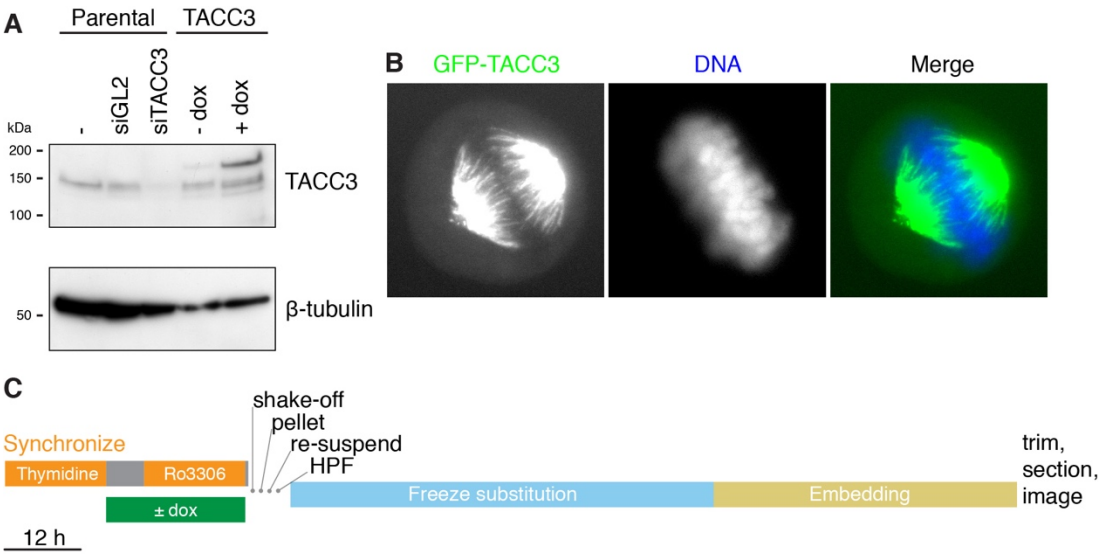

Inducible expression of GFP-TACC3 in HeLa cells to alter the composition of mesh.

A: Western blot to show the extent of overexpression of TACC3 caused by inducing the expression of GFP-TACC3 in a stable TetOn HeLa cell line using 0.5 µg/ml doxycycline for 24 hr. The blot was probed for TACC3 and tubulin (as a loading control). **B:** Widefield fluorescence micrographs of cells inducibly expressing GFP-TACC3. Note the strong fluorescence on K-fibers of the mitotic spindle. **C:** Workflow to show the preparation of metaphase cells for analysis by 3D EM. Cells were synchronized and GFP-TACC3 expression was induced before release from RO3306 for 30–40 min. Mitotic cells were shaken off, pelleted, resuspended, and frozen under high pressure. Following freeze substitution and embedding, cells were trimmed and sectioned before imaging by electron microscopy. For details, see ‘Materials and methods’.

Figure 4: ***Figure Supplement 1***

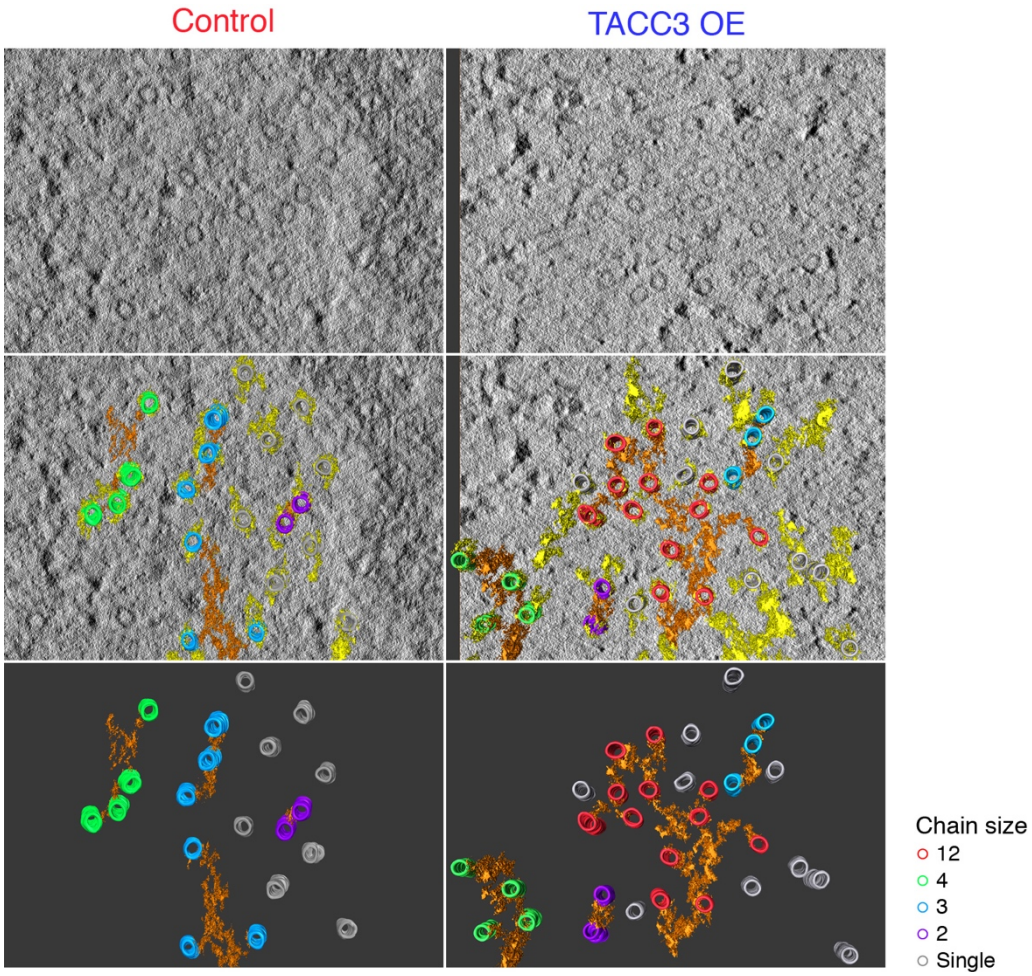

Examples of MTs chains and associated mesh.

Two example tomograms, which were annotated by 3D rendering and used to make the 2D maps illustrating MT position and chain membership in Figure 4C. MTs are colored as in Figure 4C, mesh associated with chained MTs is orange, other mesh is shown in yellow. Single orthoslice from the tomogram with rendered material is shown above, the MTs and mesh associated with chained MTs is shown below. Note that single (unchained) MTs are attached to the mesh, but that the MT/MTs to which they are attached are outside of the section. Tomogram thickness, 43.6 nm (Control), 28.8 nm (TACC3 OE). For scale, MTs are 25 nm in diameter.

Figure 5: ***Figure Supplement 1***

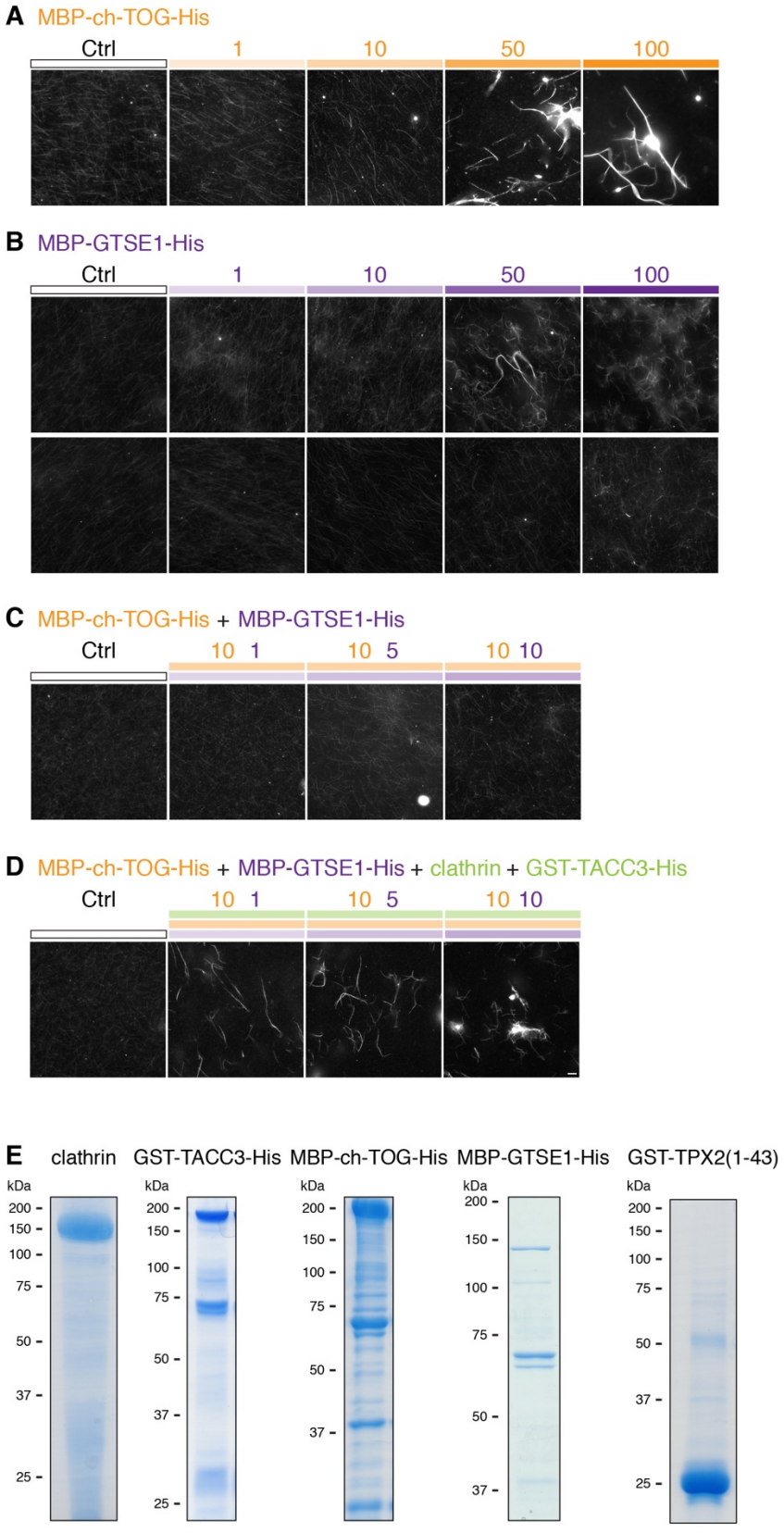

MT bundling using purified components.

Representative fluorescence micrographs of rhodamine-labeled MTs incubated with the indicated proteins. In all experiments, control was 210 nM MBP-His_6 and 100 nM GST, and the total amount of protein was supplemented with MBP-His_6 and GST to reach equimolarity. All samples were phosphorylated with Aurora A kinase and GST-TPX2(1–43). **A:** MT bundling induced by higher concentrations of MBP-ch-TOG-His6, a range of 1–100 nM is shown. **B:** Variability in MT bundling induced by higher concentrations of MBP-GTSE1-His_6, a range of 1–100 nM is shown for two experiments. In one experiment, bundling is seen at 50 nM, and in another, no bundling is seen for concentrations up to 100 nM. **C:** Combination of 10 nM MBP-ch-TOG-His6 with 1, 5, or 10 nM MBP-GTSE1 does not induce bundling. **D:** Significant bundling observed with clathrin (100 nM), GST-TACC3-His6 (100 nM), MBP-ch-TOG (10 nM), and either 1, 5, or 10 nM MBP-GTSE1-His6. **C** and **D** were performed in parallel. Scale bar, 10 µm. **E:** Coomassie blue-stained gels of purified protein components separated by SDS-PAGE. Molecular weights are indicated to the left.

Figure 5: ***Figure Supplement 2***

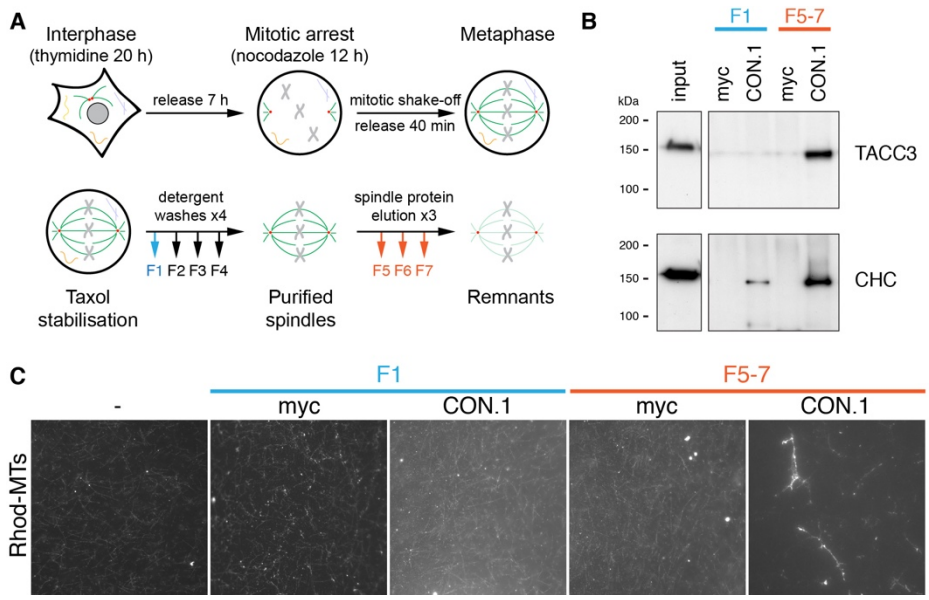

MT bundling using mesh complex immunoisolated from mitotic HeLa cells.

A: Schematic diagram of the procedure to release mitotic spindle proteins from mitotic spindles at metaphase (described in Booth et al., 2011). **B:** Western blot to show specific co-immunoprecipitation of TACC3/clathrin from spindle fractions (F5-7) but not from mitotic cytosol (F1) using an anti-clathrin light chain (CON.1). No immunoprecipitation of clathrin or TACC3 was seen with a control antibody (anti-myc). Western blots were probed with anti-TACC3 (rabbit polyclonal) or anti-clathrin heavy chain (CHC, TD.1). **C:** Representative fluorescence micrographs of rhodamine-labeled MTs incubated with beads from the immunoprecipitation shown in **B**. Significant bundling was seen for clathrin IPs from F5-7 only. No bundling activity was seen with control IPs or clathrin IPs from F1. Beads are out of frame for clarity. Scale bar, 10 μm.

Figure 7: ***Figure Supplement 1***

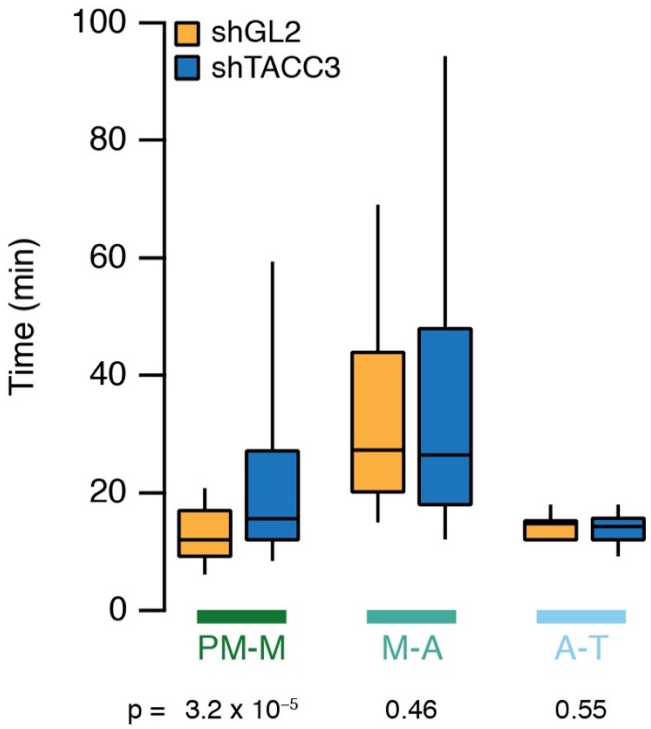

Mitotic consequences of TACC3 depletion.

Box plots to summarize mitotic progression experiments. Time taken to go from prometaphase-to-metaphase (PM-M), metaphase-to-anaphase (M-A), or anaphase-to-telophase (A-T) is shown for control (orange) or TACC3-depleted (blue) HeLa cells using shRNA-mediated knockdown. Whiskers show 90th and 10th percentiles. N_{cell} = 122–138, N_{exp} = 2.

7.2: The TACC3 mesh complex does not persist in a "spindle matrix" after depolymerisation of MTs

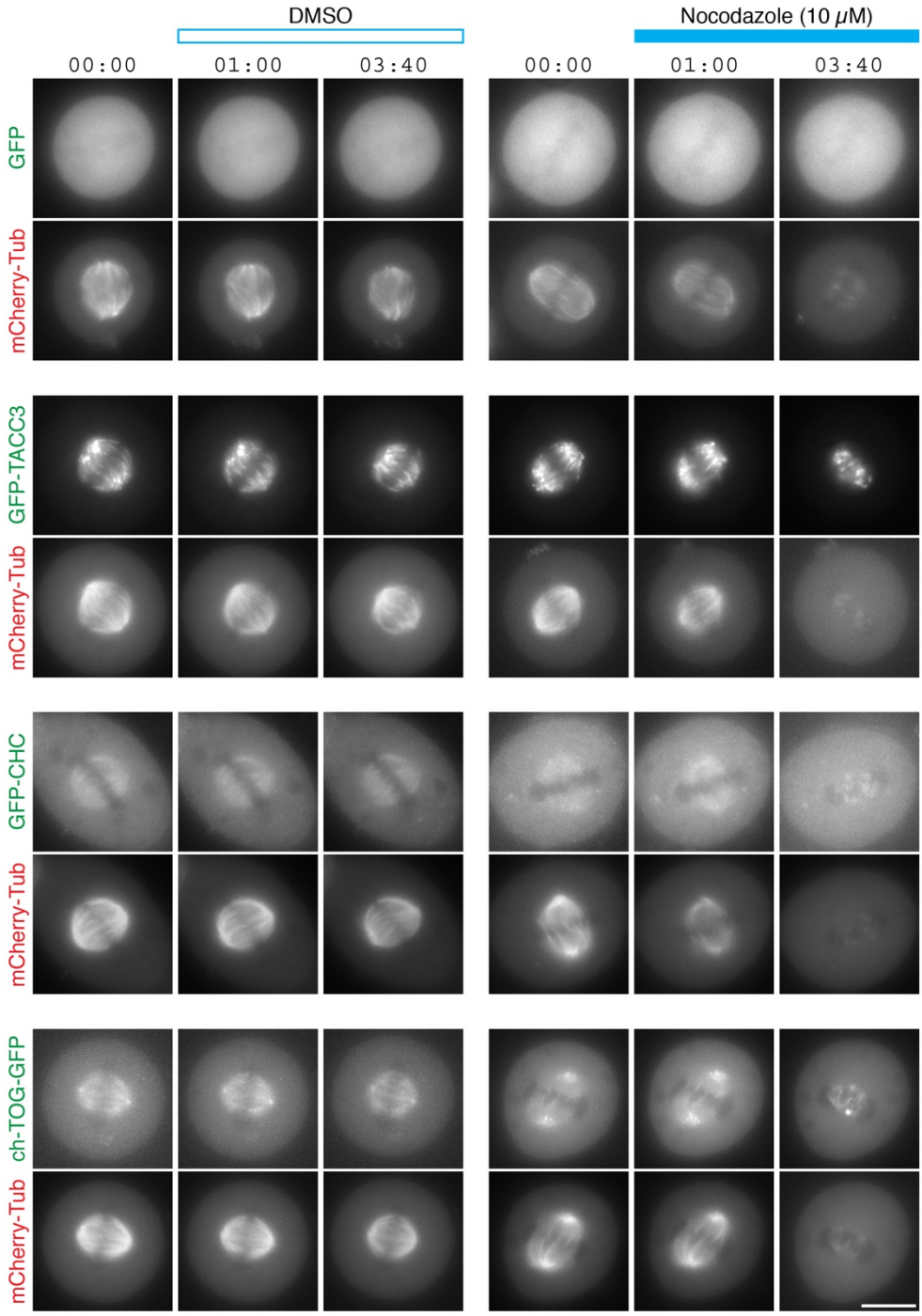

Still images from live-cell imaging experiments to visualise metaphase HeLa cells expressing mCherry-tubulin and the indicated GFP-tagged protein. Cells were exposed to DMSO (control, left) or nocodazole (10 μM, right) after 1 min. MT depolymerisation, monitored by mCherry-tubulin, caused mislocalisation of clathrin and chTOG. GFP-TACC3 forms aggregates in the absence of MTs.

8. Bibliography

Aist, J.R., and Bayles, C.J. (1991). Organelle motility within mitotic asters of the fungus Nectria haematococca. Eur. J. Cell Biol. 56, 358–363.

Amos, L., and Klug, A. (1974). Arrangement of subunits in flagellar microtubules. J. Cell Sci. 14, 523–549.

Albertson, D.G., and Thomson, J.N. (1993). Segregation of holocentric chromosomes at meiosis in the nematode, Caenorhabditis elegans. Chromosome Res. Int. J. Mol. Supramol. Evol. Asp. Chromosome Biol. 1, 15–26.

Argani, P., Lui, M.Y., Couturier, J., Bouvier, R., Fournet, J.-C., and Ladanyi, M. (2003). A novel CLTC-TFE3 gene fusion in pediatric renal adenocarcinoma with t(X;17)(p11.2;q23). Oncogene 22, 5374–5378.

Bakhoum, S.F., Genovese, G., and Compton, D.A. (2009). Deviant kinetochore microtubule dynamics underlie chromosomal instability. Curr. Biol. CB 19, 1937–1942.

Balchand, S.K., Mann, B.J., Titus, J., Ross, J.L., and Wadsworth, P. (2015). TPX2 Inhibits Eg5 by Interactions with Both Motor and Microtubule. J. Biol. Chem. 290, 17367–17379.

Bamburg, J.R., Bray, D., and Chapman, K. (1986). Assembly of microtubules at the tip of growing axons. Nature 321, 788–790.

Barr, F.A., and Gruneberg, U. (2007). Cytokinesis: placing and making the final cut. Cell 131, 847–860.

Bastmeyer, M., and Fuge, H. (1986). The distribution of intermicrotubular bridges in meiotic spindles of the crane fly. Chromosoma 94, 419–424.

Bayliss, R., Sardon, T., Vernos, I., and Conti, E. (2003). Structural basis of Aurora-A activation by TPX2 at the mitotic spindle. Mol. Cell 12, 851–862.

Bellanger, J.M., and Gönczy, P. (2003). TAC-1 and ZYG-9 form a complex that promotes microtubule assembly in C. elegans embryos. Curr. Biol. CB 13, 1488–1498.

Bhisey, A.N., and Freed, J.J. (1971). Cross-bridges on the microtubules of cooled interphase HeLa cells. J. Cell Biol. 50, 557–561.

Bieling, P., Telley, I.A., and Surrey, T. (2010). A minimal midzone protein module controls formation and length of antiparallel microtubule overlaps. Cell 142, 420–432.

Biggins, S., Severin, F.F., Bhalla, N., Sassoon, I., Hyman, A.A., and Murray, A.W. (1999). The conserved protein kinase Ipl1 regulates microtubule binding to kinetochores in budding yeast. Genes Dev. 13, 532–544.

Birky, C.W. (1983). The partitioning of cytoplasmic organelles at cell division. Int. Rev. Cytol. Suppl. 15, 49–89.

Blixt, M.K.E., and Royle, S.J. (2011). Clathrin heavy chain gene fusions expressed in human cancers: analysis of cellular functions. Traffic Cph. Den. 12, 754–761.

Bobinnec, Y., Khodjakov, A., Mir, L.M., Rieder, C.L., Eddé, B., and Bornens, M. (1998). Centriole disassembly in vivo and its effect on centrosome structure and function in vertebrate cells. J. Cell Biol. 143, 1575–1589.

Booth, D.G. (2011). An ultrastructural study of the role of clathrin as an inter-microtubule bridge in kinetochore fibres. Ph. D Thesis. University of Liverpool.

Booth, D.G., Hood, F.E., Prior, I.A., and Royle, S.J. (2011). A TACC3/ch-TOG/clathrin complex stabilises kinetochore fibres by inter-microtubule bridging. EMBO J. 30, 906–919.

Booth, D.G., Cheeseman, L.P., Prior, I.A., and Royle, S.J. (2013). Studying kinetochore-fiber ultrastructure using correlative light-electron microscopy. Methods Cell Biol. 115, 327–342.

Bornens, M. (2002). Centrosome composition and microtubule anchoring mechanisms. Curr. Opin. Cell Biol. 14, 25–34.

Boveri, T. (1914). Zur Frage der Entstehung maligner Tumoren (G. Fischer).

Braun, M., Lansky, Z., Fink, G., Ruhnow, F., Diez, S., and Janson, M.E. (2011). Adaptive braking by Ase1 prevents overlapping microtubules from sliding completely apart. Nat. Cell Biol. 13, 1259–1264.

Bringmann, H., and Hyman, A.A. (2005). A cytokinesis furrow is positioned by two consecutive signals. Nature 436, 731–734.

Brinkley, B.R., and Cartwright, J. (1971). Ultrastructural analysis of mitotic spindle elongation in mammalian cells in vitro. Direct microtubule counts. J. Cell Biol. 50, 416–431.

Brinkley, B.R., Valdivia, M.M., Tousson, A., and Brenner, S.L. (1984). Compound kinetochores of the Indian muntjac. Evolution by linear fusion of unit kinetochores. Chromosoma 91, 1–11.

Brittle, A.L., and Ohkura, H. (2005). Mini spindles, the XMAP215 homologue, suppresses pausing of interphase microtubules in Drosophila. EMBO J. 24, 1387–1396.

Brodsky, F.M., Hill, B.L., Acton, S.L., Näthke, I., Wong, D.H., Ponnambalam, S., and Parham, P. (1991). Clathrin light chains: arrays of protein motifs that regulate coated-vesicle dynamics. Trends Biochem. Sci. 16, 208–213.

Brust-Mascher, I., and Scholey, J.M. (2011). Mitotic motors and chromosome segregation: the mechanism of anaphase B. Biochem. Soc. Trans. 39, 1149–1153.

Brust-Mascher, I., Civelekoglu-Scholey, G., Kwon, M., Mogilner, A., and Scholey, J.M. (2004). Model for anaphase B: role of three mitotic motors in a switch from poleward flux to spindle elongation. Proc. Natl. Acad. Sci. U. S. A. 101, 15938–15943.

Burbank, K.S., Mitchison, T.J., and Fisher, D.S. (2007). Slide-and-cluster models for spindle assembly. Curr. Biol. CB 17, 1373–1383.

Cai, S., Weaver, L.N., Ems-McClung, S.C., and Walczak, C.E. (2009). Kinesin-14 family proteins HSET/XCTK2 control spindle length by cross-linking and sliding microtubules. Mol. Biol. Cell 20, 1348–1359.

Cao, L.G., and Wang, Y.L. (1990). Mechanism of the formation of contractile ring in dividing cultured animal cells. II. Cortical movement of microinjected actin filaments. J. Cell Biol. 111, 1905–1911.

Carlton, J.G., Agromayor, M., and Martin-Serrano, J. (2008). Differential requirements for Alix and ESCRT-III in cytokinesis and HIV-1 release. Proc. Natl. Acad. Sci. U. S. A. 105, 10541–10546.

Chan, J., Jensen, C.G., Jensen, L.C., Bush, M., and Lloyd, C.W. (1999). The 65-kDa carrot microtubule-associated protein forms regularly arranged filamentous cross-bridges between microtubules. Proc. Natl. Acad. Sci. U. S. A. 96, 14931–14936.

Chan, Y.W., Jeyaprakash, A.A., Nigg, E.A., and Santamaria, A. (2012). Aurora B controls kinetochore-microtubule attachments by inhibiting Ska complex-KMN network interaction. J. Cell Biol. 196, 563–571.

Chang, P., Jacobson, M.K., and Mitchison, T.J. (2004). Poly(ADP-ribose) is required for spindle assembly and structure. Nature 432, 645–649.

Charrasse, S., Mazel, M., Taviaux, S., Berta, P., Chow, T., and Larroque, C. (1995). Characterization of the cDNA and pattern of expression of a new gene over-expressed in human hepatomas and colonic tumors. Eur. J. Biochem. FEBS 234, 406–413.

Charrasse, S., Schroeder, M., Gauthier-Rouviere, C., Ango, F., Cassimeris, L., Gard, D.L., and Larroque, C. (1998). The TOGp protein is a new human microtubule-associated protein homologous to the Xenopus XMAP215. J. Cell Sci. 111 (Pt 10), 1371–1383.

Cheeseman, I.M., and Desai, A. (2008). Molecular architecture of the kinetochore-microtubule interface. Nat. Rev. Mol. Cell Biol. 9, 33–46.

Cheeseman, I.M., Brew, C., Wolyniak, M., Desai, A., Anderson, S., Muster, N., Yates, J.R., Huffaker, T.C., Drubin, D.G., and Barnes, G. (2001). Implication of a novel multiprotein Dam1p complex in outer kinetochore function. J. Cell Biol. 155, 1137–1145.

Cheeseman, I.M., Anderson, S., Jwa, M., Green, E.M., Kang, J. seog, Yates, J.R., Chan, C.S.M., Drubin, D.G., and Barnes, G. (2002). Phospho-regulation of kinetochore-microtubule attachments by the Aurora kinase Ipl1p. Cell 111, 163–172.

Cheeseman, I.M., Chappie, J.S., Wilson-Kubalek, E.M., and Desai, A. (2006). The conserved KMN network constitutes the core microtubule-binding site of the kinetochore. Cell 127, 983–997.

Cheeseman, L.P., Booth, D.G., Hood, F.E., Prior, I.A., and Royle, S.J. (2011). Aurora A kinase activity is required for localization of TACC3/ch-TOG/clathrin inter-microtubule bridges. Commun. Integr. Biol. 4, 409–412.

Cheeseman, L.P., Harry, E.F., McAinsh, A.D., Prior, I.A., and Royle, S.J. (2013). Specific removal of TACC3-ch-TOG-clathrin at metaphase deregulates kinetochore fiber tension. J. Cell Sci. 126, 2102–2113.

Chen, W., and Zhang, D. (2004). Kinetochore fibre dynamics outside the context of the spindle during anaphase. Nat. Cell Biol. 6, 227–231.

Chen, Z., Hafidh, S., Poh, S.H., Twell, D., and Berger, F. (2009). Proliferation and cell fate establishment during Arabidopsis male gametogenesis depends on the Retinoblastoma protein. Proc. Natl. Acad. Sci. U. S. A. 106, 7257–7262.

Cherry, L.M., and Johnston, D.A. (1987). Size variation in kinetochores of human chromosomes. Hum. Genet. 75, 155–158.

Chikatsu, N., Kojima, H., Suzukawa, K., Shinagawa, A., Nagasawa, T., Ozawa, H., Yamashita, Y., and Mori, N. (2003). ALK+, CD30-, CD20- large B-cell lymphoma containing anaplastic lymphoma kinase (ALK) fused to clathrin heavy chain gene (CLTC). Mod. Pathol. Off. J. U. S. Can. Acad. Pathol. Inc 16, 828–832.

Church, K., and Lin, H.P. (1982). Meiosis in Drosophila melanogaster. II. The prometaphase-I kinetochore microtubule bundle and kinetochore orientation in males. J. Cell Biol. 93, 365–373.

Ciemerych, M.A., and Sicinski, P. (2005). Cell cycle in mouse development. Oncogene 24, 2877–2898.

Clarke, P.R., and Zhang, C. (2004). Spatial and temporal control of nuclear envelope assembly by Ran GTPase. Symp. Soc. Exp. Biol. 193–204.

Cleveland, D.W., Mao, Y., and Sullivan, K.F. (2003). Centromeres and kinetochores: from epigenetics to mitotic checkpoint signaling. Cell 112, 407–421.

Compton, D.A. (2002). Chromosome segregation: pulling from the poles. Curr. Biol. CB 12, R651–R653.

Cools, J., Wlodarska, I., Somers, R., Mentens, N., Pedeutour, F., Maes, B., De Wolf-Peeters, C., Pauwels, P., Hagemeijer, A., and Marynen, P. (2002). Identification of novel fusion partners of ALK, the anaplastic lymphoma kinase, in anaplastic large-cell lymphoma and inflammatory myofibroblastic tumor. Genes. Chromosomes Cancer 34, 354–362.

Dechant, R., and Glotzer, M. (2003). Centrosome separation and central spindle assembly act in redundant pathways that regulate microtubule density and trigger cleavage furrow formation. Dev. Cell 4, 333–344.

DeLuca, J.G., Gall, W.E., Ciferri, C., Cimini, D., Musacchio, A., and Salmon, E.D. (2006). Kinetochore microtubule dynamics and attachment stability are regulated by Hec1. Cell 127, 969–982.

Desai, A., and Mitchison, T.J. (1997). Microtubule polymerization dynamics. Annu. Rev. Cell Dev. Biol. 13, 83–117.

Dhonukshe, P., Vischer, N., and Gadella, T.W.J. (2006). Contribution of microtubule growth polarity and flux to spindle assembly and functioning in plant cells. J. Cell Sci. 119, 3193–3205.

Ding, R., McDonald, K.L., and McIntosh, J.R. (1993). Three-dimensional reconstruction and analysis of mitotic spindles from the yeast, Schizosaccharomyces pombe. J. Cell Biol. 120, 141–151.

Ding, Y., Yao, C., Lince-Faria, M., Rath, U., Cai, W., Maiato, H., Girton, J., Johansen, K.M., and Johansen, J. (2009). Chromator is required for proper microtubule spindle formation and mitosis in Drosophila. Dev. Biol. 334, 253–263.

Dong, Y., Vanden Beldt, K.J., Meng, X., Khodjakov, A., and McEwen, B.F. (2007). The outer plate in vertebrate kinetochores is a flexible network with multiple microtubule interactions. Nat. Cell Biol. 9, 516–522.

Duncan, C.G., Killela, P.J., Payne, C.A., Lampson, B., Chen, W.C., Liu, J., Solomon, D., Waldman, T., Towers, A.J., Gregory, S.G., et al. (2010). Integrated genomic analyses identify ERRFI1 and TACC3 as glioblastoma-targeted genes. Oncotarget 1, 265–277.

Dunsch, A.K., Linnane, E., Barr, F.A., and Gruneberg, U. (2011). The astrin-kinastrin/SKAP complex localizes to microtubule plus ends and facilitates chromosome alignment. J. Cell Biol. 192, 959–968.

Earnshaw, W.C., and Rothfield, N. (1985). Identification of a family of human centromere proteins using autoimmune sera from patients with scleroderma. Chromosoma 91, 313–321.

Elia, N., Sougrat, R., Spurlin, T.A., Hurley, J.H., and Lippincott-Schwartz, J. (2011). Dynamics of endosomal sorting complex required for transport (ESCRT) machinery during cytokinesis and its role in abscission. Proc. Natl. Acad. Sci. U. S. A. 108, 4846–4851.

Elting, M.W., Hueschen, C.L., Udy, D.B., and Dumont, S. (2014). Force on spindle microtubule minus ends moves chromosomes. J. Cell Biol. 206, 245–256.

Endow, S.A., and Komma, D.J. (1996). Centrosome and spindle function of the Drosophila Ncd microtubule motor visualized in live embryos using Ncd-GFP fusion proteins. J. Cell Sci. 109 (Pt 10), 2429–2442.

Evans, L., Mitchison, T., and Kirschner, M. (1985). Influence of the centrosome on the structure of nucleated microtubules. J. Cell Biol. 100, 1185–1191.

Evans, T., Rosenthal, E.T., Youngblom, J., Distel, D., and Hunt, T. (1983). Cyclin: a protein specified by maternal mRNA in sea urchin eggs that is destroyed at each cleavage division. Cell 33, 389–396.

Eyers, P.A., and Maller, J.L. (2004). Regulation of Xenopus Aurora A activation by TPX2. J. Biol. Chem. 279, 9008–9015.

Flemming, W. (1882). Zellsubstanz, Kern und Zelltheilung. (Leipzig: Vogel).

Fotin, A., Cheng, Y., Sliz, P., Grigorieff, N., Harrison, S.C., Kirchhausen, T., and Walz, T. (2004). Molecular model for a complete clathrin lattice from electron cryomicroscopy. Nature 432, 573–579.

Fu, J., Hagan, I.M., and Glover, D.M. (2015). The centrosome and its duplication cycle. Cold Spring Harb. Perspect. Biol. 7, a015800.

Fu, W., Tao, W., Zheng, P., Fu, J., Bian, M., Jiang, Q., Clarke, P.R., and Zhang, C. (2010). Clathrin recruits phosphorylated TACC3 to spindle poles for bipolar spindle assembly and chromosome alignment. J. Cell Sci. 123, 3645–3651.

Gaillard, J., Neumann, E., Van Damme, D., Stoppin-Mellet, V., Ebel, C., Barbier, E., Geelen, D., and Vantard, M. (2008). Two microtubule-associated proteins of Arabidopsis MAP65s promote antiparallel microtubule bundling. Mol. Biol. Cell 19, 4534–4544.

Ganem, N.J., and Compton, D.A. (2006). Functional roles of poleward microtubule flux during mitosis. Cell Cycle Georget. Tex 5, 481–485.

Gangisetty, O., Lauffart, B., Sondarva, G.V., Chelsea, D.M., and Still, I.H. (2004). The transforming acidic coiled coil proteins interact with nuclear histone acetyltransferases. Oncogene 23, 2559–2563.

Garcia, M.A., Vardy, L., Koonrugsa, N., and Toda, T. (2001). Fission yeast ch-TOG/XMAP215 homologue Alp14 connects mitotic spindles with the kinetochore and is a component of the Mad2-dependent spindle checkpoint. EMBO J. 20, 3389–3401.

Gard, D.L., and Kirschner, M.W. (1987). A microtubule-associated protein from Xenopus eggs that specifically promotes assembly at the plus-end. J. Cell Biol. 105, 2203–2215.

Garrett, S., Auer, K., Compton, D.A., and Kapoor, T.M. (2002). hTPX2 is required for normal spindle morphology and centrosome integrity during vertebrate cell division. Curr. Biol. CB 12, 2055–2059.

Garriga-Canut, M., and Orkin, S.H. (2004). Transforming acidic coiled-coil protein 3 (TACC3) controls friend of GATA-1 (FOG-1) subcellular localization and regulates

the association between GATA-1 and FOG-1 during hematopoiesis. J. Biol. Chem. 279, 23597–23605.

Gascoigne, K.E., and Cheeseman, I.M. (2013). CDK-dependent phosphorylation and nuclear exclusion coordinately control kinetochore assembly state. J. Cell Biol. 201, 23–32.

Gascoyne, R.D., Lamant, L., Martin-Subero, J.I., Lestou, V.S., Harris, N.L., Müller-Hermelink, H.-K., Seymour, J.F., Campbell, L.J., Horsman, D.E., Auvigne, I., et al. (2003). ALK-positive diffuse large B-cell lymphoma is associated with Clathrin-ALK rearrangements: report of 6 cases. Blood 102, 2568–2573.

Gelfand, V.I., and Bershadsky, A.D. (1991). Microtubule dynamics: mechanism, regulation, and function. Annu. Rev. Cell Biol. 7, 93–116.

Gergely, F., Karlsson, C., Still, I., Cowell, J., Kilmartin, J., and Raff, J.W. (2000a). The TACC domain identifies a family of centrosomal proteins that can interact with microtubules. Proc. Natl. Acad. Sci. U. S. A. 97, 14352–14357.

Gergely, F., Kidd, D., Jeffers, K., Wakefield, J.G., and Raff, J.W. (2000b). D-TACC: a novel centrosomal protein required for normal spindle function in the early Drosophila embryo. EMBO J. 19, 241–252.

Gergely, F., Draviam, V.M., and Raff, J.W. (2003). The ch-TOG/XMAP215 protein is essential for spindle pole organization in human somatic cells. Genes Dev. 17, 336–341.

Gesk, S., Gascoyne, R.D., Schnitzer, B., Bakshi, N., Janssen, D., Klapper, W., Martín-Subero, J.I., Parwaresch, R., and Siebert, R. (2005). ALK-positive diffuse large B-cell lymphoma with ALK-Clathrin fusion belongs to the spectrum of pediatric lymphomas. Leukemia 19, 1839–1840.

Gillies, A.R., Bushong, E.A., Deerinck, T.J., Ellisman, M.H., and Lieber, R.L. (2014). Three-dimensional reconstruction of skeletal muscle extracellular matrix ultrastructure. Microsc. Microanal. Off. J. Microsc. Soc. Am. Microbeam Anal. Soc. Microsc. Soc. Can. 20, 1835–1840.

Godinho, S.A., and Pellman, D. (2014). Causes and consequences of centrosome abnormalities in cancer. Philos. Trans. R. Soc. Lond. B. Biol. Sci. 369.

Goldstein, J.L., Brown, M.S., Anderson, R.G., Russell, D.W., and Schneider, W.J. (1985). Receptor-mediated endocytosis: concepts emerging from the LDL receptor system. Annu. Rev. Cell Biol. 1, 1–39.

Gómez-Baldó, L., Schmidt, S., Maxwell, C.A., Bonifaci, N., Gabaldón, T., Vidalain, P.-O., Senapedis, W., Kletke, A., Rosing, M., Barnekow, A., et al. (2010). TACC3-TSC2 maintains nuclear envelope structure and controls cell division. Cell Cycle Georget. Tex 9, 1143–1155.

Goodman, B., and Zheng, Y. (2006). Mitotic spindle morphogenesis: Ran on the microtubule cytoskeleton and beyond. Biochem. Soc. Trans. 34, 716–721.

Gorbsky, G.J., Sammak, P.J., and Borisy, G.G. (1987). Chromosomes move poleward in anaphase along stationary microtubules that coordinately disassemble from their kinetochore ends. J. Cell Biol. 104, 9–18.

Gorbsky, G.J., Sammak, P.J., and Borisy, G.G. (1988). Microtubule dynamics and chromosome motion visualized in living anaphase cells. J. Cell Biol. 106, 1185–1192.

Goshima, G., Nédélec, F., and Vale, R.D. (2005). Mechanisms for focusing mitotic spindle poles by minus end-directed motor proteins. J. Cell Biol. 171, 229–240.

Goshima, G., Wollman, R., Goodwin, S.S., Zhang, N., Scholey, J.M., Vale, R.D., and Stuurman, N. (2007). Genes required for mitotic spindle assembly in Drosophila S2 cells. Science 316, 417–421.

Goshima, G., Mayer, M., Zhang, N., Stuurman, N., and Vale, R.D. (2008). Augmin: a protein complex required for centrosome-independent microtubule generation within the spindle. J. Cell Biol. 181, 421–429.

Gould, R.R., and Borisy, G.G. (1977). The pericentriolar material in Chinese hamster ovary cells nucleates microtubule formation. J. Cell Biol. 73, 601–615.

Grishchuk, E.L., Molodtsov, M.I., Ataullakhanov, F.I., and McIntosh, J.R. (2005). Force production by disassembling microtubules. Nature 438, 384–388.
de Grouchy, J. (1970). [21 p-maternal in duplicate in a case of trisomy 21]. Ann. Génétique 13, 52–55.

Gruber, J., Harborth, J., Schnabel, J., Weber, K., and Hatzfeld, M. (2002). The mitotic-spindle-associated protein astrin is essential for progression through mitosis. J. Cell Sci. 115, 4053–4059.

Gruss, O.J., Wittmann, M., Yokoyama, H., Pepperkok, R., Kufer, T., Silljé, H., Karsenti, E., Mattaj, I.W., and Vernos, I. (2002). Chromosome-induced microtubule assembly mediated by TPX2 is required for spindle formation in HeLa cells. Nat. Cell Biol. 4, 871–879.

Guizetti, J., Schermelleh, L., Mäntler, J., Maar, S., Poser, I., Leonhardt, H., Müller-Reichert, T., and Gerlich, D.W. (2011). Cortical constriction during abscission involves helices of ESCRT-III-dependent filaments. Science 331, 1616–1620.

Gutiérrez-Caballero, C., Burgess, S.G., Bayliss, R., and Royle, S.J. (2015). TACC3-ch-TOG track the growing tips of microtubules independently of clathrin and Aurora-A phosphorylation. Biol. Open 4, 170–179.

Ha, G.-H., Kim, J.-L., Breuer, E.-K., and Breuer, E.-K.Y. (2013). TACC3 is essential for EGF-mediated EMT in cervical cancer. PloS One 8, e70353.

Hansemann, D. (1890). Ueber asymmetrische Zelltheilung in Epithelkrebsen und deren biologische Bedeutung. Arch. Für Pathol. Anat. Physiol. Für Klin. Med. 119, 299–326.

Harper, J.W., Burton, J.L., and Solomon, M.J. (2002). The anaphase-promoting complex: it's not just for mitosis any more. Genes Dev. 16, 2179–2206.

Hayward, D., Metz, J., Pellacani, C., and Wakefield, J.G. (2014). Synergy between multiple microtubule-generating pathways confers robustness to centrosome-driven mitotic spindle formation. Dev. Cell 28, 81–93.

Hepler, P.K., McIntosh, J.R., and Cleland, S. (1970). Intermicrotubule bridges in mitotic spindle apparatus. J. Cell Biol. 45, 438–444.

Hogan, C.J., and Cande, W.Z. (1990). Antiparallel microtubule interactions: spindle formation and anaphase B. Cell Motil. Cytoskeleton 16, 99–103.

Holcomb, P.S., Hoffpauir, B.K., Hoyson, M.C., Jackson, D.R., Deerinck, T.J., Marrs, G.S., Dehoff, M., Wu, J., Ellisman, M.H., and Spirou, G.A. (2013). Synaptic inputs compete during rapid formation of the calyx of Held: a new model system for neural development. J. Neurosci. Off. J. Soc. Neurosci. 33, 12954–12969.

Holy, T.E., and Leibler, S. (1994). Dynamic instability of microtubules as an efficient way to search in space. Proc. Natl. Acad. Sci. U. S. A. 91, 5682–5685.

Hood, F.E., and Royle, S.J. (2009). Functional equivalence of the clathrin heavy chains CHC17 and CHC22 in endocytosis and mitosis. J. Cell Sci. 122, 2185–2190.

Hood, F.E., Williams, S.J., Burgess, S.G., Richards, M.W., Roth, D., Straube, A., Pfuhl, M., Bayliss, R., and Royle, S.J. (2013). Coordination of adjacent domains mediates TACC3-ch-TOG-clathrin assembly and mitotic spindle binding. J. Cell Biol. 202, 463–478.

Hsu, K.-S., and Toda, T. (2011). Ndc80 internal loop interacts with Dis1/TOG to ensure proper kinetochore-spindle attachment in fission yeast. Curr. Biol. CB 21, 214–220.

Huang, Z.-L., Lin, Z.-R., Xiao, Y.-R., Cao, X., Zhu, L.-C., Zeng, M.-S., Zhong, Q., and Wen, Z.-S. (2015). High expression of TACC3 in esophageal squamous cell carcinoma correlates with poor prognosis. Oncotarget 6, 6850–6861.

Hubner, N.C., Bird, A.W., Cox, J., Splettstoesser, B., Bandilla, P., Poser, I., Hyman, A., and Mann, M. (2010). Quantitative proteomics combined with BAC TransgeneOmics reveals in vivo protein interactions. J. Cell Biol. 189, 739–754.

Hwang, H.C., and Clurman, B.E. (2005). Cyclin E in normal and neoplastic cell cycles. Oncogene 24, 2776–2786.

Ichimura, K., Miyazaki, N., Sadayama, S., Murata, K., Koike, M., Nakamura, K.-I., Ohta, K., and Sakai, T. (2015). Three-dimensional architecture of podocytes revealed by block-face scanning electron microscopy. Sci. Rep. 5, 8993.

Jantsch-Plunger, V., Gönczy, P., Romano, A., Schnabel, H., Hamill, D., Schnabel, R., Hyman, A.A., and Glotzer, M. (2000). CYK-4: A Rho family gtpase activating protein (GAP) required for central spindle formation and cytokinesis. J. Cell Biol. 149, 1391–1404.

Jiang, W., Jimenez, G., Wells, N.J., Hope, T.J., Wahl, G.M., Hunter, T., and Fukunaga, R. (1998). PRC1: a human mitotic spindle-associated CDK substrate protein required for cytokinesis. Mol. Cell 2, 877–885.

Jin, A.J., and Nossal, R. (2000). Rigidity of triskelion arms and clathrin nets. Biophys. J. 78, 1183–1194.

Johansen, K.M., Forer, A., Yao, C., Girton, J., and Johansen, J. (2011). Do nuclear envelope and intranuclear proteins reorganize during mitosis to form an elastic, hydrogel-like spindle matrix? Chromosome Res. Int. J. Mol. Supramol. Evol. Asp. Chromosome Biol. 19, 345–365.

Jokelainen, P.T. (1967). The ultrastructure and spatial organization of the metaphase kinetochore in mitotic rat cells. J. Ultrastruct. Res. 19, 19–44.

Jones, L.A., Villemant, C., Starborg, T., Salter, A., Goddard, G., Ruane, P., Woodman, P.G., Papalopulu, N., Woolner, S., and Allan, V.J. (2014). Dynein light intermediate chains maintain spindle bipolarity by functioning in centriole cohesion. J. Cell Biol. 207, 499–516.

Jung, C.K., Jung, J.H., Park, G.S., Lee, A., Kang, C.S., and Lee, K.Y. (2006). Expression of transforming acidic coiled-coil containing protein 3 is a novel independent prognostic marker in non-small cell lung cancer. Pathol. Int. 56, 503–509.

Kakui, Y., Sato, M., Okada, N., Toda, T., and Yamamoto, M. (2013). Microtubules and Alp7-Alp14 (TACC-TOG) reposition chromosomes before meiotic segregation. Nat. Cell Biol. 15, 786–796.

Kalab, P., and Heald, R. (2008). The RanGTP gradient - a GPS for the mitotic spindle. J. Cell Sci. 121, 1577–1586.

Karsenti, E., Newport, J., Hubble, R., and Kirschner, M. (1984). Interconversion of metaphase and interphase microtubule arrays, as studied by the injection of centrosomes and nuclei into Xenopus eggs. J. Cell Biol. 98, 1730–1745.

Kauffman, E.C., Ricketts, C.J., Rais-Bahrami, S., Yang, Y., Merino, M.J., Bottaro, D.P., Srinivasan, R., and Linehan, W.M. (2014). Molecular genetics and cellular features of TFE3 and TFEB fusion kidney cancers. Nat. Rev. Urol. 11, 465–475.

Kaur, S., Fielding, A.B., Gassner, G., Carter, N.J., and Royle, S.J. (2014). An unmet actin requirement explains the mitotic inhibition of clathrin-mediated endocytosis. eLife 3, e00829.

Kawamura, E., and Wasteneys, G.O. (2008). MOR1, the Arabidopsis thaliana homologue of Xenopus MAP215, promotes rapid growth and shrinkage, and suppresses the pausing of microtubules in vivo. J. Cell Sci. 121, 4114–4123.

Khodjakov, A., Cole, R.W., Oakley, B.R., and Rieder, C.L. (2000). Centrosome-independent mitotic spindle formation in vertebrates. Curr. Biol. CB 10, 59–67.

Khodjakov, A., Copenagle, L., Gordon, M.B., Compton, D.A., and Kapoor, T.M. (2003). Minus-end capture of preformed kinetochore fibers contributes to spindle morphogenesis. J. Cell Biol. 160, 671–683.

Kimura, K., and Hirano, T. (1997). ATP-dependent positive supercoiling of DNA by 13S condensin: a biochemical implication for chromosome condensation. Cell 90, 625–634.

Kinoshita, K., Noetzel, T.L., Pelletier, L., Mechtler, K., Drechsel, D.N., Schwager, A., Lee, M., Raff, J.W., and Hyman, A.A. (2005). Aurora A phosphorylation of TACC3/maskin is required for centrosome-dependent microtubule assembly in mitosis. J. Cell Biol. 170, 1047–1055.

Kirchhausen, T., and Harrison, S.C. (1981). Protein organization in clathrin trimers. Cell 23, 755–761.

Kirschner, M.W., and Mitchison, T. (1986). Microtubule dynamics. Nature 324, 621.
Kiyomitsu, T., and Cheeseman, I.M. (2012). Chromosome- and spindle-pole-derived signals generate an intrinsic code for spindle position and orientation. Nat. Cell Biol. 14, 311–317.

Kleylein-Sohn, J., Pöllinger, B., Ohmer, M., Hofmann, F., Nigg, E.A., Hemmings, B.A., and Wartmann, M. (2012). Acentrosomal spindle organization renders cancer cells dependent on the kinesin HSET. J. Cell Sci. 125, 5391–5402.

Komma, D.J., and Endow, S.A. (1997). Enhancement of the ncdD microtubule motor mutant by mutants of alpha Tub67C. J. Cell Sci. 110 (Pt 2), 229–237.

Kotak, S., Busso, C., and Gönczy, P. (2012). Cortical dynein is critical for proper spindle positioning in human cells. J. Cell Biol. 199, 97–110.

Kufer, T.A., Silljé, H.H.W., Körner, R., Gruss, O.J., Meraldi, P., and Nigg, E.A. (2002). Human TPX2 is required for targeting Aurora-A kinase to the spindle. J. Cell Biol. 158, 617–623.

Kurasawa, Y., Earnshaw, W.C., Mochizuki, Y., Dohmae, N., and Todokoro, K. (2004). Essential roles of KIF4 and its binding partner PRC1 in organized central spindle midzone formation. EMBO J. 23, 3237–3248.

Kuriyama, R., and Borisy, G.G. (1981). Microtubule-nucleating activity of centrosomes in Chinese hamster ovary cells is independent of the centriole cycle but coupled to the mitotic cycle. J. Cell Biol. 91, 822–826.

Kwon, M., Godinho, S.A., Chandhok, N.S., Ganem, N.J., Azioune, A., Thery, M., and Pellman, D. (2008). Mechanisms to suppress multipolar divisions in cancer cells with extra centrosomes. Genes Dev. 22, 2189–2203.

Larijani, B., and Poccia, D.L. (2009). Nuclear envelope formation: mind the gaps. Annu. Rev. Biophys. 38, 107–124.

Le Bot, N., Tsai, M.C., Andrews, R.K., and Ahringer, J. (2003). TAC-1, a regulator of microtubule length in the C. elegans embryo. Curr. Biol. CB 13, 1499–1505.

Lecland, N., and Lüders, J. (2014). The dynamics of microtubule minus ends in the human mitotic spindle. Nat. Cell Biol. 16, 770–778.

Lee, M.J., Gergely, F., Jeffers, K., Peak-Chew, S.Y., and Raff, J.W. (2001). Msps/XMAP215 interacts with the centrosomal protein D-TACC to regulate microtubule behaviour. Nat. Cell Biol. 3, 643–649.

LeRoy, P.J., Hunter, J.J., Hoar, K.M., Burke, K.E., Shinde, V., Ruan, J., Bowman, D., Galvin, K., and Ecsedy, J.A. (2007). Localization of human TACC3 to mitotic spindles is mediated by phosphorylation on Ser558 by Aurora A: a novel pharmacodynamic method for measuring Aurora A activity. Cancer Res. 67, 5362–5370.

Liao, G., Nagasaki, T., and Gundersen, G.G. (1995). Low concentrations of nocodazole interfere with fibroblast locomotion without significantly affecting microtubule level: implications for the role of dynamic microtubules in cell locomotion. J. Cell Sci. 108 (Pt 11), 3473–3483.

Lin, C.-H., Hu, C.-K., and Shih, H.-M. (2010). Clathrin heavy chain mediates TACC3 targeting to mitotic spindles to ensure spindle stability. J. Cell Biol. 189, 1097–1105.
Lince-Faria, M., Maffini, S., Orr, B., Ding, Y., Cláudia Florindo, null, Sunkel, C.E., Tavares, A., Johansen, J., Johansen, K.M., and Maiato, H. (2009). Spatiotemporal control of mitosis by the conserved spindle matrix protein Megator. J. Cell Biol. 184, 647–657.

Liu, D., Vader, G., Vromans, M.J.M., Lampson, M.A., and Lens, S.M.A. (2009). Sensing chromosome bi-orientation by spatial separation of aurora B kinase from kinetochore substrates. Science 323, 1350–1353.

Loïodice, I., Staub, J., Setty, T.G., Nguyen, N.-P.T., Paoletti, A., and Tran, P.T. (2005). Ase1p organizes antiparallel microtubule arrays during interphase and mitosis in fission yeast. Mol. Biol. Cell 16, 1756–1768.

Lopez, B.J., and Valentine, M.T. (2015). Molecular control of stress transmission in the microtubule cytoskeleton. Biochim. Biophys. Acta 1853, 3015–3024.

Ma, L., Tsai, M.-Y., Wang, S., Lu, B., Chen, R., Iii, J.R.Y., Zhu, X., and Zheng, Y. (2009). Requirement for Nudel and dynein for assembly of the lamin B spindle matrix. Nat. Cell Biol. 11, 247–256.

Mack, G.J., and Compton, D.A. (2001). Analysis of mitotic microtubule-associated proteins using mass spectrometry identifies astrin, a spindle-associated protein. Proc. Natl. Acad. Sci. U. S. A. 98, 14434–14439.

Maiato, H., Rieder, C.L., and Khodjakov, A. (2004). Kinetochore-driven formation of kinetochore fibers contributes to spindle assembly during animal mitosis. J. Cell Biol. 167, 831–840.

Maldonado, M., and Kapoor, T.M. (2011). Constitutive Mad1 targeting to kinetochores uncouples checkpoint signalling from chromosome biorientation. Nat. Cell Biol. 13, 475–482.

Malumbres, M., and Barbacid, M. (2005). Mammalian cyclin-dependent kinases. Trends Biochem. Sci. 30, 630–641.

Mandelkow, E.M., Schultheiss, R., Rapp, R., Müller, M., and Mandelkow, E. (1986a). On the surface lattice of microtubules: helix starts, protofilament number, seam, and handedness. J. Cell Biol. 102, 1067–1073.

Mandelkow, E.M., Rapp, R., and Mandelkow, E. (1986b). Microtubule structure studied by quick freezing: cryo-electron microscopy and freeze fracture. J. Microsc. 141, 361–373.

Marais, A., Ji, Z., Child, E.S., Krause, E., Mann, D.J., and Sharrocks, A.D. (2010). Cell cycle-dependent regulation of the forkhead transcription factor FOXK2 by CDK·cyclin complexes. J. Biol. Chem. 285, 35728–35739.

Marc, J. (1997). Microtubule-organizing centres in plants. Trends Plant Sci. 2, 223–230.

Maro, B., Johnson, M.H., Pickering, S.J., and Louvard, D. (1985). Changes in the distribution of membranous organelles during mouse early development. J. Embryol. Exp. Morphol. 90, 287–309.

Marshall, W.F. (2001). Centrioles take center stage. Curr. Biol. CB 11, R487–R496.

Mastronarde, D.N., McDonald, K.L., Ding, R., and McIntosh, J.R. (1993). Interpolar spindle microtubules in PTK cells. J. Cell Biol. 123, 1475–1489.

Masuda, H., McDonald, K.L., and Cande, W.Z. (1988). The mechanism of anaphase spindle elongation: uncoupling of tubulin incorporation and microtubule sliding during in vitro spindle reactivation. J. Cell Biol. 107, 623–633.

Matthies, H.J., McDonald, H.B., Goldstein, L.S., and Theurkauf, W.E. (1996). Anastral meiotic spindle morphogenesis: role of the non-claret disjunctional kinesin-like protein. J. Cell Biol. 134, 455–464.

Mazia, D. (1967). Fibrillar structure in the mitotic apparatus. In Formation and Fate of Cell Organelles, (New York: Academic Press Inc.), pp. 39–54.

McDonald, K.L., Edwards, M.K., and McIntosh, J.R. (1979). Cross-sectional structure of the central mitotic spindle of Diatoma vulgare. Evidence for specific interactions between antiparallel microtubules. J. Cell Biol. 83, 443–461.

McDonald, K.L., O'Toole, E.T., Mastronarde, D.N., and McIntosh, J.R. (1992). Kinetochore microtubules in PTK cells. J. Cell Biol. 118, 369–383.

McEwen, B.F., Arena, J.T., Frank, J., and Rieder, C.L. (1993). Structure of the colcemid-treated PtK1 kinetochore outer plate as determined by high voltage electron microscopic tomography. J. Cell Biol. 120, 301–312.

McEwen, B.F., Heagle, A.B., Cassels, G.O., Buttle, K.F., and Rieder, C.L. (1997). Kinetochore fiber maturation in PtK1 cells and its implications for the mechanisms of chromosome congression and anaphase onset. J. Cell Biol. 137, 1567–1580.

McEwen, B.F., Hsieh, C.E., Mattheyses, A.L., and Rieder, C.L. (1998a). A new look at kinetochore structure in vertebrate somatic cells using high-pressure freezing and freeze substitution. Chromosoma 107, 366–375.

McEwen, B.F., Ding, Y., and Heagle, A.B. (1998b). Relevance of kinetochore size and microtubule-binding capacity for stable chromosome attachment during mitosis in PtK1 cells. Chromosome Res. Int. J. Mol. Supramol. Evol. Asp. Chromosome Biol. 6, 123–132.

McIntosh, J.R., and Landis, S.C. (1971). The distribution of spindle microtubules during mitosis in cultured human cells. J. Cell Biol. 49, 468–497.
McIntosh, J.R., and McDonald, K.L. (1989). The mitotic spindle. Sci. Am. 261, 48–56.

McIntosh, J.R., and Pfarr, C.M. (1991). Mitotic motors. J. Cell Biol. 115, 577–585.

McIntosh, J.R., McDonald, K.L., Edwards, M.K., and Ross, B.M. (1979). Three-dimensional structure of the central mitotic spindle of Diatoma vulgare. J. Cell Biol. 83, 428–442.

McIntosh, J.R., Grishchuk, E.L., and West, R.R. (2002). Chromosome-microtubule interactions during mitosis. Annu. Rev. Cell Dev. Biol. 18, 193–219.

McIntosh, J.R., Grishchuk, E.L., Morphew, M.K., Efremov, A.K., Zhudenkov, K., Volkov, V.A., Cheeseman, I.M., Desai, A., Mastronarde, D.N., and Ataullakhanov, F.I. (2008). Fibrils connect microtubule tips with kinetochores: a mechanism to couple tubulin dynamics to chromosome motion. Cell 135, 322–333.

McIntosh, J.R., Molodtsov, M.I., and Ataullakhanov, F.I. (2012). Biophysics of mitosis. Q. Rev. Biophys. 45, 147–207.

Megraw, T.L., Kao, L.R., and Kaufman, T.C. (2001). Zygotic development without functional mitotic centrosomes. Curr. Biol. CB 11, 116–120.

Mendoza, M., Norden, C., Durrer, K., Rauter, H., Uhlmann, F., and Barral, Y. (2009). A mechanism for chromosome segregation sensing by the NoCut checkpoint. Nat. Cell Biol. 11, 477–483.

Merdes, A., Ramyar, K., Vechio, J.D., and Cleveland, D.W. (1996). A complex of NuMA and cytoplasmic dynein is essential for mitotic spindle assembly. Cell 87, 447–458.

Mikhaylova, M., Cloin, B.M.C., Finan, K., van den Berg, R., Teeuw, J., Kijanka, M.M., Sokolowski, M., Katrukha, E.A., Maidorn, M., Opazo, F., et al. (2015). Resolving bundled microtubules using anti-tubulin nanobodies. Nat. Commun. 6, 7933.

Mikula, S., and Denk, W. (2015). High-resolution whole-brain staining for electron microscopic circuit reconstruction. Nat. Methods 12, 541–546.

Mitchison, T.J. (1989). Polewards microtubule flux in the mitotic spindle: evidence from photoactivation of fluorescence. J. Cell Biol. 109, 637–652.

Mitchison, T.J., and Salmon, E.D. (1992). Poleward kinetochore fiber movement occurs during both metaphase and anaphase-A in newt lung cell mitosis. J. Cell Biol. 119, 569–582.

Mitchison, T., and Kirschner, M. (1984a). Dynamic instability of microtubule growth. Nature 312, 237–242.

Mitchison, T., and Kirschner, M. (1984b). Microtubule assembly nucleated by isolated centrosomes. Nature 312, 232–237.

Mollinari, C., Kleman, J.-P., Jiang, W., Schoehn, G., Hunter, T., and Margolis, R.L. (2002). PRC1 is a microtubule binding and bundling protein essential to maintain the mitotic spindle midzone. J. Cell Biol. 157, 1175–1186.

Mori, Y., Taniyama, Y., Tanaka, S., Fukuchi, H., and Terada, Y. (2015). Microtubule-bundling activity of the centrosomal protein, Cep169, and its binding to microtubules. Biochem. Biophys. Res. Commun. 467, 754–759.

Moritz, M., Braunfeld, M.B., Sedat, J.W., Alberts, B., and Agard, D.A. (1995). Microtubule nucleation by gamma-tubulin-containing rings in the centrosome. Nature 378, 638–640.

Mountain, V., Simerly, C., Howard, L., Ando, A., Schatten, G., and Compton, D.A. (1999). The kinesin-related protein, HSET, opposes the activity of Eg5 and cross-links microtubules in the mammalian mitotic spindle. J. Cell Biol. 147, 351–366.

Moutinho-Santos, T., Sampaio, P., Amorim, I., Costa, M., and Sunkel, C.E. (1999). In vivo localisation of the mitotic POLO kinase shows a highly dynamic association with the mitotic apparatus during early embryogenesis in Drosophila. Biol. Cell Auspices Eur. Cell Biol. Organ. 91, 585–596.

Musacchio, A. (2011). Spindle assembly checkpoint: the third decade. Philos. Trans. R. Soc. Lond. B. Biol. Sci. 366, 3595–3604.

Musacchio, A., and Hardwick, K.G. (2002). The spindle checkpoint: structural insights into dynamic signalling. Nat. Rev. Mol. Cell Biol. 3, 731–741.

Musacchio, A., and Salmon, E.D. (2007). The spindle-assembly checkpoint in space and time. Nat. Rev. Mol. Cell Biol. 8, 379–393.

Muscat, C.C., Torre-Santiago, K.M., Tran, M.V., Powers, J.A., and Wignall, S.M. (2015). Kinetochore-independent chromosome segregation driven by lateral microtubule bundles. eLife 4, e06462.

Nasmyth, K., Peters, J.M., and Uhlmann, F. (2000). Splitting the chromosome: cutting the ties that bind sister chromatids. Science 288, 1379–1385.

Neef, R., Grüneberg, U., and Barr, F.A. (2005). Assay and functional properties of Rabkinesin-6/Rab6-KIFL/MKlp2 in cytokinesis. Methods Enzymol. 403, 618–628.

Nezi, L., and Musacchio, A. (2009). Sister chromatid tension and the spindle assembly checkpoint. Curr. Opin. Cell Biol. 21, 785–795.

Nicklas, R.B. (1983). Measurements of the force produced by the mitotic spindle in anaphase. J. Cell Biol. 97, 542–548.

Nicklas, R.B., Kubai, D.F., and Hays, T.S. (1982). Spindle microtubules and their mechanical associations after micromanipulation in anaphase. J. Cell Biol. 95, 91–104.

Nigg, E.A. (2001). Mitotic kinases as regulators of cell division and its checkpoints. Nat. Rev. Mol. Cell Biol. 2, 21–32.

Nigg, E.A., Čajánek, L., and Arquint, C. (2014). The centrosome duplication cycle in health and disease. FEBS Lett. 588, 2366–2372.

Nikonova, A.S., Astsaturov, I., Serebriiskii, I.G., Dunbrack, R.L., and Golemis, E.A. (2013). Aurora A kinase (AURKA) in normal and pathological cell division. Cell. Mol. Life Sci. CMLS 70, 661–687.

Nixon, F.M., Gutiérrez-Caballero, C., Hood, F.E., Booth, D.G., Prior, I.A., and Royle, S.J. (2015). The mesh is a network of microtubule connectors that stabilizes individual kinetochore fibers of the mitotic spindle. eLife 4.

Norden, C., Mendoza, M., Dobbelaere, J., Kotwaliwale, C.V., Biggins, S., and Barral, Y. (2006). The NoCut pathway links completion of cytokinesis to spindle midzone function to prevent chromosome breakage. Cell 125, 85–98.

Nurse, P. (1990). Universal control mechanism regulating onset of M-phase. Nature 344, 503–508.

Nwagbara, B.U., Faris, A.E., Bearce, E.A., Erdogan, B., Ebbert, P.T., Evans, M.F., Rutherford, E.L., Enzenbacher, T.B., and Lowery, L.A. (2014). TACC3 is a microtubule plus end-tracking protein that promotes axon elongation and also regulates microtubule plus end dynamics in multiple embryonic cell types. Mol. Biol. Cell 25, 3350–3362.

Oakley, B.R., and Heath, I.B. (1978). The arrangement of microtubules in serially sectioned spindles of the alga Cryptomonas. J. Cell Sci. 31, 53–70.

O'Brien, L.L., Albee, A.J., Liu, L., Tao, W., Dobrzyn, P., Lizarraga, S.B., and Wiese, C. (2005). The Xenopus TACC homologue, maskin, functions in mitotic spindle assembly. Mol. Biol. Cell 16, 2836–2847.

Odajima, J., Wills, Z.P., Ndassa, Y.M., Terunuma, M., Kretschmannova, K., Deeb, T.Z., Geng, Y., Gawrzak, S., Quadros, I.M., Newman, J., et al. (2011). Cyclin E constrains Cdk5 activity to regulate synaptic plasticity and memory formation. Dev. Cell 21, 655–668.

Okamoto, C.T., McKinney, J., and Jeng, Y.Y. (2000). Clathrin in mitotic spindles. Am. J. Physiol. Cell Physiol. 279, C369–C374.

Pannu, V., Rida, P.C.G., Ogden, A., Turaga, R.C., Donthamsetty, S., Bowen, N.J., Rudd, K., Gupta, M.V., Reid, M.D., Cantuaria, G., et al. (2015). HSET overexpression fuels tumor progression via centrosome clustering-independent mechanisms in breast cancer patients. Oncotarget 6, 6076–6091.
Pereira, G., and Schiebel, E. (1997). Centrosome-microtubule nucleation. J. Cell Sci. 110 (Pt 3), 295–300.

Peretti, D., Maraschio, P., Lambiase, S., Lo Curto, F., and Zuffardi, O. (1986). Indirect immunofluorescence of inactive centromeres as indicator of centromeric function. Hum. Genet. 73, 12–16.

Peset, I., Seiler, J., Sardon, T., Bejarano, L.A., Rybina, S., and Vernos, I. (2005). Function and regulation of Maskin, a TACC family protein, in microtubule growth during mitosis. J. Cell Biol. 170, 1057–1066.

Pickett-Heaps, J., Spurck, T., and Tippit, D. (1984). Chromosome motion and the spindle matrix. J. Cell Biol. 99, 137s – 143s.

Pines, J., and Rieder, C.L. (2001). Re-staging mitosis: a contemporary view of mitotic progression. Nat. Cell Biol. 3, E3–E6.

Preble, A.M., Giddings, T.M., and Dutcher, S.K. (2000). Basal bodies and centrioles: their function and structure. Curr. Top. Dev. Biol. 49, 207–233.

Qi, H., Rath, U., Wang, D., Xu, Y.-Z., Ding, Y., Zhang, W., Blacketer, M.J., Paddy, M.R., Girton, J., Johansen, J., et al. (2004). Megator, an essential coiled-coil protein that localizes to the putative spindle matrix during mitosis in Drosophila. Mol. Biol. Cell 15, 4854–4865.

Qi, H., Rath, U., Ding, Y., Ji, Y., Blacketer, M.J., Girton, J., Johansen, J., and Johansen, K.M. (2005). EAST interacts with Megator and localizes to the putative spindle matrix during mitosis in Drosophila. J. Cell. Biochem. 95, 1284–1291.

Radford, S.J., Jang, J.K., and McKim, K.S. (2012). The chromosomal passenger complex is required for meiotic acentrosomal spindle assembly and chromosome biorientation. Genetics 192, 417–429.

Raemaekers, T., Ribbeck, K., Beaudouin, J., Annaert, W., Van Camp, M., Stockmans, I., Smets, N., Bouillon, R., Ellenberg, J., and Carmeliet, G. (2003). NuSAP, a novel microtubule-associated protein involved in mitotic spindle organization. J. Cell Biol. 162, 1017–1029.

Raff, J.W., Jeffers, K., and Huang, J.-Y. (2002). The roles of Fzy/Cdc20 and Fzr/Cdh1 in regulating the destruction of cyclin B in space and time. J. Cell Biol. 157, 1139–1149.

Rath, U., Wang, D., Ding, Y., Xu, Y.-Z., Qi, H., Blacketer, M.J., Girton, J., Johansen, J., and Johansen, K.M. (2004). Chromator, a novel and essential chromodomain protein interacts directly with the putative spindle matrix protein skeletor. J. Cell. Biochem. 93, 1033–1047.

Reynolds, E.S. (1963). The use of lead citrate at high pH as an electron-opaque stain in electron microscopy. J. Cell Biol. 17, 208–212.

Ribbeck, K., Groen, A.C., Santarella, R., Bohnsack, M.T., Raemaekers, T., Köcher, T., Gentzel, M., Görlich, D., Wilm, M., Carmeliet, G., et al. (2006). NuSAP, a mitotic RanGTP target that stabilizes and cross-links microtubules. Mol. Biol. Cell 17, 2646–2660.

Rieder, C.L. (1981). Effect of hypothermia (20-25 degrees C) on mitosis in PtK1 cells. Cell Biol. Int. Rep. 5, 563–573.

Rieder, C.L. (1982). The formation, structure, and composition of the mammalian kinetochore and kinetochore fiber. Int. Rev. Cytol. 79, 1–58.

Rieder, C.L. (2005). Kinetochore fiber formation in animal somatic cells: dueling mechanisms come to a draw. Chromosoma 114, 310–318.

Rieder, C.L., and Borisy, G.G. (1981). The attachment of kinetochores to the pro-metaphase spindle in PtK1 cells. Recovery from low temperature treatment. Chromosoma 82, 693–716.

Robinson, M.S. (1994). The role of clathrin, adaptors and dynamin in endocytosis. Curr. Opin. Cell Biol. 6, 538–544.
Roth, T.F., and Porter, K.R. (1964). Yolk protein uptake in the oocyte of the mosquito aedes aegypti. L. J. Cell Biol. 20, 313–332.

Royle, S.J., and Lagnado, L. (2006). Trimerisation is important for the function of clathrin at the mitotic spindle. J. Cell Sci. 119, 4071–4078.

Royle, S.J., Bright, N.A., and Lagnado, L. (2005). Clathrin is required for the function of the mitotic spindle. Nature 434, 1152–1157.

Russell, P., and Nurse, P. (1986). cdc25+ functions as an inducer in the mitotic control of fission yeast. Cell 45, 145–153.

Sadek, C.M., Pelto-Huikko, M., Tujague, M., Steffensen, K.R., Wennerholm, M., and Gustafsson, J.-A. (2003). TACC3 expression is tightly regulated during early differentiation. Gene Expr. Patterns GEP 3, 203–211.

Sato, M., Vardy, L., Angel Garcia, M., Koonrugsa, N., and Toda, T. (2004). Interdependency of fission yeast Alp14/TOG and coiled coil protein Alp7 in microtubule localization and bipolar spindle formation. Mol. Biol. Cell 15, 1609–1622.

Sauer, G., Körner, R., Hanisch, A., Ries, A., Nigg, E.A., and Silljé, H.H.W. (2005). Proteome analysis of the human mitotic spindle. Mol. Cell. Proteomics MCP 4, 35–43.

Saxton, W.M., and McIntosh, J.R. (1987). Interzone microtubule behavior in late anaphase and telophase spindles. J. Cell Biol. 105, 875–886.

Saxton, W.M., Stemple, D.L., Leslie, R.J., Salmon, E.D., Zavortink, M., and McIntosh, J.R. (1984). Tubulin dynamics in cultured mammalian cells. J. Cell Biol. 99, 2175–2186.

Schatz, C.A., Santarella, R., Hoenger, A., Karsenti, E., Mattaj, I.W., Gruss, O.J., and Carazo-Salas, R.E. (2003). Importin alpha-regulated nucleation of microtubules by TPX2. EMBO J. 22, 2060–2070.

Schmidt, J.C., Arthanari, H., Boeszoermenyi, A., Dashkevich, N.M., Wilson-Kubalek, E.M., Monnier, N., Markus, M., Oberer, M., Milligan, R.A., Bathe, M., et al. (2012). The kinetochore-bound Ska1 complex tracks depolymerizing microtubules and binds to curved protofilaments. Dev. Cell 23, 968–980.

Schnapp, B.J., and Reese, T.S. (1989). Dynein is the motor for retrograde axonal transport of organelles. Proc. Natl. Acad. Sci. U. S. A. 86, 1548–1552.

Schneider, L., Essmann, F., Kletke, A., Rio, P., Hanenberg, H., Wetzel, W., Schulze-Osthoff, K., Nürnberg, B., and Piekorz, R.P. (2007). The transforming acidic coiled coil 3 protein is essential for spindle-dependent chromosome alignment and mitotic survival. J. Biol. Chem. 282, 29273–29283.

Schneider, L., Essmann, F., Kletke, A., Rio, P., Hanenberg, H., Schulze-Osthoff, K., Nürnberg, B., and Piekorz, R.P. (2008). TACC3 depletion sensitizes to paclitaxel-induced cell death and overrides p21WAF-mediated cell cycle arrest. Oncogene 27, 116–125.

Schrader, F. (1953). Mitosis, the Movements of Chromosomes in Cell Division (New York: Columbia University Press).

Schroer, T.A., Steuer, E.R., and Sheetz, M.P. (1989). Cytoplasmic dynein is a minus end-directed motor for membranous organelles. Cell 56, 937–946.

Schweizer, N., Weiss, M., and Maiato, H. (2014). The dynamic spindle matrix. Curr. Opin. Cell Biol. 28, 1–7.

Schweizer, N., Pawar, N., Weiss, M., and Maiato, H. (2015). An organelle-exclusion envelope assists mitosis and underlies distinct molecular crowding in the spindle region. J. Cell Biol. 210, 695–704.

Sharp, D.J., Yu, K.R., Sisson, J.C., Sullivan, W., and Scholey, J.M. (1999). Antagonistic microtubule-sliding motors position mitotic centrosomes in Drosophila early embryos. Nat. Cell Biol. 1, 51–54.

Sharp, D.J., Rogers, G.C., and Scholey, J.M. (2000a). Microtubule motors in mitosis. Nature 407, 41–47.

Sharp, D.J., Brown, H.M., Kwon, M., Rogers, G.C., Holland, G., and Scholey, J.M. (2000b). Functional coordination of three mitotic motors in Drosophila embryos. Mol. Biol. Cell 11, 241–253.

Sherr, C.J., and Roberts, J.M. (1999). CDK inhibitors: positive and negative regulators of G1-phase progression. Genes Dev. 13, 1501–1512.

Shimamoto, Y., Maeda, Y.T., Ishiwata, S. 'ichi, Libchaber, A.J., and Kapoor, T.M. (2011). Insights into the micromechanical properties of the metaphase spindle. Cell 145, 1062–1074.

Sikirzhytski, V., Magidson, V., Steinman, J.B., He, J., Le Berre, M., Tikhonenko, I., Ault, J.G., McEwen, B.F., Chen, J.K., Sui, H., et al. (2014). Direct kinetochore-spindle pole connections are not required for chromosome segregation. J. Cell Biol. 206, 231–243.

Silljé, H.H.W., Nagel, S., Körner, R., and Nigg, E.A. (2006). HURP is a Ran-importin beta-regulated protein that stabilizes kinetochore microtubules in the vicinity of chromosomes. Curr. Biol. CB 16, 731–742.

Singh, D., Chan, J.M., Zoppoli, P., Niola, F., Sullivan, R., Castano, A., Liu, E.M., Reichel, J., Porrati, P., Pellegatta, S., et al. (2012). Transforming fusions of FGFR and TACC genes in human glioblastoma. Science 337, 1231–1235.

Spurck, T., Forer, A., and Pickett-Heaps, J. (1997). Ultraviolet microbeam irradiations of epithelial and spermatocyte spindles suggest that forces act on the kinetochore fibre and are not generated by its disassembly. Cell Motil. Cytoskeleton 36, 136–148.

Srayko, M., Kaya, A., Stamford, J., and Hyman, A.A. (2005). Identification and characterization of factors required for microtubule growth and nucleation in the early C. elegans embryo. Dev. Cell 9, 223–236.

Steffen, W., Fuge, H., Dietz, R., Bastmeyer, M., and Müller, G. (1986). Aster-free spindle poles in insect spermatocytes: evidence for chromosome-induced spindle formation? J. Cell Biol. 102, 1679–1687.

Steigemann, P., Wurzenberger, C., Schmitz, M.H.A., Held, M., Guizetti, J., Maar, S., and Gerlich, D.W. (2009). Aurora B-mediated abscission checkpoint protects against tetraploidization. Cell 136, 473–484.

Subramanian, R., Wilson-Kubalek, E.M., Arthur, C.P., Bick, M.J., Campbell, E.A., Darst, S.A., Milligan, R.A., and Kapoor, T.M. (2010). Insights into antiparallel microtubule crosslinking by PRC1, a conserved nonmotor microtubule binding protein. Cell 142, 433–443.

Sutherland, H.G., Mumford, G.K., Newton, K., Ford, L.V., Farrall, R., Dellaire, G., Cáceres, J.F., and Bickmore, W.A. (2001). Large-scale identification of mammalian proteins localized to nuclear sub-compartments. Hum. Mol. Genet. 10, 1995–2011.

Szollosi, D., Calarco, P., and Donahue, R.P. (1972). Absence of centrioles in the first and second meiotic spindles of mouse oocytes. J. Cell Sci. 11, 521–541.

Tanaka, T.U., Rachidi, N., Janke, C., Pereira, G., Galova, M., Schiebel, E., Stark, M.J.R., and Nasmyth, K. (2002). Evidence that the Ipl1-Sli15 (Aurora kinase-INCENP) complex promotes chromosome bi-orientation by altering kinetochore-spindle pole connections. Cell 108, 317–329.

Tang, N.H., Takada, H., Hsu, K.-S., and Toda, T. (2013). The internal loop of fission yeast Ndc80 binds Alp7/TACC-Alp14/TOG and ensures proper chromosome attachment. Mol. Biol. Cell 24, 1122–1133.

Terry, L.J., Shows, E.B., and Wente, S.R. (2007). Crossing the nuclear envelope: hierarchical regulation of nucleocytoplasmic transport. Science 318, 1412–1416.

Thadani, R., Ling, Y.C., and Oliferenko, S. (2009). The fission yeast TACC protein Mia1p stabilizes microtubule arrays by length-independent crosslinking. Curr. Biol. CB 19, 1861–1868.

Thein, K.H., Kleylein-Sohn, J., Nigg, E.A., and Gruneberg, U. (2007). Astrin is required for the maintenance of sister chromatid cohesion and centrosome integrity. J. Cell Biol. 178, 345–354.

Theurkauf, W.E., Smiley, S., Wong, M.L., and Alberts, B.M. (1992). Reorganization of the cytoskeleton during Drosophila oogenesis: implications for axis specification and intercellular transport. Dev. Camb. Engl. 115, 923–936.

Tikhonenko, I., Irizarry, K., Khodjakov, A., and Koonce, M.P. (2015). Organization of microtubule assemblies in Dictyostelium syncytia depends on the microtubule crosslinker, Ase1. Cell. Mol. Life Sci. CMLS.

Tiwari, S.C., Wick, S.M., Williamson, R.E., and Gunning, B.E. (1984). Cytoskeleton and integration of cellular function in cells of higher plants. J. Cell Biol. 99, 63s – 69s.

Touriol, C., Greenland, C., Lamant, L., Pulford, K., Bernard, F., Rousset, T., Mason, D.Y., and Delsol, G. (2000). Further demonstration of the diversity of chromosomal changes involving 2p23 in ALK-positive lymphoma: 2 cases expressing ALK kinase fused to CLTCL (clathrin chain polypeptide-like). Blood 95, 3204–3207.

Tournebize, R., Popov, A., Kinoshita, K., Ashford, A.J., Rybina, S., Pozniakovsky, A., Mayer, T.U., Walczak, C.E., Karsenti, E., and Hyman, A.A. (2000). Control of microtubule dynamics by the antagonistic activities of XMAP215 and XKCM1 in Xenopus egg extracts. Nat. Cell Biol. 2, 13–19.

Tsou, A.-P., Yang, C.-W., Huang, C.-Y.F., Yu, R.C.-T., Lee, Y.-C.G., Chang, C.-W., Chen, B.-R., Chung, Y.-F., Fann, M.-J., Chi, C.-W., et al. (2003). Identification of a novel cell cycle regulated gene, HURP, overexpressed in human hepatocellular carcinoma. Oncogene 22, 298–307.

Tulu, U.S., Fagerstrom, C., Ferenz, N.P., and Wadsworth, P. (2006). Molecular requirements for kinetochore-associated microtubule formation in mammalian cells. Curr. Biol. CB 16, 536–541.

Uehara, R., Nozawa, R., Tomioka, A., Petry, S., Vale, R.D., Obuse, C., and Goshima, G. (2009). The augmin complex plays a critical role in spindle microtubule generation for mitotic progression and cytokinesis in human cells. Proc. Natl. Acad. Sci. U. S. A. 106, 6998–7003.

Uhlmann, F., Lottspeich, F., and Nasmyth, K. (1999). Sister-chromatid separation at anaphase onset is promoted by cleavage of the cohesin subunit Scc1. Nature 400, 37–42.

Uhlmann, F., Wernic, D., Poupart, M.A., Koonin, E.V., and Nasmyth, K. (2000). Cleavage of cohesin by the CD clan protease separin triggers anaphase in yeast. Cell 103, 375–386.

Wainman, A., Buster, D.W., Duncan, T., Metz, J., Ma, A., Sharp, D., and Wakefield, J.G. (2009). A new Augmin subunit, Msd1, demonstrates the importance of mitotic spindle-templated microtubule nucleation in the absence of functioning centrosomes. Genes Dev. 23, 1876–1881.

Walczak, C.E., Verma, S., and Mitchison, T.J. (1997). XCTK2: a kinesin-related protein that promotes mitotic spindle assembly in Xenopus laevis egg extracts. J. Cell Biol. 136, 859–870.

Walker, D.L., Wang, D., Jin, Y., Rath, U., Wang, Y., Johansen, J., and Johansen, K.M. (2000). Skeletor, a novel chromosomal protein that redistributes during mitosis provides evidence for the formation of a spindle matrix. J. Cell Biol. 151, 1401–1412.
Wang, H., Brust-Mascher, I., and Scholey, J.M. (2014). Sliding filaments and mitotic spindle organization. Nat. Cell Biol. 16, 737–739.

Warner, F.D. (1976). Ciliary inter-microtubule bridges. J. Cell Sci. 20, 101–114.

Weisenberg, R.C., Deery, W.J., and Dickinson, P.J. (1976). Tubulin-nucleotide interactions during the polymerization and depolymerization of microtubules. Biochemistry (Mosc.) 15, 4248–4254.

Welburn, J.P.I., Grishchuk, E.L., Backer, C.B., Wilson-Kubalek, E.M., Yates, J.R., and Cheeseman, I.M. (2009). The human kinetochore Ska1 complex facilitates microtubule depolymerization-coupled motility. Dev. Cell 16, 374–385.

Welburn, J.P.I., Vleugel, M., Liu, D., Yates, J.R., Lampson, M.A., Fukagawa, T., and Cheeseman, I.M. (2010). Aurora B phosphorylates spatially distinct targets to differentially regulate the kinetochore-microtubule interface. Mol. Cell 38, 383–392.

Williams, S.V., Hurst, C.D., and Knowles, M.A. (2013). Oncogenic FGFR3 gene fusions in bladder cancer. Hum. Mol. Genet. 22, 795–803.

Wilson, E.B. (1925). Cell In Development And Heredity (New York: Macmillan Company).

Wilson, H.J. (1969). Arms and bridges on microtubules in the mitotic apparatus. J. Cell Biol. 40, 854–859.

Witt, P.L., Ris, H., and Borisy, G.G. (1981). Structure of kinetochore fibers: microtubule continuity and inter-microtubule bridges. Chromosoma 83, 523–540.

Woodard, G.E., Huang, N.-N., Cho, H., Miki, T., Tall, G.G., and Kehrl, J.H. (2010). Ric-8A and Gi alpha recruit LGN, NuMA, and dynein to the cell cortex to help orient the mitotic spindle. Mol. Cell. Biol. 30, 3519–3530.

Wurzenberger, C., and Gerlich, D.W. (2011). Phosphatases: providing safe passage through mitotic exit. Nat. Rev. Mol. Cell Biol. 12, 469–482.

Yamada, K.M., Spooner, B.S., and Wessells, N.K. (1971). Ultrastructure and function of growth cones and axons of cultured nerve cells. J. Cell Biol. 49, 614–635.

Yang, C.H., and Snyder, M. (1992). The nuclear-mitotic apparatus protein is important in the establishment and maintenance of the bipolar mitotic spindle apparatus. Mol. Biol. Cell 3, 1259–1267.

Ybe, J.A., Greene, B., Liu, S.H., Pley, U., Parham, P., and Brodsky, F.M. (1998). Clathrin self-assembly is regulated by three light-chain residues controlling the formation of critical salt bridges. EMBO J. 17, 1297–1303.

Ye, F., Tan, L., Yang, Q., Xia, Y., Deng, L.-W., Murata-Hori, M., and Liou, Y.-C. (2011). HURP regulates chromosome congression by modulating kinesin Kif18A function. Curr. Biol. CB 21, 1584–1591.

Zaytsev, A.V., and Grishchuk, E.L. (2015). Basic mechanism for biorientation of mitotic chromosomes is provided by the kinetochore geometry and indiscriminate turnover of kinetochore microtubules. Mol. Biol. Cell 26, 3985–3998.

Zheng, Z., Wan, Q., Liu, J., Zhu, H., Chu, X., and Du, Q. (2013). Evidence for dynein and astral microtubule-mediated cortical release and transport of Gαi/LGN/NuMA complex in mitotic cells. Mol. Biol. Cell 24, 901–913.

Zhu, C., and Jiang, W. (2005). Cell cycle-dependent translocation of PRC1 on the spindle by Kif4 is essential for midzone formation and cytokinesis. Proc. Natl. Acad. Sci. U. S. A. 102, 343–348.